Thèse
de doctorat
de l'UTT

Zihao GUO

Experimental Study and Multi-scale Modeling of Stainless Steel Evolutions Induced by SMAT

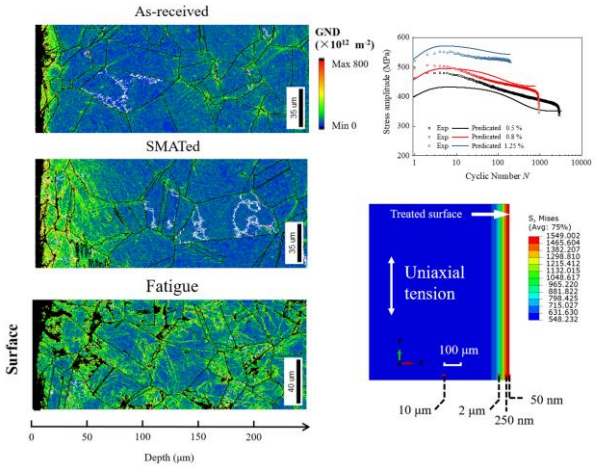

Champ disciplinaire :
Sciences pour l'Ingénieur

2024TROY0040

Année 2024

utt
UNIVERSITÉ DE TECHNOLOGIE
TROYES

THESE

pour l'obtention du grade de

DOCTEUR
de l'UNIVERSITE DE TECHNOLOGIE DE TROYES

en SCIENCES POUR L'INGENIEUR

Spécialité : MATERIAUX, MECANIQUE, OPTIQUE ET NANOTECHNOLOGIE

présentée et soutenue par

Zihao GUO

le 4 décembre 2024

Experimental Study and Multi-scale Modeling of Stainless Steel Evolutions Induced by SMAT

JURY

M. Thierry GROSDIDIER	PROFESSEUR DES UNIVERSITES	Président
M. Lahouari BENABOU	PROFESSEUR DES UNIVERSITES	Rapporteur
Mme Marion RISBET	PROFESSEURE DES UNIVERSITES	Rapporteure
M. Laurent DELANNAY	PROFESSEUR	Examinateur
M. Xavier FEAUGAS	PROFESSEUR DES UNIVERSITES	Examinateur
Mme Delphine RETRAINT	PROFESSEURE DES UNIVERSITES	Examinatrice
M. Benoît PANICAUD	PROFESSEUR DES UNIVERSITES	Directeur de thèse
M. Zhidan SUN	PROFESSEUR ASSOCIE UTT	Directeur de thèse

Acknowledgment

First and foremost, I would like to extend my deepest gratitude to my supervisors, Prof. Benoît PANICAUD and Dr Zhidan SUN, for their kind support and patient guidance throughout my PhD journey at UTT. Their guidance has been instrumental in cultivating my research skills and academic habits, contributing significantly to both my personal and professional growth. I am also profoundly grateful to Prof. Delphine RETRAINT, for insightful comments and constructive feedback on my thesis, which greatly enhanced the quality of my work.

In addition, I appreciate Dr Bruno GUELORGET, Prof. Manuel FRANCOIS and Mr. Matthieu STRUB for their technical expertise and assistance with the experiments. Their contributions were crucial to the successful completion of my PhD thesis.

I would like to express my sincere appreciation to my colleagues at UTT and my friends in Troyes for their camaraderie and support, both academically and personally. They are Yufei GONG, Tingting ZHAI, Yuhan ZHAO, Yufeng SHUAI, Zhihao GAO, Guanting WU, Ke CAO, Hui CHEN, and Xiao LIU. Their presence has made this journey all the more enriching.

My heartfelt thanks go to my family and relatives, whose unwavering love and encouragement have been my greatest source of strength. Their belief in me and constant support have made this achievement possible. Forever love to my wife Zhenyi WANG. Thank you for your companionship, which has given me a peaceful and cozy home in Troyes with ErGOU and Mika. I still found you in a world so vast.

Zihao GUO

Sep. 2024, at Troyes

Abstract

This work explores the mechanical response and associated microstructural evolution of SMATed materials. Comprehensive experimental analyses are conducted to investigate the in-depth microhardness, residual stress and microstructures in SMATed 316L stainless steel using nanoindentation, XRD, and EBSD, respectively. The cyclic deformation response of SMATed 316L stainless steel is also analyzed at different strain amplitudes to examine the macroscopic low cycle fatigue behavior. In addition, comparative analyses of microstructures between as-received and SMATed samples provide insights into both macroscopic and microscopic behavior during low cycle fatigue.

A dislocation density-based model, incorporating transformation-induced plasticity, twinning-induced plasticity and grain size effects, is introduced to describe the tensile responses, particularly considering the different stacking fault energy associated with the deformation mechanisms. The influence of dynamic twinning and residual stress on tensile response is studied using a 2D finite element model. Moreover, a physically-based model is developed to link the cyclic deformation response with the corresponding microstructural evolution. The effects of grain size and mechanical twining on cyclic deformation behavior are considered.

Keywords: Surface treatment, Stainless steel, Microstructure, Strain hardening, Low cycle fatigue, Multiscale modeling

Résumé

Ce travail explore la réponse mécanique et l'évolution microstructurale associée d'aciers inoxydables traités par SMAT. Des analyses expérimentales complètes sont menées pour étudier en profondeur la microdureté, les contraintes résiduelles et les microstructures dans un acier inoxydable 316L traité par SMAT, en utilisant respectivement la nanoindentation, la diffraction des rayons X et la diffraction des électrons rétrodiffusés. La réponse à la déformation cyclique de l'acier traité par SMAT est également analysée à différentes amplitudes de déformation, afin d'examiner le comportement macroscopique en fatigue oligocyclique. De plus, des analyses comparatives des microstructures entre des échantillons à l'état initial et des échantillons traités par SMAT fournissent des informations sur le comportement macroscopique et microscopique pendant la fatigue oligocyclique.

Un modèle basé sur la densité de dislocations, incorporant la plasticité induite par transformation, la plasticité induite par maclage et les effets de la taille des grains, est introduit pour décrire les réponses en traction, en tenant particulièrement compte des différentes énergies de défaut d'empilement associées aux mécanismes de déformation. L'influence du maclage dynamique et des contraintes résiduelles sur la réponse en traction est étudiée à l'aide d'un modèle par éléments finis en 2D. De plus, un modèle basé sur des principes physiques est développé pour relier la réponse à la déformation cyclique à l'évolution microstructurale correspondante. Les effets de la taille des grains et du maclage mécanique sur les comportements de déformation cyclique sont pris en compte.

Mots-clés : Traitements de surface, Acier inoxydable, Microstructure (physique), Écrouissage, Fatigue oligocyclique, Modélisation multi-échelle

Contents

Acknowledgment I
Abstract II
Résumé III
Contents IV
List of figures VII
List of tables XII
List of abbreviations and acronyms XIII
General introduction 1
Chapter 1: Literature review 5
1.1 Introduction to SMAT 5
1.2 Surface nanocrystallization mechanisms during the SMAT process 6
1.3 Multi-gradient microstructure materials 9
1.3.1 Sources of strengthening 10
1.3.2 Influence of dislocations 11
1.3.3 Deformation twinning and phase transformation 14
1.3.4 Residual stresses 16
1.4 Mechanical behaviors of gradient-microstructure materials 17
1.4.1 Tensile properties and strain hardening 17
1.4.2 Fatigue properties 21
1.5 Modeling of gradient-microstructure materials 25
1.5.1 Simulation of SMAT process 25
1.5.2 Modeling of GMS material 26
1.5.3 Plasticity modeling of 316L during cyclic loading 27
1.6 Conclusion 28
Chapter 2: Materials characterization 29
2.1 Material preparation and SMAT process 29
2.1.1 Material 29
2.1.2 SMAT process 30
2.1.3 Material preparation 31
2.2 Microstructure characteristics by EBSD observations 32
2.2.1 Crystal orientation 33
2.2.2 Grain size and grain boundaries 35
2.2.3 Misorientation and dislocation 36
2.2.4 Inhomogeneity deformation 41
2.3 Hardness and Young's modulus measurements 42

2.4 Residual stress analysis by grazing-incidence X-ray diffraction 46
2.4.1 Grazing-incidence X-ray diffraction method 47
2.4.2 Experimental procedures 50
2.4.3 Results 51
2.5 Conclusion 55
Chapter 3: Experimental study of LCF behavior of SMATed 316L SS 57
3.1 Experimental procedures for fatigue tests 57
3.2 Cyclic deformation behavior under symmetric loading in LCF conditions 59
3.2.1 Hysteresis loops 59
3.2.2 Effective stress and back stress 64
3.3 Effect of asymmetric loading on the LCF behavior 67
3.3.1 Cyclic stress response 67
3.3.2 Bauschinger effect 70
3.4 Microstructure investigation of as-received 316L SS 73
3.4.1 Microstructure characteristics of the fatigued specimen without SMAT 73
3.4.2 Microstructure evolution during cyclic loading without SMAT 76
3.4.3 Relationships between back stresses and GND 80
3.6 Conclusion 81
Chapter 4: Influence of TRIP and TWIP effects on deformation behavior based on a dislocation density model 83
4.1 Model description of twinning and martensitic transformation 83
4.1.1 Formation of martensite and twin 83
4.1.2 Evolution of martensite and twin 86
4.1.3 Evolution of dislocation density 87
4.2 Microstructures evolution of 304 SS with TWIP/TRIP effects 89
4.2.1 Grain size and SFE dependent deformation mechanisms 89
4.2.2 Parameters associated with microstructure evolution of 304 SS during tension 92
4.3 Conclusions 94
Chapter 5: Tensile behavior of SMATed TWIP 316L SS accounting for residual fields 96
5.1 Depth-dependent residual fields 96
5.1.1 Distribution of grain size and twin 96
5.1.2. Distribution of residual stress 98
5.1.3. Distribution of initial dislocation density 99
5.2 Constitutive model for GMS material 100
5.2.1 Evolution of yield stress 101
5.2.2. Evolution of dislocation density including twinning 101
5.3 Finite element model 103
5.3.1 FE model for tensile simulation 104

5.3.2 Validation of stress-strain relationship and yield strength 105
5.3 Simulation results of microstructural quantities and discussion 108
5.3.3 Effect of residual stress in GMS 108
5.3.4 Predicted evolution of twin volume fraction 111
5.3.5 Dislocation density distribution within GMS 112
5.3.6. Effect of deformation twinning in GMS 113
5.4 Conclusions 117
Chapter 6: Cycle deformation response and microstructure 119
6.1 Relationships between macroscale response and microstructure 119
6.1.1 Summary of cycle stress response 119
6.1.2 SFE dependence deformation mechanism 122
6.1.3 Strain amplitude dependent deformation mechanism 123
6.1.4 Grain size dependent deformation mechanism 123
6.2 Dislocation-based internal stresses model 124
6.3 Results on stress evolution and discussion 126
6.3.1 Modeling of cyclic deformation response for as-received 316L SS 126
6.3.2 Influence of grain size on cyclic deformation response 127
6.3.3 Effect of deformation twinning on cyclic deformation response 129
6.3.4 Effect of gradient microstructure on cyclic deformation response 131
6.4 Conclusions 132
Chapter 7: Conclusions and prospects 133
7.1 Conclusion 133
7.2 Prospects 135
Résumé en français 138
Appendix 170
Appendix A: Numerical integration 170
Appendix B: Consistent tangent modulus 172
References 175

List of figures

Fig. 1-1. Schematic illustrations of (a) the SMAT set-up and (b) localized plastic deformation in the surface layer caused by the impact of a shot [66]. 6

Fig. 1-2. Deformation-controlling mechanisms (dislocation slip, deformation twinning and martensite transformation) vary with different SFE as a function of temperature [74]. 7

Fig. 1-3. Schematic illustrations of grain refinement in SMATed materials with (a) high SFE [11], (b) low SFE [69] and (c) moderate SFE [13]. 9

Fig. 1-4. EBSD observations on the cross-section of a SMATed 316L SS specimen. (a) typical microstructure observed in a periphery region, and (b) mechanically affected region showing three different areas: (c) edge periphery area, (d) intermediate area and (e) ultra-fine grain area [48]..... 9

Fig. 1-5. (a) Variation of average grain sizes along depth [9], and (b) tensile yield strength as a function of the inverse square root of mean grain size using measurement results for 316L as reported in [8]..... 11

Fig. 1-6. (a) GND map obtained from EBSD measurement in 316L SS after 20 min SMAT with 60 μm vibrating amplitude, and (b) The corresponding evolution of the average GND density (black dots) and the indexing rate (red dots) from the top surface. [35]. 12

Fig. 1-7. Microstructural parameters of a SMATed steel, including crystallite size, dislocation density and twin density evaluated by XRD [80]. 14

Fig. 1-8. (a) A schematic illustration of gradient microstructure of SMATed sample [97], (b) volume fraction of phase content (γ austenite and α'-martensite) with depth in SMATed 304 SS, distinguishing between low impact velocity (SMAT-L) and high impact velocity (SMAT-H), and (c) critical twin thickness (λ) and twin density at different depths in the SMAT-H sample [98]..... 15

Fig. 1-9. Schematic illustration of twinning and martensite transformation processes for an austenitic 304 SS [95]. 16

Fig. 1-10. In-depth distribution of residual stress after SMAT [100]. 17

Fig. 1-11. (a) Tensile response with engineering stress-strain curves for the nanocrystalline layer produced by SMAT on 301 SS with different durations, and the CG bulk material [102], and (b) the trade-off relationship between strength and uniform elongation influenced by different microstructures and strengthening of GMS materials [103]..... 18

Fig. 1-12. Evolution of strain hardening rate (Θ) associated with uniaxial tension behavior presented in Fig.1-11a. The vertical dotted lines illustrate the separation between the three Θ stages for a homogeneous CG sample [102]. 19

Fig. 1-13. (a) Hardness evolution with tensile strains along the depth in GMS 304 SS sample and in as-annealed CG sample for comparison [105], and (b) Variation of hardness increment of nanocrystalline interstitial free steel samples subjected to various tensile strains (0.05, 0.1 and 0.25) with respect to the depth [110]. 21

Fig. 1-14. S-N curves of different treatment conditions for SMAT 316L SS samples and as-received sample for comparison [30]. 22

Fig. 1-15. Microstructural evolution for a strain amplitude of ±0.4% observed in LCF tests for 316L SS observed by TEM [86]. 24

Fig. 1-16. Schematic illustration of the inter-granular dislocation evolution during the accommodation of plastic deformation in a polycrystalline material. 25

Fig. 1-17. Illustration of homogenization scheme used in the multi-scale simulations by CPFEM approach [12]. 27

Fig. 2-1. Cylindrical shape specimens of as-received and SMATed 316L SS for testing. 30

Fig. 2-2. Schematic diagram of the experimental setup to perform SMAT on cylindrical specimens. 31

Fig. 2-3. Embedded specimens within resin, prepared for further measurements and characterization. 31

Fig. 2-4. Scanning electron microscopy with an EBSD detector, used at LASMIS laboratory. 33

Fig. 2-5. EBSD maps of IPF overlaid with IQ on cross-section of as-received and SMATed samples. The deformation-induced twin is highlighted within a rectangular zone marked by a red dashed line. 34

Fig. 2-6. EBSD maps of IQ with boundaries for both the as-received and SMATed samples. LAGBs are marked by the green lines, HAGBs by the blue lines and twin boundaries (TB) by the red lines, respectively. 35

Fig. 2-7. In-depth average grain size evolution for both the as-received and SMATed samples. 36

Fig. 2-8. Schematic diagram of the KAM calculation method. 37

Fig. 2-9. EBSD maps of KAM on cross-section of as-received and SMATed samples, with threshold angle 5°. 38

Fig. 2-10. (a) GND maps of cross-section and (b) in-depth average GND distribution of both as-received and SMATed samples, with and without correction of the sample preparation. 40

Fig. 2-11. (a) GOS and (b) GROD maps on cross-section of as-received and SMATed samples. White color indicates that the GOS value is below the critical threshold for undeformed grains. 42

Fig. 2-12. Nano indenter®XP instrumented indentation system, used at LASMIS laboratory. 44

Fig. 2-13. Load-depth curves at different depths. 45

Fig. 2-14. Variation as a function of depth from the treated surface for SMATed specimens (a) hardness and (b) Young's modulus. 46

Fig. 2-15. (a) XRD goniometer with detector and X-rays source, used at LASMIS laboratory and (b) geometry configuration of the grazing incident and $\sin^2\psi$ method.

..... 47

Fig. 2-16. The mean penetration depth with $\sin^2\psi$ for various incident angles..... 48

Fig. 2-17. Intensity versus 2θ angle XRD pattern of a SMATed 316 SS sample with different incident angles for (a) – (c): the Miller indices {111} peak at φ angles of 0°, 45°, and 90°, respectively; (d) the Miller indices {200} peak; and (e) the Miller indices {220} peak. 52

Fig. 2-18. $\ln 1\sin\theta - \ln 1\sin\theta 0$ with $\sin^2\psi$ of a SMATed 316L SS and Fe powder at φ = 0°. 54

Fig. 2-19. Stress variations of different components on the near surface of (a) SMATed samples and (b) stress-free Fe powder. 55

Fig. 3-1. The servo-hydraulic fatigue testing system with a cylindrical specimen. 58

Fig. 3-2. Selected hysteresis loops of (a) as-received and (b) SMATed 316L SS samples, at strain amplitudes of 0.5 %, 0.8 % and 1.25 % under symmetric loading (load ratio R = −1)..... 61

Fig. 3-3. Stress amplitude versus the number of cycles for (a) as-received and (b) SMATed 316L SS samples, at strain amplitudes of 0.5 %, 0.8 % and 1.25 % under symmetric loading (load ratio R = −1). Note that the cycle numbers are represented on a logarithmic scale. (c) is the predicted relationship of strain amplitude and fatigue life of as-received and SMATed 316L SS samples. (d) Cyclic hardening/softening degree for all the samples (positive values indicate hardening, while negative values indicate softening). 63

Fig. 3-4. (a) Scheme for partition of hysteresis loops to identify the yield stress, back stress and effective stress by the Cottrell's method and (b) evolutions of maximum stress, effective stress and back stress as a function of number of cycles at strain amplitude of 0.5 %. 65

Fig. 3-5. Comparison of the evolutions of (a) effective stress and (b) back stress as function of the accumulated plastic strain, between the as-received and SMATed 316L samples. 67

Fig. 3-6. Scheme for symmetric and asymmetric of strain-control LCF..... 68

Fig. 3-7. Selected stress–strain hysteresis loops of (a) as-received and (b) SMATed 316L SS samples, at strain amplitudes of 0.5 %, 0.8 % and 1.25 % under asymmetric loading (R = -0.5). 69

Fig. 3-8. Cyclic stress amplitude curves under different strain amplitudes of (a) as-received; (b) SMATed samples, with symmetric and asymmetric loadings. 70

Fig. 3-9. First hysteresis loop of as-received and SMATed 316L samples, at different strain amplitudes under (a) symmetric and (b) asymmetric loading. 72

Fig. 3-10. EBSD maps of IPF overlaid with IQ on the cross-section of the as-received sample after fatigue test at strain amplitude of 1.25 % under symmetric loading... 74

Fig. 3-11. (a) EBSD maps of KAM and (b) GND maps on cross-section (c) In-depth average GND based on the GND maps; of the fatigued sample at strain amplitude of 1.25 % under symmetric loading. 75

Fig. 3-12. (a) GOS and (b) GROD maps on cross-section of the fatigued sample at strain amplitude of 1.25 % under symmetric loading. White color in the middle indicates that the GOS value is below the threshold for undeformed grains..... 76

Fig. 3-13. IPF maps on cross-section at strain amplitudes of 0.5 %, 0.8 % and1.25 % in columns, and at different cycle numbers of as-received, 4th, 20th and failure in rows, under symmetric loading. 77

Fig. 3-14. GND maps on cross-section at strain amplitudes of 0.5 %, 0.8 % and1.25 % in columns, and at different cycle numbers of as-received, 4th,20th and failure in rows, under symmetric loading. 79

Fig. 3-15. Average (a) GND and (b) GOS at different cycle numbers of as-received, 4th, 20th and failure under symmetric loading. 80

Fig. 4-1. Schematic diagram of the formation and evolution mechanism of ε-martensite, twin and α'-martensite [202], [206]. 84

Fig. 4-2. Evolution of critical shear stress (solid line) and stacking fault width (dashed line) in ε-martensite (red) and twinning (blue) calculated with Eqs. 4-1,4-1a to 1c..... 90

Fig. 4-3. Variation of nucleation rate with (a) SFE for a grain size of 15 μm and (b) grain size with SFE = 17.8 mJ/m^2, calculated from Eqs. 4-4a to 4c..... 91

Fig. 4-4. (a) Lengths and (b) volume fractions versus axial strain of ε-martensite, twinning and α'-martensite. (c) macroscale stress-strain curve and strain hardening rate as function of axial strain. Corresponding experimental data of 304 SS are displayed by scattering points at (b) and (c) during tensile loading. (d) Contributions of martensite, twinning, and dislocation to the stress-strain relationship. 93

Fig. 4-5. Predicted evolution of dislocation density versus strain. 94

Fig. 5-1. In-depth distribution profiles of (a) grain size and twin thickness; (b) twin volume fraction. 98

Fig. 5-2. In-depth distribution of residual stress after SMAT. 99

Fig. 5-3. In-depth distribution profiles of initial dislocation density and accumulated plastic strain. 100

Fig. 5-4. Section of a SMATed sample: (a) geometrical model and boundary conditions, (b) FE model showing the mesh. 105

Fig. 5-5. Comparison between numerical and experimental results on the yield strength versus grain size. 106

Fig. 5-6. (a) Comparison of predicted local stress-strain curve between nanocrystalline and coarse grains, and (b) comparison of predicted overall stress-strain curve between untreated structure and GMS during uniaxial tensile loading. 107

Fig. 5-7 (a) Distributions of von Mises stress after tensile loading, and (b) stress-strain curve at different grain sizes with residual stress (in solid line) and without residual stress (in dashed line). 109

Fig. 5-8. Evolution of equivalent plastic strain during tensile loading (at a strain of 0.2 along Y-axis). 110

Fig. 5-9. (a) Distributions of initial twin volume fraction (b) Predicted evolution of twin

volume fraction with different grain sizes (corresponding to different depths beneath the SMATed surface). 112

Fig. 5-10. (a) Distribution of dislocation density after tensile loading, and (b) predicted evolution of dislocation density with different grain sizes. 113

Fig. 5-11. Evolution of twin volume fraction with different twinning conditions at different grain sizes. 114

Fig. 5-12. Predicted evolution of dislocation density and stress-strain curve with four different grain sizes (10 μm, 2 μm, 250 nm and 50 nm). 116

Fig. 6-1. Schematic illustration of the cyclic stress response with different stages of as-received material in strain-controlled LCF. 121

Fig. 6-2. Schematic illustration of microstructure evolution at different stages of the fatigue cycle, including (stage I) initial hardening, (stage II) softening and (stage III) unstable section. The first row corresponds to high SFE values, while the second row corresponds to low SFE values. 121

Fig. 6-3. (a) Back stress, (b) effective stress and (c) cyclic stress response versus cyclic number of as-received 316L SS with different strain amplitudes. Data points represent the experimental data obtained from the Chapter 3, while the solid lines indicate predicted curves. 127

Fig. 6-4. Cyclic stress response with cyclic number of 316L SS with different grain sizes at a strain amplitude 0.6 %. Scattered data points represent experimental data obtained from the literature [277], while the solid lines indicate predicted curves obtained from the model. 129

Fig. 6-5. Predicted values of inter-granular and intra-granular back stress at different grain sizes. 129

Fig. 6-6. (a) Twinning volume fraction of samples after fatigue for different strain amplitudes, (b) twinning volume fraction evolutions with cyclic number, (c) cyclic stress response versus cyclic number of commercial-purity titanium under different strain amplitudes. Scattered data points represent experimental data obtained from the literature [265], while the solid lines indicate predicted curves obtained from the model. 130

List of tables

Table 2-1. Reference positions for austenite diffraction peaks under Cr radiation. 51

Table 3-1 Low cycle fatigue testing conditions. 59

Table 3-2. Fatigue life of as-received and SMATed at different strain amplitudes. 60

Table 3-3. The yield stress and reverse yield stress. 73

Table 4-1. The parameters of dislocation density-based model. 91

Table 5-1. The parameters of grain size and twinning models. 97

Table 5-2. The parameters of residual stress reconstruction model. 99

Table 5-3. Material parameters for the model of GMS 104

List of abbreviations and acronyms

Abbreviation	Word or phrase
CG	coarse-grained
CMSG	conventional mechanism-based strain gradient plasticity
CPFEM	crystal plasticity finite element method
DTs	dislocation tangles
DWs	dislocation walls
EBSD	electron backscatter diffraction
FEM	finite element method
GMS	gradient-microstructured
GND	geometrically necessary dislocations
SEM	scanning electron microscopy
SMAT	surface mechanical attrition treatment
SFE	stacking fault energy
SPD	severe plastic deformation
SS	stainless steel
SSD	statistically stored dislocations
TEM	transmission electron microscopy
TRIP	transformation-induced plasticity
TWIP	twinning-induced plasticity
XRD	X-ray diffraction
LCF	low cycle fatigue
IPF	inverse pole figure
IQ	image quality
LAGBs	low angle grain boundaries
HAGBs	high angle grain boundaries

General introduction

In engineering practice, most of ruin effects of materials, such as wear, corrosion, fracture, impact and fatigue, occur on their surface [1], [2], [3], [4], [5], [6]. Surface enhancement technologies have been well-recognized as an effective strategy to optimize surface conditions and enhance the overall mechanical properties of metallic materials through a trade-off between strength and ductility [7], [8], [9], [10]. Gradient microstructures, extending from the top surface to the central bulk, are a common feature of surface-strengthened components. These microstructures significantly increase material strength, particularly due to the presence of nanocrystalline grains on the top surface [11], [12], [13]. Over the past decades, various techniques have been developed to produce gradient-microstructured materials (GMS), such as electrodeposition [14], [15], laser shock peening [16], [17], [18], severe plastic deformation (SPD), surface chemical heat treatment [19], [20], [21], etc. Among them, SPD treatment provides an efficient method to improve the mechanical properties without changing the chemical compositions of materials. This typically includes surface mechanical grinding treatment (SMGT) [1], [22], [23], ultrasonic surface rolling process (USRP) [24], [25], surface mechanical attrition treatment (SMAT) [5], [10], [11], [26], [27]. During SPD processes, the accumulative plastic deformation is introduced locally on the treated surface and gradually reduced to the interior. This process fabricates gradient microstructures associated with gradient plastic strain and strain rate along depth.

Low-carbon austenitic stainless steel (SS) is widely used in the automotive, aerospace, rail, and nuclear industries [1], [5], [28], [29], [30], [31], [32]. However, it has low mechanical strength and poor anti-friction properties, which limits its potential applications. SMAT provides a promising way to improve strength and surface hardness of such materials by forming gradient microstructures. Consequently, SMATed metallic materials have attracted significant scientific interest over the past few years [10], [33], [34], [35].

Experimental studies have demonstrated that SMAT significantly enhances strength by transforming coarse grains into nanocrystalline grains on the top surface, with process known as surface nanocrystallization [11], [12], [13], [36], [37], [38], [39], [40].

Given the promising application potential of SMAT, extensive research has been conducted on microstructure evolution to reveal the formation mechanism of such surface nanocrystallization, as well as optimizing treatment conditions to further improve mechanical properties. The in-depth investigations of the microstructure and the effects of treatment conditions in experimental studies have shown that the deformation mechanisms of SMATed materials are highly influenced by their crystal structure and stacking fault energy (SFE) [33], [34], [41]. On the one hand, the impact of SMAT on materials was investigated by analyzing both macroscale mechanical properties and microstructural evolution during uniaxial tensile loadings. During monotonic deformation, the gradient microstructure in the near-surface region enhances strength, while the central bulk region contributes to ductility, thereby improving the overall mechanical properties [42], [43], [44]. On the other hand, the fatigue properties of SMATed materials have been investigated through analysis of cyclic deformation behavior and fractography [30], [45], [46], [47], [48]. The results of fatigue tests have demonstrated that the fatigue life and resistance of SMATed samples are considerably improved, as compared to as-received samples under both low cycle fatigue (LCF) or high cycle fatigue (HCF) conditions.

From a theoretical point of view, current research primarily focuses on microstructure-based deformation mechanisms in GMS during monotonic deformation, including dislocation movement, twinning and martensite transformation [49], [50], [51], [52], [53]. However, these methods typically take into account the gradient grain size and dislocation density. In contrast, the residual fields of GMS generated during the SPD processes, such as residual stresses, initial volume fraction and thickness of microstructures, are generally not considered or often overlooked. In order to comprehensively and accurately investigate the mechanical properties of GMS obtained by SMAT, it would be highly beneficial to take these residual fields into account. Although simulations of GMS have already been conducted using combined grain size-dependent and dislocation density-based constitutive models, there is still room for exploring size-dependent deformation twinning. Few investigations have been performed on the initiation and dynamic evolution of twinning in gradient grain size. Most studies of LCF properties have focused on hardening and softening behavior, often modeled and fitted using Armstrong-Frederick or Chaboche models. There are also fewer investigations of cyclic behavior based on physical models to examine the underlying deformation mechanisms during cyclic loading.

This work aims to investigate the mechanical properties, including uniaxial tension and LCF, of GMS obtained by SMAT, through multi-scale experiments and numerical simulations. The objectives of the present work are:

- To experimentally measure the effects of SMAT on the microstructure, deformation inhomogeneity, microhardness and residual stress in 316L SS.
- To experimentally study the influence of SMAT and asymmetric loading on the LCF properties at the macro-length scale;
- To explore the relationship between macroscale cyclic behavior and microstructure evolution, with particular emphasis on geometrically necessary dislocations (GND).
- To develop a size-dependent and dislocation density-based constitutive model to analyze the LCF properties taking into account residual fields;
- To investigate the effect of grain size-dependent deformation twinning on the tensile properties of GMS materials.
- To develop a grain size-dependent and dislocation density-based cyclic plasticity model to describe the cyclic hardening/softening behavior, incorporating the TWIP effect and grain size.

The structure of this manuscript is outlined as follows: In Chapter 1, a comprehensive literature review is presented, providing an overview of SMAT technology and grain refinement mechanisms. Mechanical properties, including tensile and fatigue behaviors, are analyzed alongside microstructure evolution during deformation. Chapter 2 presents the SMAT process and examines the effect of SMAT on the microstructure gradient using Electron BackScatter Diffraction (EBSD). The inhomogeneous deformation is analyzed based on GNDs and grain orientation spread. Additionally, microhardness and Young's modulus are evaluated through nanoindentation, while near-surface residual stress is measured using grazing-incidence X-Ray Diffraction (XRD). Chapter 3 investigates the LCF behavior of both as-received and SMATed 316L SS, through the effective stress and back stress extracted from hysteresis loops. The effect of asymmetric loading on the LCF behavior is also analyzed, focusing on cyclic stress response and the Bauschinger effect. The microstructure evolution of as-received 316L SS is examined based on EBSD observations to explore the evolution of back stress associated with GNDs during cyclic deformation. In Chapter 4, a size-dependent dislocation density-based constitutive model incorporating

Stacking Fault Energy (SFE) is developed to investigate the influence of deformation mechanisms on tensile behavior. The model is implemented using MATLAB to analyze how these factors affect material response under tension. In Chapter 5, the size-dependent and dislocation density-based constitutive model is introduced and implemented using user material subroutines UMAT of Abaqus. In addition, existing experimental observations of gradient microstructures are summarized and expressed numerically with depth-dependent formulations of residual fields to be incorporated into the model. For the finite element simulations, a two-dimensional (2D) axisymmetric cylindrical structure model is built to predict the mechanical response influenced by twinning in a SMATed 316L SS. In Chapter 6, a grain size-dependent and dislocation density-based cyclic plasticity model is developed to describe the cyclic hardening/softening behavior, taking into account the TWIP effect and grain size. Based on the results obtained from experiments and simulations. Chapter 7 draws the main conclusions of this project, and provides an outlook on future research directions, highlighting areas for further investigation and development.

Chapter 1: Literature review

1.1 Introduction to SMAT

The mechanical properties, such as toughness or yield strength or fatigue resistance, of material surfaces highly influence failures that originate from the surface [22], [54], [55], [56], [57]. As a result, surface treatment technologies using severe plastic deformation (SPD) have attracted significant scientific interest over the past decades to improve mechanical properties of materials. Surface mechanical attrition treatment (SMAT), a type of SPD method, forms a gradient-microstructured (GMS) layer on material surfaces, resulting in significantly enhanced yield strength and fatigue resistance. SMAT was first introduced by K. Lu and J. Lu in 1999 [58]. It originates from the conventional shot peening process but involves random directions and high-frequency impact of balls generated by a vibration generator through a sonotrode [45], [49], [59]. Fig. 1-1a schematically represents the experimental set-up of SMAT process. The sample is placed in the reflecting chamber and repeatedly impacted by shots. As shown in Fig. 1-1b, the high strain and strain rate deformation is induced by each impact in the near-surface layer of the sample. The depth of the affected plastic zone increases with the kinetic energy of the shot. Consequently, the repeated multidirectional impacts with SPD induce surface nanocrystallization and leading to a notable increase in yield strength. It should be noted that the strengthening effect is closely related to the grain size and thickness of the nanostructured surface layer. These factors are associated with material properties and SMAT conditions, including shot diameter, treatment duration, shot material, shot velocity, and other parameters [24], [27], [51], [60], [61], [62], [63]. For example, Yang et al.[64] found that the strengthening effect is more significant for the tensile mechanical behaviors in SMATed copper when the volume fraction of the gradient-microstructured layer is within a certain range (with fraction between 0.2 and 0.3). This results in a combination of higher yield strength and uniform elongation. The tensile results also indicate that yield strength increases with longer SMAT duration and different numbers of balls [65].

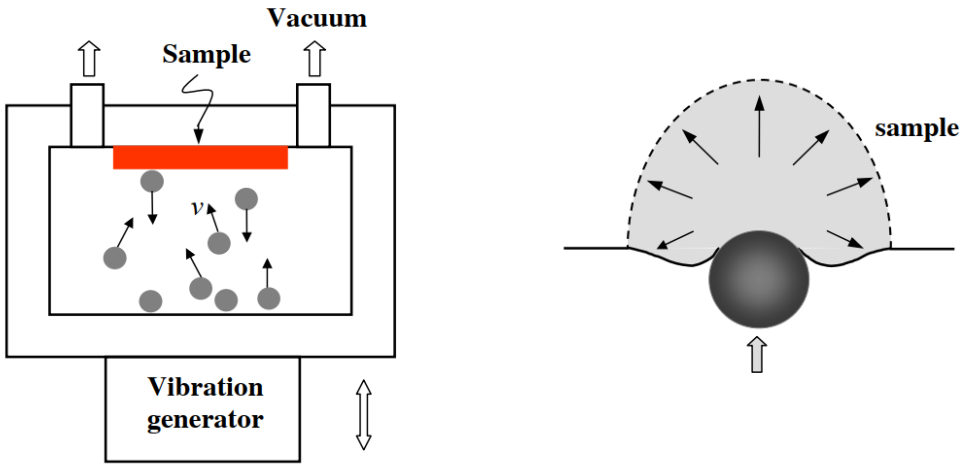

(a) (b)

Fig. 1-1. Schematic illustrations of (a) the SMAT set-up and (b) localized plastic deformation in the surface layer caused by the impact of a shot [66].

1.2 Surface nanocrystallization mechanisms during the SMAT process

Nanocrystalline metals, characterized by an average grain size of less than 100 nm, typically demonstrate remarkable strength due to an increased proportion of grain boundaries, although this is often accompanied by reduced ductility [1], [2], [11], [22], [25]. As mentioned above, the micrometric grains of materials are refined to the nanometer scale on the top surface layer without changing their chemical composition by means of SMAT. Therefore, plastic deformation-induced surface nanocrystallization is crucial for understanding and developing SMAT. Many experimental characterizations have been systematically carried out to reveal the mechanisms of nanocrystallization formation and evolution using scanning electron microscopy (SEM) or transmission electron microscopy (TEM) [11], [67], [68], [69]. As the SMAT-induced strain and strain rate decrease from the top surface layer to the strain-free bulk material, various microstructures are observed at different depths. The SMAT parameters influence the grain refinement process, thereby determining the grain size and volume fraction of the gradient microstructured layer [31], [40], [60], [64], [70], [71], [72].

Previous studies showed that stacking fault energy (SFE) has a substantial impact on strain-induced grain refinement [13], [66], [73]. Recent investigations about the influences of SFE on the deformation mechanisms are shown in Fig. 1-2. It indicates

that deformation twinning is promoted at a range of 20 – 60 mJ/m^2. In contrast, martensitic transformation occurs when SFE is less than 20 mJ/m^2, whereas dislocation glide can be favored at SFE exceeding 60 mJ/m^2. Note that the magnitude of SFE is influenced by additional chemical elements, temperature and strain conditions [41], [61], [73]. The tensile behaviors of SMATed Cu-Al-Zn alloys with different SFE, achieved by modifying chemical composition, are investigated based on their microstructural characteristics [73]. The results show that the strength of the alloys can be improved by reducing the SFE and increasing the SMAT duration. It can be inferred that martensitic transformation and deformation twinning contribute to the materials' strength through additional strengthening mechanisms.

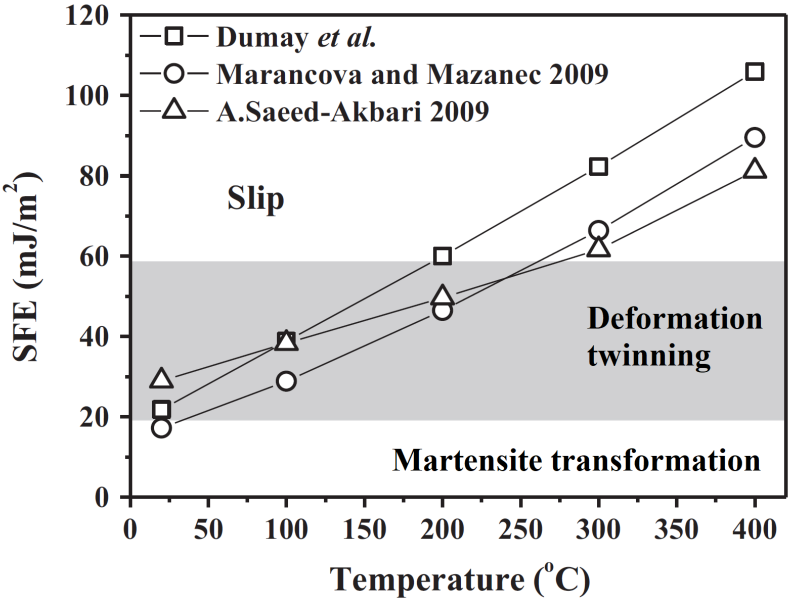

Fig. 1-2. Deformation-controlling mechanisms (dislocation slip, deformation twinning and martensite transformation) vary with different SFE as a function of temperature [74].

The three typical processes of grain refinement can be seen in Fig. 1-3, illustrating that materials with different SFE have different deformation and grain refinement mechanisms. First, metallic materials with high SFE typically exhibit plastic deformation behavior dominated by dislocation activities, as observed in materials such as Fe [11], W [67] and α-Ti [26]. A schematic diagram illustrating the nanocrystallization mechanism of pure Fe is shown in Fig. 1-3a, where dislocation walls (DWs) and dislocation tangles (DTs) are formed within grains to accommodate

plastic deformation. These DWs and DTs gradually transform into sub-boundaries with small misorientations, which then further evolve into high-angle grain boundaries through dislocation glide. Ultimately, a stable nano-scale grain size is achieved.

Second, in contrast, mechanical twinning dominates the plastic deformation process within low SFE metals, commonly observed in materials such as 304 stainless steel [75], [76], Cu-Ti alloy [27] and pure Ti [68]. Fig. 1-3b shows the grain refinement process of low SFE metals, which involves extensive formation of planar dislocation arrays, twins and their intersections. This process ultimately leads to grain sub-division by providing high angle grain boundaries [6], [76], [77].

Third, materials with moderate SFE are typically controlled by mechanisms that involve a combination of dislocation activities and mechanical twinning [13]. Several researchers have comprehensively investigated the nanocrystallization mechanisms of 316L, as illustrated in Fig.1-3c [5], [13], [39], [78]. Cell blocks and DWs facilitate the grain sub-division during the initial deformation stages. Subsequently, the DWs split into micro-bands and shear bands, which undergo dynamic recrystallization and recrystallization twinning to eventually form nanocrystalline grains.

(a) (b)

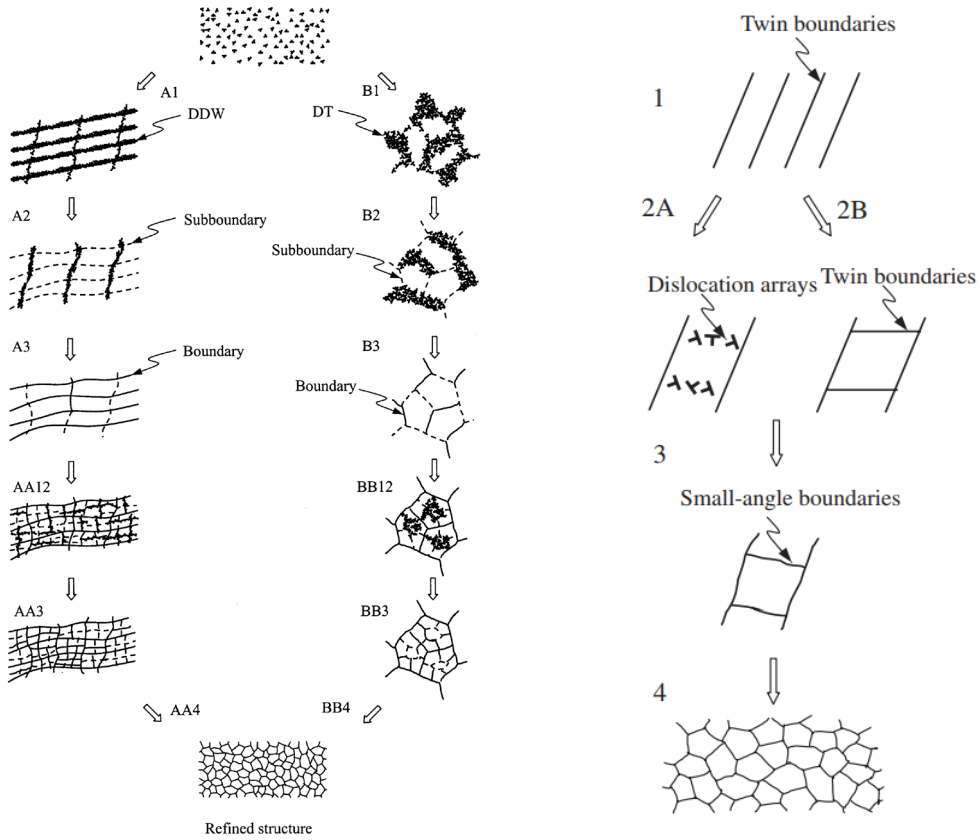

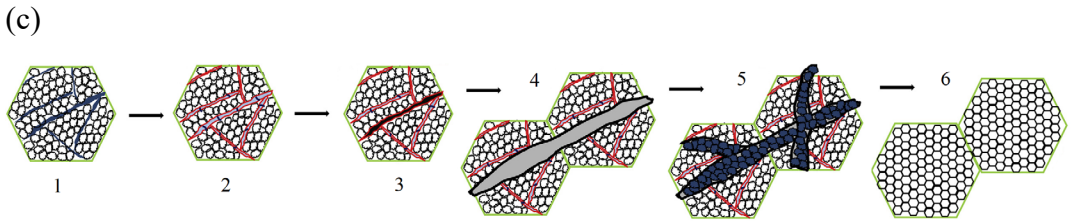

Fig. 1-3. Schematic illustrations of grain refinement in SMATed materials with (a) high SFE [11], (b) low SFE [69] and (c) moderate SFE [13].

1.3 Multi-gradient microstructure materials

During the SMAT process, a complex microstructure is induced due to the gradient strain distribution, which has been extensively investigated using TEM, optical microscopy, EBSD or XRD [7], [18], [23], [35], [51], [67], [79]. GMS materials typically exhibit multiple gradient features such as grain size, deformation twinning, and martensite transformation from the top surface to the central bulk region. Fig. 1-4 shows gradient microstructures on the cross-section of a SMATed 316L SS specimen observed using EBSD. There are three typical regions which can be distinguished: Zone I, featuring ultra-fine grain areas with nanocrystalline grains in a highly deformed region (Fig. 1-4e); Zone II, an intermediate area where the original grains are partially transformed into nanocrystalline grains (Figs. 1-4c and 1-4d); Zone III, an undeformed or strain-free region in the bulk material (Fig. 1-4a).

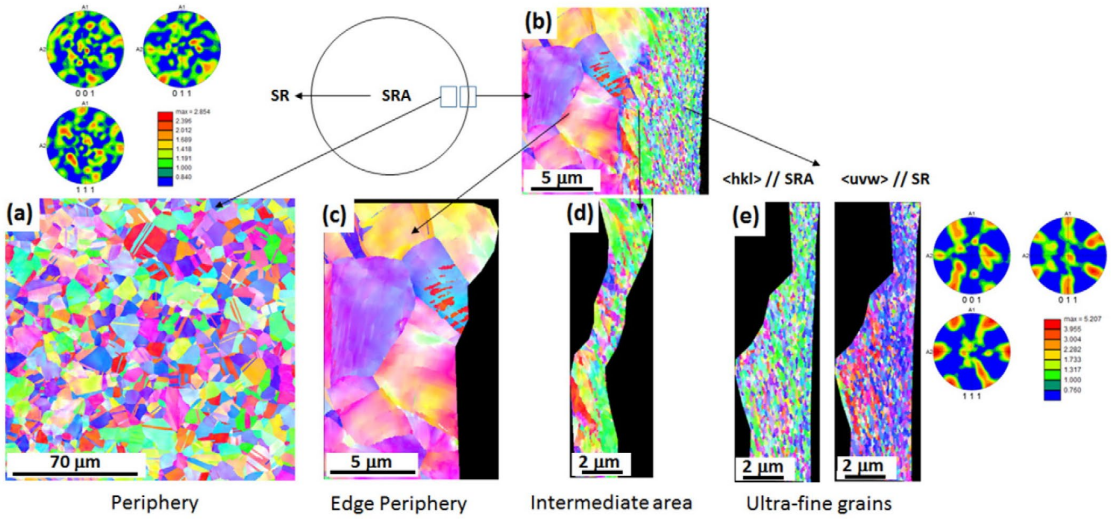

Fig. 1-4. EBSD observations on the cross-section of a SMATed 316L SS specimen. (a) typical microstructure observed in a periphery region, and (b) mechanically affected

region showing three different areas: (c) edge periphery area, (d) intermediate area and (e) ultra-fine grain area [48].

1.3.1 Sources of strengthening

By means of SMAT, a grain size distribution from the nanometer scale to several microns is thus generated along the depth from the top surface to the bulk of SMATed samples, as shown in Fig. 1-5a. Generally, the refined grains and large quantities of dislocations are two major sources of strengthening in GMS materials with high SFE [7], [13], [49], [71], [80]. The increase in yield stress caused by grain boundaries can be estimated by the Hall-Petch model [81], [82]. As shown in Fig. 1-5b, there is a linear relationship between tensile yield strength and the inverse square root of mean grain size reported from measurement results for 316L, meaning that the Hall-Petch relation is valid. It is noted that there can be a limitation of the grain boundary strengthening due to the grain rotation and grain boundary sliding processes when the grain size is reduced to the nanoscale [27], [62], [66]. In addition, the well-known Taylor relationship can be used to describe the increase in yield stress σ_y caused by the isotropic hardening related to the dislocation interactions. Therefore, the yield stress evolution can be determined with the contributions of both stored dislocations and grain size [24], [38], [65] according to:

$$\sigma_y = \sigma_0 + \frac{k_{HP}}{\sqrt{D}} + M\alpha\mu b\sqrt{\rho} \qquad \text{(Eq. 1-1)}$$

where σ_0 is the lattice friction stress; k_{HP} is the Hall-Petch slope; D is the grain size; M is the Taylor factor; α is a material constant around 0.3; μ is the shear modulus; b is the Burger vector norm; ρ is the dislocation density.

Additionally, deformation twinning further enhances strength by accumulating dislocations at the twin boundaries in both low and intermediate SFE materials [57], [80]. In low SFE materials, martensitic transformation contributes to material strengthening, as martensite possesses a higher yield strength than austenite phase [76]. Detailed strengthening mechanisms are further discussed in Sections 1.3.3 and 1.4.1.

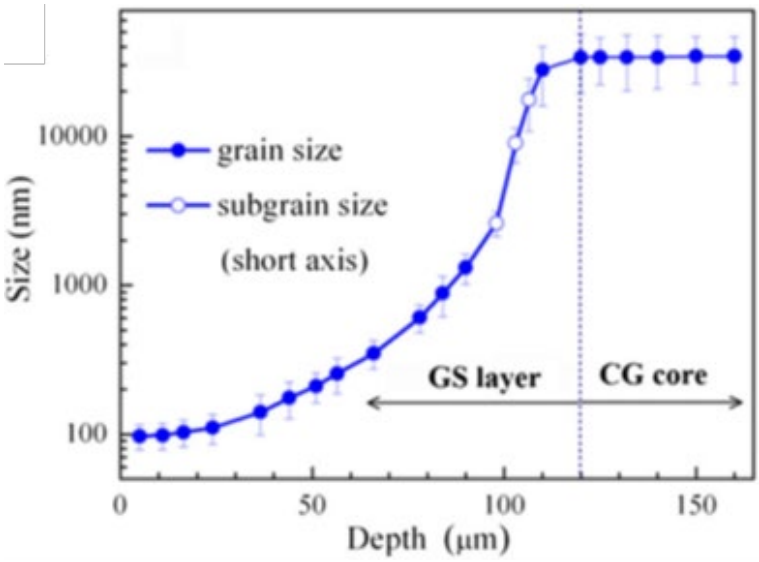

(a)

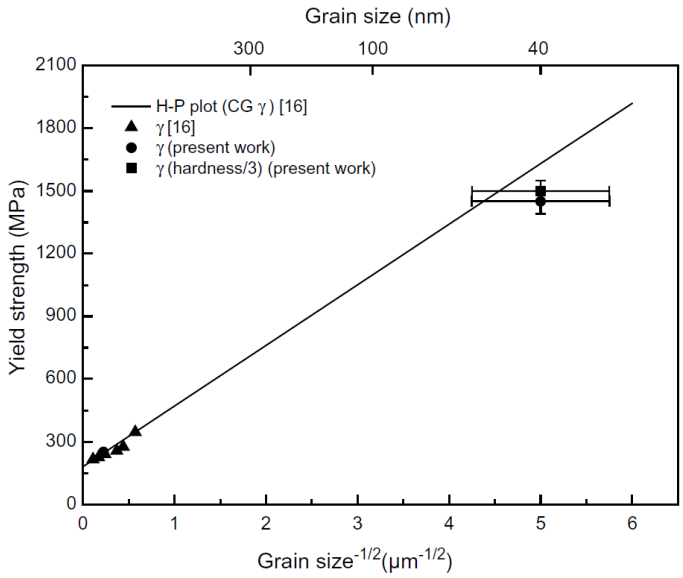

(b)

Fig. 1-5. (a) Variation of average grain sizes along depth [9], and (b) tensile yield strength as a function of the inverse square root of mean grain size using measurement results for 316L as reported in [8].

1.3.2 Influence of dislocations

Dislocations are linear defects in a crystal structure that play a critical role in determining the mechanical behavior of materials. Two types of dislocations generally exist in polycrystalline materials: GNDs and statistically stored dislocations (SSDs). GNDs are dislocations that are required to accommodate heterogeneous deformation,

particularly in plastic strain gradient fields, such as near grain boundaries or inclusions. GNDs accumulate to ensure compatibility deformation across different regions. Meanwhile, SSD are dislocations within grains that form randomly from dislocation multiplication and interaction with each other during homogeneous plastic deformation [83], [84].

(a)

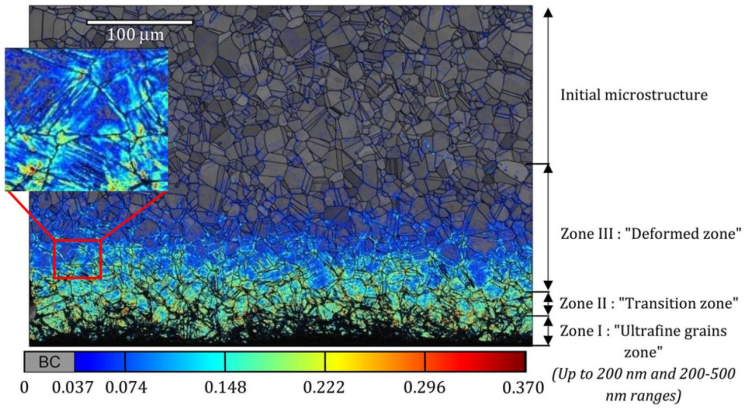

(b)

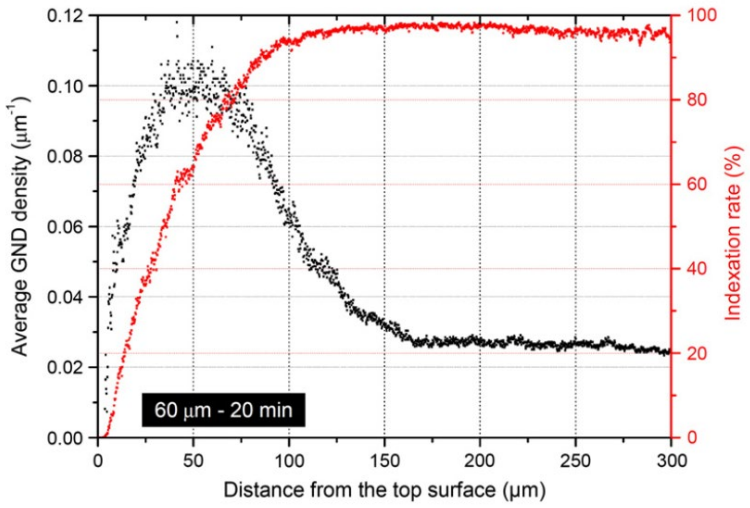

Fig. 1-6. (a) GND map obtained from EBSD measurement in 316L SS after 20 min SMAT with 60 µm vibrating amplitude, and (b) The corresponding evolution of the average GND density (black dots) and the indexing rate (red dots) from the top surface. [35].

Several researchers have reported that SMAT induces grain refinement through extensive dislocation activities [13], [26], [66]. However, it is challenging to obtain a direct quantitative estimation of dislocations state (density, movement…) in polycrystalline materials at the macro scale by experimental methods. Commonly,

TEM is used to directly observe dislocation lines and grain boundaries at the atomic level in a limited field of view on the nanometer scale, making this method suitable for investigating localized microstructural features [11], [33], [36], [85]. Dislocation density can be quantified by counting the dislocation lines in a given area. Pham et al. [86] quantified the density of the dislocations walls and channels by measuring the cell-to-cell misorientation, cell size and thickness of dislocation walls using TEM investigations. Based on the latter, the dislocations walls and channels can proportionally estimate GND and the fraction of walls. In contrast, EBSD provides crystallographic information related to dislocation structures. It is capable of mapping the grain orientations and detect misorientations, which can be correlated with dislocation activities. In details, the determination of GND density becomes feasible through the pixel-based measured misorientation by EBSD, resulting from lattice curvature [87], [88]. As shown in Fig.1-6 from [35], in-depth GND evolution is quantitatively analyzed in the GMS produced by SMAT. At the nanocrystalline layer at the bottom of Fig.1-6a, the indexation rate is close to 0, which indicates that the GND of this layer cannot be measured correctly. Nevertheless, a continuous decrease in the distribution of GND is clearly seen below this layer. The maximum value is located at about 50 μm from the end of the nanocrystalline layer.

In addition, XRD can detect the distortions caused by dislocations, providing indirectly analysis of total dislocations (sum of SSDs and GNDs) in materials. Strain-induced peak broadening in the XRD pattern, often characterized by the full width at half maximum (FWHM), is also used to roughly estimate the dislocation density, for example, the Williamson Hall method [89], [90]. This method can distinguish the individual contributions of grain size and strain to peak broadening, where the contribution of dislocations can be calculated from the strain component. For example, Kalsar and Suwas [80] used diffraction patterns to determine the dislocation distribution as a function of depth from the top surface. Their results in Fig.1-7 confirm the presence of a high density of dislocations at the top surface after SMAT.

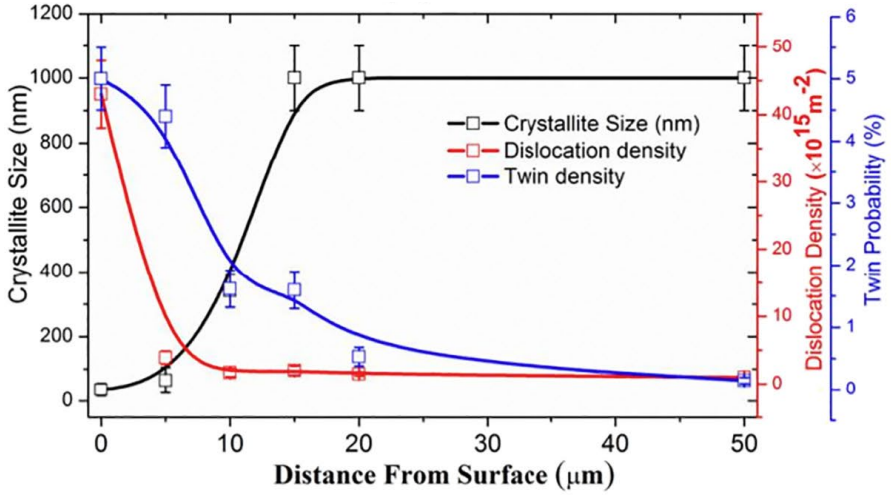

Fig. 1-7. Microstructural parameters of a SMATed steel, including crystallite size, dislocation density and twin density evaluated by XRD [80].

1.3.3 Deformation twinning and phase transformation

For low SFE materials [24], [47], [38], [72], deformation twinning and phase transformation have also been observed in SMATed samples, since they can significantly affect the mechanical behavior through twinning-induced plasticity (TWIP) or transformation-induced plasticity (TRIP) effects [5], [13], [24], [39], [78]. It has been discovered that twin boundaries can effectively impede dislocation motion, resulting in dislocations being stored at twin boundaries in TWIP materials [57], [80]. As a result, deformation twins accompanied by dislocations contribute to higher strength in SMATed materials.

A series of investigations have shown that dislocation slips, martensitic transformation and deformation twinning are strongly dependent on strain rate [24], [91], [92] and temperature [47], [61], [93]. Specifically, the results indicated that the cryogenic temperature and high strain rate can promote mechanical twinning and phase transformation. At low temperatures, the thermal motion of atoms decreases, facilitating the formation of layer defects and thereby reducing the SFE, especially in face-centered cubic (FCC) metals [94]. On the one hand, recent observations in [76] indicate that the volume fraction of α′-martensitic significantly increases when the strain exceeds 20% in a nanostructured AISI 304 stainless steel. On the other hand, deformation twinning increases with strain until reaching 5%, and decreases afterward [95]. Specifically, it has been reported that deformation activity is more readily

observed in materials with larger grain sizes as compared to those with smaller grain sizes [96].

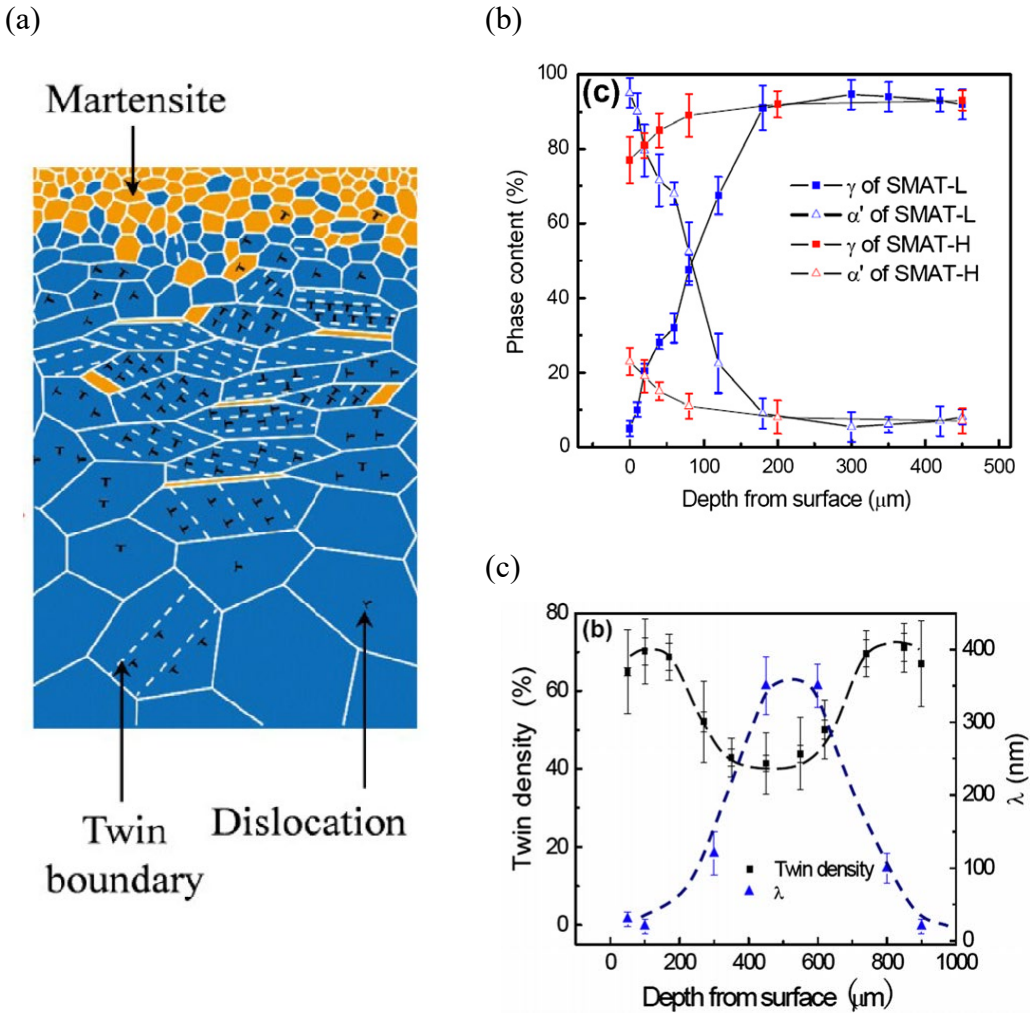

Fig. 1-8. (a) A schematic illustration of gradient microstructure of SMATed sample [97], (b) volume fraction of phase content (γ austenite and α'-martensite) with depth in SMATed 304 SS, distinguishing between low impact velocity (SMAT-L) and high impact velocity (SMAT-H), and (c) critical twin thickness (λ) and twin density at different depths in the SMAT-H sample [98].

It can be seen from the illustration of gradient microstructures in Fig. 1-8a that with an increasing strain along the depth towards the top surface, dislocations and deformation twins gradually appear in the intermediate area (under low strain and strain rates). By contrast, at the ultra-fine grain area under high strain and strain rate level, strain-induced martensitic transformation (γ austenite → twinning / ε-martensitic → α'-martensitic as shown in Fig.1-9) increases with increasing strain, which causes the abrupt drop of deformation twinning, as depicted in Figs. 1-8b and 1-8c. It is worth

noting that during the strain-induced transformation from γ austenite to α'-martensite, the formation of ε-martensite, as an intermediate state, is influenced by the material's chemical composition, such as the content of manganese and carbon [99].

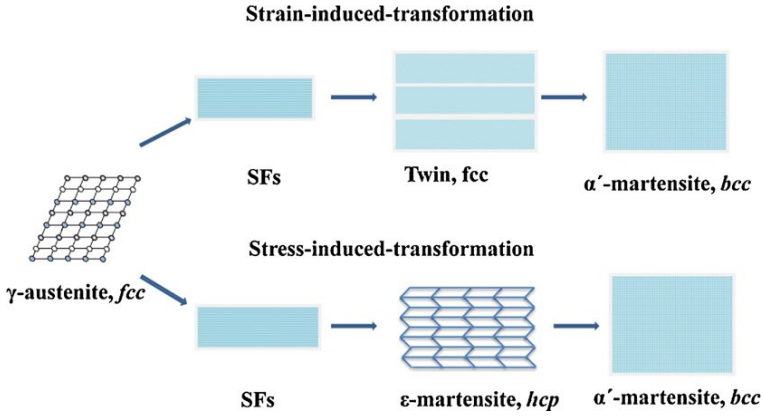

Fig. 1-9. Schematic illustration of twinning and martensite transformation processes for an austenitic 304 SS [95].

1.3.4 Residual stresses

Meanwhile, high compressive residual stresses are inevitably introduced into the near-surface region during the SMAT process, which can improve fatigue resistance [1], [4], [6], [22], [38], [45], [47]. The depth and values of the maximum residual compressive stress are sensitive to the SMAT parameters. The XRD technique, coupled with the iterative electrolytic polishing method, is usually used to obtain the in-depth variation of the residual stress of a SMAT sample [45], [100], [101]. Fig. 1-10 shows the in-depth distribution of residual stress components in the axial and circumferential directions. It can be seen that these residual stresses exhibit a remarkable compressive nature with a thickness of about 500 μm. Beyond this depth in the bulk region, tensile residual stresses counterbalance the compressive residual stresses throughout the cylindrical structure, ensuring overall mechanical balance.

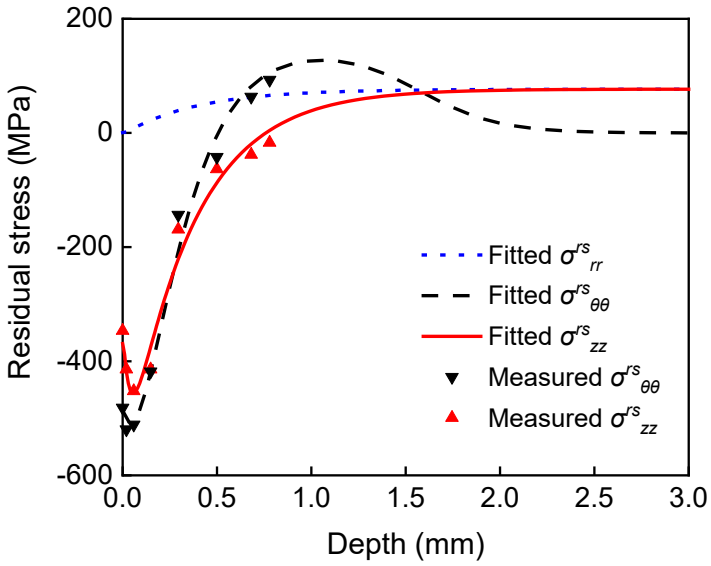

Fig. 1-10. In-depth distribution of residual stress after SMAT [100].

1.4 Mechanical behaviors of gradient-microstructure materials

1.4.1 Tensile properties and strain hardening

Mechanical properties measurements of the SMAT materials have indicated that the nanostructured surface layer and gradient microstructures can significantly increase tensile strength. Fig. 1-11a shows uniaxial tensile stress-strain curves for the nanocrystalline layer, coarse grain (CG) matrix and samples in 301 SS subjected to different treatment durations of SMAT. It can be seen in Fig.1-11a that the nanocrystalline layer's yield strength (0.2% offset) is as high as 1750 MPa, about 4.4 times that of the CG counterpart. However, the nanocrystalline layer exhibits a short plastic phase, exhibiting significant ductility loss with a strain at failure of less than 0.1. In comparison, the SMAT sample exhibits a significantly higher strength compared to the as-received one, without much loss of ductility (embodied by total elongation to failure) [42], [43], [44]. Fig. 1-11b illustrates the correlation between strength and uniform elongation for both homogeneous and gradient microstructures. It can be seen that gradient microstructures (twin and grain size) provide better elongation compared to homogeneous microstructure, particularly within the nano-scale grains. In addition, the gradient nano-twinned microstructure presents additional strengthening and work hardening by impeding dislocation motion. These results indicate that the

nanostructured layer provides high strength, while the coarse grains in the middle contribute to superior ductility in GMS materials. The evolution of microstructure is influenced by the material's SFE, which significantly affects the formation of surface nanocrystallization and the mechanisms of tensile deformation.

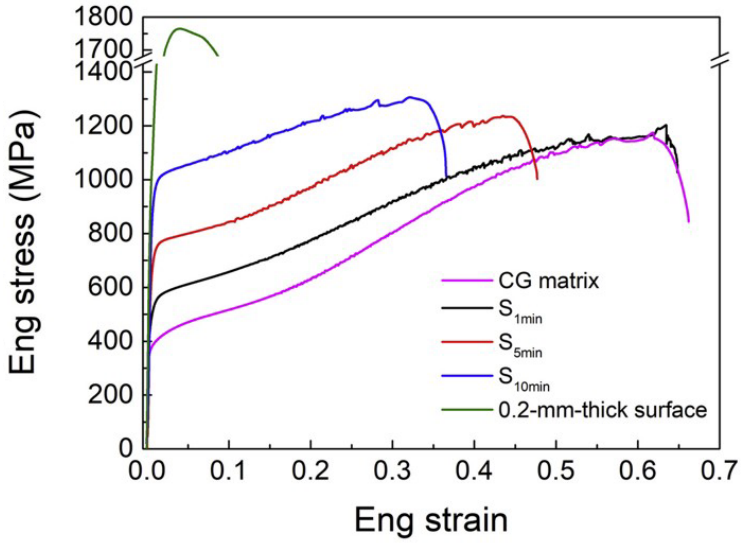

(a)

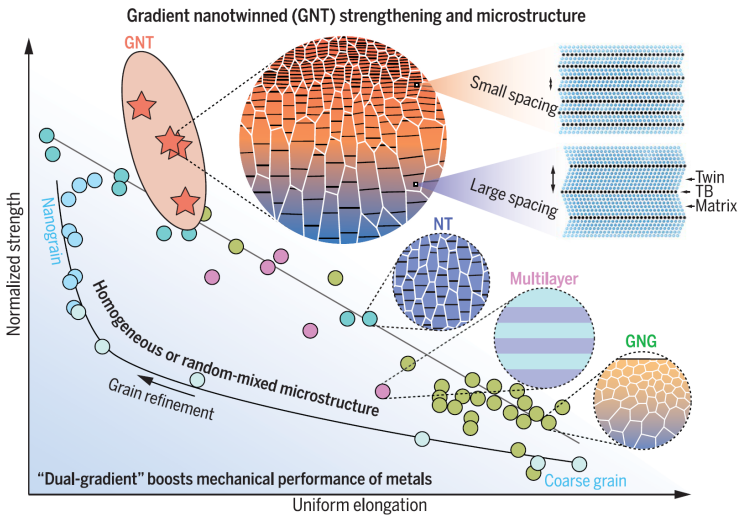

(b)

Fig. 1-11. (a) Tensile response with engineering stress-strain curves for the nanocrystalline layer produced by SMAT on 301 SS with different durations, and the CG bulk material [102], and (b) the trade-off relationship between strength and uniform elongation influenced by different microstructures and strengthening of GMS materials [103].

Before fracture, several hardening mechanisms act collectively to produce high strain hardening in terms of mechanical behavior. To understand each mechanism involved in the microstructure evolution during plastic deformation, numerous experiments focused on studying the evolution of the strain hardening rate ($\Theta = \partial\sigma/\partial\varepsilon$) of the SMAT samples [62], [65], [71], [73], [104], [105], [106]. A three-stage change is generally visible in the stress-strain curves. During the initial deformation stage, a significant decrease in strain hardening rate is observed, characterized by low flow stress, which is attributed to planar dislocations slip and the formation of ε-martensite [105]. The second stage begins with a rapid increase in strain hardening rate, driven by strain-induced mechanical twinning and strain-induced martensitic transformation [44], [107], [108]. As mentioned above, twin boundaries can impede dislocation motion (similar to regular grain boundaries) and act as slip planes to accommodate dislocations, resulting in a progressive increase in strain-hardening. Fig. 1-12 illustrates the strain hardening rate of TWIP steel (in a case without martensite transformation). The strain hardening rate gradually increases during the second stage of tensile deformation. At the same time, strain-induced martensitic transformation may generally also contribute to higher strain hardening and improve yield strength [109]. The final stage shows a decrease in strain hardening rate that is attributed to saturation of TWIP and TRIP with increasing strain, along with the dynamic recovery of dislocations [24], [30], [106].

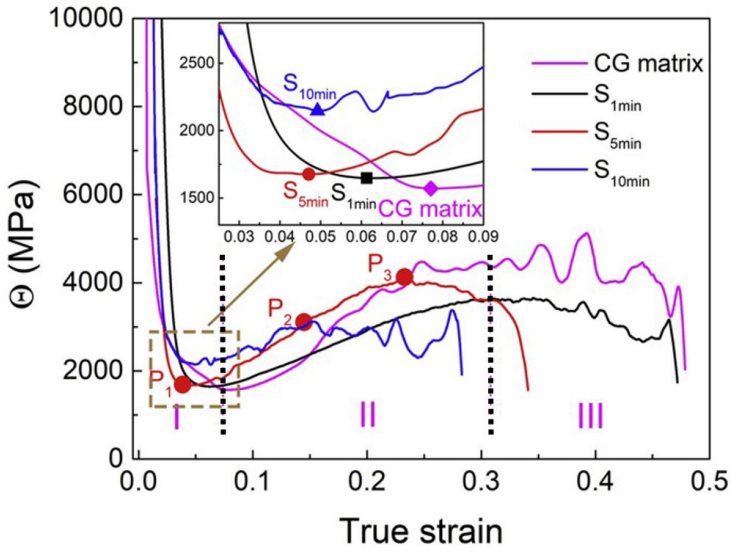

Fig. 1-12. Evolution of strain hardening rate (Θ) associated with uniaxial tension behavior presented in Fig.1-11a. The vertical dotted lines illustrate the separation between the three Θ stages for a homogeneous CG sample [102].

As discussed in Section 1.3.1, the SMAT structure presents a gradient of grain sizes in the near-surface region, which results in inhomogeneous deformation during tensile loading [110], [111]. During tensile loading, the deformation spreads outward from the soft CG to the nanocrystalline grains [33]. In the early stages of deformation, the CG in bulk begins to undergo plastic deformation due to its gradient yield strength, while the nanocrystalline grains in the surface layer still deform elastically. For example, Shao et al. [62] evaluated the strain gradient by quasi-in situ observation of photoetched surface and the hardness evolution at different positions of a GMS plate sample during tensile deformation. The results show that the grains in the center may experience higher plastic deformation than those on the top surface, suggesting a strain gradient in the GMS sample during tension. Mechanical incompatibilities within the near-surface SMAT-affected region could generate a large strain gradient, which consequently leads to a high level of GND to accommodate the strain [25], [33], [35].

The hardness variation may also reveal the strain gradient locally in the GMS samples during tensile deformation. Several researchers have reported a significant increase in hardness along the depth from the treated surface, generally determined by nanoindentation measurements along the SMAT samples [18], [29], [105], [112], [113]. Due to gradient of plastic deformation, hardness is highest at the impacted surface and decreases gradually towards the bulk center. Wu et al. [29] found the maximum hardness of 5.06 GPa at the top surface in a SMAT 316LSS sample, nearly twice that the one of the non-affected bulk material. At the initial deformation stage, a uniform increase in hardness is observed in the central CG bulk material, whereas hardness remains unchanged in the gradient microstructures layer due to its very low dislocation storage efficiency inside tiny grains, as illustrated in Fig. 1-13a. However, the different layers tend to deform uniformly with increasing strain [9], [105]. This indicates that inhomogeneous deformation induces strain hardening gradient during tension, leading to an increased hardness in the intermediate area between gradient microstructure and coarse grains, as shown in Fig. 1-13b.

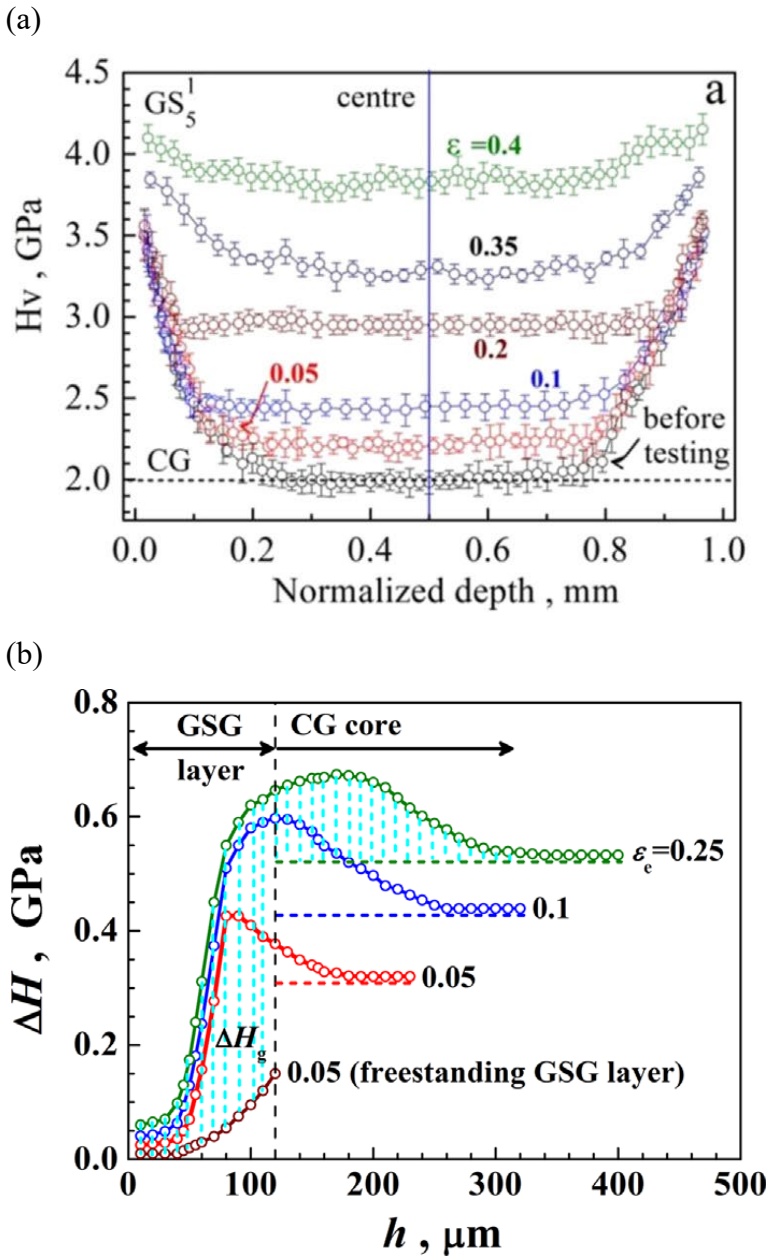

Fig. 1-13. (a) Hardness evolution with tensile strains along the depth in GMS 304 SS sample and in as-annealed CG sample for comparison [105], and (b) Variation of hardness increment of nanocrystalline interstitial free steel samples subjected to various tensile strains (0.05, 0.1 and 0.25) with respect to the depth [110].

1.4.2 Fatigue properties

In the last several decades, much attention has been paid to fatigue damage and failure in many engineering applications. SMAT provides a structure-strengthening strategy to improve the fatigue properties of materials. Fatigue tests showed that the fatigue life and resistance of SMAT samples are significantly enhanced compared to

the as-received samples in both the low cycle fatigue (LCF) [45], [101], [114] and HCF regimes [30], [46], [55], [115], [116]. For example, Fig. 1-14 displays the fatigue behavior of a surface nanostructured AISI 316L stainless steel with different shot diameters. The results reveal that shot with larger diameter lead to an improvement in fatigue strength in both low and high-amplitude stress regimes, which is considerably increased compared to the as-received material. The improved fatigue behaviors are attributed to the combined effect of compressive residual stress, strain hardening, gradient microstructure and nanostructured surface layer. The strain-induced nanostructured layer and high compressive residual stress enhance the strength of the surface, which can effectively improve fatigue resistance [6], [15], [117]. In addition, the high-volume fraction of grain boundaries can resist dislocation sliding and, hence, prevent crack nucleation. On the other hand, a high amount of dislocation walls, dislocation tangles, twinning and sub-grains in the intermediate area can also constrain the growing cracks and decrease the propagation rate of cracks in such an area [6]. However, it is reported that the micro-cracks at the surface and high tensile residual stresses in the subsurface induced by high-intensity SMAT can decrease the fatigue performance on crack initiation in the very high cycle fatigue (VHCF) regime [4]. It should be noted that crack initiation in the LCF and HCF regimes is usually observed on the specimen surface, whereas crack initiation is mainly concentrated inside the materials in the VHCF regime [4], [118], [119].

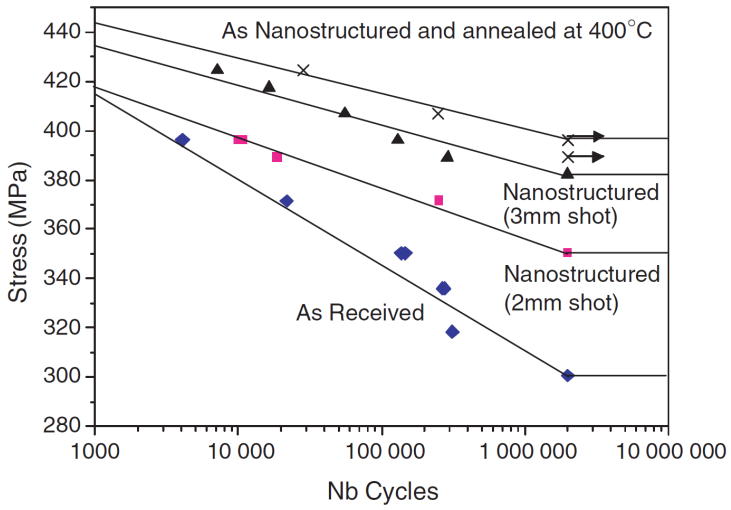

Fig. 1-14. S-N curves of different treatment conditions for SMAT 316L SS samples and as-received sample for comparison [30].

The cyclic stress response associated with internal stress variables (i.e. effective and back stresses) is helpful to analyze the relation with microstructure and to build numerical models with isotropic and kinematic hardening laws [28], [86], [120]. The effective stress is related to overcoming the short-range obstacles, for example, the resistance of dislocation motion and other defects [121], [122], [123]. The back stress is a directional kinematic component developed through long-range interactions of dislocations arising from inhomogeneous plastic deformation with microstructural heterogeneities, such as grains, sub-grains, cells and dislocation walls/channels [84], [123]. The effective stress and back stress represent respectively the expansion or contraction of the radius and the shift of the center of the yield surface in principal space.

It is well established that the yield strength of some metallic materials in one direction is higher than that observed in the reverse loading during cyclic deformation, a phenomenon known as the Bauschinger effect, that can be described/explained by kinematic hardening. In the initial loading direction, dislocations accumulate, resulting in an increase in back stress within the material, which impedes further movement in the same direction. The dislocation structures and back stresses generated during deformation are still present when the load direction is reversed. Consequently, the back stress now aligns with the reversed applied stress, thereby reducing the resolved effective stress for dislocation movement in the opposite direction and facilitating easier yielding of the material [34], [124]. The strong Bauschinger effect and important back stress have been identified in GMS materials [124]. In fact, SFE also plays an important role in the back stress hardening of GMS materials. For example, varied SFE in the Cu-Al alloys, achieved through different aluminum contents, were examined to assess their impact on back stress hardening and the GND evolution [34]. The results indicate that the GND density decreases with a decrease in SFE (with an increase in Al content), resulting in an increased back stress. In addition, the quicker GND rearrangement under higher strain causes a sharp decrease in back stress. On the other hand, twin boundaries are also beneficial for forming back stress by increasing pile-up dislocations [116], [125].

To elucidate the different deformation mechanisms of cyclic softening/hardening, the evolutions of back stress and effective stress are separated and analyzed using hysteresis loops [28], [56], [126], [127]. The fatigue tests for 316L SS reveal that the influence of back stress is more significant than that of effective stress on cyclic softening/hardening in LCF [28]. The results reveal a cyclic hardening in the initial

phase, followed by a transition to cyclic softening, and a subsequent stabilization phase before eventual failure. Moreover, the TEM observations are used to identify microstructural evolution associated with the evolution of back stress during strain-controlled cyclic loading, specifically for dislocation density evolution (Fig. 1-15) [86]. During the early stage of cyclic loading, dislocations (mainly of the GND type) pile up adjacent to grain boundaries to accommodate different degrees of plastic deformation between grains, as schematically illustrated in Fig. 1-16. During the cyclic hardening stage, the dislocation density inside grains increases with plastic deformation, thereby reducing the gradient of dislocation density within grains. Furthermore, the secondary slip activity leads to an increase in dislocations and a more uniform distribution of dislocations within grains. In the subsequent softening stage, when dislocations become denser within grains, dislocations start rearranging to form grain fragmentation (dislocation cells, cellular structure, dislocation walls), which allows to release the intergranular back stress [121], [127].

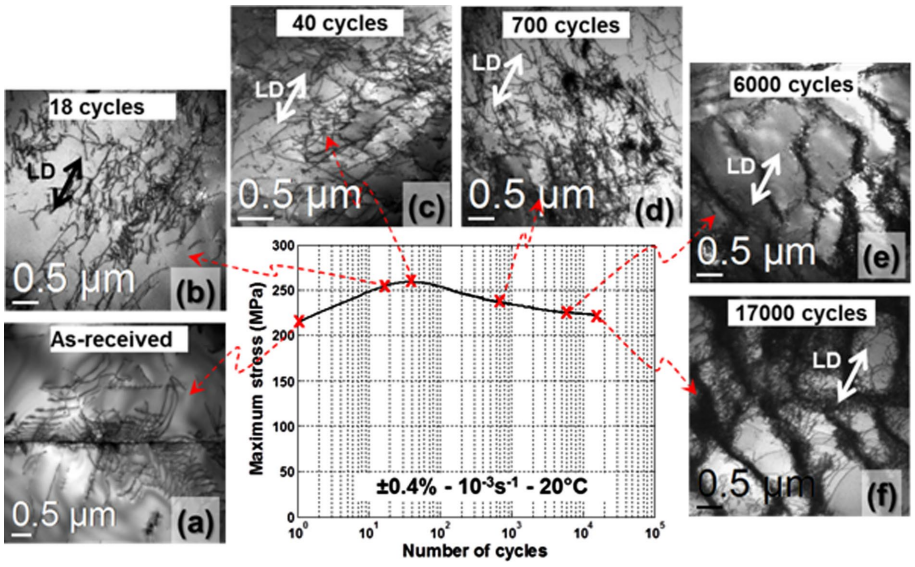

Fig. 1-15. Microstructural evolution for a strain amplitude of ±0.4% observed in LCF tests for 316L SS observed by TEM [86].

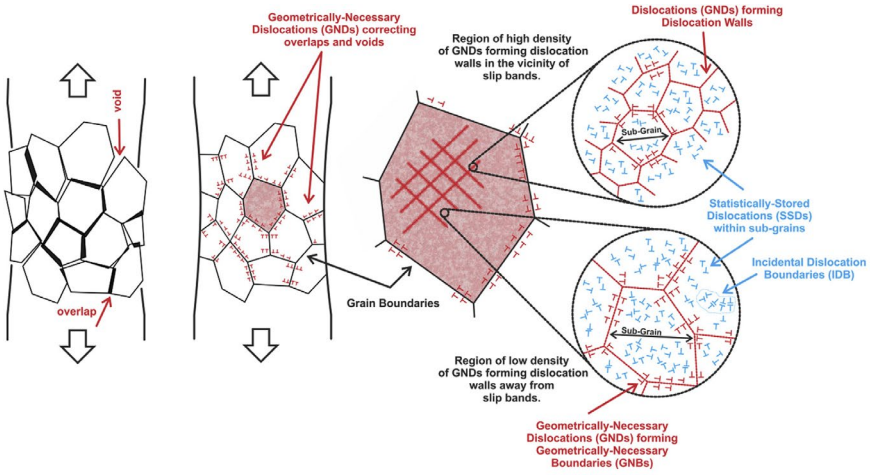

Fig. 1-16. Schematic illustration of the inter-granular dislocation evolution during the accommodation of plastic deformation in a polycrystalline material.

1.5 Modeling of gradient-microstructure materials

1.5.1 Simulation of SMAT process

Theoretical modeling can provide quantitative expressions to complement experimental investigations. To control and optimize the SMAT technique, numerical modeling has been developed to predict plastic deformation during the SMAT process [26], [45], [66], [69]. Numerical modeling is a complex process, involving severe localized plastic deformation and grain refinement under high strain and high strain rate (at least of the order of 10^4 s^{-1}) due to multidirectional impacts on the material surface by shot [32], [37], [128], [129].

The Finite Element method (FEM) is widely applied in numerical modeling of material behavior in processing, manufacturing and exploitation. It is capable of solving problems involving complex structures under different deformation conditions, such as compression, tension, cyclic loading. In addition, the mechanical constitutive behavior of most materials and complex loading conditions can be defined in user subroutines. Many computational and theoretical models have been attempted to reconstruct the SMAT process by FEM. For instance, a single high-rate shot impact process is studied to investigate the formation of a plastic deformation layer in grain-order work hardening [104]. Moreover, deformation and damage evolution can be also predicted in the case of a single impact using the Gurson-Tvergaard-Needleman (GTN) yield criterion [130]. In works [36], [51], [131], the effects of treatment conditions, including

duration, shot number, shot size and impact angle, on residual stresses, plastic deformation and roughness of SMAT samples were evaluated. In addition, Petit et al. [42] proposed a multilayer model by combining the tensile behavior of nanocrystalline, CG and transition layers to directly predict the macroscopic elastoplastic behavior of the SMAT sample.

1.5.2 Modeling of GMS material

Experimental investigations have already revealed that the mechanical properties of SMAT materials are strongly dependent on the gradient microstructure, such as grain refinement, dislocation motions, deformation twinning and martensitic phase transformation. Grain size-dependent and dislocation-based simulation models can be reasonably proposed to account for the microstructure evolution of SMAT materials during deformation [23], [132]. At the mesoscopic scale, crystal plasticity finite element method (CPFEM) is widely employed to investigate the mechanical responses of GMS materials [12], [85]. Zeng et al. [132] extend the classical CPFEM by incorporating grain-size-dependent constitutive model to study the mechanisms of strain hardening induced by strain gradients. Specifically, the gradient grain size structure is created by adapting the conventional Voronoï tessellation method [133]. Furthermore, Lu et al. [12], [117] established a crystal plasticity model containing dislocation slipping and deformation twinning to predict and optimize the mechanical properties of a gradient nanostructured TWIP steel.

On the one hand, to further formulate relationships between microstructure and macroscopic mechanical response, multi-scale models combing CPFEM of the SMAT process can be considered. For example, the mechanical responses of the polycrystalline representative volume elements (RVEs) are contained at integration points as shown in Fig. 1-17. The loading is applied to the macro-scale structure along the X-axis positive direction, and the other boundary conditions are imposed on the other nodes. The combined representative volume elements in CPFEM can provide accurate macro-scale behavior and offer detailed insight into the state of microstructures, including grain size, grain boundaries, and twins. However, it is accompanied by a complicated finite element model and generally long calculation process.

On the other hand, the conventional mechanism-based strain gradient plasticity

(CMSG) models have the capacity to directly build the multiscale material response based on physical experimental equations, without establishing the whole geometry of the microstructure [17], [52], [134], [135]. Concerning ingredients, the strain gradient accommodated by GND is often employed to evaluate the strain hardening resulting from deformation heterogeneities. The Kocks-Mecking-Estrin (KME) model [136], [137] was developed to describe the dynamic accumulation and annihilation of dislocation processes in relation to plastic strain rate and grain size. Dislocation density is a crucial internal variable that reflects the microstructural state of a material in terms of plasticity. Based on that, deformation twining is considered through the mean free path of dislocation accumulation. The contribution of martensitic transformation can be described using volume fraction by a mixture law [50].

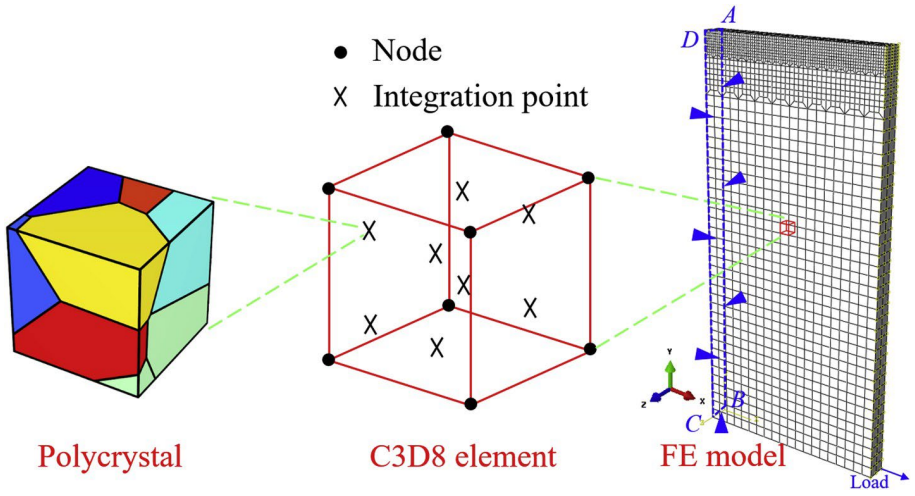

Fig. 1-17. Illustration of homogenization scheme used in the multi-scale simulations by CPFEM approach [12].

1.5.3 Plasticity modeling of 316L during cyclic loading

Several researchers have developed numerical models for the radius and shift of the yield surface with different hardening rules during cyclic loading [113], [138], [138], [139]. It is well established that the evolution of back stress is essential for correctly characterizing the kinematic hardening behavior of metals. Various approaches have been proposed to quantify back stress-induced kinematic hardening. Linear kinematic hardening framework was introduced by Prager in 1956 [140]. Based upon this, Armstrong and Fredrick developed a nonlinear model (in Eq. 1-2) that incorporates a dynamic recovery term to characterize the Bauschinger effect under different loading conditions [138]. Furthermore, Chaboche introduced the concept of multiple back

stresses to minimize the deviation from the experimental curve (in Eq. 1-3) [139]. In the micro-scale, back stress induced by accommodated GND is expressed in terms of the number of GND pileups and grain size [52], [53].

$$\Delta\alpha^{(i)} = \alpha_{n+1}^{(i)} - \alpha_n^{(i)} = \frac{2}{3} C_i \Delta e^p - \gamma_i \alpha_{n+1}^{(i)} \Delta \bar{e}^p \quad \text{(Eq. 1-2)}$$

$$\alpha = \sum_{i=1}^{n} \Delta\alpha^{(i)} \quad \text{(Eq. 1-3)}$$

In contrast, M.S. Pham develops a dislocation density-based physical model of back stress, which accurately describes cyclic deformation behavior in LCF [86]. The total back stress is divided into intragranular and intergranular components associated with dislocations evolution.

1.6 Conclusion

In this chapter, SMAT is first introduced as a type of SPD method for producing GMS materials, with a focus on elucidating the experimental set-up, the treatment procedure and the outstanding mechanical properties of the treated materials. Subsequently, the mechanisms of surface nanocrystallization induced by SMAT are discussed according to the SFE values of the materials. Additionally, a detailed description of the gradient microstructures is presented in this chapter, covering aspects such as grain size, dislocations, hardness, deformation twinning and martensite transformation. Several deformation mechanisms are discussed at different stages of the strain hardening ratio during tensile landing, including dislocation motions, deformation twinning, martensite transformation and strain gradient effects. Furthermore, the deformation mechanisms of cyclic softening/hardening are described through the evolutions of back stress and effective stress associated with microstructures. A brief introduction to the simulation of the SMAT process, numerical models on GMS materials and cyclic plasticity modeling is also presented at the end of this chapter.

Chapter 2: Materials characterization

SMAT offers a direct and efficient method for achieving microstructural modifications through the application of SPD on the materials surface. During the treatment process, SMAT induces nanocrystallization in the near-surface region, thereby enhancing the mechanical properties of the material [4], [29], [45], [49], [50], [66]. To comprehensively investigate the mechanical behavior and understand the strengthening mechanisms, it is necessary to examine the impact of SMAT on the microstructure. This chapter presents the details of SMAT setup and conditions applied to cylindrical shape specimens. An in-depth analysis of microhardness and residual stress in SMATed 316L SS was conducted using nanoindentation and XRD, respectively. Comprehensive analysis of the microstructure, including both as-received and SMATed specimens, was performed using EBSD. Additionally, the inhomogeneity deformation induced by the SMAT process was analyzed through GBs, misorientation, and GNDs.

2.1 Material preparation and SMAT process

2.1.1 Material

316L SS is widely used in both industrial applications and research, owing to its excellent mechanical properties, high temperature performance, and fatigue resistance [28], [29], [32]. The 316L SS, employed in the present research, has the following chemical composition (in wt.%): 0.013 C, 1.70 Mn, 0.26 Si, 0.017 P, 0.003 S, 17.37 Cr, 14.52 Ni, 2.8 Mo, 0.08 Cu, 0.088 N, <0.005 Ti, 0.07 V and balance Fe. As mentioned in Chapter 1, SFE is a critical parameter to determine the deformation behavior and mechanical properties of austenitic SS. However, calculation of SFE is often complex and typically requires models based on experimental data. Several empirical formulas for estimating the SFE of austenitic SS are employed in the present research 316L:

$\gamma = 5.53 + 1.40Ni - 0.16Cr + 17.10N = 24.58$ mJ/m² [141],

$\gamma = 16.7 + 2.1Ni - 0.9Cr + 26C = 31.90$ mJ/m² [142],

and $\gamma = 2.2 + 1.9Ni - 2.9Si + 0.77Mo + 0.5Mn + 40C - 0.016N = 32.56$ mJ/m² [143]. With an SFE ranging from 24.58 to 32.56 mJ/m², this 316L SS can be classified as having a medium-to-high or moderate SFE. It indicates that the material primarily

deforms through dislocation glide, with potential occurrence of deformation twinning. Martensite transformation-based mechanisms should not occur. Cylindrical specimens were machined with a gauge diameter of 6 mm and a gauge length of 12 mm, as illustrated in Fig. 2-1.

2.1.2 SMAT process

The configuration of the SMAT setup is described in Fig. 2-2. The specimen is positioned within a cylindrical chamber, which can rotate around the center axis at a constant speed driven by an electric motor. Inside the chamber, steel shot with a diameter of 3 mm and a mass of 20 g are enclosed. The specimen is situated 12 mm away from the vibrating platform, called sonotrode, which is boosted by an ultrasonic device or vibrating generator at a high frequency of 20 kHz. Consequently, the entire gauge section undergoes multiple randomized impacts at high strain and strain rate, due to the rotation of the specimen and the impacts of steel shot. In this study, the SMAT process was initiated with a duration of 15 minutes at a low generator power (30% of the maximum amplitude), followed by another 5 minutes at a higher generator power (50% of the maximum amplitude). Finally, SMATed samples were successfully obtained, as illustrated in Fig. 2-1, exhibiting the characteristics of nanocrystalline grains on the top surface and CG structure in the bulk. The uniformly distributed indentations resulting from the SPD caused by impacts are clearly visible to the naked eye on the surface of the gauge section of the SMATed sample.

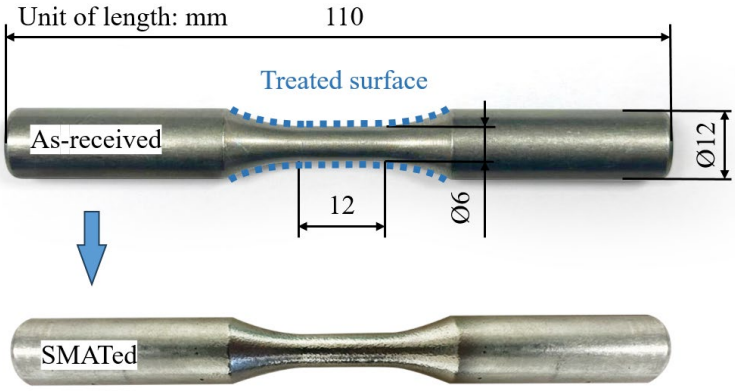

Fig. 2-1. Cylindrical shape specimens of as-received and SMATed 316L SS for testing.

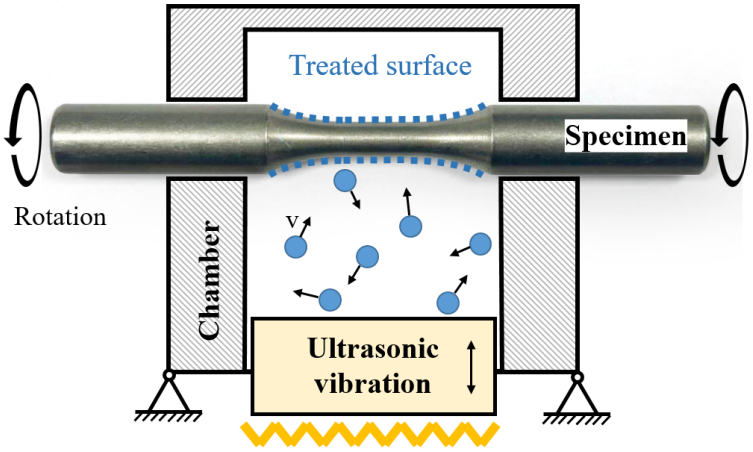

Fig. 2-2. Schematic diagram of the experimental setup to perform SMAT on cylindrical specimens.



Fig. 2-3. Embedded specimens within resin, prepared for further measurements and characterization.

2.1.3 Material preparation

During SMAT, the specimen is rotated along its cylindrical axis, and the impact of the steel shot creates a gradient structure along the radial direction. Consequently, the cross-section in the mid-gauge region is selected to observe microstructural changes. First, the central portion (up to about 4 mm in the axial direction) of the specimens was extracted using a cutting disk operating at a low speed to minimize the impact of the cutting process. Next, the cross-sections of the cut specimens were oriented with the surface facing down and then embedded in a conductive carbon resin, as illustrated in Fig. 2-3. Mechanical polishing was then used to achieve mirror-flatness of the cross-

section. This was done by successively using abrasive discs of 800, 1200 and 2400-grit silicon carbide, followed by 3, 1, and then 0.25 μm diamond polishing paste on a MetaServ 250 grinder-polisher combined with a Vector® LC 250 automatic operation power head. For EBSD observations, the specimens were lightly etched in Adler solution (hydrochloric acid, ferric chloride hexahydrate and ammonium tetrachlorocuprate (II) dihydrate) to improve the quality of diffraction patterns. All the experimental procedures were performed at room temperature.

2.2 Microstructure characteristics by EBSD observations

The SMAT process involves a complex in-depth microstructural development through SPD, resulting in changes in the mechanical properties and deformation mechanisms, as reviewed in Chapter 1. For metallic materials, the microstructure is often characterized by parameters such as grain size, crystal orientation, phase, dislocation, and twinning [11], [35], [48], [51], [75], [80]. Several methods are available to observe microstructures, with the most commonly used techniques including EBSD, TEM, and XRD [7], [29], [51], [83], [103]. TEM methods are primarily used for localized visualization of crystal structures with high resolution at the atomic levels. However, they often provide poor statistical correlation due to the heterogeneous distribution of deformation and dislocations at the polycrystalline scale [5], [33]. XRD methods allow indirect estimation of grain size, microscopic strain or lattice distortion, and dislocation density from the shape of the diffraction peaks, typically employing the Williamson-Hall method [144], [145]. In contrast, EBSD is widely used in materials science to analyze statistically representative microstructural characteristics of crystalline materials. During an EBSD measurement, a focused electron beam interacts with atoms on the specimen surface, resulting in scattering interactions. A fraction of the diffracted electrons is captured by the detector, which encodes valuable information about crystallographic structures [146], [147]. Therefore, EBSD provides an efficient approach to quantitatively characterize the microstructures of the nanoscale near-surface region affected by the SMAT.

In this work, EBSD measurements were performed on the cross-section to study the gradient microstructure induced by SMAT. The observations were conducted using the high-resolution SEM TESCAN MIRA system equipped with an EDAX Velocity™ camera for wide-field emission scanning, as shown in Fig.2-4. A high-energy electron

beam of 20 kV and a sample tilt angle of 70° were used during EBSD data acquisition. The observations were performed over an area of 100 µm × 250 µm with a scan step size of 0.5 µm. Only one observation was made for the as-received and SMATed samples, respectively. EBSD map data analysis is subsequently carried out using OIM Analysis™ V8 software for inverse pole figure (IPF), Kernel average misorientation (KAM), grain orientation spread (GOS), and grain reference orientation deviation (GROD).

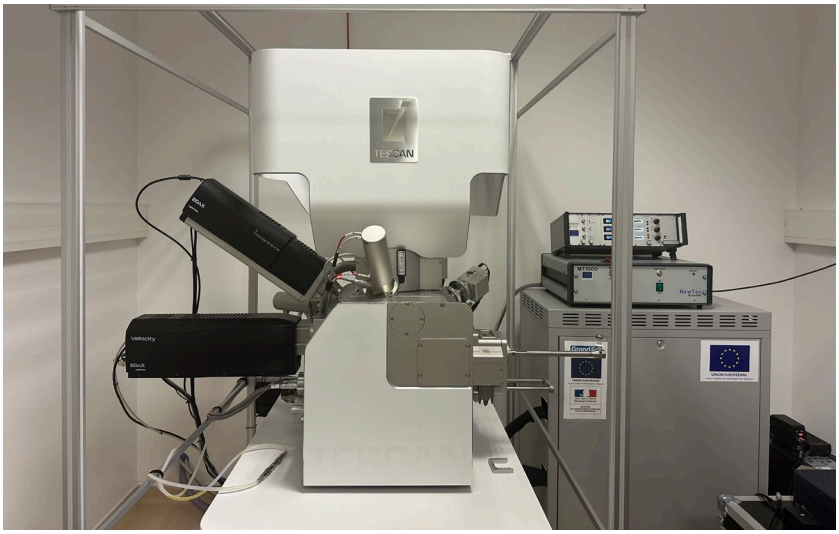

Fig. 2-4. Scanning electron microscopy with an EBSD detector, used at LASMIS laboratory.

2.2.1 Crystal orientation

EBSD observations were employed to observe the microstructures on the cross-section of both as-received and SMATed specimens in 316L SS. The IPF serves as a direct measurement result obtained from EBSD, providing crucial information about the crystal structure and orientation of the material. These details are essential for understanding the microstructure and mechanical properties of the material. As shown in Fig. 2-5, the IPF overlaid with the image quality (IQ) map reveals a dark area of approximately 5 µm thickness in the near-surface region, located at the junction of the resin and samples. In the as-received specimen, the observed degradation in the near-surface region is basically attributed to deformation induced by specimen preparation (cutting and mechanical polishing). In contrast, a gradient degradation is observed in the SMATed specimens extending over a larger region (approximately 80 µm in depth). This is attributed to grain refinement and severe plastic deformation, as supported by

previous studies [148]. Indeed, this darkening phenomenon is particularly pronounced in areas characterized by small grains (typically on the order of a few tens of nanometers) or regions subjected to heavy strain deformation as described in [35], [149]. However, it is challenging to distinguish the nanocrystalline grains in the IPF of the SMATed sample in Fig. 2-5.

It is well known that austenitic steel with moderate SFE can be deformed through both dislocation glide and deformation twinning [150], [151], [152]. Throughout the generated gradient region, deformation-induced twins along with a high density of dislocations generated due to high strain rate can be observed in the red dashed rectangular zone (magnified on the right in Fig. 2-5). It is noteworthy that no deformation twins were observed closer to the surface (where the material experiences a higher level of strain) and in the bulk (where the material sustains relatively lower strain levels). This observation is consistent with deformation twins being activated at specific strain levels, as described in several works [13], [96]. In addition, only single-phase austenite grains were detected in the measurements, which indicates that the SMAT process does not involve phase transformation in the 316L SS investigated in the present study.

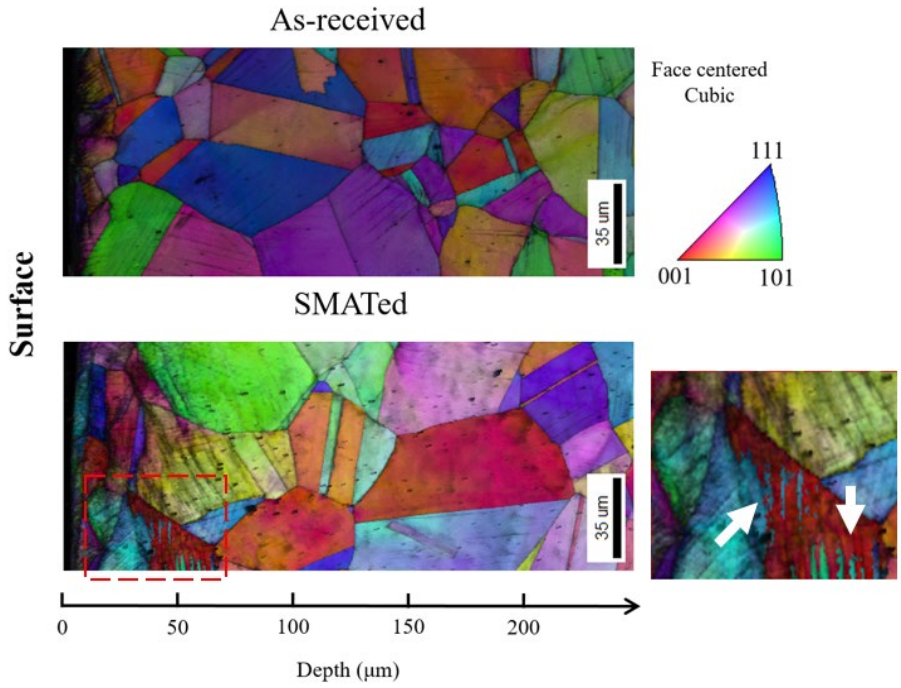

Fig. 2-5. EBSD maps of IPF overlaid with IQ on cross-section of as-received and SMATed samples. The deformation-induced twin is highlighted within a rectangular

zone marked by a red dashed line.

2.2.2 Grain size and grain boundaries

After detection, misorientation was used to distinguish boundaries, with low angle grain boundaries (LAGBs) defined as misorientation in the range of 2° to 15°, high angle grain boundaries (HAGBs) characterized by misorientation greater than 15 degrees, and annealing twin boundaries with misorientation of 60° along the <111> axis. In the as-received specimens, LAGBs are predominantly concentrated near the surface at approximately 9 μm, with no significant gradient change, as observed in Fig. 2-6. This is mainly due to the deformation caused by the preparation of the sample by polishing and cutting. Conversely, in the SMATed specimen, the fraction of LAGBs gradually increases from a thickness of about 9 to 65 μm. Furthermore, the distributions of LAGBs and HAGBs become more uniform within the bulk of both samples. It can be inferred that the gradient-distributed LAGBs are dislocation walls formed as a result of dislocation accumulation induced by the gradient strain introduced by SMAT [11], [127], [153].

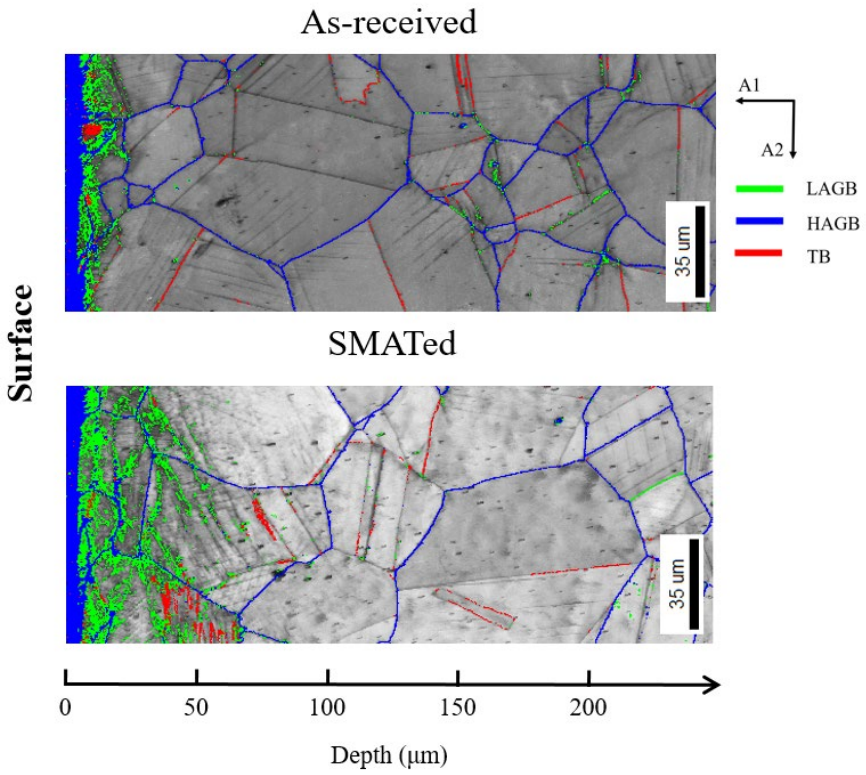

Fig. 2-6. EBSD maps of IQ with boundaries for both the as-received and SMATed

samples. LAGBs are marked by the green lines, HAGBs by the blue lines and twin boundaries (TB) by the red lines, respectively.

Fig. 2-7 presents the in-depth average grain size variation with depth from the treated surface, for both the as-received and SMATed samples. By comparing the grain size evolution between as-received and SMATed specimens, the SMATed sample exhibits a smaller grain size (about 30 μm.) in the near-surface region. However, the detection of nanograin regions on the treated surface based on grain size distribution is challenging due to the influence of specimen preparation. In the region with a depth ranging from 9 to 75 μm, a gradient variation of grain size ranging from 40 to 79 μm is observed in the as-received sample. In the range of depth from 9 to 125 μm, a gradient variation in grain size from 30 to 83 μm is observed in the SMATed sample. These results indicate that the grain distribution is significantly influenced by the deformation induced by the specimen preparation process, primarily due to the SMAT. In addition, the maximum grain size of the bulk region is found to be approximately 80 μm for both samples. It is important to remind that such a curve is not a statistically representative result, only showing trends due to the limited number of grains contained in the measurement area.

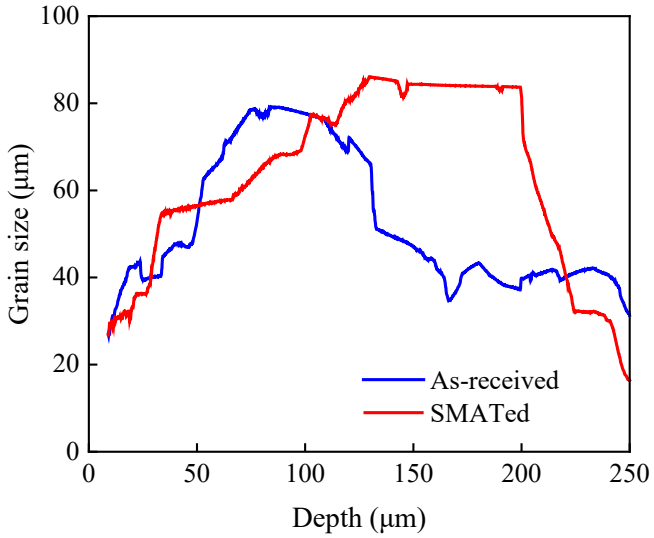

Fig. 2-7. In-depth average grain size evolution for both the as-received and SMATed samples.

2.2.3 Misorientation and dislocation

The KAM is as a means of visually representing small orientation variations on a map. The KAM represents the average misorientation angle, as schematically explained in Fig. 2-8. It is calculated from a given point with respect to its neighboring pixels at a fixed neighborhood distance. Additionally, only neighboring pixels with a misorientation angle below a certain threshold (5°) are considered in the calculation to exclude misorientations attributed to grain boundaries. Consequently, the KAM map can provide a quantitative assessment of the degree of inhomogeneous plastic deformation or increased defect density [148], [154].

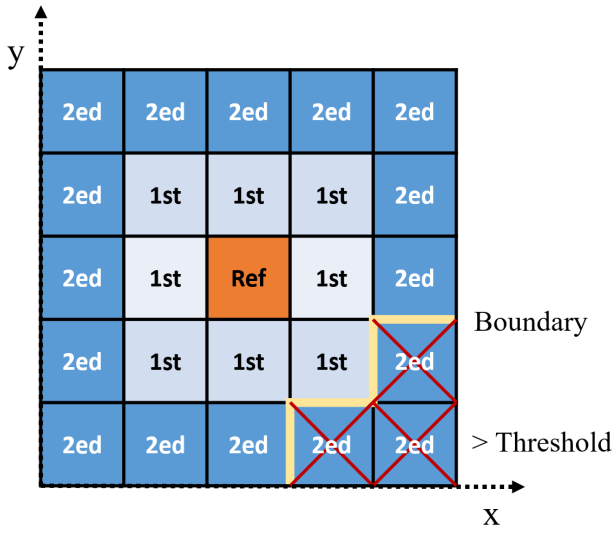

Fig. 2-8. Schematic diagram of the KAM calculation method.

Fig. 2-9 shows the KAM maps calculated from the EBSD measurements of the as-received and SMATed samples, respectively. In the untreated specimen, misorientations caused by polishing and cutting accumulate at the boundaries close to the surface. However, with the application of SMAT, the material experiences a strain gradient, resulting in a gradual decrease in misorientation observed from the surface down to 65 µm. Notably, the misorientation at the surface (3.8°) is significantly larger compared to the bulk region (measured at 0.2°).

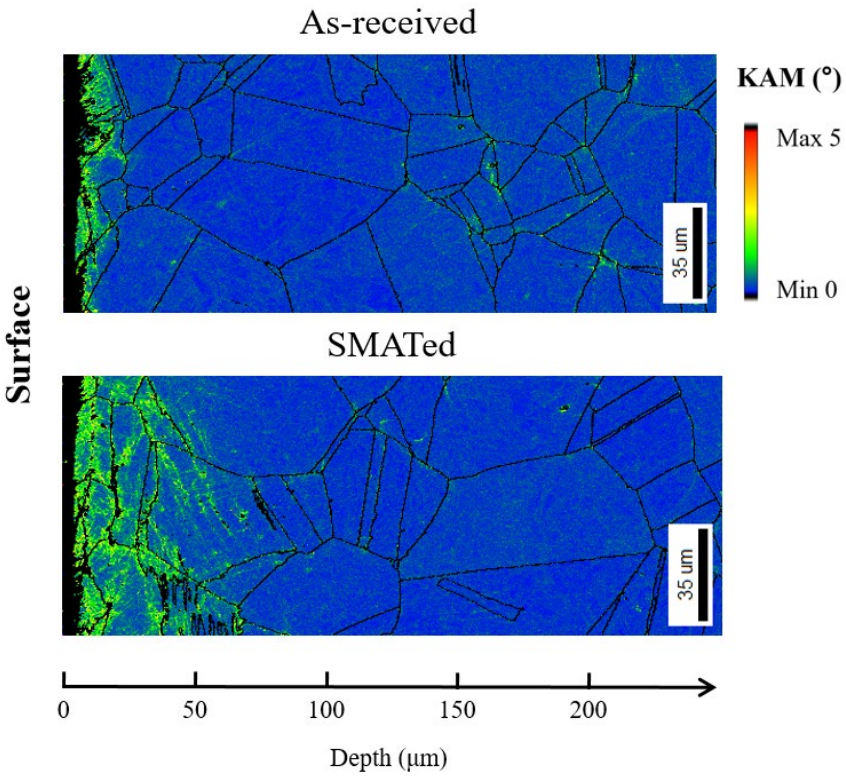

Fig. 2-9. EBSD maps of KAM on cross-section of as-received and SMATed samples, with threshold angle 5°.

When plastic deformation is induced by the macroscopic applied strain, dislocations can extend through the lattice to accommodate the geometric deformations in the material [155]. During SMAT, the surface undergoes impact-induced inhomogeneous compressive deformation with a large quantity of dislocation motions [156]. The variation of lattice curvature induced by plastic deformation can be captured in EBSD measurements by local misorientations, specifically for GND type. It is assumed that lattice curvature caused by elastic strain is neglected in such analyses. The variation of KAM values directly reflects the local misorientation, which can be employed to calculate the GND. A simplified model for calculating GND density ρ_{GND} from misorientation angle θ_{mis} derived from KAM is provided in Eq. 2-1 [157], with k being a constant depending on the arrays of edge and screw dislocations (2 for 304 SS [158]) and s being step size of two scanning (0.5 μm). The Burgers vector b is 0.256 nm for 316L [159]. In summary, the varying distribution of GNDs along the depth can serve as a valuable indicator for the plastic changes induced by SMAT.

$$\rho_{\mathrm{GND}} = \frac{k\theta_{mis}}{bs} \quad \text{(Eq. 2-1)}$$

Fig. 2-10a illustrates the cross-sectional distribution of GND for as-received and SMATed 316L SS samples, respectively. Close to the treated surface, there is a corresponding increase in GND density of both samples. Compared to the as-received specimen, the SMATed specimen exhibits a thicker GND region, with the GND gradually decreasing from 9 to about 126 μm. In addition, the position of the high-density GND distribution corresponds to the KAM and LAGBs positions. The curves in Fig. 2-10b represent the average GND density along the depth, calculated from the average GND value at the same depth. Additionally, the average GND from the as-received specimen ρ_{GND}^{ARed} is used to correct for the change in average GND in the SMATed specimen ρ_{GND}^{SMATed}, as indicated by the green line in the figure. The GND on the surface of the as-received sample was assumed to result only from the plastic deformation introduced during sample preparation. Both the SMATed and the as-received samples underwent the same preparation process and were measured using identical parameters. Consequently, the residual plastic deformation was assumed to be the same for both samples. The SMATed samples were then utilized to subtract the GND from the as-received sample to obtain the corrected GND values, removing the effect of sample preparation, $\rho_{GND}^{Corrected} = \rho_{GND}^{SMATed} - \rho_{GND}^{ARed}$. Notably, for the SMATed specimen, the average GND density initially grows rapidly, reaching a maximum value of 250 × 10^{12} /m^2 at 35 μm, before gradually decreasing to the initial level of 87.5 × 10^{12} /m^2 at 125 μm.

The distribution of GND in SMATed samples is characterized by four distinct regions of varying thickness, as delimited by the green dashed lines in Fig. 2-10b. The gradient microstructure consists of regions I to III, from depths starting from 9 μm. Dislocations are present at a lower level in the near-surface region I. This is attributed to the change in the deformation mechanisms of the material within the nanograin region, transitioning from dislocation motion and deformation twinning to grain rotation [27], [62], [66]. It is worth noting that the closer the material is to the surface, the higher the applied plastic strain. In the deformation region III, as the strain increases, dislocations accumulate at grain boundaries and twins, leading to an increase in GND. In the SPD region II, dislocations accumulate at the boundaries until they reach a maximum value, which corresponds to the maximum value of GND at a depth of 35

μm. As strain continues to increase in region II, the dislocations within the grains increase, resulting in a decreased dislocation gradient and consequently lowering the GND. In the region III, there is a gradual grain refinement that corresponds to the evolution of grain size, as shown in Fig. 2-7. Region IV is an unaffected area where the GND remains at a stable level.

(a)

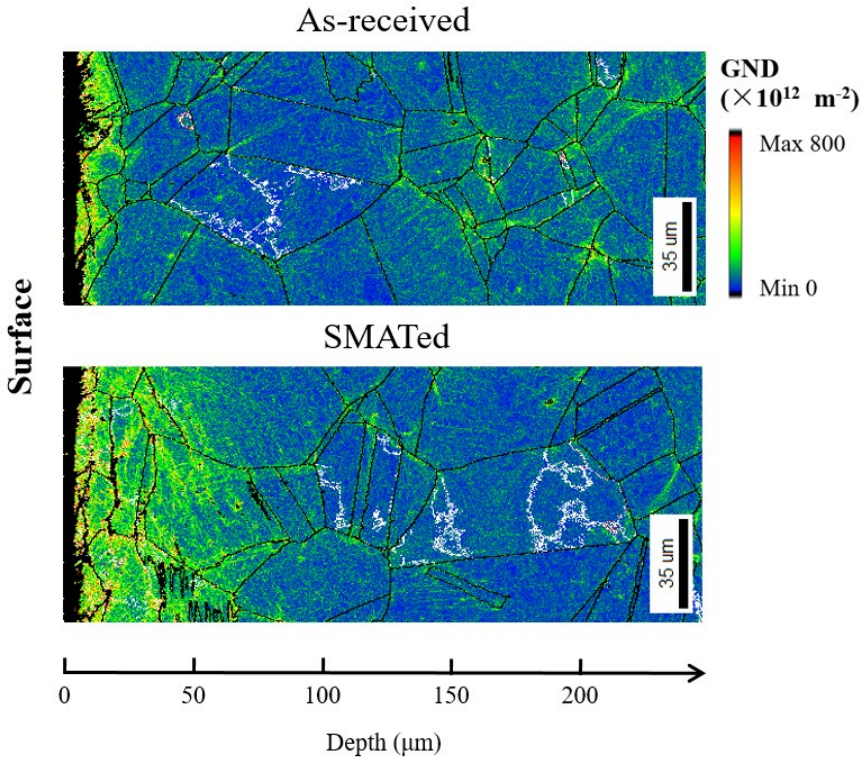

(b)

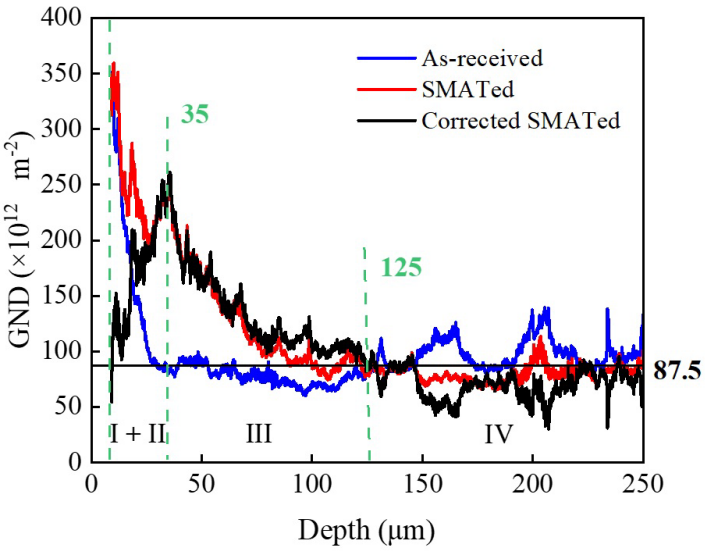

Fig. 2-10. (a) GND maps of cross-section and (b) in-depth average GND distribution of both as-received and SMATed samples, with and without correction of the sample

preparation.

2.2.4 Inhomogeneity deformation

In the previous section, the distribution patterns of KAM and GND, which serve as indicators of local lattice orientation variations within a crystal, were examined in SMATed samples. Unlike KAM, GOS and Grain Reference Orientation Deviation (GROD) are primarily used to characterize the distribution of orientation across an entire grain or a collection of crystals [160], [161]. GOS quantifies the degree of dispersion of lattice orientations within a single grain, thereby measuring the heterogeneity or inhomogeneity of lattice orientations within the considered grain. A smaller GOS value indicates more uniform lattice orientations within the grain, suggesting a grain with a single orientation. A GOS threshold value of 2.5° is commonly used to distinguish between deformed and undeformed grains [161], [162]. Fig. 2-11a illustrates the cross-sectional GOS distribution images of untreated and SMATed samples, where white color indicates that the GOS value is below the critical threshold for undeformed grains. In comparison to the untreated sample, the thickness of the SMAT deformed grain region increases to approximately 130 μm. Notably, the location of the deformed region coincides with the trend of GND distribution, and the gradual decrease in GOS value from the surface reflects the gradual reduction in the degree of deformation.

GROD represents the disparity between the lattice orientation of a given grain and a predefined reference orientation [163]. A larger GROD value indicates a greater deviation between the grain's orientation and the reference orientation. The average orientation of the bulk material serves as the reference orientation to compute the grain's orientation deviation GROD, facilitating the analysis of orientation deviation in both the deformed region near the surface and the less deformed bulk material. Although plastic deformation of polycrystals may appear homogeneous at a macroscopic scale, it can exhibit significant inhomogeneity when comparing different grains together or even within a single grain. As depicted in Fig. 2-11b, there is a gradient deformation within a grain, with greater deformation observed near the surface compared to the bulk. The analysis of GROD reveals that SMAT-induced plastic deformation has transformed the material from initially homogeneously distributed grains to a gradient microstructure.

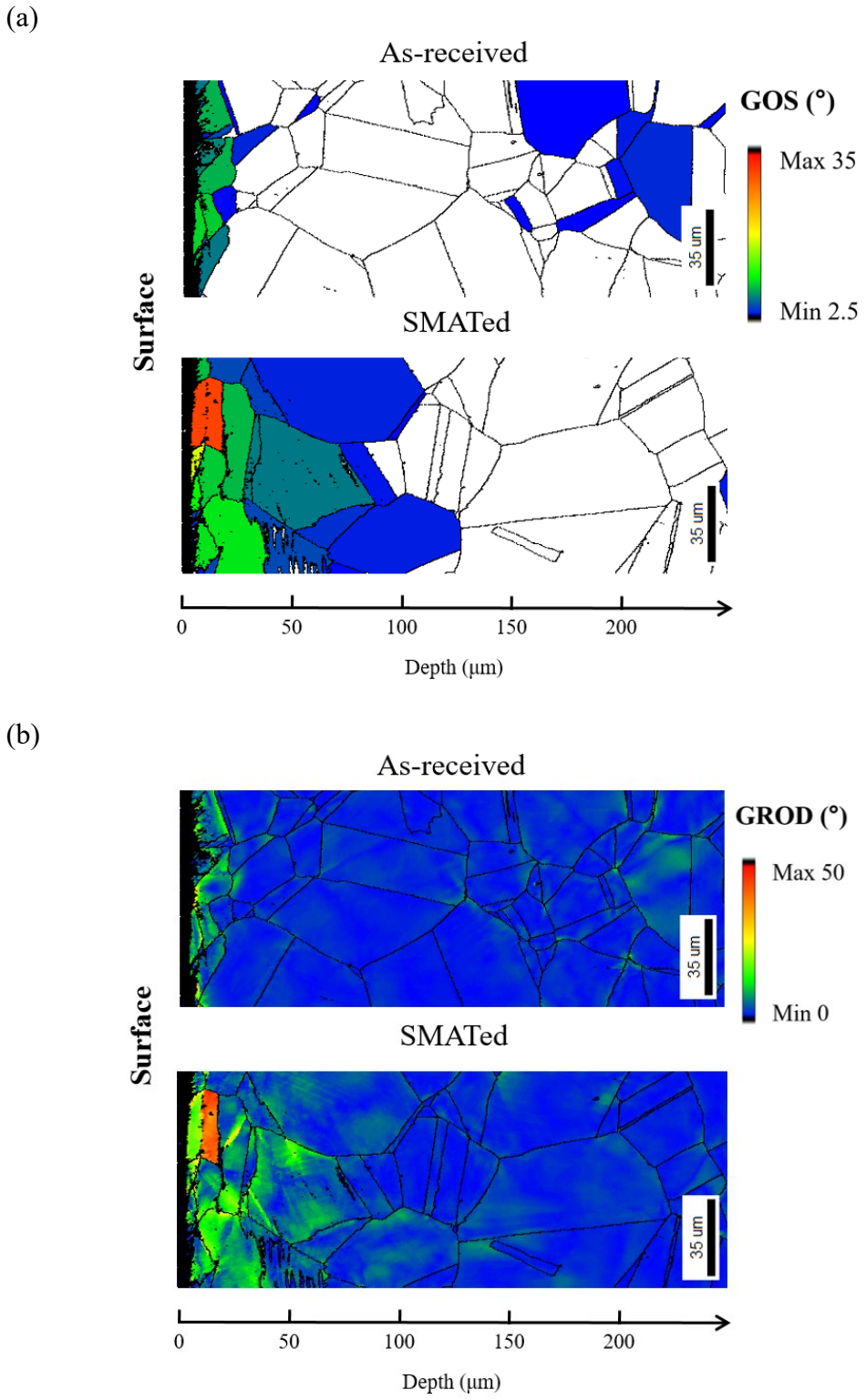

Fig. 2-11. (a) GOS and (b) GROD maps on cross-section of as-received and SMATed samples. White color indicates that the GOS value is below the critical threshold for undeformed grains.

2.3 Hardness and Young's modulus measurements

During SMAT, samples undergo significant plastic deformation at the surface, leading to strain hardening and grain refinement in the near-surface region [105], [156], [164]. This process results in gradient microstructures associated with inhomogeneous mechanical properties. By performing measurements at different depths on the cross-section, variations in microhardness can be observed to understand gradient properties created by SMAT.

In materials science, hardness is a measure of the resistance to localized plastic deformation, performed by an indentation or a scratch test. Nanoindentation is an effective method for estimating local mechanical properties and has been widely used to characterize gradient mechanical behavior, such as Young's modulus, hardness, and yield strength [165], [166], [167]. The fundamental principle of nanoindentation involves measuring the response of a hard indenter, including load and displacement, during the loading then unloading process of penetration. Typically, the indenter possesses a predetermined geometry, such as conical, spherical, Vickers (pyramidal square-based), or Berkovich (pyramidal triangle-based) tips. For hardness measurement, nanoindentation offers precise control over force and displacement during indentation at a nanometer scale. Conventional hardness tests such as Brinell, Rockwell, Vickers and Knoop, measure hardness as a single value by determining the size of the indentation. However, nanoindentation can provide more detailed mechanical properties through analysis of force and displacement curves, including hardness, Young's Modulus creep, fracture toughness. Hardness is determined by dividing the applied load by the contact area [168], [169]:

$$H = \frac{P_{max}}{A} \quad \text{(Eq. 2-2)}$$

where P_{max} is the maximum of applied force; A is the projected contact area, which is determined by the contact depth of the indenter and sample h_c. For a perfect Berkovich diamond indenter, contact area is $A = 24.56h_c^2$ with contact depth $h_c = h_{max} - \varepsilon \frac{P}{S}$. P is the applied force; ε is a constant, about 0.75 for Berkovich indenter; h_{max} the is maximum indentation depth; S is the contact stiffness, defined as the slope of the unloading curve, $S = dP/dh_c$. During the withdrawal of the indenter, the material's elastic recovery is analyzed to determine the reduced modulus (E_r) from contact stiffness, as follows:

$$E_r = \frac{\sqrt{\pi}}{2}\frac{S}{\sqrt{A}} \quad \text{(Eq. 2-3)}$$

Furthermore, the reduced modulus is used to correct the geometry and properties of the indenter material to obtain Young's modulus of the sample, expressed as:

$$E = (1-v^2)\left[\frac{1}{E_r} - \frac{1-v_I^2}{E_I}\right]^{-1} \quad \text{(Eq. 2-4)}$$

where E and v are elastic modulus and Poisson's ratio of the sample, and E_I and v_I are the same parameters for the indenter.

To determine the gradient microhardness and Young's modulus induced by SMAT, measurements are taken at different depths: 5 µm, 10 µm, 15 µm, 20 µm, 40 µm, 80 µm, 100 µm, 300 µm, and 500 µm. Note that the minimum depth starts at 5 µm to avoid edge effects and deformation caused by cutting. In addition, five indentations are performed for each distance to minimize the measurement error in a SMATed sample. All instrumented indentation tests were performed using the Nanoindenter®XP (MTS systems corporation, Eden Praire, USA) equipped with a Berkovich indenter, as shown in Fig. 2-12. The maximum indentation depth is 500 nm. The force and displacement curves obtained are presented in Fig. 2-13.



Fig. 2-12. Nano indenter®XP instrumented indentation system, used at LASMIS laboratory.

Fig. 2-14a presents the in-depth variation of hardness in the near-surface region for the SMATed specimens. It demonstrates that the hardness near the treated surface exhibits a notable increase, with maximum values reaching as high as around 5.6 GPa, gradually decreasing to approximately 3.5 GPa. It is interesting to notice that there is a plateau of high microhardness roughly extending to a depth of 40 µm. This phenomenon is consistent with the microstructure that has been observed for GND and GOS variations from EBSD presented in Figs. 2-10 and 2-11a. Fig. 2-14b shows in-depth Young's modulus variation for the SMATed specimens. It can be seen that Young's

modulus of SMATed specimens remains nearly constant with medium fluctuation, approximately around 200 GPa along the depth. Moreover, some cases present high uncertainties that contains the range of mean values.

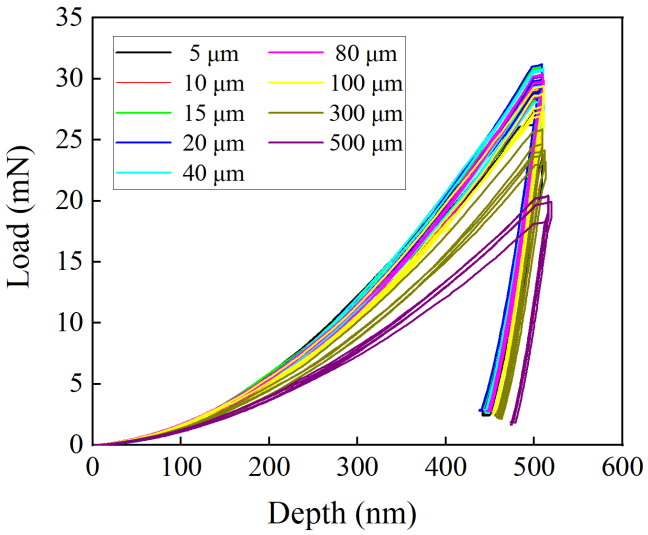

Fig. 2-13. Load-depth curves at different depths.

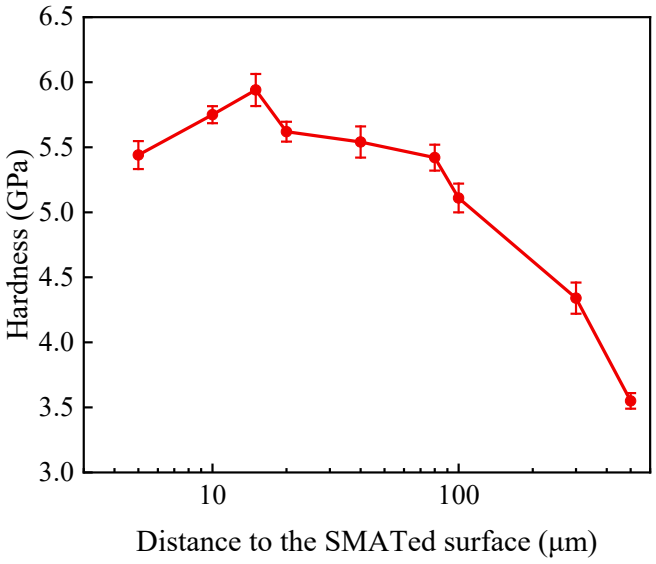

(a)

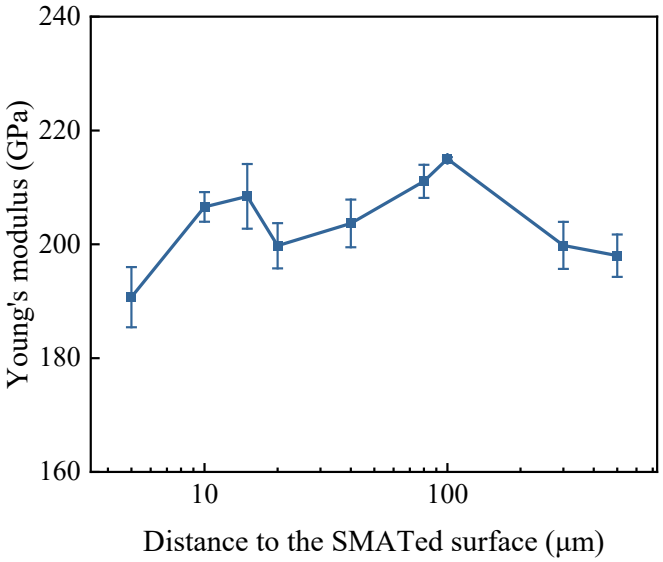

(b)

Fig. 2-14. Variation as a function of depth from the treated surface for SMATed specimens (a) hardness and (b) Young's modulus.

2.4 Residual stress analysis by grazing-incidence X-ray diffraction

X-ray diffraction is a powerful tool for detecting/measuring the crystallographic texture, defects, grain size, lattice distortion, chemical phase and residual stresses [18], [170], [171]. Residual stress is inevitably generated due to plastic deformation during SMAT, which significantly influences the mechanical behavior of materials. Residual stress fields induced by SMAT are expected to be inhomogeneous with respect to depth, especially in the near-surface region. Several experiments and simulations have demonstrated that high compressive surface residual stresses (about -300 to -1000 MPa) are located in the near-surface region, followed by a decreasing gradient towards the bulk region [10], [47], [165], [172].

Both destructive and non-destructive methods can be used to obtain the distribution of residual stress. Iterative electrolytic polishing, developed in last decades, focuses on the depth distribution of residual stress. However, this method alters the internal stress state of the component during polishing, requiring careful correction of the measured data for accuracy. In comparison, the grazing incidence diffraction method is non-destructive and provides a reliable tool for determining the residual stress at different depths below the sample surface. This is why we try to use it.

2.4.1 Grazing-incidence X-ray diffraction method

The $\sin^2\psi$ method, proposed and developed by [173], is an interesting tool for residual stress analysis. It uses the shift of the diffraction peak positions and the out-of-plane tilt angle (ψ) to determine the lattice strains and calculates the residual stresses via Hooke's model. Based on this, the grazing incident method provides a non-destructive way to determine residual stress for different penetration depths below the sample surface by changing the incident angle α.

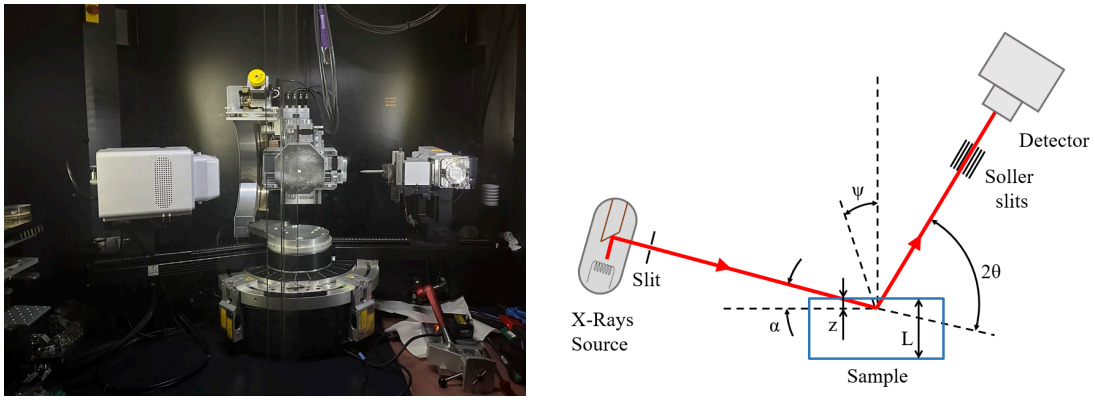

(a) (b)

Fig. 2-15. (a) XRD goniometer with detector and X-rays source, used at LASMIS laboratory and (b) geometry configuration of the grazing incident and $\sin^2\psi$ method.

In a geometry as shown in Fig. 2-15b, the diffraction planes, which are related to the incident and diffracted beam, remains consistently perpendicular to the direction defined by the angle ψ. When the diffraction conditions are fulfilled according to Bragg's relation ($\lambda = 2d_{hkl}\sin\theta$, where λ is the wavelength, d_{hkl} the interreticular distance or interplanar spacing, and θ the Bragg's angle as defined in Fig. 2.15), a diffraction peak can be observed on the diffractogram, corresponding to the diffraction planes of the Miller indices {hkl}. Moreover, the diffracted beam propagates from all the penetrated depth reached by the incident beam. This average penetration depth can be determined as [174], [175]:

$$p(\alpha) = \frac{\beta}{\mu\rho}\left(\frac{1}{\sin\alpha} + \frac{1}{\sin(2\theta-\alpha)}\right)^{-1} \quad \text{(Eq. 2-5)}$$

where α is the angle between the beam and the surface of the sample; θ is the Bragg's angle; μ is the specific absorption coefficient, which depends on the material and the wavelength: for chromium radiation presently used, the value $\mu \approx 112.3$ cm^2/g; ρ is the mass density: for 316L SS, ρ = 7.85 g/cm^3; β is the coefficient, which depends on the

mean value considered: for Genzel [176], $\beta = 1$. The average penetration depth can now be plotted versus $\sin^2\psi$, accounting for the different incidence angles, as shown in Fig. 2-16. It is important to note that ψ is defined as the difference between the Bragg's angle and the incidence angle, such as $\psi = \theta - \alpha$. Various incident angles α (3, 5, 7, 9, 11, or 15°) were chosen to obtain diverse penetration depths. It is noted that the penetration distance rises as the angle of incidence increases, culminating in a maximum value at 2.3 µm, for $\alpha_{max} = 15°$. Fig. 2-16 illustrates that there is a plateau for all the incidence angles for $\sin^2\psi$ values ranging between 0.1 and 0.8. In order to guarantee the same mean penetration depth for a given set of measurements at a given depth, the range of possible Bragg's angles is selected according to $\sin^2\psi$ values, as $2\theta \in [50°+2\alpha;\ 130°+2\alpha]$. In addition, to determine the different stress components, every XRD measurement is conducted at each incident angle (thus for each depth) for three orientations φ (angle of rotation of the sample around its normal surface direction): 0, 45, and 90°.

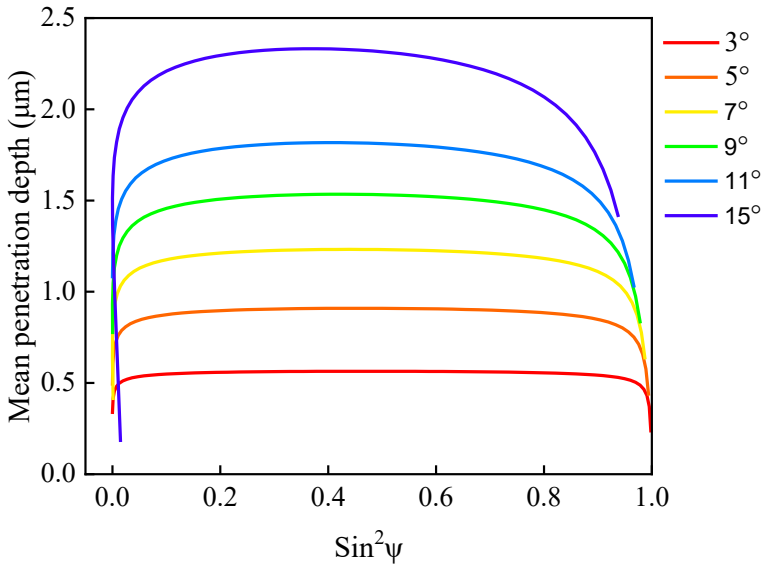

Fig. 2-16. The mean penetration depth with $\sin^2\psi$ for various incident angles.

As we previously write, it is necessary to relate the measured quantities to a mean position $\bar{Z}$ in the materials. It is however important to note that the corresponding mean position in general is not equal to the mean penetration depth, especially when the sample thickness L is finite. Instead, the corresponding mean position represents the average value of the z-depth over the depth, weighted by an attenuation factor [175]:

$$\bar{Z} = \frac{\int_0^L z e^{-z/p} dz}{\int_0^L e^{-z/p} dz} = \begin{cases} p & for\ L \to \infty \\ p - \frac{p e^{-\frac{L}{p}}}{1 - e^{-\frac{L}{p}}} = p\left(\frac{1 - 2e^{-\frac{L}{p}}}{1 - e^{-\frac{L}{p}}}\right) & for\ finite\ L \end{cases} \quad \text{(Eq. 2-6)}$$

The mean lattice strain ε can be determined from the interplanar spacing d_{hkl} measured in the direction of the scattering vector, defined by the peak position at Bragg's position θ, and the incident angle α. For a given incident angle α, corresponding to an average position $\bar{Z}$ of the measured quantity, we can use several ψ, thus different θ by using the relation $\psi = \theta - \alpha$, and different orientations φ. We also remind that a given Bragg's angle is associated with {hkl} indices through Bragg's relation and crystallographic structure. Typically, for austenite of cubic lattice system, $d_{hkl} = \frac{a}{\sqrt{h^2+k^2+l^2}}$ with a the lattice spacing. The mean lattice strain $\bar{\varepsilon}$ corresponds to an average over the depth, weighted by an attenuation factor and is related to the mean interplanar spacing $\bar{d}_{hkl}$ by the following relationship relevant for finite deformation:

$$\bar{\varepsilon}\left(\varphi, \psi = \theta(hkl) - \alpha, \bar{Z}\left(p(\alpha)\right)\right) = \ln\left(\frac{\bar{d}_{hkl}(\varphi,\psi,\bar{Z})}{d^0_{hkl}}\right) \quad \text{(Eq. 2-7)}$$

where d^0_{hkl} is the free stress lattice spacing. The stress can then be assessed by measuring the different Bragg's angle of selected peaks, along the scattering vector direction for the corresponding ψ, and different orientations φ. Indeed, according to Bragg's law and from Hooke's model adapted for isotropic crystallites [177], [178], we can write:

$$\bar{\varepsilon}(\varphi,\psi,\bar{Z}) = \ln\left(\frac{\sin\theta_0}{\sin\theta}\right) = \ln\left(\frac{1}{\sin\theta}\right) - \ln\left(\frac{1}{\sin\theta_0}\right) = S^1_{\{hkl\}}(\bar{\sigma}_{11} + \bar{\sigma}_{22} + \bar{\sigma}_{33}) +$$
$$\frac{1}{2}S^2_{\{hkl\}}\bar{\sigma}_{33}\cos^2\psi + \frac{1}{2}S^2_{\{hkl\}}(\bar{\sigma}_{13}\cos\varphi + \bar{\sigma}_{23}\sin\varphi)\sin 2\psi + \frac{1}{2}S^2_{\{hkl\}}(\bar{\sigma}_{11}\cos^2\varphi +$$
$$\bar{\sigma}_{22}\sin^2\varphi + \bar{\sigma}_{12}\sin 2\varphi)\sin^2\psi \quad \text{(Eq. 2-8)}$$

where $\bar{\sigma}_{ij}$ are the mean macroscale stress components; $S^1_{\{hkl\}}$ and $S^2_{\{hkl\}}$ are the radio-crystallographic elastic coefficients calculated for different {hkl} reflections or plane families. It is frequently assumed that $\bar{\sigma}_{j3} = 0$ for superficial measurements. It is important to note that the mean stress corresponds to an average over the depth, weighted by an attenuation factor. To obtain the stress at the mean position, it is necessary to develop polynomial expressions of the stress. It is easy to prove that for linear dependence with depth, the average over depth with exponential weighting function, leads to the equality between the stress and the mean stress as function of the mean position. For higher series expansion, the relation is a little bit more complicated, but will be useless at first approximation in our cases as further seen.

2.4.2 Experimental procedures

The residual stresses of the SMATed 316L sample were characterized by XRD using a Bruker D8 advance X-ray diffractometer (Cr-Ka radiation) as shown in Fig. 2-15a. The XRD incident slit size is equal to 0.2 mm, and the detector slit size is 0.6 mm. The X-ray beam directed toward the sample is monochromatic, with a wavelength of 0.229 nm and an energy of 20 keV. Table 2-1 lists the expected {hkl} diffraction and Bragg's angle for free stress state, for austenite 316L stainless steel (FCC with lattice parameter a_0 = 0.358 nm).

Table 2-1 also provides the variation range of different possible 2θ from 67° to 130°, and the angle of incidence α are chosen possibly varying from 3° to 15°. After calculations, the variation range of ψ (ψ = θ – α) is approximately between 18.5° and 62°. The values of $\sin^2\psi$ range then from 0.10 to 0.78, falling within the range necessary to ensure a constant mean penetration depth, for the different studied peaks when considering a given incident angle, as shown in Fig. 2-16. In addition, an XRD measurement was performed for different measurement conditions (angle of incidence, diffraction peaks and orientations φ angle).

Uncertainty in XRD measurements impacts both precision and accuracy. This uncertainty arises from various factors, including instrumental uncertainty (such as wavelength calibration and sample stage or detector misalignment) and analytical uncertainty (such as peak fitting and background subtraction). Typically, powders of the same material or materials with similar peak positions, which are generally unstressed, are employed to correct for the uncertainty related to the instrumental misalignment or mismatch. For each peak in the powder sample, the shift between the measured and theoretical values is used to correct the peak position of the measured sample. In this work, iron powder was used to account for the offsets in peak positions introduced by the instrumental uncertainty. The measured shifts relative to the theoretical peak positions of 68.78, 105.90, and 156.10 are -0.17, -0.13, and -0.13, respectively.

Table 2-1. Reference positions for austenite diffraction peaks under Cr radiation.

h	k	l	$2\theta_0$ (°)
1	1	1	67.27
2	0	0	79.52
2	2	0	129.51

2.4.3 Results

This section employs a stress measurement method based on grazing incident X-ray diffraction, which serves as a tool for analyzing samples with stress gradients. This method is particularly crucial for SMATed samples, where it is necessary to characterize the distribution of residual stresses in the near-surface region to understand the material properties. For stress-free materials, the stress value should ideally be zero. Measurements on unstressed materials are frequently employed to validate experimental methods or correct from measurement errors and bias. Fig. 2-19b presents the measurement results of ferrite powder samples using grazing incident X-ray diffraction. The results indicate that the three components of the stress are nearly 0 MPa at various depths.

Figs. 2-17a, 2-17d, and 2-17e show the XRD patterns of the Miller indices {111}, {200}, and {220} peaks under varying incidence angles, respectively, for a SMATed 316 SS sample at $\varphi = 0°$. It is clearly observed that the different intensities vary for the three peaks, and the diffraction intensity increases with increasing incidence angle. In Figs. 2-17, the positions of the peak are shifted to the left with increasing incident angle. In addition, the diffraction intensity presents low sensitivity to changes in φ angles, as seen when comparing for indices {111} for the three orientations (Figs 2-17a, 2-17b and 2-17c).

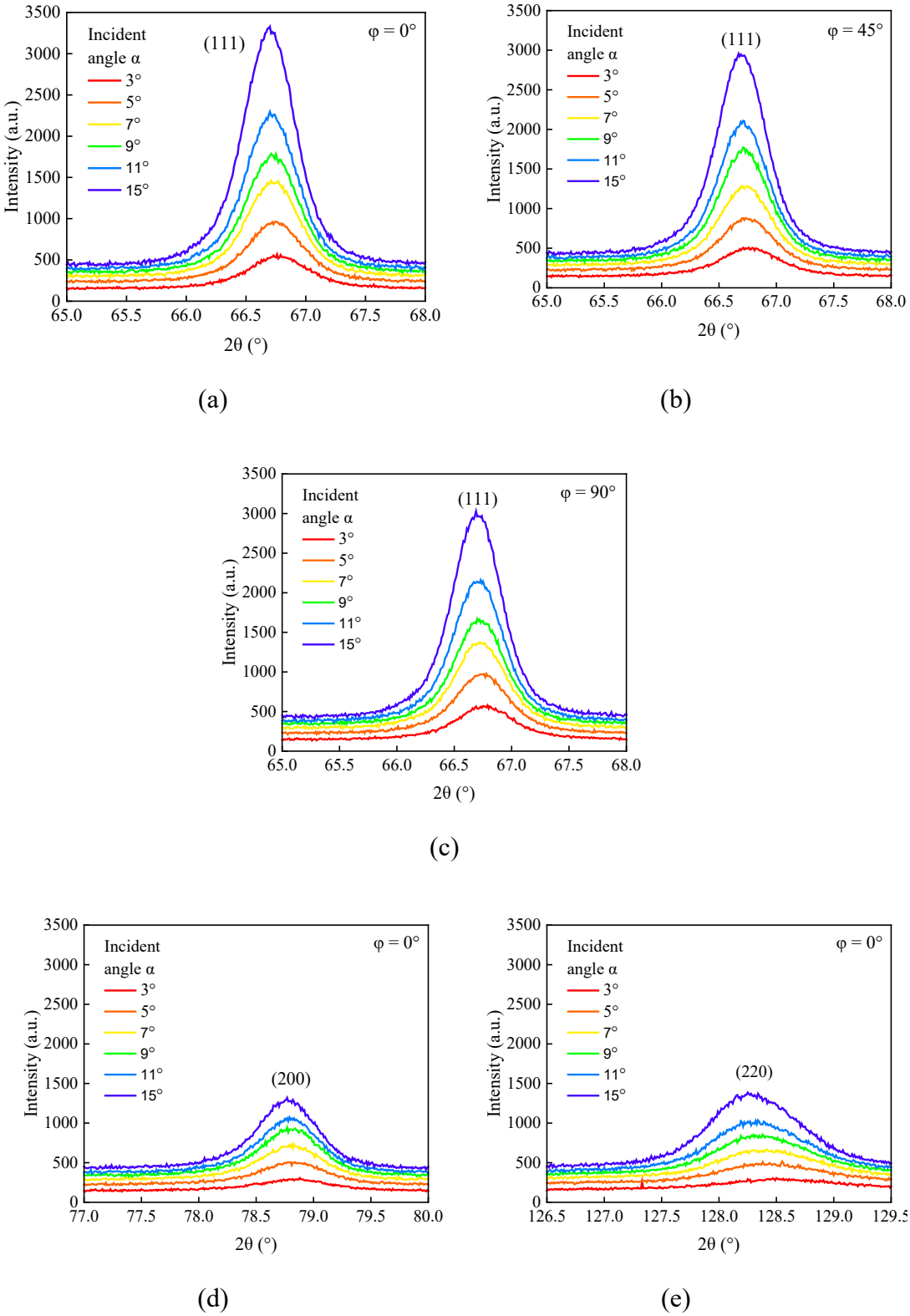

Fig. 2-17. Intensity versus 2θ angle XRD pattern of a SMATed 316 SS sample with different incident angles for (a) – (c): the Miller indices {111} peak at φ angles of 0°, 45°, and 90°, respectively; (d) the Miller indices {200} peak; and (e) the Miller indices

{220} peak.

Fig 2-18 illustrates the variation of $\ln\left(\frac{1}{\sin\theta}\right) - \ln\left(\frac{1}{\sin\theta_0}\right)$ with $\sin^2\psi$ at $\varphi = 0°$ for Fe powder and SMATed 316L SS. It can be observed that the variation is almost stable at 0 for Fe powder, whereas it is more pronounced for SMATed 316L. In general, the use of classical $\sin^2\psi$ method requires to have at least 13 different ψ (7 with $\psi > 0$ and 6 with $\psi < 0$) [179]. Actually, only 3 peaks can be used in the present grazing incident approach. The results have thus to be considered as a trend.

The φ angles of 0°, 45°, and 90° are considered for calculating the in-plane stress components, with the stress components $\bar{\sigma}_{33}$, $\bar{\sigma}_{23}$, and $\bar{\sigma}_{13}$ assumed to be 0. Fig. 2-19a depicts the stress distribution of the SMATed samples from depths ranging from 0.5 to 2.3 μm, corresponding to the 6 values of incident angles. It can be observed that stress for 11 and 22 components exhibits similar compressive evolution along the depth. The 12 component is close to 0 at the different depths. We can conclude that this is an in-plane stress state for the SMATed sample. It is also observed that the maximum stresses (in absolute values) of components 11 and 22 are 392.5 ± 119.6 MPa and 421.8 ± 142.9 MPa, respectively. These significant surface compressive stresses are consistent with the observed variation in residual stress using the chemical step-by-step removal method described in [100]. It is noteworthy to mention the large error values of the stresses for both the SMATed and powder samples, which are associated with the discrepancies in peak positions and their uncertainties, as shown in Fig. 2-18. For components 11 and 22 the spatial evolution is roughly constant over the range of observation. This limited depth range of the measurements is due to constraints on the incident angle, which hinders the observation of significant gradient features in the results.

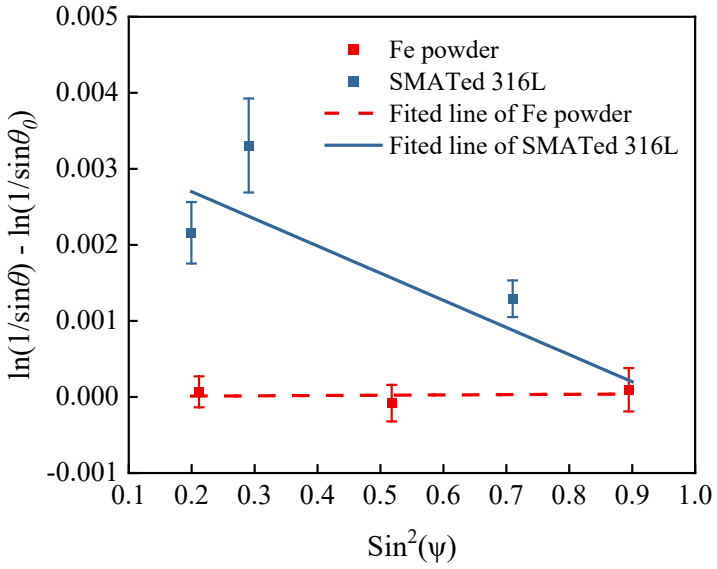

Fig. 2-18. $\ln\left(\frac{1}{\sin\theta}\right) - \ln\left(\frac{1}{\sin\theta_0}\right)$ with sin²ψ of a SMATed 316L SS and Fe powder at φ = 0°.

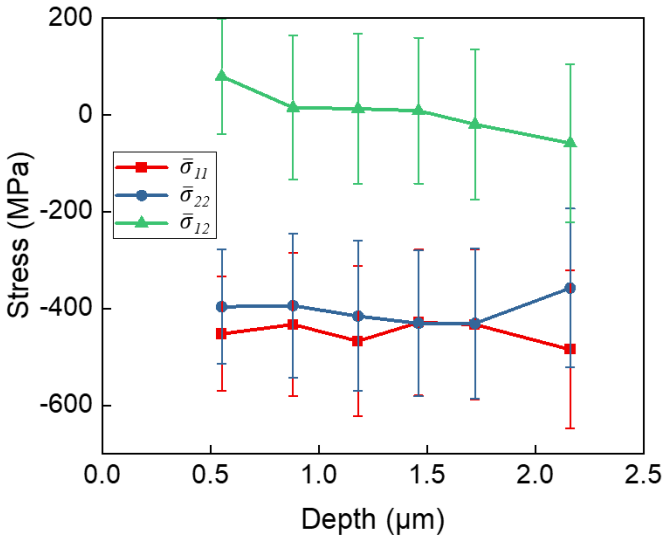

(a)

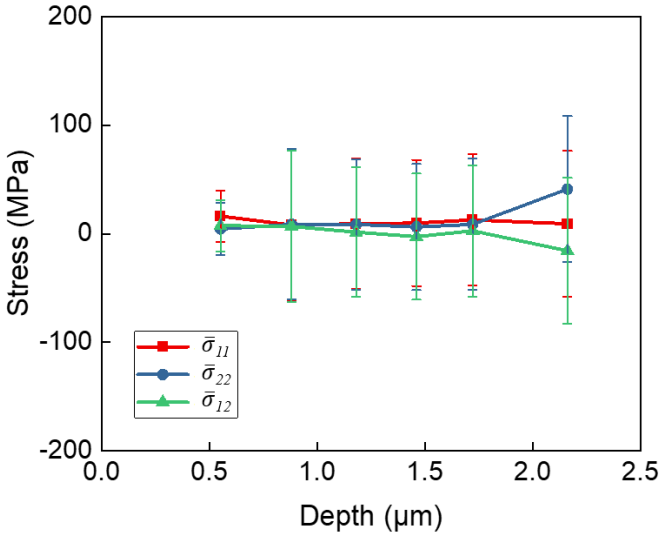

(b)

Fig. 2-19. Stress variations of different components on the near surface of (a) SMATed samples and (b) stress-free Fe powder.

2.5 Conclusion

The purpose of this chapter is to investigate the microstructure and properties of SMATed 316L SS compared to the as-received specimens. The materials studied and the characterization techniques employed are first described. The microstructure was observed at different depths using EBSD to characterize the deformation zones produced by SMAT. To gain detailed insight into the mechanical behavior of the material, mechanical properties such as hardness and Young's modulus were measured using nanoindentation. XRD was used to accurately measure the residual stresses induced by SMAT in the near-surface region. The experimental results are summarized as follows:

- EBSD observations reveal that the grains in SMATed specimen exhibit gradient misorientation and distribution of LAGBs and GNDs. The GOS map illustrates a gradual decrease in deformed grains in the depth direction. This suggests that the strain and strain rate induced during the SMAT result in the formation of a gradient microstructure in the surface region, which consequently affects the material properties.
- Nanoindentation tests showed a significant gradient in hardness within the near-

surface region of the SMATed samples, with hardness values gradually decreasing from the surface to the depth. Moreover, some changes in Young's modulus were observed in the near-surface region, although these changes were not as pronounced and cannot be definitively attributed to the SMAT process.

- Furthermore, this study focused on in-depth stress measurement on a SMATed sample using a non-destructive grazing-incidence method. While compressive stresses were observed in the near-surface region, there is ample room for improvement. This includes exploring the selection of multiple beam sources to improve accuracy and depth investigation, as well as conducting measurements on untreated specimens to evaluate residual stresses introduced by specimen preparation.

Chapter 3: Experimental study of LCF behavior of SMATed 316L SS

In engineering applications, LCF represents one of the primary failure modes of components, characterized by large plastic strains under a low number of load cycles. The study of material behavior under LCF conditions offers valuable insights into phenomena, such as crack propagation, process softening, strain concentration, and work hardening [28], [56], [180]. As highlighted in Chapter 1, the surface nanocrystallization associated with microstructure evolution during SMAT has been extensively studied by both experimental and numerical methods. It is interesting to give more attention to the mechanical behavior of gradient microstructure features in the LCF regime.

In order to elucidate the macroscopic LCF behavior of 316L SS, a comparative analysis was conducted between the as-received and SMATed samples at different strain amplitudes. Particular attention was paid to analyze the evolution of back stress and effective stress, as defined in Section 1.4.3, from each hysteresis loop under LCF [56], [181]. Furthermore, the fatigue properties have been compared between the as-received and SMATed samples to examine the Bauschinger effect under both symmetric and asymmetric loading scenarios. Detailed measurements of fatigued 316L SS were performed to examine the microstructure evolution under fatigue loading. A comparison was given for the as-received and SMATed samples. In addition, to investigate the LCF behavior of the as-received samples, microstructure changes were studied at different numbers of cycles using EBSD measurements. Specifically, the evolutions of KAM, GNDs and GOS during fatigue cycling were analyzed to understand the microscale fatigue properties in relation to the observed macroscopic behavior.

3.1 Experimental procedures for fatigue tests

A comprehensive description of the material preparation and SMAT processes is provided in Chapter 2. The strain-controlled LCF tests were performed by a servo-hydraulic testing system (Denison Mayes Group, 50 kN) at ambient temperature. The ends of the cylindrical specimen were fixed by hydraulic clamping, as illustrated in Fig.

3-1. An extensometer with a gauge length of 10 mm was attached to the gauge of the sample. In strain-controlled fatigue testing, a constant or variable strain amplitude is applied to the specimen, which is controlled and monitored by the extensometer. A force sensor located at the end of hydraulic clamping measure the resulting reaction force response. Simultaneously, the measurement system records the number of cycles until failure. It is noted that the fatigue life, N_f, was defined as either a 30% decrease in reaction force or a complete rupture of the specimen for all the fatigue tests. Three different strain amplitudes, 0.5 %, 0.8 % and 1.25 %, were applied at a constant strain rate of 4×10^{-3} s^{-1}. Both uniaxial tension/compression (load ratio R = −1) and asymmetric loading (load ratio R = −0.5) are employed for as-received or SMATed specimens. Table 3-1 outlines all the testing conditions, with one measurement for each test condition. EBSD measurements (with step size 0.1 μm) were additionally performed on the specimens' cross-section, with detailed specimen preparation outlined in Chapter 2. Following the LCF test, based on the characteristics of stress amplitude variation with the number of cycles, four different cycle numbers (as-received, 4th, 20th and failure) were chosen to evaluate the microstructural changes by one EBSD measurement for each cycle number.

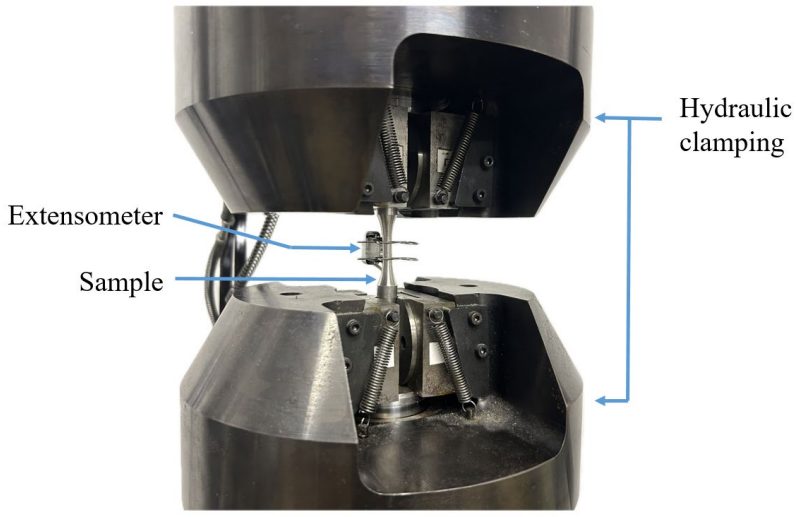

Fig. 3-1. The servo-hydraulic fatigue testing system with a cylindrical specimen.

Table 3-1 Low cycle fatigue testing conditions.

Condition	Load ratio R	Strain amplitude ±Δε (%)
As-received	-0.5	0.5; 0.8; 1.25
	-1	0.5; 0.8; 1.25
SMAT	-0.5	0.5; 0.8; 1.25
	-1	0.5; 0.8; 1.25

3.2 Cyclic deformation behavior under symmetric loading in LCF conditions

3.2.1 Hysteresis loops

Hysteresis curves provide a visual representation of the cyclic deformation properties of materials. In LCF test, the strain can be computed using the deformed gauge length measured by the extensometer and the initial length. The engineering stress was also determined using the reaction force in the loading direction and the initial cross-sectional area. In Fig. 3-2, the hysteresis loops of both as-received and SMATed 316L SS are presented for strain amplitudes 0.5 %, 0.8 % and 1.25 % under symmetric loading (load ratio R = −1). The number of cycles at failure varies depending on the magnitude of the applied strain amplitude as shown in Fig. 3-3. For the stress amplitude ±Δε = 1.25%, the Nf is approximately 200; it is about 945 cycles for ±Δε = 0.8 %; and it extends to roughly 2925 cycles for ±Δε = 0.5 %, as listed in Table 3-2. The Coffin-Manson relationship is a widely used empirical formula in LCF to describe the relationship between strain amplitude and fatigue life. This relationship is typically expressed as:

$$\Delta\varepsilon = \varepsilon'_f (2N_f)^c \qquad \text{(Eq. 3-1)}$$

where ε'_f is the fatigue ductility coefficient and c is the fatigue ductility exponent, typically a negative value. Fig. 3-3c predicts the strain amplitude with fatigue life for as-received and SMATed 316L SS samples, by use of Eq. 3-1 with the parameters ε'_f = 9.01 and c = -0.33 for as received; ε'_f = 10.7 and c = -0.35 for SMATed samples. We can see that SMATed 316L SS exhibits a higher fatigue life at the same strain amplitude in LCF regime.

Table 3-2. Fatigue life of as-received and SMATed at different strain amplitudes.

Strain amplitude	Fatigue life N_f	
$\pm\Delta\varepsilon$ (%)	As-received	SMATed
0.5	2925	3781
0.8	945	759
1.25	200	258

Five cycle numbers, including the 2nd cycle and four others regularly distributed (0.25, 0.5, 0,75 and 0.9 times Nf), were systematically selected to present the hysteresis loop variation during fatigue. The results show that the stresses in SMATed samples are higher than those in as-received samples. It can also be observed that the differences between the hysteresis loops at 0.25, 0.5, 0.75, and 0.9 times Nf gradually decrease as cyclic loading progresses. It indicates a significant change in mechanical properties especially during the initial stage of fatigue in both materials. As the strain amplitude increases, the variation of maximum stress per cycle diminishes with the cycle, which is particularly noticeable at 1.25 % strain amplitude of the as-received material (Fig. 3-2a). For the as-received samples, the difference in maximum stress between the 2nd and 0.75Nf cycle is 104.5 MPa for a strain amplitude of 0.5%, 91.0 MPa for a strain amplitude of 0.8%, and 22.6 MPa for a strain amplitude of 1.25%. Moreover, the SMATed materials exhibit a more pronounced (about 15% overall) deviation of maximum stress per cycle compared to the as-received materials. For example, the deviation is 124.5 MPa at a strain amplitude of 0.5%, 115.6 MPa at 0.8%, and 71.7 MPa at 1.25%.

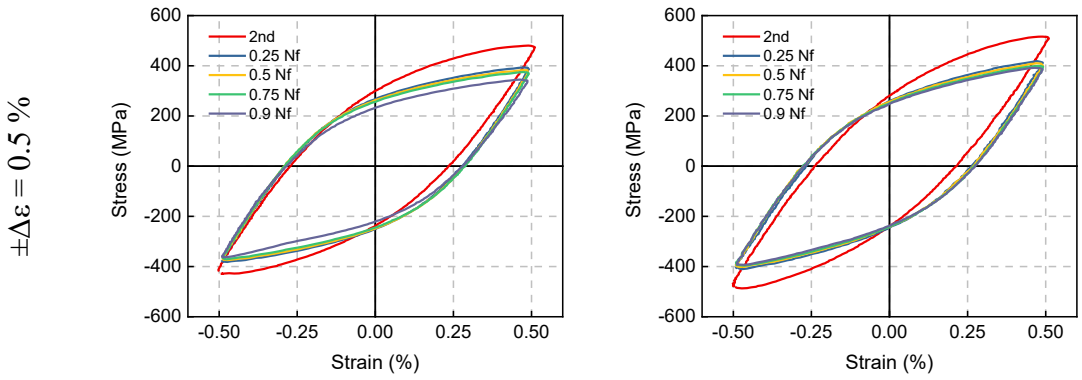

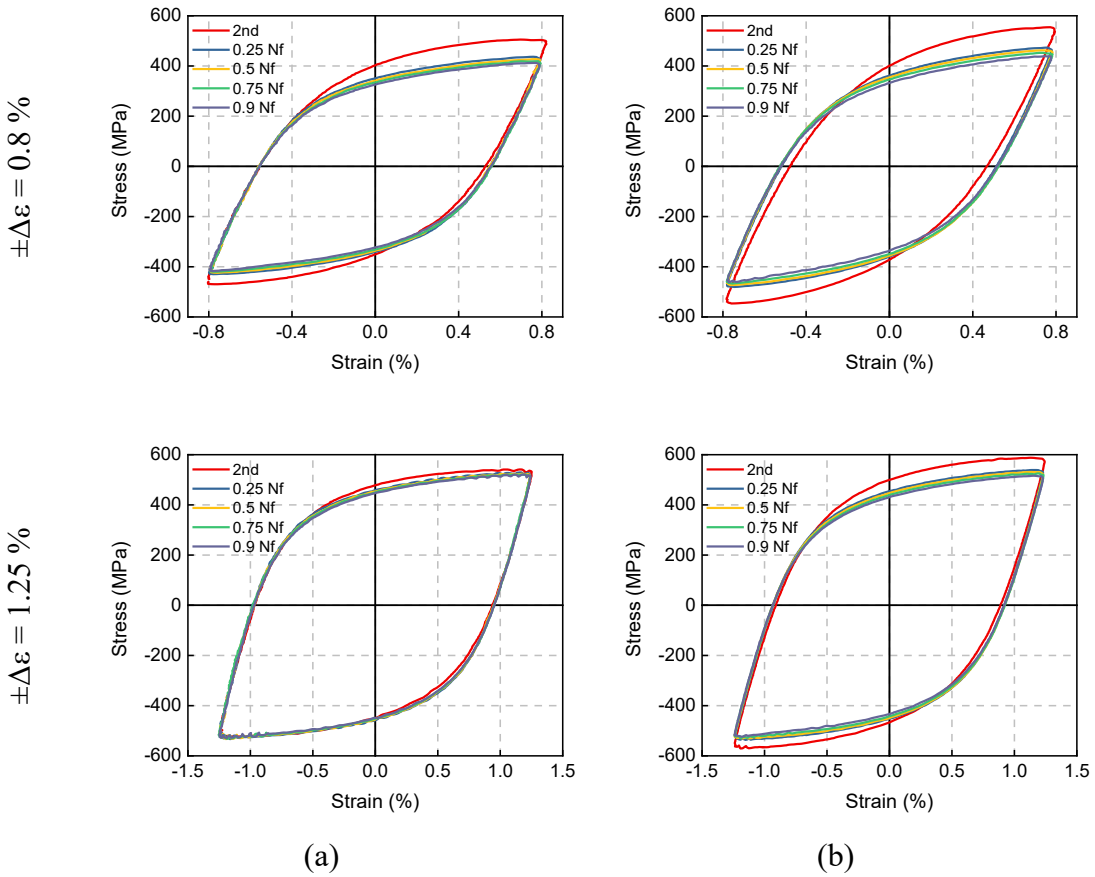

Fig. 3-2. Selected hysteresis loops of (a) as-received and (b) SMATed 316L SS samples, at strain amplitudes of 0.5 %, 0.8 % and 1.25 % under symmetric loading (load ratio R = −1).

The evolution of cyclic stress amplitudes offers an effective illustration of the cyclic behavior (hardening and softening) during fatigue loading, which can be directly illustrated with the hysteresis loops. Fig. 3-3 displays the stress amplitudes versus the cycle number, for the as-received and SMATed samples in a semi-logarithmic scale. On the one hand, the results globally reveal that the stress amplitude increases with the strain amplitudes in different samples. Compared with the as-received samples, the fatigue strengths of the SMATed samples are significantly enhanced for each strain amplitude during the LCF process. For instance, during the second cycle, the strength of the SMATed samples is improved by about 16.73 MPa and 35.26 MPa under strain amplitudes of 0.5 % and 0.8 % respectively, and enhanced about 80.5 MPa under strain amplitudes 1.25 %. In addition, the fatigue lives of SMATed samples are much higher than those of the as-received samples. On the other hand, significant hardening is

observed at the initial cycling in both as-received (up to the fourth cycle) and SMATed samples (up to the third cycle). Gradual softening then occurs as cyclic loading continues, and there is no saturated stage before final failure, as shown in Fig. 3-3. It is worth noting that the evolution of stress amplitude is sharply softening at the end for the SMATed and as-received samples, except for the as-received sample at the specific strain amplitude of 1.25 % (blue triangle curves in Fig. 3-3a), which seems to remain constant up to the failure.

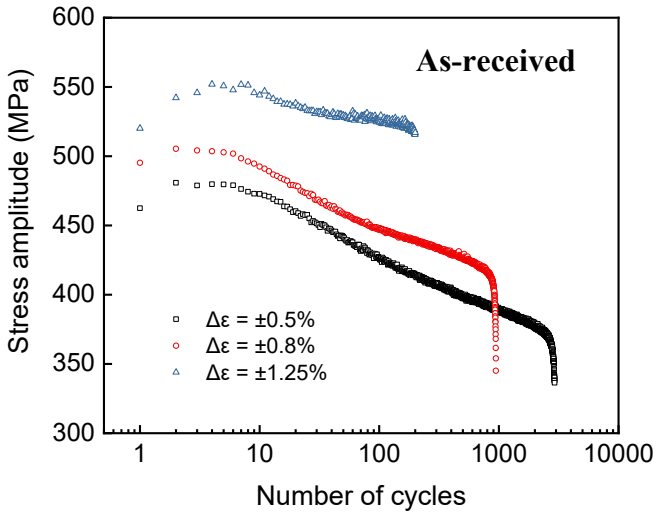

(a)

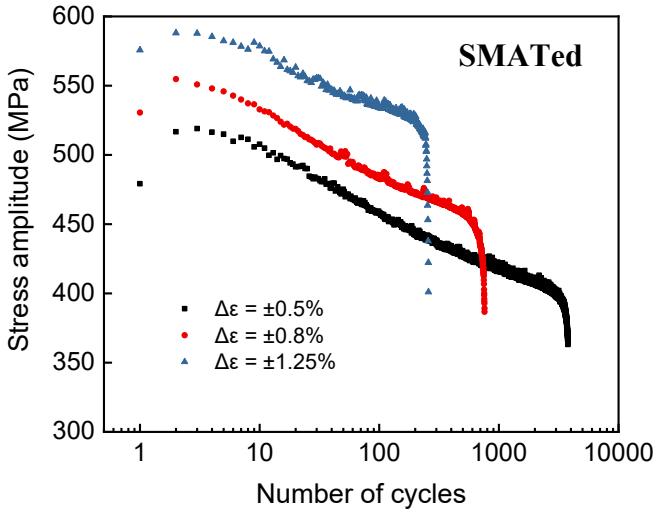

(b)

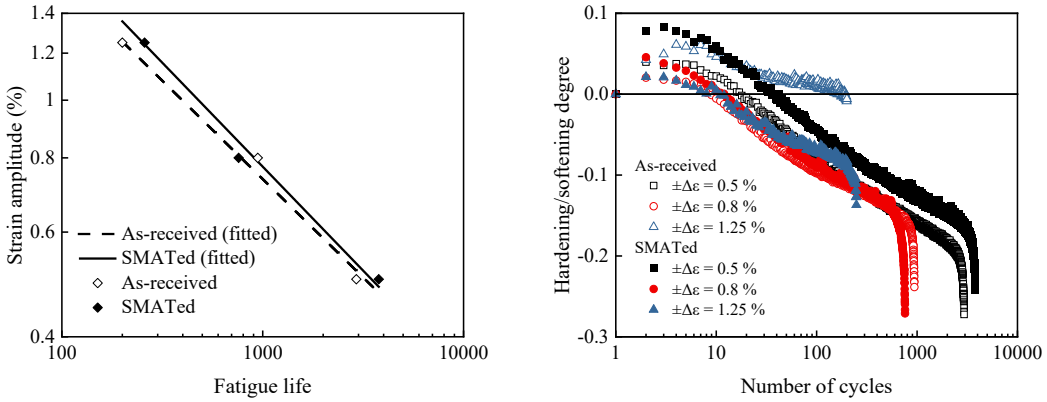

(c) (d)

Fig. 3-3. Stress amplitude versus the number of cycles for (a) as-received and (b) SMATed 316L SS samples, at strain amplitudes of 0.5 %, 0.8 % and 1.25 % under symmetric loading (load ratio R = −1). Note that the cycle numbers are represented on a logarithmic scale. (c) is the predicted relationship of strain amplitude and fatigue life of as-received and SMATed 316L SS samples. (d) Cyclic hardening/softening degree for all the samples (positive values indicate hardening, while negative values indicate softening).

To better describe the cyclic behavior, the degree of hardening/softening H_i is provided as a function of the cycle number calculated as:

$$H_i = \frac{\Delta\sigma_i - \Delta\sigma_1}{\Delta\sigma_1} \text{ for } i = 2, 3,,, N_f \qquad \text{(Eq. 3-2)}$$

where $\Delta\sigma_1$ and $\Delta\sigma_i$ are the stress amplitude at first and i-cycle, respectively. At low strain amplitude levels (0.5% and 0.8%), both as-received and SMATed 316L SS exhibit similar cyclic deformation tendencies. In the initial stage of cyclic deformation, the SMATed samples exhibited a greater hardening degree compared to the as-received specimens (see Fig. 3-3d). However, at higher strain amplitude level of 1.25% for the as-received samples demonstrate a continuous hardening without softening part (because $\forall i, H_i > 0$), whereas the SMATed specimens maintain the same cyclic deformation behavior as observed at low strain amplitude levels. It suggests that the cyclic deformation mechanisms at high strain amplitudes may be altered by SMAT.

3.2.2 Effective stress and back stress

To further characterize the cyclic behavior of LCF, Cottrell's method is used to extract the evolution of effective stress and back stress from hysteresis loops, as presented in Fig. 3-4a [182]. Each hysteresis loop was systematically divided into four different regions: the tensile and compressive sections divided by strain range, with each section further subdivided into elastic and plastic regions based on the yield points. It is worth noting that the yield points of tensile and compressive sections were determined by the point of intersection between the stress-strain curve and the setting of the strain offset parallel with elastic modulus. The strain offset is equal to 5×10^{-5} in this work, which is sensitive to the extensometer, the sampling frequency, and signal analysis [183], [184], [185], [186]. The maximum and minimum of stress and strain can be directly obtained in tensile and compressive sections. The yield stress σ_y can also be read at the yield point in tensile section, similarly the reverse yield stress σ_y^r can be obtained from the compressive section, respectively. The effective stress σ_{eff} and the back stress X can be calculated according to:

$$\sigma_{\text{eff}} = (\sigma_{\max} + \sigma_y)/2 \quad \text{(Eq. 3-3)}$$

$$X = (\sigma_{\max} - \sigma_y)/2 \quad \text{(Eq. 3-4)}$$

For example, Fig. 3-4b shows the calculated effective stress and back stress with the number of cycles at strain amplitude of 0.5 %. When comparing these three types of stresses, it can be found that maximum stress and back stress exhibit the same tendency during cyclic deformation, whereas the evolution of the effective stress presents only slight linear variations. There is indeed a slightly continuous decreasing of effective stress from 210.22 MPa to 185.13 MPa until final failure. It can therefore be inferred that the variation in maximum stress is primarily correlated to changes in back stress.

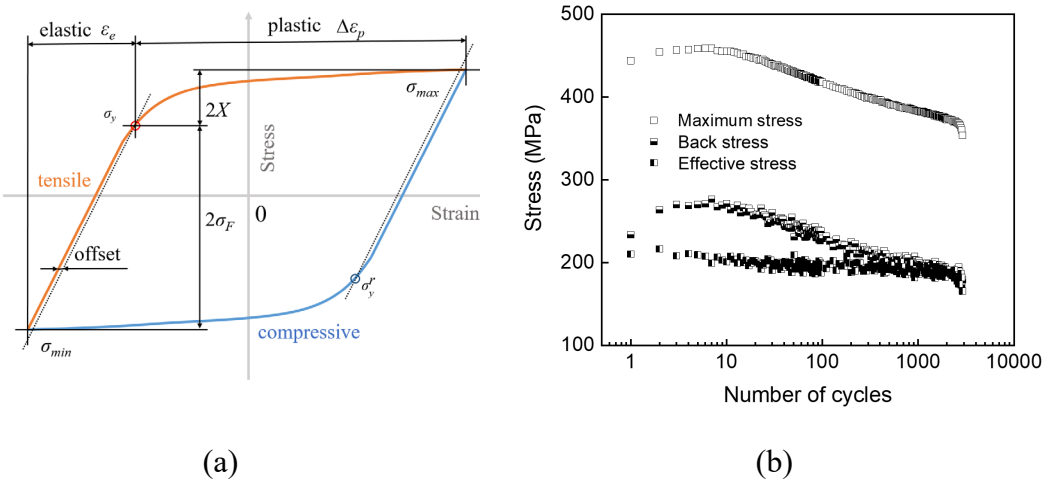

(a) (b)

Fig. 3-4. (a) Scheme for partition of hysteresis loops to identify the yield stress, back stress and effective stress by the Cottrell's method and (b) evolutions of maximum stress, effective stress and back stress as a function of number of cycles at strain amplitude of 0.5 %.

The effective stress and the back stress represent the isotropic hardening and kinematic hardening during plastic deformation, respectively [52], [139], [187]. Fig. 3-5 presents the evolutions of effective stress and back stress with the accumulated plastic strain for the as-received and SMATed 316L samples. It is noteworthy that the cumulative plastic strain is computed by summing the plastic strains generated separately during tensile and compressive sections in each fatigue cycle, as explained in the partition of hysteresis curve in Fig. 3-4a. It can be seen in Fig. 3-5a that the effective stress exhibits a decreasing trend with increasing cumulative plastic strain in both the as-received and SMAT samples. In addition, the reduction in effective stress amplifies with higher strain magnitudes. The SMATed samples have a weaker softening compared with the as-received samples. As mentioned above, the microstructure induced by SMATed improves the material's strength by different mechanisms (see the description in Section 1.4 of Chapter 1), leading to a lower effective stress for the same strain level than the as-received ones. The results indicate that the effective stress decreasing highly depends on the plastic strain level. The larger the plastic deformation, the lower the effective stress. This phenomenon is also documented in [188]. It is attributed to crystal rotation induced by cyclic deformation, resulting in a decrease in effective stress. As the strain amplitude or cycle number increases, the accumulated plastic strain rises, consequently intensifying the crystal

rotation.

As mentioned above, the back stress has a significant influence on the evolution of stress amplitude. A slight increase in magnitude of back stress is observed at low accumulated plastic strain during the initial fatigue stage, then gradually decreases until the end of fatigue loading, as seen in Fig. 3-5b. Compared with the as-received samples, the SMATed samples have systematically higher back stress, for all the strain amplitudes during LCF. The results indicated that the SMAT promotes the back stress, increasing during cyclic deformation. It is well-established that the back stress is associated with microstructural heterogeneities [189], [190], [191]. The previous studies show that the gradient microstructures induced by SMAT generate inhomogeneous plastic deformation within coarse grains toward bulk material [192], [189], [193]. Therefore, microstructure should be further investigated to reveal precisely the effect of SMAT on LCF. It will be presented in Section 3.4 through EBSD measurements. Uncertainties associated with the force sensor and extensometer during measurement were accounted for in the data analysis, with the resulting error estimated to be approximately 3.2 MPa.

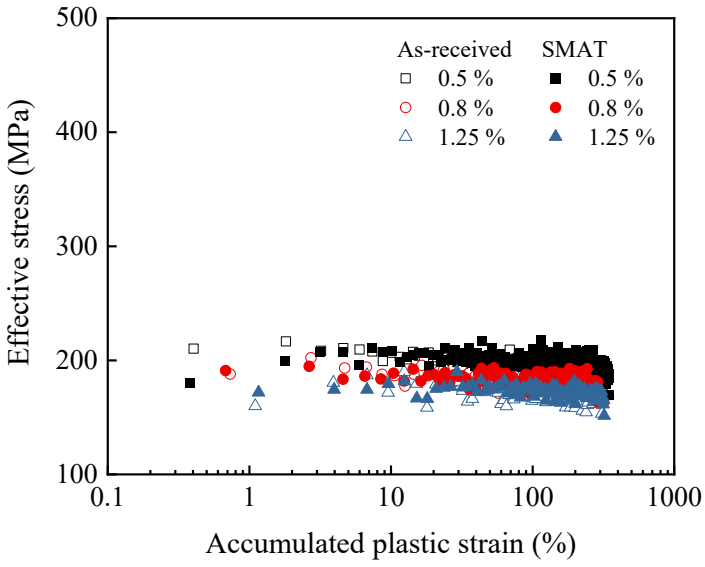

(a)

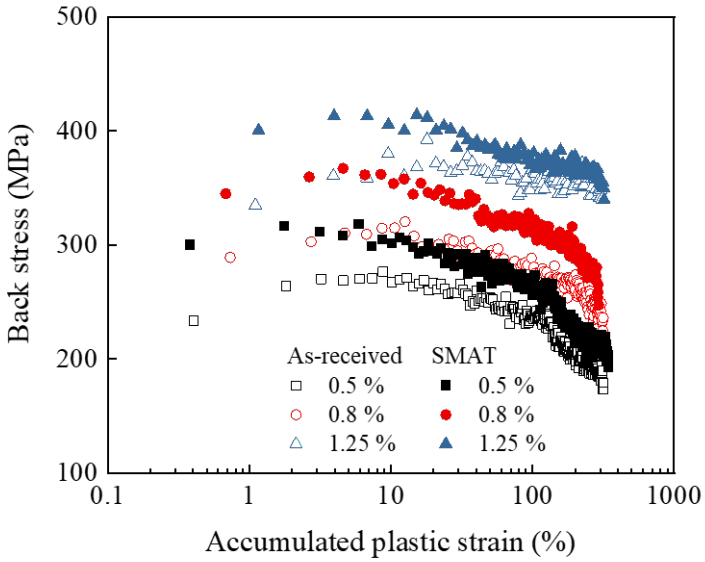

(b)

Fig. 3-5. Comparison of the evolutions of (a) effective stress and (b) back stress as function of the accumulated plastic strain, between the as-received and SMATed 316L samples.

3.3 Effect of asymmetric loading on the LCF behavior

3.3.1 Cyclic stress response

The asymmetric loading is considered to investigate the influence of load ratio on the LCF behavior of as-received and SMATed samples. The load ratio R = -0.5, defined as the ratio of the minimum to maximum value of the strain amplitude, is used in this section, as shown in Fig. 3-6. It is worth noting that the symmetric and asymmetric loadings have the same amplitude, but have different proportions of tension and compression loading.

The stress–strain hysteresis loops of as-received and SMATed samples are obtained from strain-control LCF under asymmetric loading in Fig. 3-7. The same strategy for cyclic number selection is used as in Fig. 3-2. The second cycle is distinct under asymmetric LCF, which means that fatigue properties have changed during the initial stage and vary slightly after, up to the final failure. In comparison with hysteresis loops with symmetric loading, the asymmetric ones have the same distribution of maximum stress. However, the hysteresis loops show an asymmetric shape during

cyclic deformation.

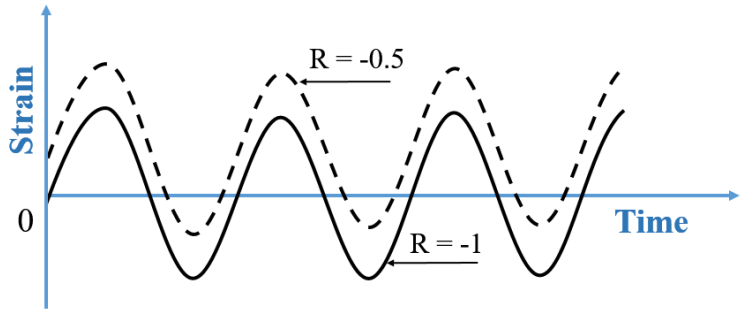

Fig. 3-6. Scheme for symmetric and asymmetric of strain-control LCF.

To illustrate the differences between symmetric and asymmetric loadings, Fig. 3-8 presents the cyclic stress amplitude curves under different strain amplitudes of as-received and SMATed samples. Similarly, significant hardening occurs at the initial stage and gradually softens until failure under asymmetric loading. In the same way, the SMAT improves the cyclic strength and fatigue life. The results show that there is a small deviation in stress amplitude (with a maximum around 20 MPa) between symmetric and asymmetric loadings for all the strain amplitudes. It indicates that the asymmetric loading has a lower influence on stress amplitude for both as-received and SMATed samples at a load ratio of -0.5 in LCF regimes. In addition, this influence of asymmetric loading is a little bit higher for as-received materials that for SMATed ones, at least for 0.5% and 0.8% of strain amplitude.

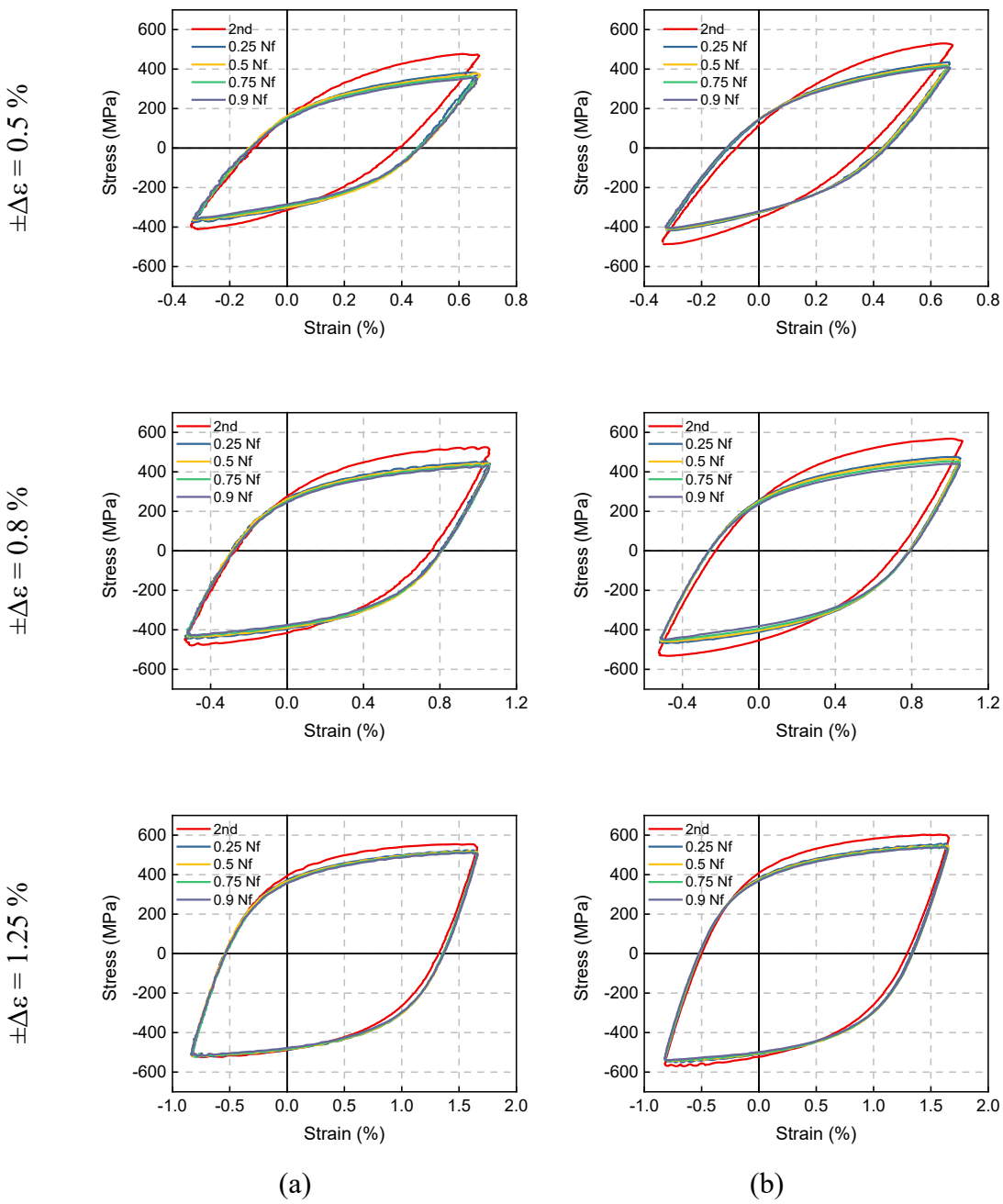

Fig. 3-7. Selected stress–strain hysteresis loops of (a) as-received and (b) SMATed 316L SS samples, at strain amplitudes of 0.5 %, 0.8 % and 1.25 % under asymmetric loading (R = -0.5).

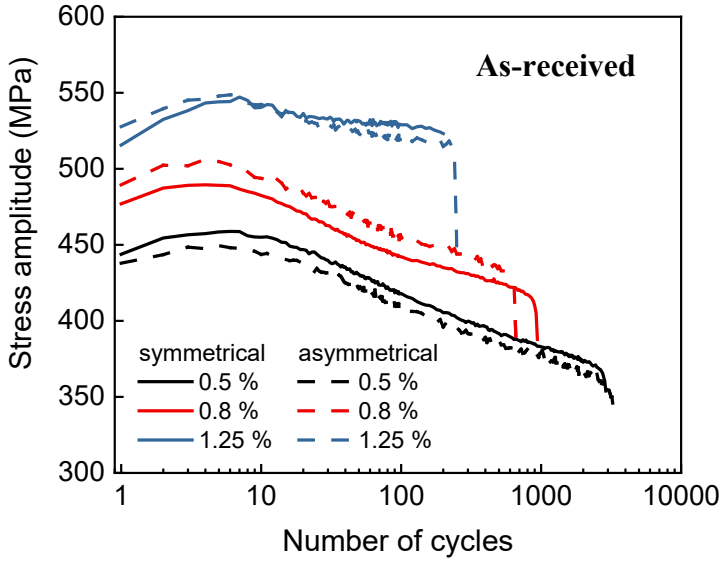

(a)

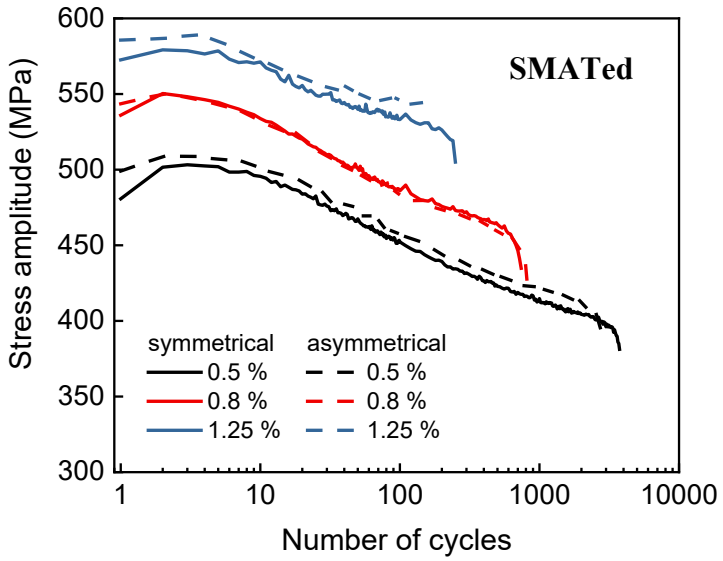

(b)

Fig. 3-8. Cyclic stress amplitude curves under different strain amplitudes of (a) as-received; (b) SMATed samples, with symmetric and asymmetric loadings.

3.3.2 Bauschinger effect

It has been evidenced that the Bauschinger effect has a critical issue in cyclic deformation, which is known as the reduction in yield strength in the reverse loading direction [184], [194], [195]. This phenomenon arises from the difference in dislocation

motion and annihilation between the tensile and compressive loading, as reviewed in [34], [124], [138]. As mentioned above, symmetric and asymmetric loadings have different load paths, which can cause a different influence on dislocations evolution in relation to Bauschinger effect during cyclic deformation, especially for asymmetric loading. Fig. 3-9 shows the tensile and compressive sections of the first hysteresis loop under symmetric or asymmetric loading.

The Bauschinger effect is observed in both the as-received and SMATed samples respectively, with symmetric and asymmetric loading. This effect mainly addresses the properties in plastic domain, whereas the material properties in elastic domain should remain unchanged whatever the level of tension or compression. It is noticeable that the as-received and SMATed 316L samples exhibit nearly overlapping elastic portions in the stress-strain curves, as shown in Fig. 3-9. The Young's modulus, calculated by the ratio of stress to strain in the linear elasticity regime of strain-stress curves, is 193.7 GPa for symmetric and 194.8 GPa for asymmetric loading. It indicates that the loading conditions have less influence on elastic modulus.

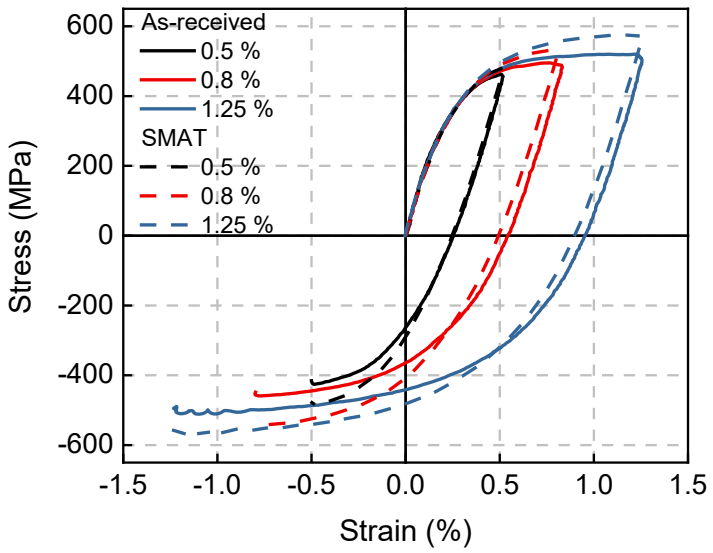

(a)

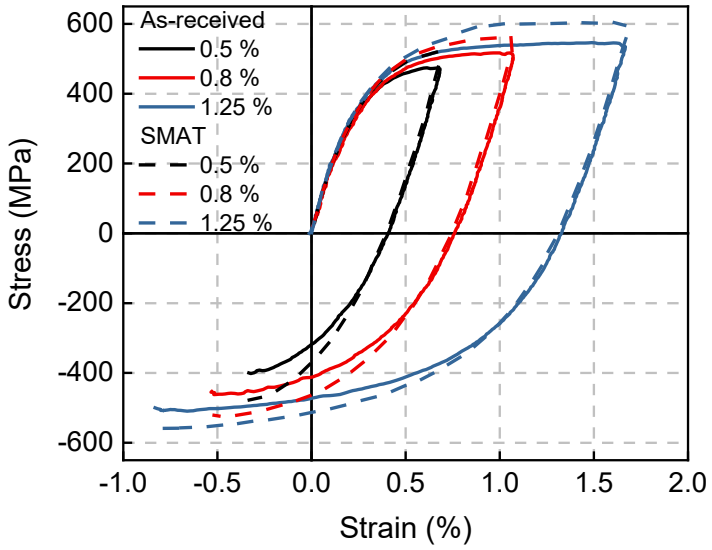

(b)

Fig. 3-9. First hysteresis loop of as-received and SMATed 316L samples, at different strain amplitudes under (a) symmetric and (b) asymmetric loading.

According to Fig. 3-9, the yield stress and reverse yield stress of different samples are listed in Table 3-3, which are calculated by setting strain offset in the first cycle of reverse loading in Fig. 3-4a. As mentioned above, the SMATed sample provides a strengthened gradient microstructure. Therefore, the results show that the yield stress of the as-received sample is 239.4 MPa, whereas it is 259.23 MPa for the SMATed sample. When increasing strain amplitude, the reverse yield stress increases for as-received and SMATed samples, under symmetric or asymmetric loading. By comparison with the symmetric loading, the asymmetric loading lowers reverse yield stress, for all samples conditions. It means that the asymmetric loading has a more substantial Bauschinger effect, both in as-received and SMATed samples. In addition, SMAT weakens the Bauschinger effect: for example, at a symmetricly loaded strain amplitude of 1.25%, the inverse yield stress of SMATed samples compared to the yield stress is reduced by 24.1%, which is much smaller than the corresponding reduction of the as-received samples (40.96%).

Table 3-3. The yield stress and reverse yield stress.

Sample	Load ratio	Strain amplitude (%)	Yield stress (MPa)	Reverse yield stress (MPa)
As-received	R = -1	0.5	232.07	102.83
		0.8	235.70	121.95
		1.25	245.73	145.07
	R = -0.5	0.5	242.74	95.83
		0.8	241.10	114.66
		1.25	239.28	139.74
SMAT	R = -1	0.5	260.65	162.21
		0.8	261.16	171.98
		1.25	261.64	198.56
	R = -0.5	0.5	252.52	116.74
		0.8	261.89	143. 87
		1.25	257.52	149.35

3.4 Microstructure investigation of as-received 316L SS

In the previous sections of this chapter, the fatigue behavior at the macroscale of both the as-received and SMATed specimens was investigated especially through hysteresis curves. Subsequently, the microstructure of the specimen (**without SMAT**) has been measured in cross-sectional by EBSD after the fatigue test, aiming to investigate the microscale fatigue properties in relation to the previous observed macroscopic behavior. Comparison is thus done between EBSD maps, for as-received (provided at Chapter 2) and fatigued specimens.

3.4.1 Microstructure characteristics of the fatigued specimen without SMAT

Microstructures distribution features are examined within the near-surface region of the fatigued specimen. Fig. 3-10 displays the IPF and IQ overlaid on the sample cross-section under symmetric loading fatigue test with a strain amplitude of 1.25%. The plastic deformation leads to lattice distortion and is accompanied with dislocation motions and other defects within the crystal structure. Plastic deformation induces

complex structural changes that significantly affect the scattering of the electron beam, thereby influencing the quality of the EBSD images [66], [83]. By comparing with the as-received and unloaded specimen in Fig. 2-5, the IQ of the fatigued specimen shows a plastic deformation in the top surface and near surface regions. This observation suggests that the fatigued specimen undergoes homogenous plastic deformation.

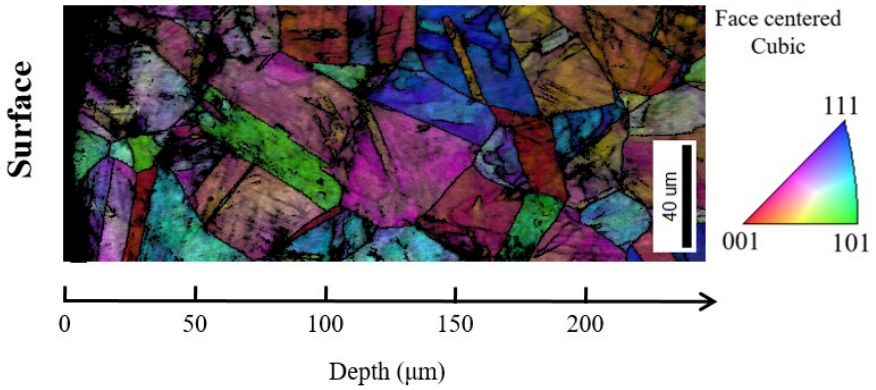

Fig. 3-10. EBSD maps of IPF overlaid with IQ on the cross-section of the as-received sample after fatigue test at strain amplitude of 1.25 % under symmetric loading.

The homogenous plastic strain results in overall uniform distribution of misorientation angles and GND between grains, as confirmed in Fig. 3-11(a) and (b). Inside the grain, misorientation and GND accumulate at GBs, as well as twin boundaries to accommodate the deformation. The average GND, calculated from the GND values at the same depths, is presented in Fig. 3-11c to reveal its in-depth evolution of fatigued sample. At the near-surface regions, the fatigued specimen exhibits lower GND density value of 159.7×10^{12} /m^2, compared to the as-received specimen. It suggests that the plastic deformation introduced during the specimen preparation is reduced during cyclic deformation. At different depths, the average GND is uniformly distributed and fluctuates around 150.0×10^{12} /m^2, which is 70% higher than the as-received specimen.

In comparison to the as-received specimen in Fig. 2-11a, the undeformed grains (white region in Fig.3-12a) are rare and randomly distributed in the fatigued specimen. In addition, the majority of the grains have lower GOS values (around 5°). For individual grains within fatigued specimen, GROD maps display a gradient distribution from GBs to bulk in the grain.

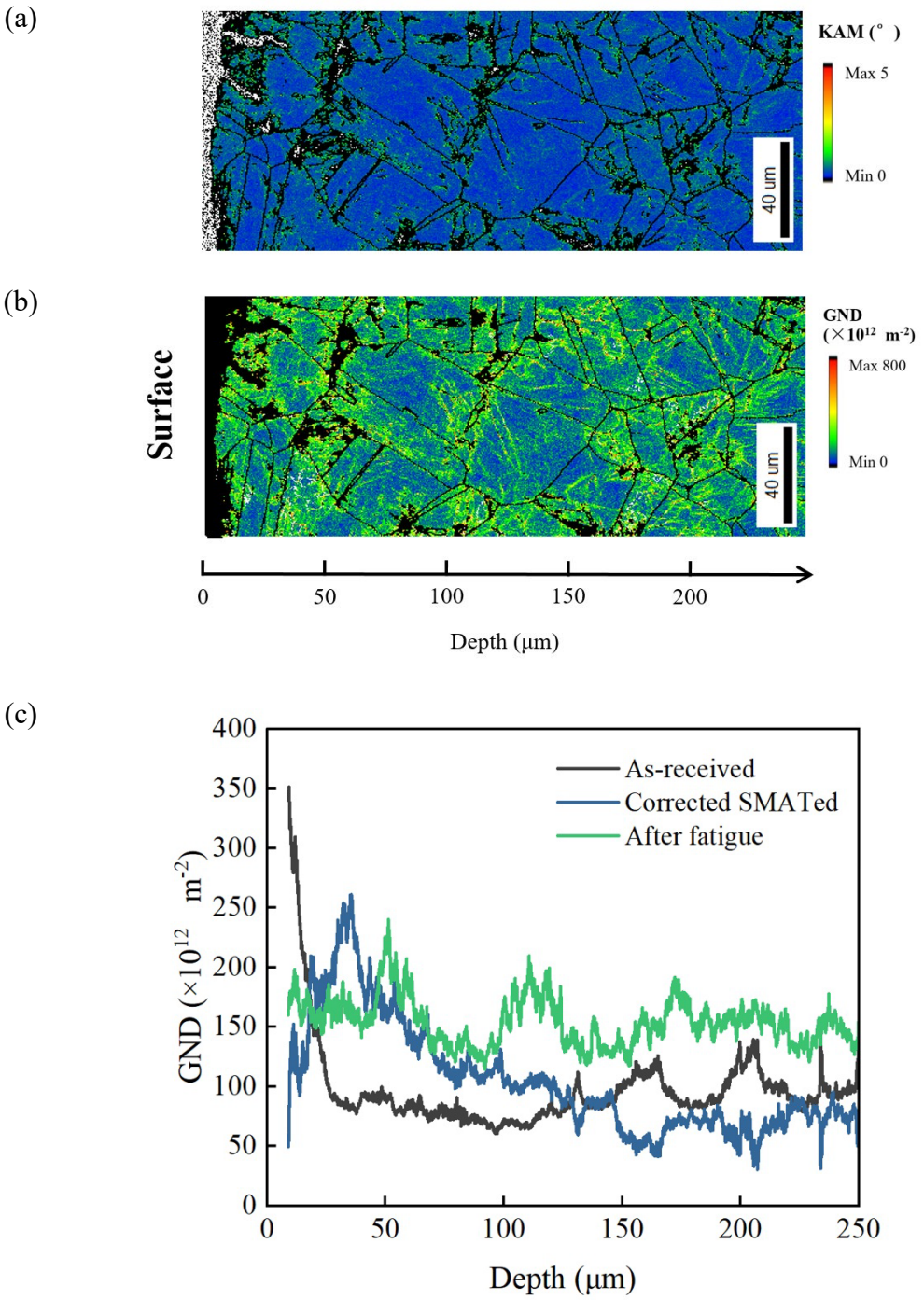

Fig. 3-11. (a) EBSD maps of KAM and (b) GND maps on cross-section (c) In-depth average GND based on the GND maps; of the fatigued sample at strain amplitude of 1.25 % under symmetric loading.

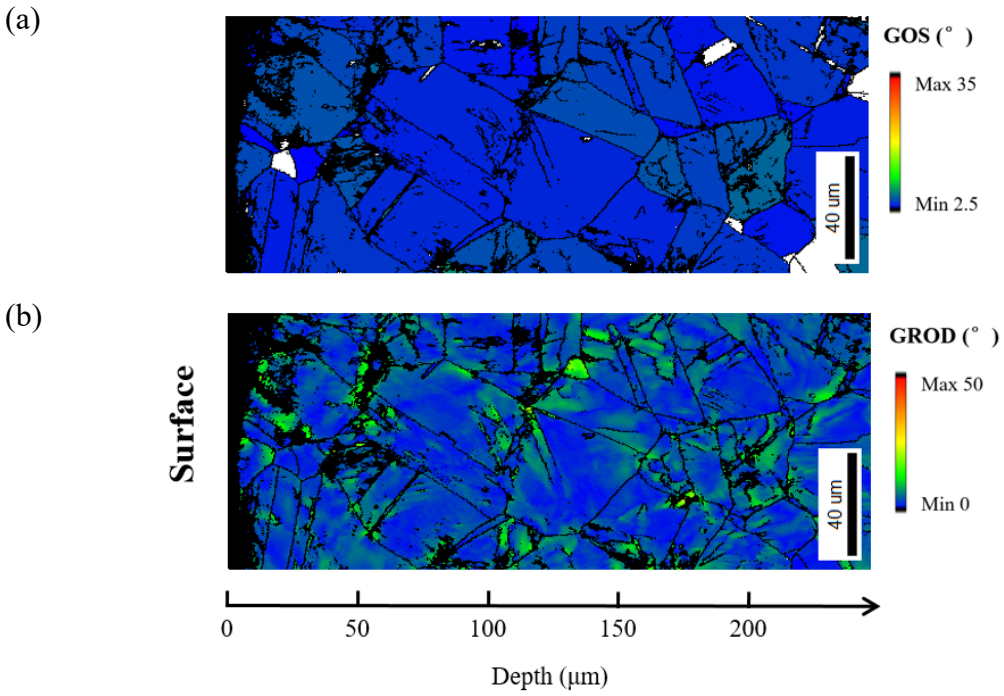

Fig. 3-12. (a) GOS and (b) GROD maps on cross-section of the fatigued sample at strain amplitude of 1.25 % under symmetric loading. White color in the middle indicates that the GOS value is below the threshold for undeformed grains

3.4.2 Microstructure evolution during cyclic loading without SMAT

Based on the microstructural characteristic's distribution of the fatigued specimen, it can be inferred that the specimen undergoes uniform deformation after fatigue in the near-surface region. In this section, we focus on the larger central region of the specimen (350 µm × 350 µm), employing a faster measurement with a step size of 0.4 µm, to investigate the microstructure evolution during cyclic loading. Since the step size was changed compared to the previous mapping in Fig. 3-10, different values of GND densities are expected in Fig. 3-14. Increasing the step size reduces the resolution of small-scale crystal orientation changes, leading to an underestimation of the local dislocation density (with lower values in this case) [148], [154]. Fig. 3-13 shows the IPF on the cross-section with different strain amplitudes for different numbers of cycles. It can be seen that no deformation twin is observed even at the highest strain amplitude of 1.25%. However, a large number of annealed twins are present in the specimen in each IPF maps as presented in Fig. 3-13.

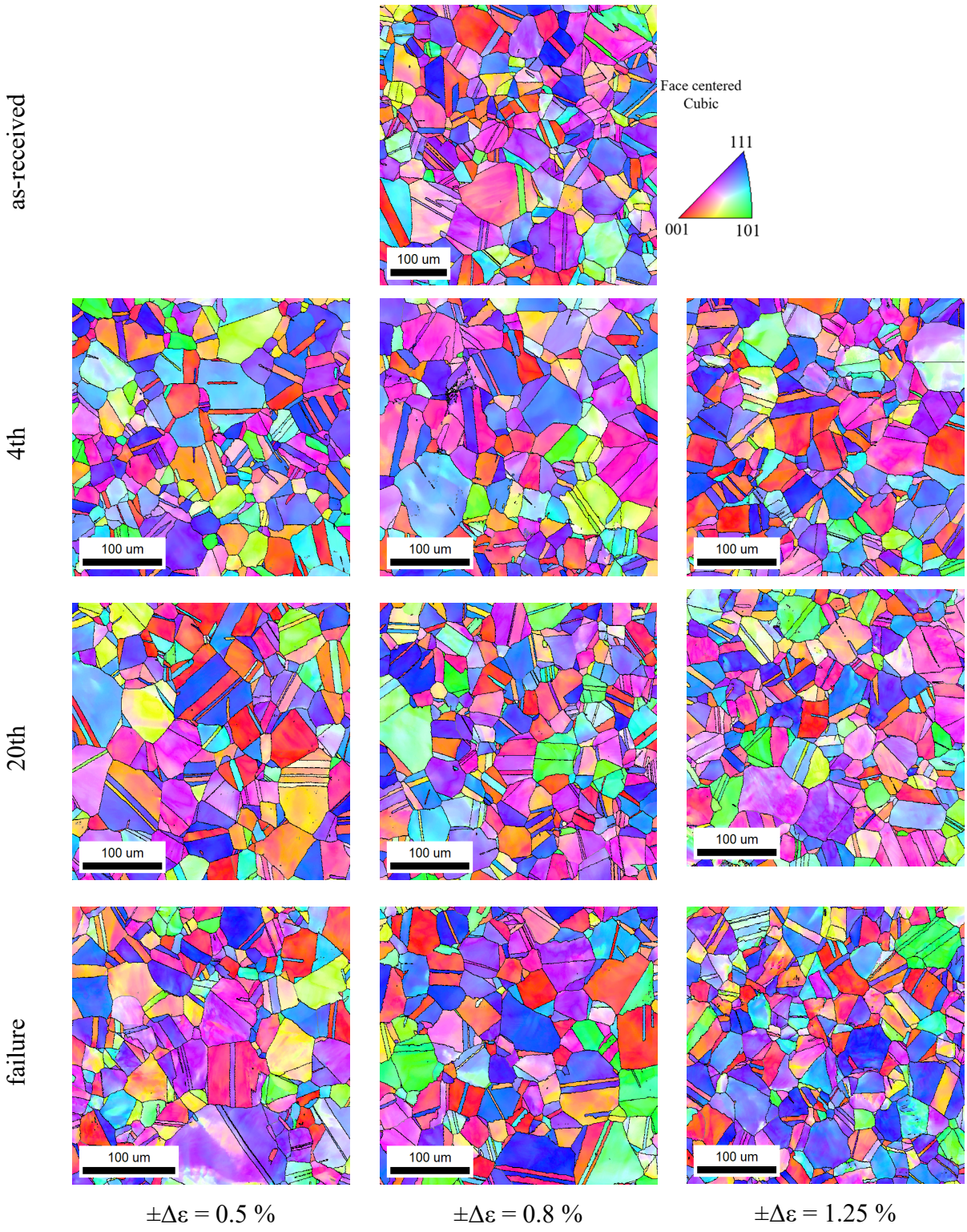

Fig. 3-13. IPF maps on cross-section at strain amplitudes of 0.5 %, 0.8 % and1.25 % in columns, and at different cycle numbers of as-received, 4th, 20th and failure in rows, under symmetric loading.

The distributions of GND on the cross-section for different numbers of cycles and

strain amplitudes are presented in Fig 3-14. For a constant stress amplitude of 1.25%, a GND value of approximately 150×10^{12} /m^2 is attained with the smaller measurement size (as used in Fig. 3-11c), while the GND value with the larger measurement step size (0.4 μm) is 65×10^{12} /m^2, as shown in Fig. 3-14. Therefore, a finer step size facilitates the detection of finer microstructural features that might remain unnoticed with larger step sizes. As a result, a decrease in the measurement step size leads to an increase in the observed GND density [87], [196], [197]. For each row of figures in Fig.3.14, with increasing strain amplitudes, GND show a gradual increase for a same cycle number. Similarly, for each column of figures in Fig.3.14, with increasing cycle number, there is a gradual increase in GND for a given strain amplitude. An increase in either strain amplitude or cycle number leads to an increase in plastic strain, consequently resulting in an increase in GND, as already observed in [25], [35], [83]. The calculated average value presented in Fig. 3-15a provides a quantifiable approach to study the evolution of GND. For example, at a strain of 1.25%, the average GND increases from 27.6×10^{12} /m^2 at the number cycle 4th to 56.8×10^{12} /m^2 at failure.

It is interesting to note that the GND tends to concentrate in the GB regions at low cycle numbers and strain amplitude, indicating a low strain level. However, as the cycle number and strain amplitude increase, suggesting a higher strain level, the GND within the grains also increases gradually. This shift is particularly observed in the GND distribution at failure in Fig. 3.14. The increase in GND within grains under high plastic strain contributes to a more uniform distribution of GND. Average GOS for different number of cycles and strain amplitudes validates this observation, as seen in Fig. 3-15b. It is worth emphasizing that the smaller the value of GOS, the higher the consistency of grain orientation, the weaker the stress concentration at GBs and the greater the strengthening effect of GBs, as confirmed in [48]. It illustrates that with an increasing number of cycles, the GOS initially increases, then subsequently decreases at the same strain amplitude.

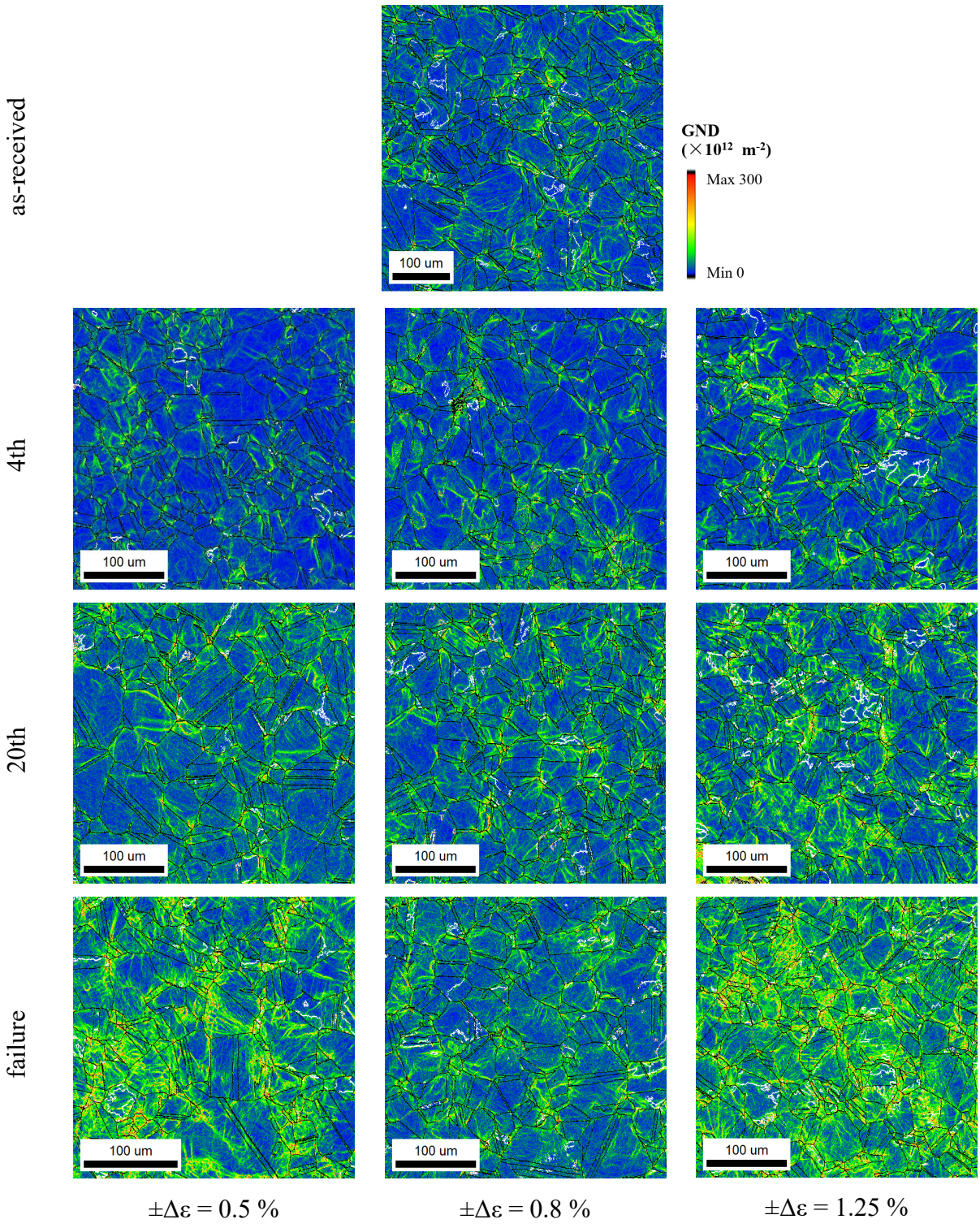

Fig. 3-14. GND maps on cross-section at strain amplitudes of 0.5 %, 0.8 % and1.25 % in columns, and at different cycle numbers of as-received, 4th,20th and failure in rows, under symmetric loading.

(a)

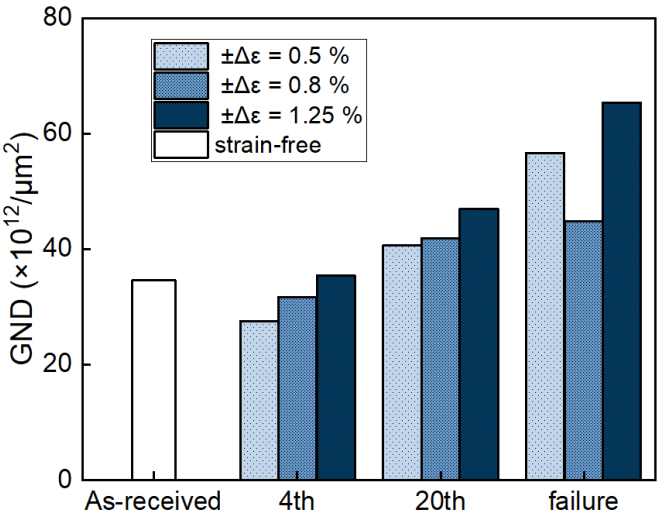

(b)

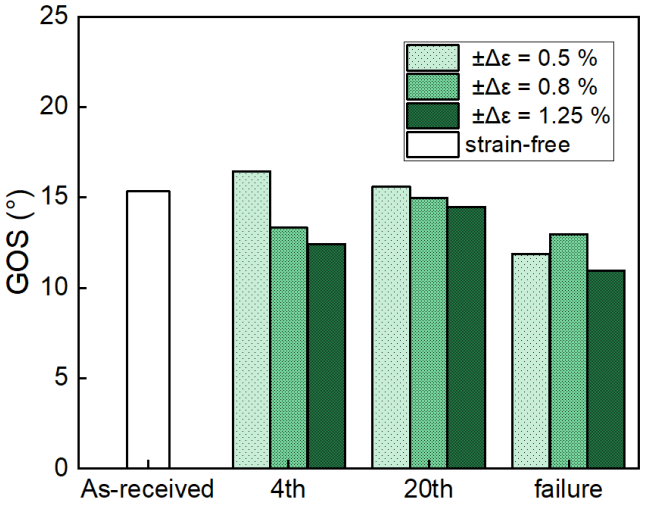

Fig. 3-15. Average (a) GND and (b) GOS at different cycle numbers of as-received, 4th, 20th and failure under symmetric loading.

3.4.3 Relationships between back stresses and GND

In Section 3.2, it has been observed that back stress has a strong influence on cyclic deformation. It is well understood that the inter-granular back stress is primarily determined by the presence and distribution of GND [33], [34]. Combining the macroscopic cyclic deformation behavior and the microstructure observed by EBSD, It can be inferred: in the initial stages of cyclic plastic deformation, the GND accumulate

near GBs and twin boundaries to accommodate plastic deformation within the grain, as shown in Fig. 3-14. This gradient distribution of GND within the grain associated with inhomogeneous plastic deformation, results in an increase in inter-granular back stress, as observed in Fig. 3-8b. With subsequent plastic deformation, the increase in GND within the grains leads to a diminished gradient between the vicinity of GBs and the interior of the grains, as noticed in Figs. 3-14 and 3-15. Consequently, inter-granular back stress decreases with increasing of GND.

3.6 Conclusion

In this chapter, the macroscale LCF behavior of as-received and SMATed samples is analyzed through experimental investigations at different strain amplitudes, under symmetric and asymmetric loadings. The evolutions of effective stress, back stress and yield stress are extracted from hysteresis loops. In addition, EBSD measurements at the microscopic scale were performed at different cycle numbers to quantify the microstructural changes during fatigue testing. Based on the obtained results, the following conclusions can be drawn:

- During LCF, both as-received and SMATed samples exhibit significant hardening in the initial cycles, followed by gradual softening generally without reaching saturation before final failure.
- The cyclic behavior is mainly influenced by the back stress, which initially increases, and then gradually decreases with accumulated plastic strain. Moreover, the effective stress decreases slightly but gradually with increasing strain amplitudes, particularly at low accumulated plastic strain.
- SMATed samples show higher back stress at different strain amplitudes during fatigue, suggesting that SMAT promotes back stress due to microstructural heterogeneities.
- The Bauschinger effect was observed in as-received and SMAT samples under symmetric and asymmetric loadings. Under asymmetric loading, the Bauschinger effect is more pronounced than under symmetric loading. Additionally, SMAT tends to mitigate the Bauschinger effect by showing a higher reverse yield stress compared to the as-received material.

- Microstructural examination of fatigued specimens, without SMAT treatment, reveals uniform plastic strain within the specimen, leading to the uniform distribution of dislocation tangle and GND between grains.
- The evolution of the microstructure during cyclic loading was investigated using a rapid measurement method focused on the central region. No deformation twins were observed even at the highest strain amplitude of 1.25%. However, a significant presence of annealing twins was observed in all specimens.
- The evolution of GNDs and GOS during cyclic plastic deformation indicates that GNDs influence the intergranular back stress distribution within the material, which subsequently affects the intergranular back stress. As plastic deformation accumulates through cycling, higher grain orientation consistency weakens the effects of grain boundary stress concentration and back stress strengthening.

Chapter 4: Influence of TRIP and TWIP effects on deformation behavior based on a dislocation density model

As mentioned in Chapter 1, numerous experimental characterizations, including TEM, EBSD, XRD, etc., have been carried out to reveal the mechanisms of GMS formation and evolution. It highlights that grain refinement involves various dislocation activities, deformation twinning, martensitic transformation and development of grain boundaries during plastic deformation. Based on experimental data and literature studies in Chapter 2 and 3, we found that the SMAT process induces virous deformation mechanisms, which depends on the SFE. Additionally, the change in grain size resulting from surface nanosizing also affects the deformation mechanisms. In addition, the deformation mechanisms are strongly dependent on the SFE of materials. To better understand, it is crucial to develop a model that accurately describes the microstructural evolution and macroscopic stress response of austenitic steels with different SFEs. In this chapter, to accurately describe the deformation responses of materials with complex strain hardening mechanisms, a dislocation density-based model incorporating both TRIP and TWIP effects is developed, taking into account the different SFEs associated with the deformation mechanisms. 304 SS is a common low SFE material that undergoes plastic deformation through the formation of deformation twins and martensitic transformation [198], [199], [200]. The combined effects of TRIP and TWIP strengthening mechanisms are investigated using the mechanical properties of 304 SS under tensile loading. It is a commonly used material to study the effects of TRIP and TWIP on macroscopic properties. It is a commonly used material to study the effects of TRIP and TWIP on macroscopic properties for which experimental results are available. For these reasons, the 304 SS material will be discussed in this chapter.

4.1 Model description of twinning and martensitic transformation

4.1.1 Formation of martensite and twin

Martensite transformation has been documented to occur in two ways: directly (γ-austenite to α'-martensite) and indirectly (γ-austenite to ε-martensite to α'-martensite) [159], [201], [202], [203]. Direct transformation typically takes place during rapid cooling, involving swift lattice slip and rearrangement to establish a martensitic

structure [204], [205]. However, indirect transformation occurs due to stress or temperature changing, leading to the formation of a hexagonal closed packed (HCP) ε-martensite structure, followed by subsequent shear or rearrangement transformation to α'-martensite. Fig. 4-1 displays a schematic diagram illustrating the indirect transformation process from austenite to martensite. Additionally, twinning was observed to accompany the conversion process during the indirect transformation. Experimental report indicates that ε-martensite and twin have similar formation and evolution mechanisms [201], [206]. Initially, the perfect dislocation splits into Shockley partials to form the stacking faults with a width of r_i and a thickness of t_i on the {111} planes, as shown in Fig. 4-1a [207]. As the intrinsic stacking fault gradually grows to a critical width r_i^*, an embryo forms. It is worth noting that an embryo of ε-martensite originates from an isolated stacking fault, whereas a twin forms by the overlapping of three stacking faults on successive planes of the austenite, as illustrated in Fig. 4-1b. The length of embryo l_i continues to propagate on successive planes within the grain. Adjacent embryos combine, maintaining a constant width r_i^*, to form a band structure of width w_i, as observed in Fig. 4-1c. As the formation of these bands increases, the volume fraction of ε-martensite or twinning also increases. Finally, the α'-martensite forms at the intersections of the deformation bands according to the Olson-Cohen mechanism [203], [208], as shown in Fig. 4-1d.

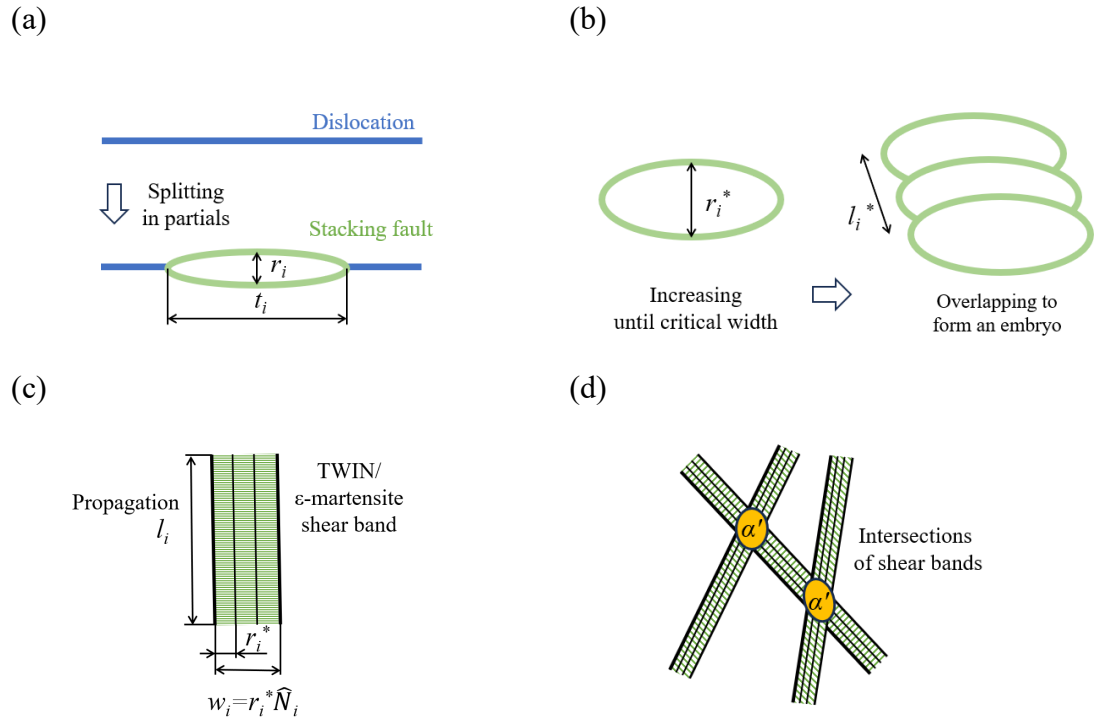

Fig. 4-1. Schematic diagram of the formation and evolution mechanism of ε-martensite,

twin and α'-martensite [202], [206].

Several experiments report that the formation and evolution of ε- and α'- martensite, as well as twinning, strongly depend on the SFE in austenitic steels [209], [210], [211]. Martensitic transformation occurs at low stacking fault energies (typically below 15 mJ/m²), whereas mechanical twinning is promoted at SFEs between 15 and 40 mJ/m². Dislocation slip dominates the deformation behavior at higher SFEs. The SFE directly influences the generation of stacking faults and determines the deformation mechanisms of materials. To determine the critical stresses for twin or ε-martensite nucleation, considering the total energy associated with the dislocation configuration has proven to be an effective method based on mesoscale model [202], [206]. The total energy E_i, as expressed in Eq.5-1, is composed of the energy required for overlapping of stacking faults (E_{dis}), the energy to form an embryo (E_{emb}) and the energy associated to form the stacking faults (E_τ).

$$E_i = E_{dis} + E_{emb} - E_\tau \,,\; i = \varepsilon,\, t \qquad \text{(Eq. 4-1)}$$

$$E_{dis} = \frac{n_i^2 \mu b^2 r}{8\pi(1-\nu)_i} \ln\left(\frac{r_i}{2n_i l_i}\right) \qquad \text{(Eq.4-1a)}$$

$$E_{emb} = (\gamma_{SFE} - 2\sigma_{HCP}) r_i t_i n_i \qquad \text{(Eq. 4-1b)}$$

$$E_\tau = \frac{\tau b r_i^2 n_i}{m_{SF}} \qquad \text{(Eq. 4-1c)}$$

where ε and t stand for ε- martensite and twinning, respectively. n_i is the layer number of stacking faults in an embryo, r_i is the width of a stacking fault, t_i is the thickness of a stacking fault, l_i is the length of a stacking fault, γ_{SFE} is the stacking fault energy, b is the magnitude of the Burgers vector, m_{SF} is the Schmid factor, μ is the shear modulus, ν is Poisson's ratio, σ_{HCP} the interfacial energy between the FCC and HCP structure, τ is the applied shear stress aiding to form the stacking faults. It can be seen that the total energy depends on the geometry of the embryo (width, thickness and length) and the fault energy. A stable twin or ε-martensite nucleation forms when a critical width is reached [202], [206]. We can minimize the total energy with respect to width to determine the critical width r_i^* and shear stress τ_i^* for twin or ε-martensite nucleation by:

$$\frac{\partial E_i}{\partial r_i} = 0 \qquad \text{(Eq. 4-2)}$$

For α'-martensite, nucleation occurs at the intersections of ε-martensite shear bands. Therefore, the critical width ($r_{\alpha'^*}$) and shear stress ($\tau_{\alpha'^*}$) of an α' embryo is assumed to be equal to that of ε-martensite.

4.1.2 Evolution of martensite and twin

Strain-induced transformation, mechanical twinning and dislocation slips are generated to accommodate additional strain from external loading. It means that these three deformation mechanisms evolve under external loading. Moreover, the extent of the formations of α'-martensite, ε-martensite and twinning are typically quantified in terms of volume fraction. The volume fraction of each microstructure f_i ($i=\alpha', \varepsilon, t$) is calculated by multiplying the number density N_i and volume $V_i=r_i^* t_i l_i$ ($i=\alpha', \varepsilon, t$) in Eqs. 4-3a to 4-3c. The reduction in the volume fraction of ε-martensite and twinning is taken into account when the volume fraction of α'-martensite increases due to the α'-martensite formation from ε-martensite and twinning.

$$f_\varepsilon = N_\varepsilon V_\varepsilon (1 - f_{\alpha'}) \quad \text{(Eq. 4-3a)}$$

$$f_{\alpha'} = N_{\alpha'} V_{\alpha'} \quad \text{(Eq. 4-3b)}$$

$$f_t = N_t V_t (1 - f_{\alpha'}) \quad \text{(Eq. 4-3c)}$$

When the applied stress equals or exceeds the threshold, nucleation becomes active. The nucleation rate for each density is described by:

$$\frac{dN_\varepsilon}{d\varepsilon} = \frac{\tau_{nuc}}{\tau_{CRSS}} \frac{r_\varepsilon^*}{bm_{SF}} N_\varepsilon (1 - f_\varepsilon) \quad \text{(Eq. 4-4a)}$$

$$\frac{dN_{\alpha'}}{d\varepsilon} = \frac{1}{2} \frac{dN_\varepsilon}{dt} \quad \text{(Eq. 4-4b)}$$

$$\frac{dN_t}{d\varepsilon} = \frac{\tau_{nuc}}{3\tau_{CRSS}} \frac{r_t^*}{bm_{SF}} N_t \left(1 - f_t\right) \quad \text{(Eq. 4-4c)}$$

where τ_{nuc} is the shear stress required to nucleate a dislocation, τ_{crss} is the critical resolved shear stress. As mentioned above, when the stacking fault reaches a critical width, it propagates along the successive planes in the length direction. In addition, the thickness is also assumed to be constant in experiments [202], [212]. The mean length of microstructure is limited by grain size D. Moreover, this mean length l_i with strain can be expressed as:

$$\frac{dl_i}{d\varepsilon} = \frac{1}{N_i}\frac{dN_i}{d\varepsilon}(D - l_i) \quad \text{(Eq. 4-5)}$$

4.1.3 Evolution of dislocation density

To take into account the contribution of ε- and α'-martensite, the total plastic strain increment $d\varepsilon$ can be associated with α'-martensite strain $\varepsilon_{\alpha'}$ and austenitic strain ε_γ as:

$$d\varepsilon = \left(1 - f_{\alpha'}\right) d\varepsilon_\gamma + \varepsilon_{\alpha'} df_{\alpha'} \quad \text{(Eq. 4-6)}$$

For dual phase, α'-martensite exhibits higher yield strength compared to austenitic structures, which means that strain accumulates preferentially in the remaining austenite [213], [214]. The strain of α'-martensite is neglected in this model ($\varepsilon_{\alpha'} = 0$) [202], because we assume that plastic deformation occurs exclusively in austenite due to the significantly higher yield strength and tensile strength of martensite compared to austenite. Taking into account this hypothesis, Eq. 4-6 becomes $d\varepsilon_\gamma/d\varepsilon = 1/(1-f_{\alpha'})$.

In addition, ε-martensite and twinning are assumed to affect dislocation behavior in austenitic structures. As a consequence, the strain in austenite ε_γ has a relationship with ε-martensite and twinning as follows:

$$d\varepsilon_\gamma = \left(1 - f_t - f_\varepsilon\right) d\varepsilon_{dis} + \frac{1}{\sqrt{2}M} df_t + \frac{2}{3} f_\varepsilon d\varepsilon_{dis} \quad \text{(Eq. 4-7)}$$

where M is the Taylor factor. ε_{dis} is the plastic strain due to dislocation slip. Rearranging the expressions described by Eq. 4-7, it gives:

$$\frac{d\varepsilon_{dis}}{d\varepsilon_\gamma} = \frac{1 - \frac{1}{\sqrt{2}M}\frac{df_t}{d\varepsilon_\gamma}}{1 - f_t - \frac{1}{3} f_\varepsilon} \quad \text{(Eq. 4-8)}$$

Combining Eqs. 4-6, 4-7 and 4-8, the evolution of the dislocation density can be expressed with respect to the total strain ε:

$$\frac{d\rho}{d\varepsilon} = \frac{d\rho}{d\varepsilon_{dis}}\frac{d\varepsilon_{dis}}{d\varepsilon_\gamma}\frac{d\varepsilon_\gamma}{d\varepsilon} = \frac{d\rho}{d\varepsilon_{dis}}\frac{1 - \frac{1}{\sqrt{2}M}\frac{df_t}{d\varepsilon_\gamma}}{1 - f_t - \frac{1}{3} f_\varepsilon}\frac{1}{(1 - f_{\alpha'})} \quad \text{(Eq. 4-9)}$$

where ε_{dis} is the strain caused by dislocation slip. Dynamic accumulation and annihilation of dislocation processes were taken into account, following the classical Kocks–Mecking–Estrin (KME) model as:

$$\frac{d\rho}{d\varepsilon_{dis}} = \frac{d\rho^{+}}{d\varepsilon_{dis}} + \frac{d\rho^{-}}{d\varepsilon_{dis}} \qquad \text{(Eq. 4-10)}$$

The rate of dislocation storage (+) is inversely related to the dislocation mean free path Λ_i, which depends on the multiplication of dislocations, the ε-martensite spacing, twin spacing, and the dislocation forest induced by dislocation interactions. The deformation-induced twins and ε-martensite positively affect the work-hardening by impeding the gliding movement of dislocations through bands boundaries. Accordingly, the generalized equation for the rate of dislocations forests evolution with strain can be expressed as:

$$\frac{d\rho^{+}}{d\varepsilon_{s}} = \frac{M}{b}(k_1\sqrt{\rho} + \frac{1}{D} + \sum_{i}\frac{1}{\Lambda_i}),\ i = \varepsilon,\ t \qquad \text{(Eq. 4-11)}$$

where k_1 is a geometric factor related to grain boundary and dislocations forests. The mean spacing is related to the width w_i and the volume fraction f_i of ε-martensite and twinning, given by:

$$\frac{1}{\Lambda_i} = \frac{1}{2w_i}\cdot\frac{f_i}{1-f_i} \qquad \text{(Eq. 4-12)}$$

Moreover, grain boundaries play an important role in strain hardening with decreasing grain size, especially in refined grains. However, the classical KME model only considers dislocation annihilation due to dynamic recovery. The grain size effect was observed in nanocrystalline grains in a SMATed Fe sample [215]. It was reported that the deformation mechanism was no longer governed by accumulation of dislocations, but by the grain rotation or grain boundary sliding processes when the grains size is reduced to few nanometers. For this purpose, an additional dynamic grain size-related recovery term has to be added to describe the decrease in work hardening due to grain refinement [216].

$$\frac{d\rho^{-}}{d\varepsilon_{s}} = -M\rho\left[k_{20}\left(\frac{\dot{\varepsilon}^{p}}{\dot{\varepsilon}_0}\right)^{-\frac{1}{n_0}} - \left(\frac{D_e}{D}\right)^{2}\right] \qquad \text{(Eq. 4-13)}$$

where k_{20} is the dynamic recovery constant, n_0 is an exponent inversely proportional to temperature, $\dot{\varepsilon}_0$ is the reference strain rate, and D_e is the reference grain size. It should be noted that the parameter n_0 is related to the SFE, which can affect the generation of GNDs and grain refinement during SMAT. A SMATed sample with high SFE has stronger back stress hardening and smaller grain sizes [201], [202], [217]. The total

stress of the material can be calculated by a mixed law based on the volume fractions of α'-martensite and γ-austenite:

$$\sigma_{total} = \left(1 - f_{\alpha'}\right)\sigma_{\gamma} + f_{\alpha'}\sigma_{\alpha'} \quad \text{(Eq. 4-14)}$$

where σ_{γ} and $\sigma_{\alpha'}$ represent the stress within austenite and martensite, respectively.

4.2 Microstructures evolution of 304 SS with TWIP/TRIP effects

4.2.1 Grain size and SFE dependent deformation mechanisms

Modeling the deformation mechanisms of materials with varying SFE and grain sizes involves considering the nucleation of various nanostructures to correctly describe the strain-induced mechanical twinning, martensite transformation and dislocation activities. Table 4-1 summarizes parameters for formation and evolution model of microstructures of 304 SS. It is worth noting that the formation of ε-martensite (as well as α'-martensite) and twinning is determined by the critical shear stress and the width of the stacking fault, which are strongly related to the grain size and SFE of material [218]. Fig. 4-2 illustrates the variation curves of critical shear stress and stacking fault width for materials with different SFEs. The critical shear stress increases significantly with increasing SFE, indicating that higher SFE makes martensite and twin initiation more difficult. Specifically, material with an SFE of approximately 26 mJ/m² requires a critical shear stress of 1000 MPa for martensitic transformation. Additionally, the critical width of stacking faults for martensitic transformation and twin formation decreases with increasing SFE. Moreover, experiments indicate that increasing the width of stacking faults enhance the frequency of dislocation pile-ups, thereby promoting the formation of new stacking faults [219].The critical shear stress and stacking fault width required for the formation of martensite and twins in different SFE materials indicate that low SFE promotes martensitic transformation, while moderate SFE facilitates the formation of deformation twins.

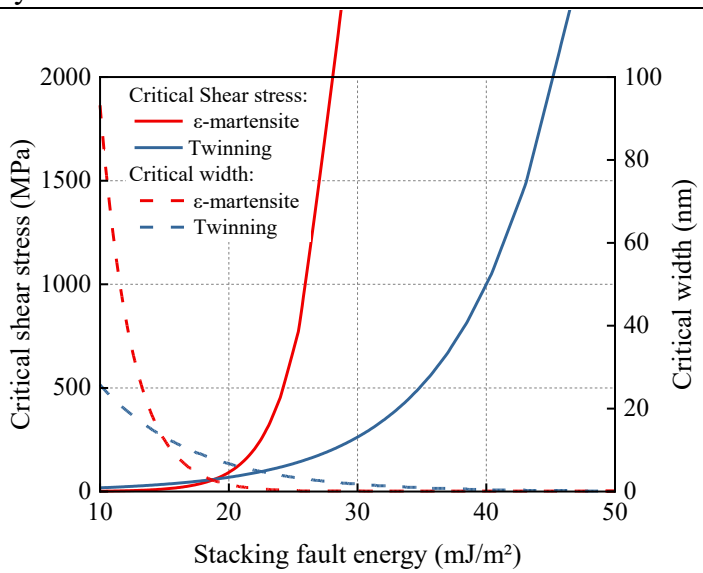

Fig. 4-2. Evolution of critical shear stress (solid line) and stacking fault width (dashed line) in ε-martensite (red) and twinning (blue) calculated with Eqs. 4-1,4-1a to 1c.

From an evolutionary perspective, embryonic nucleation is also related to the material's SFE and grain size. It means that the nucleation rate is a grain size and SFE-dependent kinetics parameter in Eqs. 4-4a to 4-4c. Fig. 4-3 illustrates the variations of the nucleation rate for different SFEs and grain sizes. At a constant grain size of 15 μm, the nucleation rate increases with decreasing SFE, indicating that nanostructures are more likely to grow at lower SFEs, as shown in Fig. 4-3a. In addition, the types of mechanism and their interactions change with varying SFE. For example, the enlarged figure in Fig. 4-3a highlights the nucleation rates of twinning, ε- and α'-martensite at an SFE of 17.8 mJ/m². It can be observed that the nucleation rate of ε-martensite is greater than that of twinning, which is greater than that of α'-martensite. This phenomenon is also reflected in the variation of nucleation rate with grain size in Fig. 4-3b. When the grain size exceeds 5 μm, the nucleation rate shows a gradual increase when increasing grain size. This observation suggests that martensitic transformation and deformation twinning propagate more rapidly in larger grains. Conversely, in fine grains (less than 1 μm), the nucleation rate decreases significantly. On the one hand, the stress required to initiate nucleation increases as the grain size decreases [220], [221]. On the other hand, at the nanoscale level, the deformation mechanism shifts to be predominantly governed by grain rotation.[222], [223].

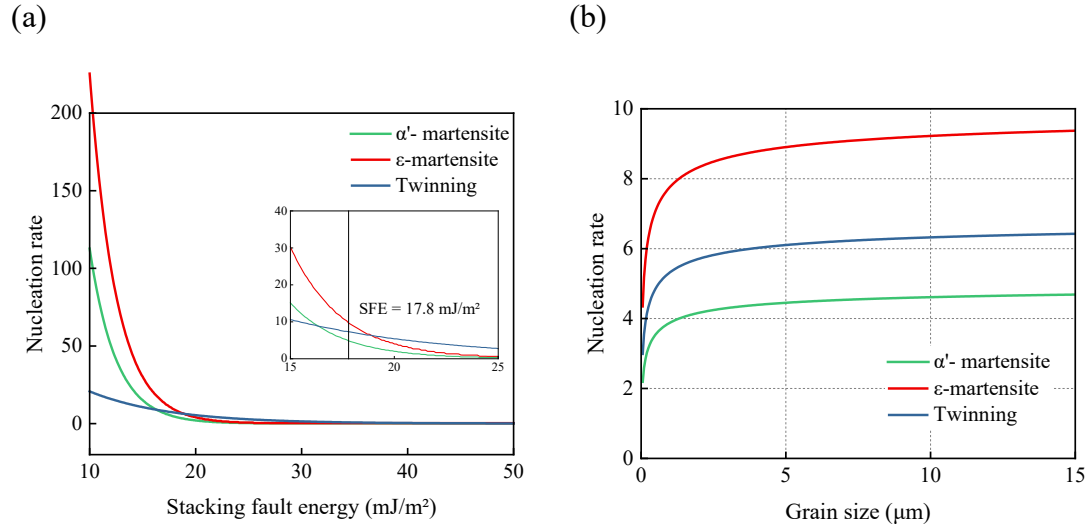

Fig. 4-3. Variation of nucleation rate with (a) SFE for a grain size of 15 μm and (b) grain size with SFE = 17.8 mJ/m^2, calculated from Eqs. 4-4a to 4c.

Table 4-1. The parameters of dislocation density-based model.

Parameters	Values
Exponent inversely proportional to temperature n_0	21.25 [224]
Burgers vector b	0.256 nm [159]
Dislocation generation constant k_1	0.03 [225]
Dislocation nucleation shear stress τ_{nuc}	15 MPa [202]
Dynamic recovery coefficient k_{20}	10 [224]
Hall-Petch constant	100 MPa·μm$^{1/2}$ [212]
Initial dislocation density	10^{13} /m^2 [212]
Interfacial energy between the FCC and HCP structure σ_{HCF}	11.5 mJ/m^2 [202]
Reference grain size D_e	540 nm [224]
Lattice parameter α	0.361 nm [225]
Poisson's ratio ν	0.31 [225]

Reference strain rate $\dot{\varepsilon}_0$	1 [224]
Schmid factor m_{SF}	0.47 [226]
Shear modulus μ	65 GPa [225]
Taylor factor M	3.06 [225]
Thickness of a stacking fault t_i	100 nm [202]

4.2.2 Parameters associated with microstructure evolution of 304 SS during tension

304 SS possesses excellent properties, including high strength, ductility, and strong corrosion resistance. Additionally, with a low SFE steel (SFE = 17.8 mJ/m² at room temperature), it has been experimentally observed that 304 SS undergoes martensitic transformation and deformation twinning. It is a commonly used material to study the effects of TRIP and TWIP on macroscopic properties [198], [199], [200]. It should be noted that the macroscale behavior of the material strongly depends on the length and volume fraction of microstructures according to Eqs. 4-11 and 4-12. Fig. 4-4a shows the evolution of microstructure length with strain, calculated from Eq. 4-5. It can be observed that at the beginning of deformation, when the strain is less than 0.2, the length of the microstructure increases rapidly from 0 to about 10 microns. As the strain continues to increase, the length of the microstructure grows more slowly until it saturates to the grain size. Similar to the nucleation rate observed in Fig. 4-3b, the lengths of the microstructures follow the order: ε-martensite being the largest, followed by twinning crystals, and then α'-martensite.

Fig. 4-4b shows the measured [227] and predicted volume fraction evolution curves, calculated from Eqs. 4-3a to 3c. During the initial deformation stage, the volume fractions of ε-martensite and twinning increase with strain, reaching maxima of 57 % and 44 % at strains of 0.45 and 0.52, respectively. As strain continues to increase, the volume fractions of ε-martensite and twinning gradually decrease to 37 % and 32 %, respectively. Conversely, the volume fraction of α'-martensite gradually increases to 62%, indicating a transformation of twin crystals and ε-martensite into α'-martensite at higher strain.

Fig. 4-4c presents the predicted macroscopic stress-strain, calculated from Eq. 4-14 and the experimental curves from the reference [227]. As the strain increases, the

stress gradually increases from the yield point of 268.6 MPa to 1033.6 MPa. The experimental curves indicate that when the strain reaches 0.58, the stress drops sharply and the specimen fails. This drop means that the material has fractured and can no longer sustain any load. It is worth noting that the effect of material failure on the properties is neglected in this simulation.

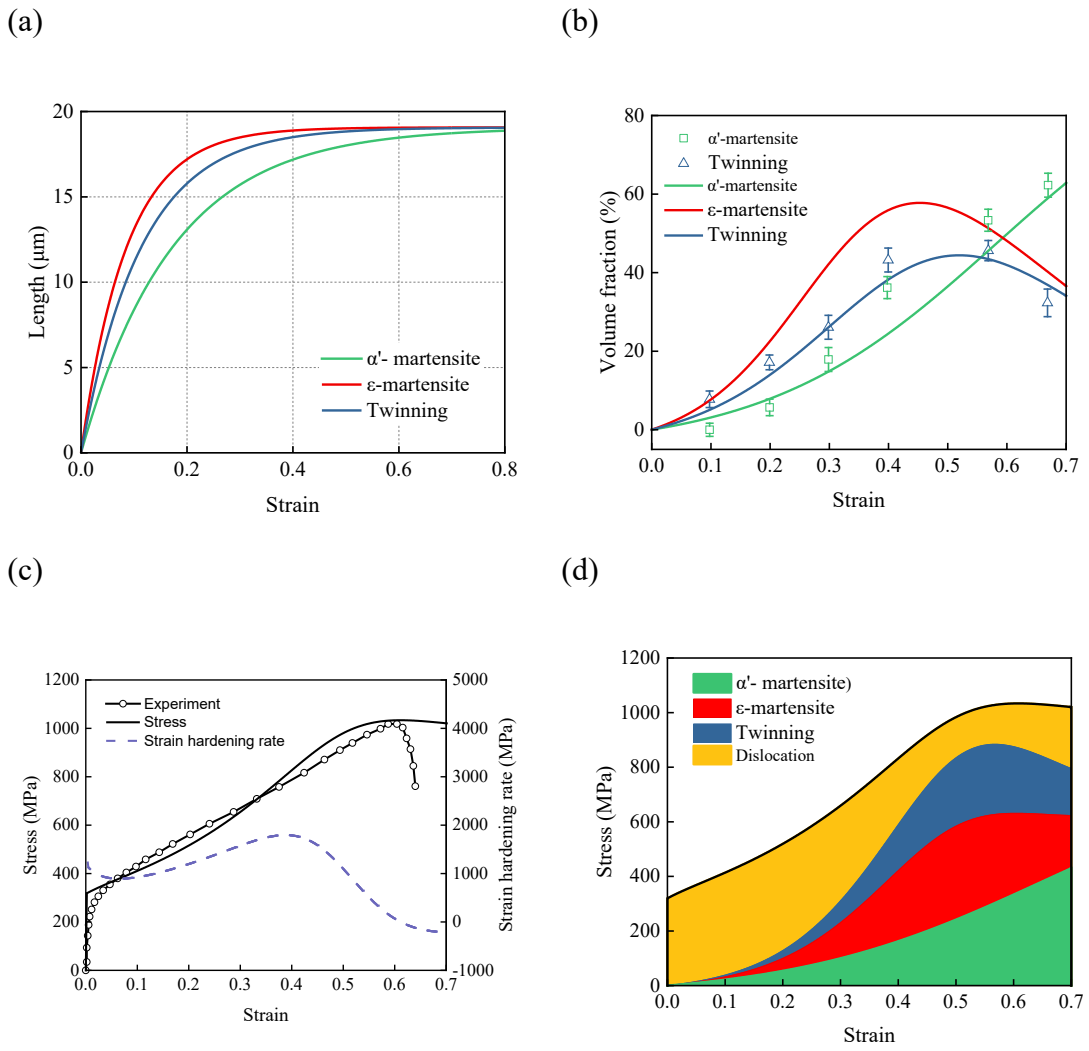

Fig. 4-4. (a) Lengths and (b) volume fractions versus axial strain of ε-martensite, twinning and α'-martensite. (c) macroscale stress-strain curve and strain hardening rate as function of axial strain. Corresponding experimental data of 304 SS are displayed by scattering points at (b) and (c) during tensile loading. (d) Contributions of martensite, twinning, and dislocation to the stress-strain relationship.

Based on the contribution of the individual microstructures on stress-strain relationship shown in Fig. 4-4d, it allows to analyze the effect of the deformation mechanisms on macroscopic stresses. At the beginning of deformation stage (strain less than 0.3), the

volume fraction of individual microstructures is low, and the dislocation density determines the deformation behavior of the material. As the volume fractions of ε-martensite and twin crystals increase with strain from 0.3 to 0.58, they contribute to the increase in stress through the TWIP and TRIP effects, respectively. The shear bands produced by ε-martensite and twin crystals impede the movement of dislocations, allowing dislocations to accumulate at the band boundaries. During this stage, the dislocation density increases significantly from 46 to 240 $\times 10^{13}$ /m² as plotted in Fig. 4-5. The α'-martensite-driven stresses continue to increase as strain increases, with ε-martensite transforming into α'-martensite. It is worth noting that martensite is assumed not to cause an increase in dislocation density within austenite as previously mentioned.

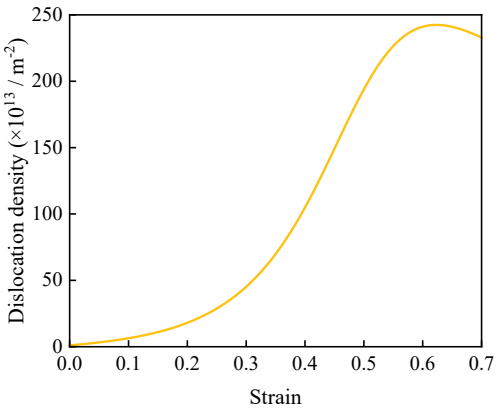

Fig. 4-5. Predicted evolution of dislocation density versus strain.

4.3 Conclusions

In this chapter, a size-dependent dislocation density-based constitutive model incorporating SFE is introduced to investigate the influence of deformation mechanisms on the tensile behavior in 304 SS with low SFE. The modeling and analysis indicate that lower SFE facilitate martensitic transformation and mechanical twinning due to reduced critical shear stress and increased nucleation rates, especially in larger grains. The interaction between SFE, grain size, and nucleation determines the material's response under uniaxial loading. Different stages of deformation are governed by microstructural evolution, including dislocation activities, twinning, and martensitic transformation. At the beginning of deformation, the dislocation motions primarily determine the material's deformation behavior. As the volume fractions of ε-martensite and twin crystals increase, the TWIP and TRIP effects contribute to the rise

in strengthening, respectively. With further straining, martensitic transformation increases, leading to a further enhancement in the material's strength. Understanding these relationships is essential for optimizing material performance in applications.

Chapter 5: Tensile behavior of SMATed TWIP 316L SS accounting for residual fields

Chapter 4 investigates the influence of TWIP, TWIP, and grain size on the deformation behavior of the material with different SFE values using a dislocation density-based model. 316L SS, as a material with moderate SFE values, primarily exhibits plastic deformation behavior dominated by mechanical twinning and dislocation. This was confirmed by microstructural observations of SMATed 316L SS in Chapter 2, where no martensite was detected. To accurately study the tensile behavior of SMATed materials, it is also essential to consider the residual fields induced by SMAT, such as dislocation, grain size, residual stress, twins. In this chapter, deformation response and the corresponding microstructural evolution of a SMATed 316L SS during tensile loading at room temperature are exhaustively studied by a two-dimensional (2D) axisymmetric cylindrical Finite Element (FE) model. In particular, empirical formulas for residual fields induced by SMAT are considered into a combined dislocation density-based and grain size-dependent constitutive model. Furthermore, the investigation explores the influence of dynamic twinning on the tensile behavior of SMATed 316L SS, taking into account of the residual fields. It is important to note that Chapter 5 from the basis for an article published by the author in 2023 (DOI:10.1016/j.mechmat.2023.104713).

5.1 Depth-dependent residual fields

5.1.1 Distribution of grain size and twin

To accurately describe the mechanical behavior of the SMATed material, the residual fields, including the grain size, twin thickness, and twin volume fraction, are considered based on experimental measurements. An exponential relationship is widely used to describe the variation of grain size [228]:

$$D = D_c\left(1-\left\{1+\exp\left[\left(z-h_g\right)/c_1\right]\right\}^{-1}\right) \qquad \text{(Eq. 5-1)}$$

where D_c is the grain size of coarse grains in the unaffected bulk region, h_g and c_1 are the fitting constants, and z is the distance from the treated surface. The SFE, grain size and strain rate have a strong influence on deformation twinning as investigated in Chapter 4. The twin volume fraction is about 20% in the unaffected region, whereas it is only about 2% in the nanocrystalline grain region [229]. To describe the distribution of twins, the initial twin volume fraction throughout the gradient region can be expressed as:

$$f_{t0} = f_{t1} - f_{t2} \exp\left(-z / c_2\right) \quad \text{(Eq. 5-2)}$$

where f_{t1}, f_{t2}, and c_2 are constants. In the absence of present experimental results, the distribution of initial twin thickness is set according to the work performed by [230]:

$$D_t = D_{t1} - D_{t2} \exp\left(z / c_3\right) \quad \text{(Eq. 5-3)}$$

where D_{t1}, D_{t2}, and c_3 are constants.

The in-depth distributions of grain size, twin thickness and twin volume fraction are plotted in Fig. 5-1 by using Eqs. 5-1 to 5-3 with the gradient distribution parameters proposed in Table 5-1. It shows that the twin thickness is strongly correlated to the grain size. These distributions are in agreement with different experimental observations. The smallest grains have a lower twin thickness [231]. TEM observations were made in SMATed austenite 304 SS [232], proving that the distribution of twin volume fraction shows a peak shape near the treated surface at about 0.8 μm as shown in Fig. 5-1b. In the unaffected bulk region, the twin volume fraction keeps a low level around 0.05, similar to that of the untreated sample. When approaching the treated surface, the increasing strain makes the volume fraction of deformation twin more and more important. However, due to the grain refinement mechanism, the deformation twins gradually transformed into grain boundaries, resulting in a rapid decrease in the volume fraction of the existing twins. Besides, there are less or no twins regenerated at the nanocrystalline grain region because twin nucleation stress was found to increase with decreasing grain size [233]. Based on that, the peak shape distribution of twin volume fraction is assumed to be the initial twin thickness with a maximum volume fraction of 20% after the SMAT process as shown in Fig. 5-1b.

Table 5-1. The parameters of grain size and twinning models.

Parameters (Unit)	Symbols	Values
Grain size function (μm)	D_c, h_g, c_1	10, 90, 18
Volume fraction function (%, %, μm)	f_{t1}, f_{t2}, c_2	20, 20, 38
Twin thickness function (μm)	D_{t1}, D_{t2}, c_3	0.01, 0.01, 39

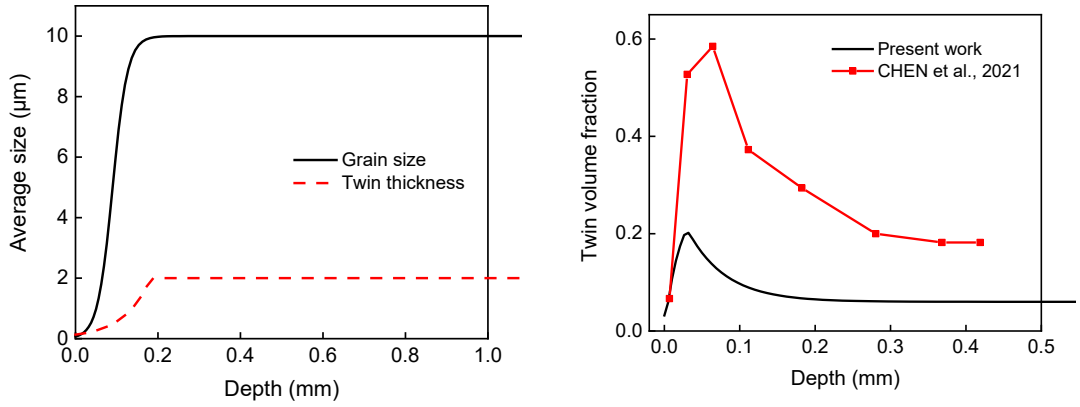

(a) (b)

Fig. 5-1. In-depth distribution profiles of (a) grain size and twin thickness; (b) twin volume fraction.

5.1.2. Distribution of residual stress

As mentioned above, a compressive residual stress field is also inevitably generated in GMS by SMAT. It has a significant effect on mechanical behavior, especially on fatigue properties [234]. The in-depth variation of the residual stress of a SMATed sample was measured by XRD in a previous work [235]. For this purpose, the classical $\sin^2\psi$ method was used. Iterative electrolytic polishing was performed to remove the material layer by layer gradually [236]. Elastic stress release is especially corrected through stress equilibrium conditions during material removal to obtain the true distribution of in-depth residual stress [237].

Fig. 5-2 shows the in-depth distribution of residual stress components in the axial and circumferential directions. It can be seen that these residual stresses exhibit remarkable compressive nature with a thickness of about 500 μm, while beyond 500 μm in the bulk region, tensile residual stresses balance the compressive residual stresses for the whole cylindrical structure. Exponential functions based on the stress equilibrium conditions are built to describe the in-depth distribution of residual stress:

$$\begin{cases} \sigma_{zz}^{rs} = \sum_{i=1}^{2} L_i \left(e^{-l_i (r_{max} - r)} \right) + L_0 \\ \sigma_{\theta\theta}^{rs} = \sum_{i=1}^{2} T_i \left(e^{-t_i (r_{max} - r)} \right) + T_0 \\ \sigma_{rr}^{rs} = \frac{1}{r} \left[\sum_{i=1}^{2} \frac{T_i}{t_i} \left(e^{-t_i (r_{max} - r)} - 1 \right) - T_0 (r_{max} - r) \right] \end{cases} \quad \text{(Eq. 5-4)}$$

where L_0, L_i, l_i, T_0, T_i and t_i are constants fitted from the residual stress profiles presented in Fig. 5-2. Table 5-2 lists the values of the parameters involved in Eq. 5-4.

It is worthwhile to note that there is no martensitic transformation after SMAT, in the present case, according to the obtained XRD patterns of as-received and SMATed samples [238].

Table 5-2. The parameters of residual stress reconstruction model.

Axial				
L_1 (MPa)	l_1 (m^{-1})	L_2 (MPa)	l_2 (m^{-1})	L_0 (MPa)
10547.64	6.95	-11303.32	6.19	188.58
Circumferential				
T_1 (MPa)	t_1 (m^{-1})	T_2 (MPa)	t_2 (m^{-1})	T_0 (MPa)
315.23	17.36	-832.24	2.84	91.60

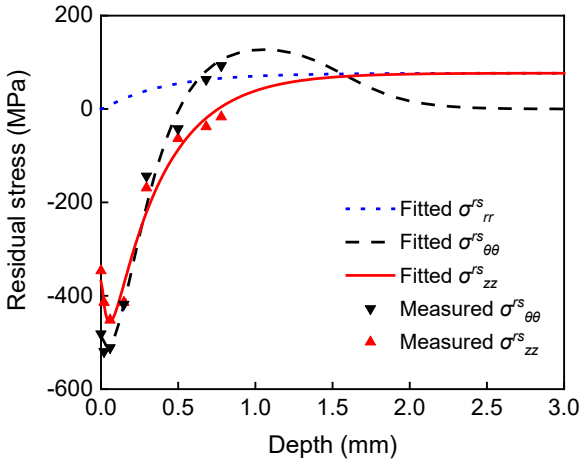

Fig. 5-2. In-depth distribution of residual stress after SMAT.

5.1.3. Distribution of initial dislocation density

It is well documented that there is a link between accumulated plastic strain and initial dislocation density ρ_0. This link can be built through the relation expressed in [89]:

$$\rho_0 = 2\sqrt{3}\frac{\varepsilon_{rs}^{p}}{bD} \qquad \text{(Eq. 5-5)}$$

where b is the magnitude of Burgers vector, ε_{rs}^{p} is the residual accumulated plastic strain, D is the grain size given by Eq. 5-1. In a previous study [100], the residual accumulated plastic strain was assessed from the full width at half maximum (FWHM) of XRD peaks. Fig. 5-3 shows the distributions of accumulated plastic strain and initial dislocation density in the near-surface SMAT-affected region. In this figure, the experimental data of initial dislocation density from [39] are also plotted in red points. It can be seen that the accumulated plastic strain gradually decreases from the treated surface to the bulk. This plastic strain gradient is gradually formed in the near-surface region during the SMAT process. Based on Eq. 5-5, it can also be seen that initial dislocation density has a similar tendency, but varies more sharply with the distance from the surface.

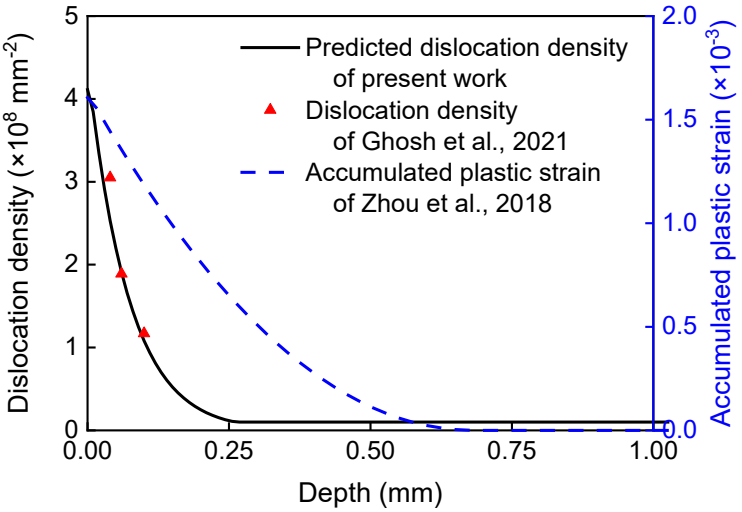

Fig. 5-3. In-depth distribution profiles of initial dislocation density and accumulated plastic strain.

5.2 Constitutive model for GMS material

The involvement of multiple acting factors including residual stress, dislocation, and twinning, leads to a complex plastic deformation behavior during tensile loading.

For the investigation of the mechanical behavior of GMS, a combined dislocation density-based and depth-dependent constitutive model is established based on the elastoplastic framework. In addition, the experimental residual fields, expressed as depth-dependent formulations in Section 5.1, are also taken into account in the model as initial conditions through a user-defined subroutine UMAT.

5.2.1 Evolution of yield stress

Generally, the refined-grains and large quantities of dislocations are two major sources of strengthening in GMS. The increase in yield stress caused by grain boundaries can be estimated by the Hall-Petch model. It is noted that there can be a limitation of grain boundary strengthening due to the grain rotation and grain boundary sliding processes when the grain size is reduced to the nanoscale [239], [240]. In addition, the well-known Taylor relationship can be used to describe the increase in yield stress σ_y caused by the isotropic hardening related to the intragranular dislocation interactions. Therefore, the yield stress evolution can be determined with the contributions of stored dislocations and grain size:

$$\sigma_y = \sigma_0 + \frac{k_{HP}}{\sqrt{D}} + M\alpha\mu b\sqrt{\rho} \qquad \text{(Eq. 5-6)}$$

where σ_0 is the lattice friction stress; k_{HP} is the Hall-Petch slope; D is the grain size; M is the Taylor factor; α is a material constant around 0.3; b is the Burgers vector norm. μ is the shear modulus; ρ is the dislocation density. Before loading, the initial yield stress at each depth can be calculated by Eq. 5-6, when the dislocation density equals the initial dislocation density ρ_0 as given in Eq. 5-5.

5.2.2. Evolution of dislocation density including twinning

Deformation twinning is a common mechanism of plastic deformation, especially in austenitic steels with low SFE as described in Chapter 1. The macroscopic strain ε and shear strain γ are linked to the Taylor factor as follows: $\varepsilon=\gamma/M$. To take into account the contribution of twinning, the total strain increment $d\varepsilon$ can be expressed by incorporating dislocation slip and twinning contributions:

$$d\varepsilon = \left(1 - f_t\right) d\varepsilon_s + \varepsilon_t df_t \qquad \text{(Eq. 5-7)}$$

where ε_s is the strain caused by dislocation slip, ε_t is the strain associated with twinning. The shear strain of twinning γ_t is $1/\sqrt{2}$ [241]. Rearranging the expressions described

by Eqs. 5-6 and 5-7, it gives:

$$\frac{d\varepsilon_s}{d\varepsilon} = \frac{1}{1-f_t}\left(1-\frac{\gamma_t}{M}\frac{df_t}{d\varepsilon}\right) \quad \text{(Eq. 5-8)}$$

where M is the Taylor factor, f_t is the twin volume fraction, which is an assumption expressed as follows [242], [243]:

$$f_t = F_{\max}\left(1-\mathrm{e}^{-\beta_t(\varepsilon-\varepsilon_{t0})}\right)^m \quad , \quad \varepsilon > \varepsilon_{t0} \quad \text{(Eq. 5-9)}$$

where F_{max} is the maximum twin fraction, β_t is the twinning kinetics parameter, and m is the intensity parameter of the TWIP effect, ε_{t0} is the critical strain for twinning initiation. It should be noticed that the sensibility of grain size on the twin volume fraction depends on the SFE of the material [231]. It means that the twinning kinetics parameter β in Eq. 5-9 is grain size-dependent. By differentiating Eq. 5-9, the twin volume fraction rate can be obtained as:

$$\frac{df_t}{d\varepsilon} = F_{max}\beta m \exp\left[-\beta\left(\varepsilon-\varepsilon_{t0}\right)\right]\left\{1-\exp\left[-\beta\left(\varepsilon-\varepsilon_{t0}\right)\right]\right\}^{m-1} \quad \text{(Eq. 5-10)}$$

Dynamic accumulation and annihilation of dislocation processes were taken into account in the classical KME model. The rate of dislocation storage is inversely related to the dislocation mean free path Λ, which depends on the multiplication of dislocations, the twin spacing, and the dislocations forest induced by dislocation interactions. The deformation-induced twins positively affect the work-hardening by impeding the gliding movement of dislocations through twinning boundaries. Accordingly, the generalized equation for the rate of dislocations forests evolution with strain can be expressed as:

$$\frac{d\rho^+}{d\varepsilon_s} = \frac{M}{\Lambda b} = \frac{M}{b}\left(\frac{1}{D}+\frac{1}{t}+k_1\sqrt{\rho}\right) \quad \text{(Eq. 5-11)}$$

where k_1 is a geometric factor related to grain boundary and dislocations forest. The average twin spacing t is related to the twin thickness D_t and the twin volume fraction f_t given by:

$$\frac{1}{t} = \frac{1}{2D_t}\cdot\frac{f_t}{1-f_t} \quad \text{(Eq. 5-12)}$$

Moreover, grain boundaries play an important role in strain hardening with decreasing grain size, especially in refined-grains. However, the classical KME model only considers dislocation annihilation due to dynamic recovery. The grain size effect was observed in nanocrystallization grain in SMATed Fe sample [66]. It is reported that

the deformation mechanism was no longer governed by accumulation of dislocations, but by the grain rotation or grain boundary sliding processes when the grain size is reduced to few nanometers. For this purpose, an additional dynamic grain size-related recovery term is added to describe the decrease in work hardening due to grain refinement [244]:

$$\frac{d\rho^{-}}{d\varepsilon_s} = -M\rho\left[k_{20}\left(\frac{\dot{\varepsilon}^p}{\dot{\varepsilon}_0}\right)^{-\frac{1}{n_0}} - \left(\frac{D_e}{D}\right)^2\right] \quad \text{(Eq. 5-13)}$$

where k_{20} is the dynamic recovery constant, n_0 is an exponent inversely proportional to temperature, $\dot{\varepsilon}_0$ is the reference strain rate, and D_e is the reference grain size. It should be noted that the parameter n_0 is related to the SFE, which may affect the generation of GNDs and grain refinement during SMAT. A SMATed sample with high SFE has stronger back stress hardening and smaller grain sizes [245], [246], [247], [248]. It can be noticed that the rate term involving the calculation of flow stress in Eq. 5-6 is not considered in Newton's iterative implementation. Combining Eqs. 5-8, 5-11 and 5-13, the evolution of the dislocation density can be eventually expressed with respect to the total strain ε:

$$\frac{d\rho}{d\varepsilon} = \frac{d\rho}{d\varepsilon_s}\frac{d\varepsilon_s}{d\varepsilon} = \left(\frac{d\rho^{+}}{d\varepsilon_s} + \frac{d\rho^{-}}{d\varepsilon_s}\right)\frac{d\varepsilon_s}{d\varepsilon} = \frac{1}{1-f_t}\left(M - \frac{1}{\sqrt{2}}\frac{df_t}{d\varepsilon}\right)\left[\frac{1}{b}\left(\frac{1}{D}+\frac{1}{t}+k\sqrt{\rho}\right) - k_{20}\left(\frac{\dot{\varepsilon}^p}{\dot{\varepsilon}_0}\right)^{-\frac{1}{n_0}}\rho - \left(\frac{d_e}{d}\right)^2\rho\right] \quad \text{(Eq. 5-14)}$$

5.3 Finite element model

The constitutive model described in Section 5.2 is used to predict the tensile response of GMS accounting for the residual fields expressed in Section 5.1 by the commercial FE software ABAQUS. The hardening of GMS is governed by the deformation twinning and dislocation densities. The depth-dependent functions describing the residual fields generated by SMAT are considered in the UMAT subroutine according to Eqs. 5-1 to 5-5. Numerical integration and consistent tangent modulus derivation are shown in the Appendix. Meanwhile, the residual stresses are introduced at the beginning of the simulation through the SIGINI subroutine. Then, the constitutive model in the plasticity framework with isotropic hardening is assigned to

the whole FE model.

5.3.1 FE model for tensile simulation

As shown in Fig. 5a, the central section of the cylindrical sample after SMAT is taken as the part of interest. In order to reduce the solving time, a representative 2D-axisymmetric model is built to analyze the tensile properties of GMS. The symmetry boundary condition is applied to the cross-section. To simulate the uniaxial tensile test, a displacement is applied to the upper border of GMS through coupling constraint. The model is meshed by using four-node axisymmetric elements (CAX4). A heterogeneous mesh size from 5 μm (on the treated surface) to 100 μm (in the bulk) has been adopted for the FE model as shown in Fig. 5b. The material parameters required for GMS description are identified by microstructural observation or from the literature as listed in Table 5-3.

Table 5-3. Material parameters for the model of GMS

Symbols	Parameters	Values
σ_0 (MPa)	Lattice frictional stress	70 [8]
K_{HP} (MPa·m$^{1/2}$)	Hall–Petch slope	0.25 [8]
M	Taylor factor	3.06 [53]
α	Taylor constant	0.3 [53]
μ (GPa)	Shear modulus	82 [39]
b (nm)	Magnitude of Burgers vector	0.256 [53]
F_{max}	Maximum twin fraction	0.35 [249]
β	Twinning kinetics parameter	8 [52]
m	Twinning intensity parameter	1.2 [52]
ε_{t0}	Critical strain for twinning initiation.	0.05 [250]
k_1	Proportionality factor	0.026 [52]

k_{20}	Dynamic recovery constant 1	2.5 [53]
n_0	Dynamic recovery constant 2	21.25 [53]
$\dot{\varepsilon}_0$ (s^{-1})	Reference strain rate	1 [53]
d_e (nm)	Reference grain size	580 [53]

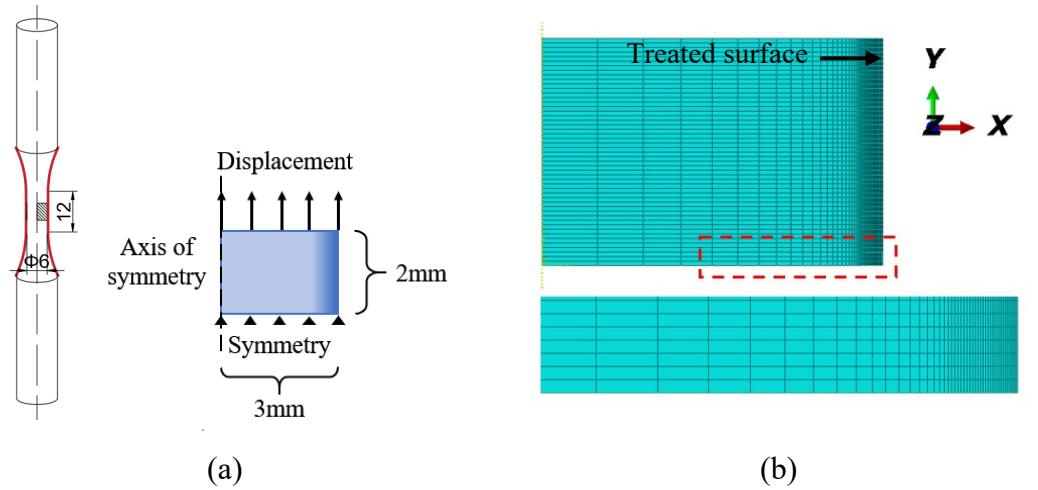

Fig. 5-4. Section of a SMATed sample: (a) geometrical model and boundary conditions, (b) FE model showing the mesh.

5.3.2 Validation of stress-strain relationship and yield strength

With the user subroutine, the finite element simulation requires approximately six hours of CPU time. Fig. 5-5 displays the yield strength evolution with the grain size of GMS. It can be seen that the yield strength significantly increases with grain size due to the combination of grain boundary strengthening effect and dislocation interaction. The yield strength in the nanocrystalline region σ_{gs} can reach 1277 MPa, whereas the yield strength in the bulk region σ_{bulk} is only 270 MPa, which is consistent with experimental results [251], [252], [253], [254].

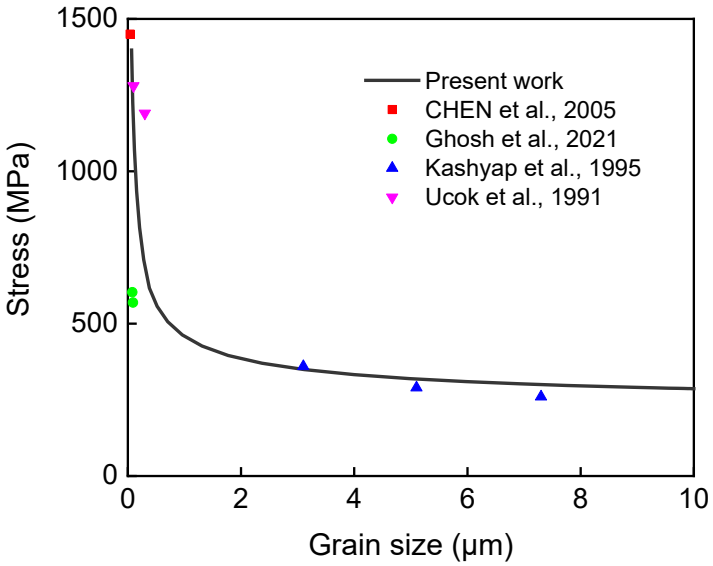

Fig. 5-5. Comparison between numerical and experimental results on the yield strength versus grain size.

In addition, the calculated local mechanical behavior of the nanocrystalline and the coarse grains (with grain sizes: 50 nm and 10 μm, respectively) are shown in Fig. 5-6a. Experimental data on stress-strain relations obtained by [251] are also presented by circular dots in the same figure for comparison. The elastic stiffness of nanocrystalline and coarse grain materials is assumed to be grain size-independent. Therefore, the two curves have the same slope at the elastic deformation stage. When comparing the plastic stage, the calculated results are in rather good agreement with the experimental measurements.

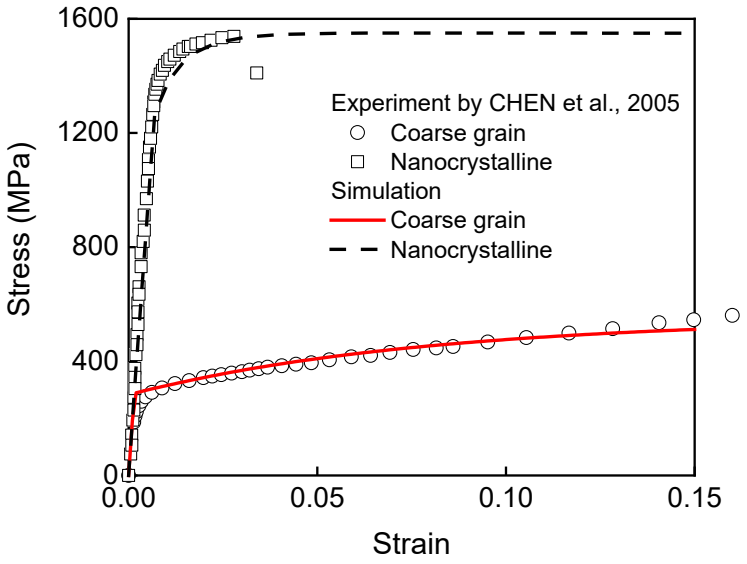

(a)

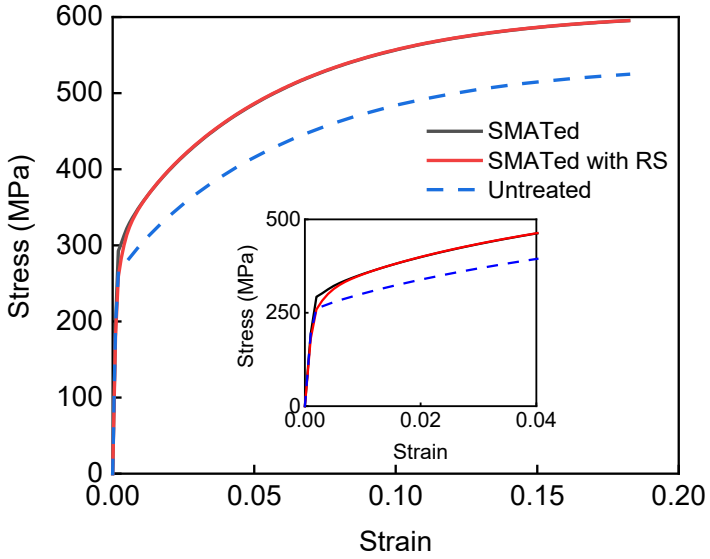

(b)

Fig. 5-6. (a) Comparison of predicted local stress-strain curve between nanocrystalline and coarse grains, and (b) comparison of predicted overall stress-strain curve between untreated structure and GMS during uniaxial tensile loading.

Fig. 5-6b displays the overall engineering stress-strain curve of untreated structure and GMS with and without residual stress, during uniaxial tension. In comparison, the yield strength is 312 MPa for the GMS without residual stress, and 297 MPa for the GMS with residual stress. It shows that the residual stresses can slightly decrease the

yield stress of GMS. This phenomenon was also found in the tensile testing of SMATed TA6V sample [30]. In addition, the yield strength of GMS is slightly higher than that of the untreated material (270 MPa). Because of the relatively thin thickness of the GMS layer in this work, the influence of strengthening by SMAT is not very significant on the tensile behavior. As mentioned above, the thickness of the nanocrystalline layer is about 5 μm on the treated surface, and the volume fraction of the nanocrystalline layer f_{gs} represents only 0.33% of the cylindrical structure. These yield stress results are basically consistent with the simple law of mixture $\bar{\sigma}_y = f_{gs}\sigma_{gs} + (1 - f_{gs})\sigma_{bulk}$ = 273.8 MPa. In other words, the volume fraction of GMS can directly influence the global tensile behavior at the macroscopic scale. The multiple strengthening mechanisms in the gradient-nanocrystallized grain materials provide higher mechanical strength as compared to the untreated sample.

5.3 Simulation results of microstructural quantities and discussion

In the previous section, a dislocation density-based model was numerically developed to describe the mechanical behavior associated with the macroscopic response of the material in uniaxial tension, with geometry described in Fig. 5.4 and parameters of the model given in Table 5.3. In this section, the finite element method is used to analyze the tensile properties of the SMATed specimen with depth-dependent residual fields. The dislocation density-based constitutive model, which incorporates the TWIP effect, is implemented through a user-defined subroutine UMAT of the ABAQUS software. In addition, this model also incorporates the grain size-dependent initial twin distribution and evolution of deformation twinning.

By using the parameters provided in Table 5-3, the stress-strain relationship and yield strength of the GMS can be calculated based on the model presented in Section 5.2. The tensile simulations are an effective way to understand the stretching process during plastic deformation of the near-surface region. After simulations, four representative depths (associated with different grain sizes: 50 nm, 250 nm, 2 μm, and 10 μm) are chosen to illustrate the mechanical properties and the evolutions of twin volume fraction and dislocation density of GMS.

5.3.3 Effect of residual stress in GMS

The tensile simulations with and without residual stresses are performed to

evaluate the effect of compressive residual stresses on the mechanical responses of GMS. Fig. 5-7a illustrates the von Mises stress distribution obtained by FE simulation for the GMS. The GMS, which wraps the unaffected bulk region, constrains the deformation along the tensile direction. It causes a high-level stress (1592 MPa) at the surface. The simulated local mechanical behavior of GMS with and without residual stress is given by solid and dashed curves in Fig. 5-7b, respectively. In comparison, it can be observed that the residual stress mainly influences the mechanical behavior at the initial stage of deformation. As the strain increases, there is little influence on the tensile mechanical behavior with different grain sizes. This is due to the fact that residual stress is internally balanced throughout the whole structure during the plastic deformation, which is similar to the overall mechanical behavior at different grain sizes as shown in Fig. 5-6b. Specifically, in the low strain level, most of the externally imposed deformation is accommodated by the bulk coarse grains. As the strain increases, there is little influence of residual stress on the tensile mechanical behavior with different grain sizes. This is due to the fact that residual stress is internally redistributed throughout the whole structure during the plastic deformation.

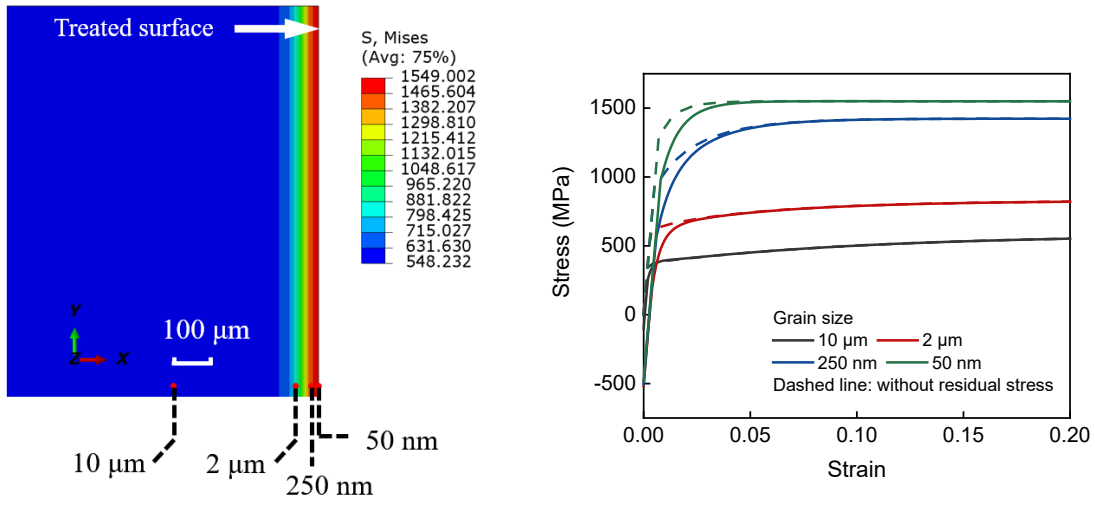

(a) (b)

Fig. 5-7 (a) Distributions of von Mises stress after tensile loading, and (b) stress-strain curve at different grain sizes with residual stress (in solid line) and without residual stress (in dashed line).

As mentioned above, the SMATed structure presents a gradient yield strength in the near-surface region, which results in inhomogeneous deformation during tensile

loading as shown in Fig. 5-8. During tensile loading, the deformation spreads outward from the soft coarse grains to the nanocrystallized grains. In the early stages of deformation, due to the gradient yield strength, the coarse grains in the bulk started to present a plastic deformation, whereas the nanocrystallized grains in the surface layer remain elastically deformed. That elastic/plastic transition throughout the near-surface SMAT affected region could generate a large strain gradient, which consequently leads to a high level of GNDs at the early deformation stage [255]. It should be noted that the tensile stresses internally present cause stronger deformation in the corresponding coarse grain region.

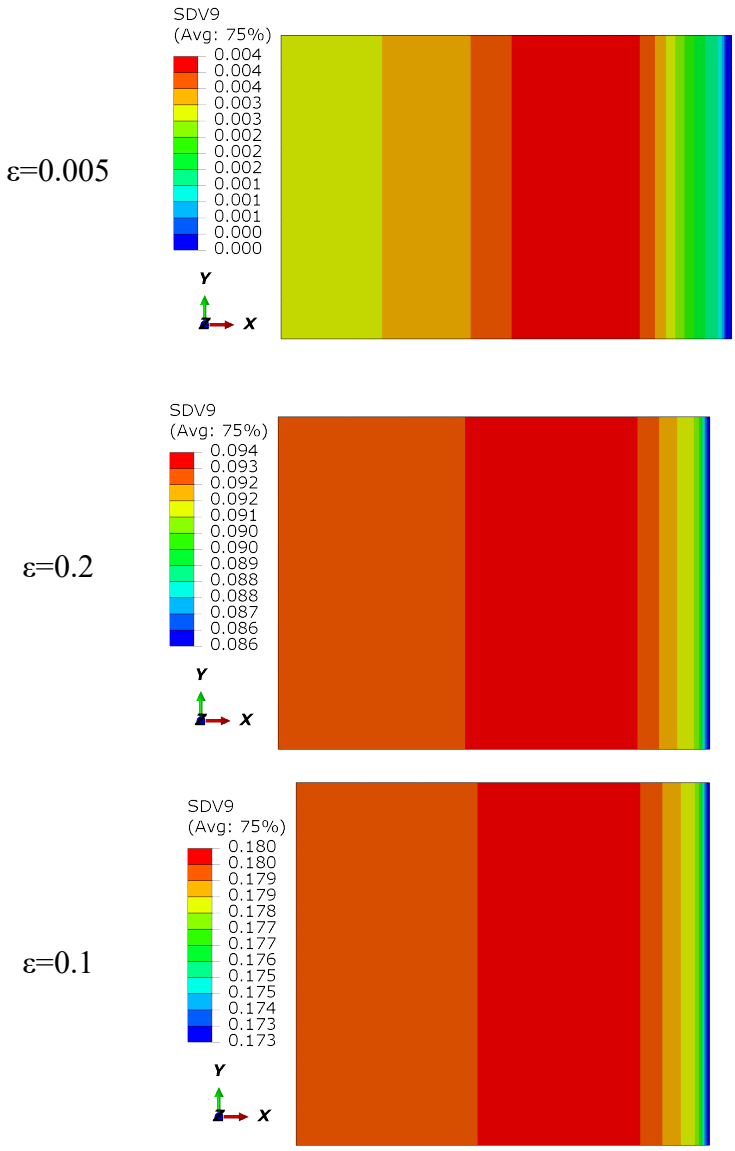

Fig. 5-8. Evolution of equivalent plastic strain during tensile loading (at a strain of 0.2 along Y-axis).

5.3.4 Predicted evolution of twin volume fraction

From the distribution of initial twin volume fraction in Fig. 5-9a, it can be seen that the points of grain size 50nm and 250nm are located on the right side of peak value, whereas the points of grain size 2μm and 10μm are situated on the opposite side. The SMAT process refines the grains down to the nanoscale (ranging from 50 nm to 250 nm) in the near-surface region, and meanwhile the existing twin structure is destroyed by the grain refinement effect. Almost no twin can be distinguished in nanocrystallized grains in a SMATed 316L sample [48]. As mentioned above, each side has a different mechanism on the evolution of deformation twinning, accumulated on the left side and transformed to grain boundaries on the other side. It has to be noticed that the constitutive model used in the present work does not implement any grain refinement with an increase in dislocations and twins at the microscale.

In addition to the twin nucleation, twin volume fraction strongly depends on the grain size in slip-dominated materials [231]. Therefore, the grain size effect is taken into account in the calculation of twin volume fraction in Eq. 5-9 by replacing the assumed β_t in Eq. 5-15, which would need further experimental study:

$$\begin{aligned} \beta_t &= \beta_0 \times coefficient(D) \\ coefficient(D) &= \left(D / D_{e2}\right)^2 \end{aligned} \qquad \text{(Eq.5-15)}$$

where β_0 is the basic twinning kinetics parameter and D_{e2} is the reference grain size for twinning. Fig. 5-9b shows the evolution of twin volume fractions at different depths (i.e. with varying grain sizes) with the increase in plastic strain during tensile loading. It can be seen that during tensile loading, the twin volume fraction increases with strain in coarse grains. The twin volume fraction significantly increases from 6.0% to 30.2% for grain size of 10μm, and increases very slightly from 13.3% to 14.5% for grain size of 2μm. However, the twin volume fraction in nanocrystallized grains barely changes during tensile loading and keeps the initial state obtained by SMAT. It means that the deformation twinning is inactive in nanocrystallized grains during tensile loading.

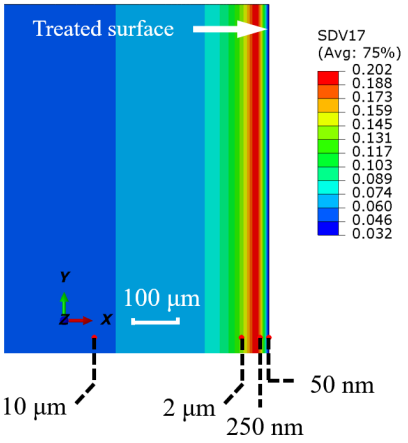

(a)

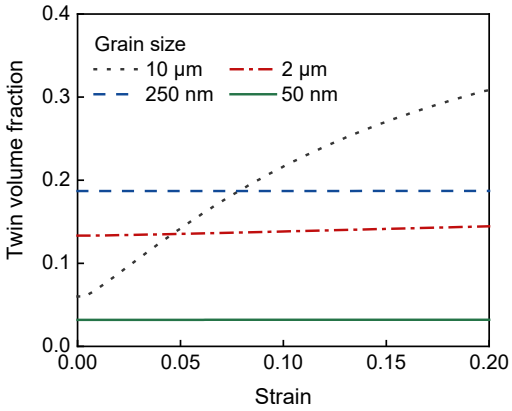

(b)

Fig. 5-9. (a) Distributions of initial twin volume fraction (b) Predicted evolution of twin volume fraction with different grain sizes (corresponding to different depths beneath the SMATed surface).

5.3.5 Dislocation density distribution within GMS

As mentioned in Section 5.2, TWIP and grain size effects are integrated into the dislocation density-based constitutive model to describe more accurately the mechanical properties of SMATed sample. Fig. 5-10a shows the distribution of such dislocation density after tensile loading simulation. The maximum dislocation density reaches 18.9 × 10^8 mm^{-2} at the sub-surface. On the treated surface, the significant reduction in dislocation density is caused by dynamic recovery as expressed by Eq. 5-13. Therefore, the maximum dislocation density is located in the sub-surface.

The evolution of dislocation density during tensile loading of the GMS is

presented in Fig. 5-10b with different grain sizes. Since the SMAT introduces a gradient density of strain-induced dislocations in the region of the treated surface, this region has a higher residual dislocation density than the coarse grain bulk before deformation. Moreover, as mentioned above, different grain sizes are associated with different yield strengths, which causes inhomogeneous deformation. The smaller grain size (with higher yield strength) delays elastic-plastic transition, which prolongs simultaneously the turning point of dislocation density. With the increase in plastic strain, the dislocation density increases from 4.8×10^8 mm^{-2} to 8.6×10^8 mm^{-2} on the treated surface, and from 1.3×10^8 mm^{-2} to 4.4×10^8 mm^{-2} in the central bulk region. As the strain increases even further, the dislocation density gradually saturates, especially in the nanocrystallized layer.

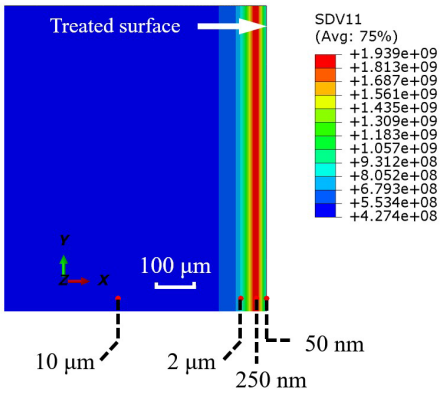

(a)

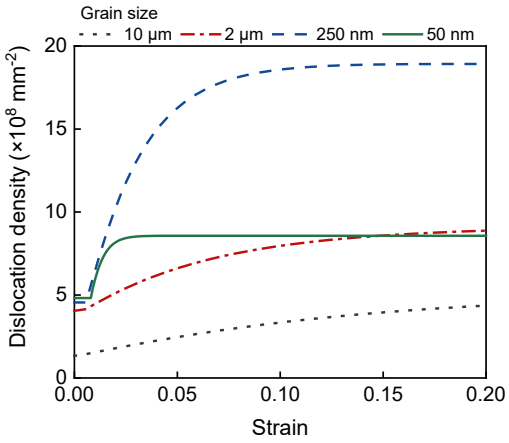

(b)

Fig. 5-10. (a) Distribution of dislocation density after tensile loading, and (b) predicted evolution of dislocation density with different grain sizes.

5.3.6. Effect of deformation twinning in GMS

Four different twinning conditions are set to study the twinning influence on the mechanical property of the GMS:

(I): No twinning mechanism involved in the constitutive model, for comparison;

(II): Normal twinning as mentioned above with initial twinning;

(III): Normal twinning without initial twinning fraction induced during loading;

(IV): Massive twinning generated by increasing the basic twinning kinetics parameter β_0 in Eq. 5-15.

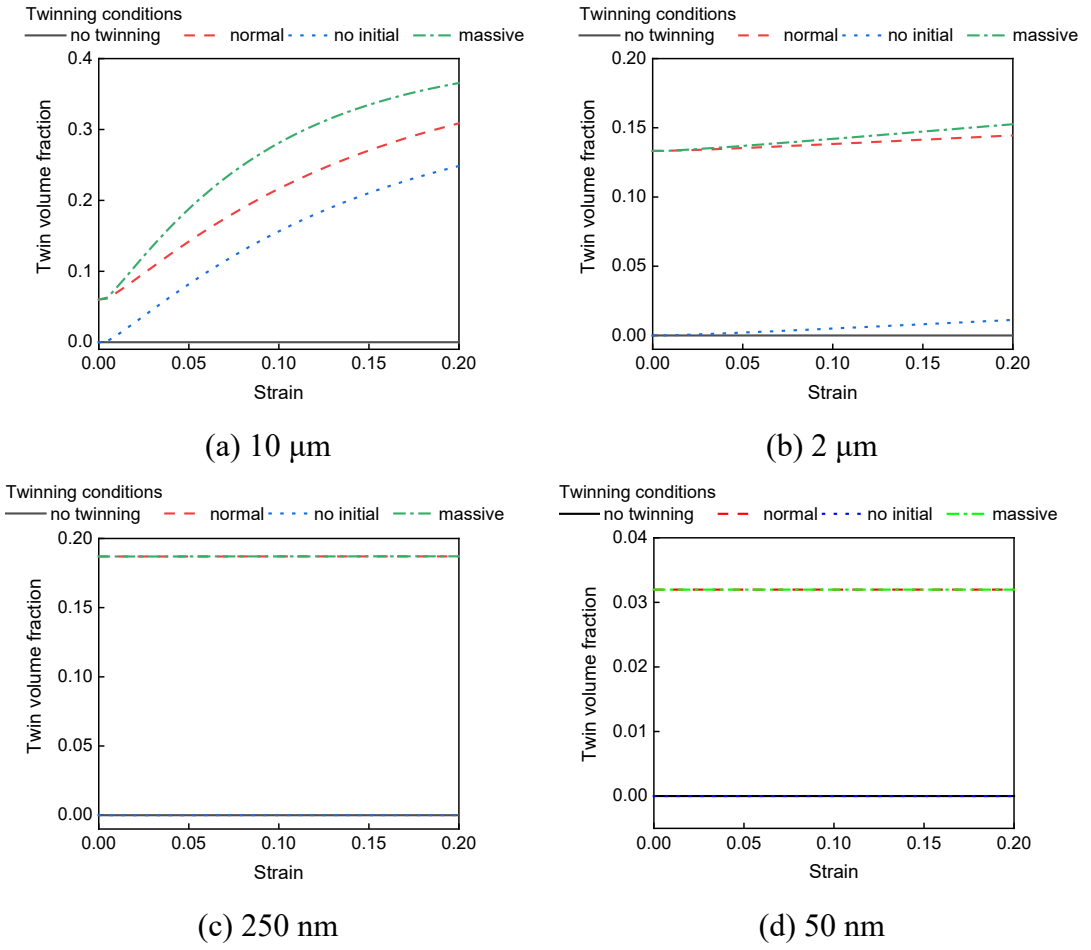

Fig. 5-11. Evolution of twin volume fraction with different twinning conditions at different grain sizes.

Fig. 5-11 shows the evolution of twin volume fraction with different twinning conditions at different grain sizes. By comparison of the normal and massive conditions, it can be seen that the twin volume fraction of the massive twinning gradient increases more than the normal one with increasing strain for grain size of 10 μm. However, the twin volume fraction has almost no variation and is equal to the initial value of all conditions for grain sizes of 250 nm and 50 nm. In addition, the no initial and normal

conditions have the same tendency, but translate the value of the initial twin volume fraction.

It can be seen in Fig. 5-12 that the evolution of dislocation density and stress-strain curve have the same change rule with twin volume fraction, whatever the grain sizes with more or less amplitude. The smaller the grain size, the weaker change of twinning conditions. During tensile loading, the twin volume fraction increases with strain, simultaneously associated with an increase in dislocation density and strain hardening, to accommodate the excess of strain from external loading [256].

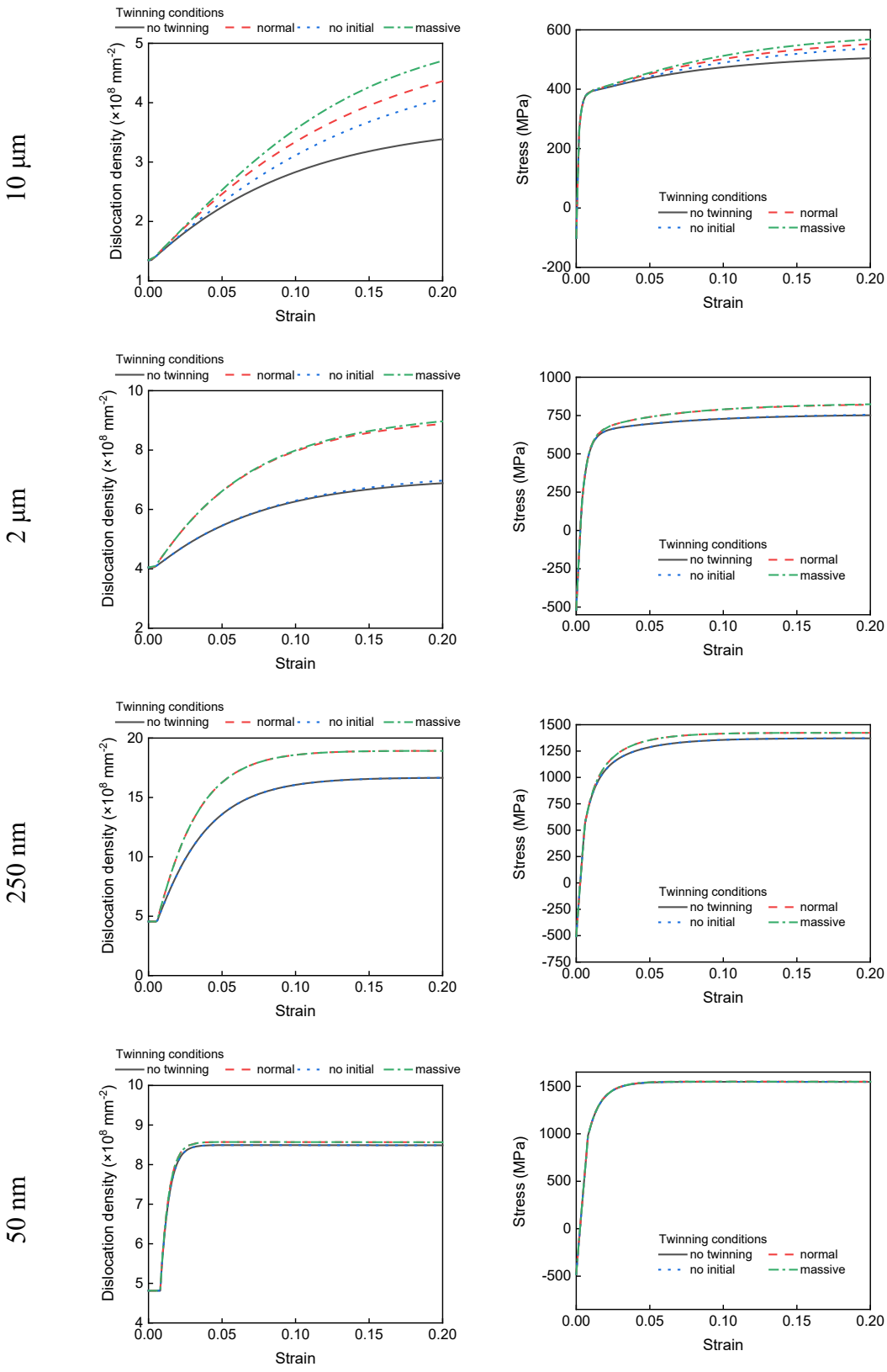

Fig. 5-12. Predicted evolution of dislocation density and stress-strain curve with four different grain sizes (10 µm, 2 µm, 250 nm and 50 nm).

5.4 Conclusions

In this work, a combined dislocation density-based and depth-dependent constitutive model incorporating microstructural parameters is built to describe the mechanical behavior of GMS at the macroscopic scale. Compared to the model developed in Chapter 4, we do not consider martensitic transformation for application to SMATed TWIP 316L SS. In addition, the depth-dependent residual fields (grain size, residual stress, dislocation density, and twinning) are considered in the FE model of a cylindrical structure. The grain size distribution has been confirmed to be the primary influence on the results also for accurate modeling of the SMAT effect. Based on the obtained results, the following conclusions can also be drawn:

- In comparison with the experimental results, the developed theoretical model is able to correctly describe the mechanical properties of the GMS obtained by SMAT.
- The GMS induced by SMAT presents inhomogeneous deformation. The coarse grains in the bulk started the plastic deformation, whereas the nanocrystallized grains in the surface layer still deformed elastically. At a low strain level, the bulk coarse grains accommodated most of the externally imposed deformation.
- The dislocation densities and twin volume fractions of layers with different grain sizes increase rapidly and gradually saturate under tensile loading.
- Detailed analysis of the local and global tensile behavior of GMS found that the surface compressive residual stress generated by SMAT plays a significant role in reducing the yield strength, especially at the initial stage of deformation. However, as the deformation increases, the residual stresses have little less influence on the tensile behavior, because the residual stress is always internally balanced as the strain progresses. In addition, due to the gradient feature of residual stress, its influence gradually decreases with increasing depth.
- The simulation results revealed that the twin volume fraction increases in coarse grains, but hardly changes in nanocrystallized grains, maintaining the initial state during tensile loading.
- By incorporating deformation twinning into the dislocation mean free path within a dislocation density-based model, it is possible to analyze both the evolution of the dislocation density and the response of the stress-strain curve over different

grain sizes during tensile loading. The results reveal that the maximum dislocation density is located in the subsurface region of the treated samples due to the dynamic surface recovery process. As the plastic strain progresses, the dislocation density increases both on the treated surface and within the central block region, eventually reaching the saturation point in the nanocrystalline layer.

Chapter 6: Cycle deformation response and microstructure

There is a close interrelation between the macroscopic mechanical response and the microscopic deformation mechanisms of materials in LCF. Previous studies have shown that the SFE determines the deformation mechanism, which affects the microstructural changes and influences the LCF properties. LCF has been investigated in Chapter 3, especially for SMATed or as-received 316L SS. During uniaxial loading (as seen in Chapters 4 and 5), mechanical properties and microstructural evolution of different materials are assessed based on elastoplastic model with physical ingredients, developed from microscopic scale with a quite good accuracy.

Stress-strain curve models, such as linear, power function, and Johnson-Cook models, are commonly used to characterize the deformation behavior of materials at various stress levels. Similarly, a numerical model can be used to efficiently analyze and describe the fatigue response of a material over different numbers of cycles. In this chapter, to accurately understand the complex cyclic deformation response, including hardening, softening and saturation at the macroscopic scale, the corresponding microstructural evolution is developed. Thus, a physically based model is considered to link the cyclic deformation response and the corresponding microstructural evolution. The effects of grain size and mechanical twining on the cyclic deformation behaviors have also been taken into consideration. In addition, a hypothesis is proposed about the effect of SMAT on cyclic deformation response of treated materials, thanks to these simulations. Due to the complexity of the SMAT's effect on LCF behavior, this section focuses exclusively on the simulation of as-received material.

6.1 Relationships between macroscale response and microstructure

Observations of microstructural evolution revealed that different deformation mechanisms are activated during LCF, including dislocation, deformation twinning, and martensite transformations. It is suggested that cyclic hardening/softening behaviors may be influenced by crystal structure, material's SFE and external loading conditions.

6.1.1 Summary of cycle stress response

In LCF, understanding the stress amplitude is a critical parameter for predicting

the fatigue life of materials subjected to high strain and low-cycle loading conditions. Fig. 6-1 schematically illustrated the typical cyclic stress response curves of as-received material at room temperature with several common features. The cyclic stress response can be divided into four stages: (I) initial hardening, (II) softening, (III) unstable section, and (IV) rapid failure. The cyclic stress response corresponding to deformation mechanisms at each stage can be described as follows:

(Stage I) The cyclic stress response shows initial hardening in stage I, the stress amplitude increases rapidly at the beginning of cyclic loading. Misorientations between grains induce plastic strain incompatibilities. As shown in Fig. 6-2, dislocations accumulate near the grain boundaries to accommodate plastic deformation, mostly of the GND type, named boundary dislocation ρ_b. The intergranular back stress, which is associated to the inhomogeneous plastic deformation between grains, increases notably with the accumulation of dislocations at grain boundaries. In the meantime, the dislocation inside grains (named internal dislocation ρ_i) also increases with a slower rate. Secondary slips, with different orientations or involving different planes compared to the primary slip system, then become activated with successive loading and unloading cycles in high SFE materials. This activation of secondary slips leads to a more uniform of internal dislocations within grains. It means that the increasing of ρ_i decreases the dislocation gradient between grain boundaries and internal region of the grain, thereby leading to a slower hardening rate [257]. In addition, when these multi-directional dislocations intersect one another within the grain, a new dislocation is formed after short-range interaction in FCC crystal. The formation of locked dislocation junctions impedes the motion of internal dislocations, leading to an increase in the effective stress [258], [259]. Thus, the initial hardening is due to the synergistic effect of increased back stress and effective stress. However, for TWIP materials with low SFE values, deformation twins can provide additional strengthening by increasing dislocation accumulation through twin boundaries [260], [261], [262].

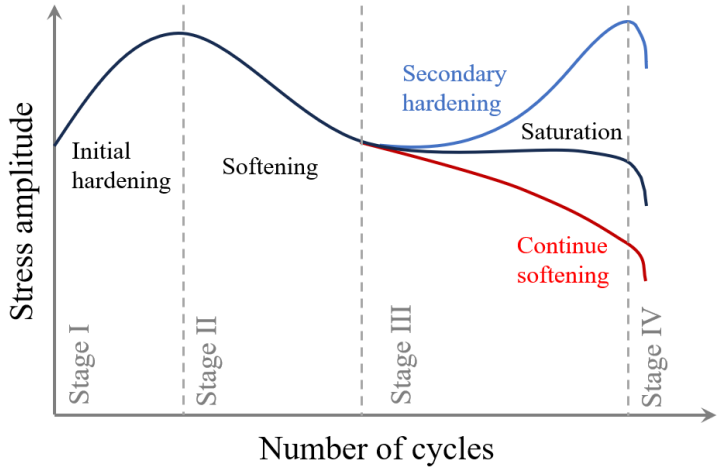

Fig. 6-1. Schematic illustration of the cyclic stress response with different stages of as-received material in strain-controlled LCF.

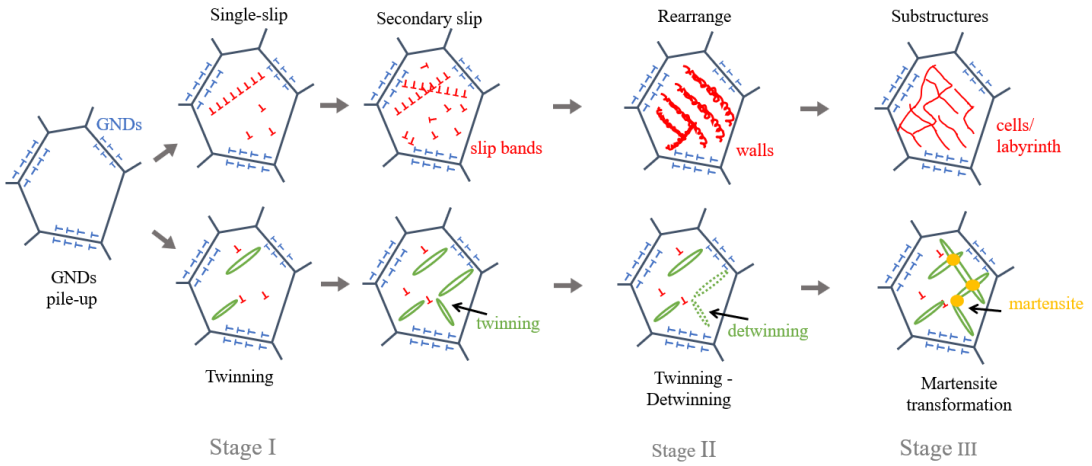

Fig. 6-2. Schematic illustration of microstructure evolution at different stages of the fatigue cycle, including (stage I) initial hardening, (stage II) softening and (stage III) unstable section. The first row corresponds to high SFE values, while the second row corresponds to low SFE values.

(Stage II) Cyclic softening is typically observed following initial hardening. With more frequent activation of secondary slips, dislocations rearrange to form substructures such as dislocation channels then walls, aiming to minimize stored dislocation strain energy in low SFE materials. Glide or cross-slip screw dislocations are observed within channels, which could mutually annihilate and deposit at edge segments along the walls. This screw dislocation motion carries a significant portion of

the imposed plastic strain during cyclic loading, contributing to the cyclic softening at this stage [263]. For TWIP materials, twinning and detwinning during cyclic loading will also provide an extraordinarily softening mechanism, as shown in Fig. 6-2II. Researchers reported that all mechanical twinning formed during the compressive load cycle detwinned during the reversed loading and near-complete detwinning occurs at stage II [264]. It is noteworthy that the volume fraction of twinning (after detwinning) eventually increases slightly with the number of fatigue cycles [264], [265].

(Stage III) Before fracture, materials with different SFE values undergo an unstable phase characterized by three potential directions of cyclic development. First, cyclic stress response may continue in accordance with the deformation mechanism of Stage II, leading to further softening. Second, a stable microstructure may form with further cycling, causing the material to deform uniformly through a dynamic equilibrium between dislocation multiplication and annihilation, resulting in a saturated phase [257]. Third, the secondary hardening observed in high SFE materials can be associated with the transformation of dislocation walls into labyrinth and cell structures where dislocations continue to rearrange, which globally decreases the mean free path of dislocation movement [266]. De-twinning will stop at a certain cyclic load in TWIP materials, and residual twins are retained throughout the cycles in stage III. The volume fraction of twinning increases linearly with cycling, contributing to the secondary strengthening of the material. For materials with lower SFE and TRIP effect, due to increased cumulative plastic strain and intensified dislocation interactions, austenite may transform into either α'- or ε- martensite in large quantities [260], [267], [268]. The high-strength martensite then contributes to secondary strengthening as illustrated in Fig. 6-2III.

(Stage IV) The rapid drop in cyclic stress amplitude is mainly due to the formation of microscopic cracks and their subsequent rapid propagation until fracture occurs.

6.1.2 SFE dependence deformation mechanism

The material with low SFE promotes the planar slip of dislocations, facilitating the stacking faults reversibility slip in the same plane during cyclic loading, which enhances fatigue resistance [269]. It is widely believed that planar dislocations are more beneficial for the formation of deformation twinning as well as martensitic transformation [270], thus providing additional deformation mechanisms during cyclic

loading, as discussed in the previous section. By contrast, a high SFE promotes cross slip, which facilitates dislocation annihilation and subsequently reduces dislocation density [270]. It indicates a noticeably lower cyclic hardening and higher cyclic softening in high SFE materials. Additionally, high SFE weakens the planarity of dislocation slip, which brings a transformation of dislocation slip from planar mode to wavy mode and facilitates the formation of cellular dislocation structures [266].

6.1.3 Strain amplitude dependent deformation mechanism

It is well known that dislocation motions and interactions increase as the strain amplitude rises [261], [271]. When the strain amplitude is low, dislocations exhibit low density, and slip bands are more widely spaced. These dislocation structures suggest that there is not a significant cyclic response at low strain amplitude compared to high strain amplitude. In addition, the dynamic evolution of deformation twinning and martensitic transformation has been demonstrated to be influenced by strain, the volume fraction of twinning and martensite increases with strain in FCC SS, as discussed in Chapter 4. Almost no deformation twins were observed at a low strain amplitude of 0.3% by TEM, indicating that the twin structure did not form well under these conditions [272].

At higher strain amplitudes, the density of dislocation motion and slip bands increases, and secondary slips begin to intersect [260], [266], [268]. Depending on the material's SFE values, this interaction promotes deformation twinning or martensitic transformation, introducing new hardening mechanisms. This explains the significant variation in cyclic response at high strain amplitudes, resulting in substantial hardening or softening effects. Additionally, dislocation slip mode changes from planar slip to wavy slip at high strain amplitude [273] and with increasing cycle number [272]. It is also well accepted that cross slip and multiple slip are essential prerequisites for the formation of cell and labyrinth structures [274], [275]. This phenomenon could explain the secondary hardening observed in Stage III in materials without TWIP and TRIP mechanisms in Fig. 6-2.

6.1.4 Grain size dependent deformation mechanism

The formation and evolution of microstructure through grain size during tensile loading were described in Chapter 4. Therefore, it is crucial to investigate the effect of

grain size on the deformation behavior of LCF over a broader range of strain amplitudes. In general, smaller grains provide more grain boundaries, which can accommodate the stacking of more dislocations in materials than coarse grains at the same geometry. The restricted dislocation movement can increase yield strength and resistance to plastic deformation due to grain boundary increasing. Consequently, fine-grained materials often exhibit improved cyclic strength and enhanced fatigue life in the LCF regime [272]. It should be noted that GND type dislocations show less interactions compared to SSD type. However, larger grains have fewer grain boundaries, which allow dislocations to move more freely and provide space for heterogeneous dislocation structures (SSD type) inside the grain compared to their fine-grained counterparts. Larger grain sizes tend to have fewer GNDs, providing a more suitable environment for the generation, movement, and storage of SSDs [272]. It indicates higher dislocation density and stronger dislocation-dislocation interactions of SSD type within the coarse grain. Based on the enhanced stacking of dislocations and the stronger interactions between dislocations, coarse grains exhibit a higher initial cyclic hardening capacity compared to fine-grained materials. This can result in lower yield strength and higher plastic deformation during cyclic loading, often leading to reduced fatigue life in the LCF regime [272]. It is well accepted that the critical stress required for the onset of twinning decreases with increasing grain size. It suggests that the presence of more mechanical twins in coarse grains also contributes to strain-hardening behavior [276].

6.2 Dislocation-based internal stresses model

The KME model is applied to calculate the rate of change in dislocation density with plastic strain, as detailed in Chapters 4 and 5, using Eqs. 4-10 and 5-14, respectively. In the present section, we only report the additional equations required to model LCF. In the competing processes of storage and recovery, the evolution of average dislocation density is assumed to be the additive superposition of two contributions. Additionally, GNDs are considered immune to the dislocation annihilation process [277]. The evolution of dislocation density during plastic deformation can be rewritten as:

$$\frac{d\rho}{d\varepsilon_p} = \frac{d\rho^{+}}{d\varepsilon_p} - \frac{d\rho^{-}}{d\varepsilon_p} = k_1 \frac{1}{\Lambda} - k_2\rho = k_1 k_\Lambda \sqrt{\rho} - k_2\rho \qquad \text{(Eq.6-1)}$$

$$\sqrt{\rho} = \frac{k_1 k_\Lambda}{k_2}(1 - e^{-k_2 \varepsilon_p / 2})$$

where k_1 and k_2 are coefficients of the generation rate and annihilation rate of dislocation density, respectively. k_Λ is the generation rate of dislocation mean free path. It is worth noting that deformation twins and grain size are assumed to affect only the mean free path Λ term of dislocation density. $k_\Lambda = k_D k_t$, k_D and k_t are coefficients of the effect of grain size and deformation twins on dislocation mean free path, respectively. Combined with the Taylor relationship with the dislocation density-induced stress, it leads to:

$$\sigma = M \alpha G b \sqrt{\rho} = M \alpha G b \frac{k_1 k_\Lambda}{k_2}(1 - e^{-k_2 \varepsilon_p / 2}) \qquad \text{(Eq.6-2)}$$

The relationships between the macroscale response and microstructure at different stages of LCF are discussed in Section 6.1. It is observed that the variation of internal stresses due to the evolution of dislocations can be separated into effective stresses, inter-granular back stresses, and intra-granular back stresses. Consequently, the stress response of the material can be calculated by overlying these terms in Eq. 6-2. The different internal stress responses during fatigue can be modeled by considering changes in dislocation conditions with respect to the number of cycles.

In Section 6.1, the inter-granular back stress depends on the difference between boundary and internal dislocations. The evolution of inter-granular back stress during cyclic loading can be described by:

$$X_{inter} = M \alpha G b \left\{ f_b \left[\sqrt{\rho_b} \cdot (1 - e^{-k_{2b} N_f / 2}) - \sqrt{\rho_i} \cdot (1 - e^{-k_{2I} N_f / 2}) \right] + \sqrt{\rho_{GNDs}^{sat}} \right\} \qquad \text{(Eq.6-3)}$$

where f_b is the area fraction occupied by boundary dislocations, which is usually smaller than 20% of the whole grains [202]. $\frac{k_{1b} k_{\Lambda b}}{k_{2b}}(1 - e^{-k_{2b} \varepsilon_p / 2})$ and $\frac{k_{1I} k_{\Lambda I}}{k_{2I}}(1 - e^{-k_{2I} \varepsilon_p / 2})$ respectively represent the evolution of ρ_b and ρ_i with cycle number developed by Eq. 6-1. ρ_{GNDs}^{sat} is the minimum GNDs required to accommodate grain-to-grain plastic strain incompatibility under stabilized conditions. Following the same approach used for the formulation of inter-granular back stress, the intra-granular back stress is expressed by:

$$X_{intra} = M \alpha G b \cdot f_w \left\{ \left[\Delta \sqrt{\rho_w} (1 - e^{-k_{2w} N_f / 2}) \right] + \sqrt{\rho_{GNDs}^0} \right\} \qquad \text{(Eq.6-4)}$$

where f_w is the fraction of walls. ρ_{GNDs}^0 is the initial GND, which is proportional to the

difference between the square root density of dislocations within walls and channels. $\Delta\sqrt{\rho_w^{sat}}$ is the difference between the square root density of dislocations within walls and channels at the stabilized condition. The dislocations rearrange rate to form dislocation structures k_{2w} is typically lower than the rate of internal dislocation annihilation k_{2i}, $k_{2w} \approx k_{2i}$. The evolution of effective stress during cyclic loading can be written as:

$$\sigma_r = M\alpha Gb \cdot \sqrt{f_j \rho_I} \qquad \text{(Eq.6-5)}$$

where f_j is the fraction of fixed dislocation junctions.

6.3 Results on stress evolution and discussion

6.3.1 Modeling of cyclic deformation response for as-received 316L SS

The physically-based model described in the previous section was used to simulate fatigue property obtained during the LCF experimental results of as-received 316L presented in Chapter 3. Fig. 6-3c presents the variation of stress amplitude versus the number of cycles, showing that the cyclic deformation response initially exhibits hardening over few cycles, followed by continuous softening. No saturation or secondary hardening was observed in stage III. In addition, EBSD results from Chapter 3 also confirm the absence of martensitic transformation and deformation twinning during cyclic loading. As discussed in Section 6.1, the dislocation-dominated cyclic deformation response indicates that the initial hardening strength increases with strain amplitude, probably due to a massif activation of planar slip and secondary slip at high strain amplitudes. The slight cyclic softening observed at a higher strain amplitude of 1.25% may be attributed to the promotion of cross-slip and the rearrangement of dislocation structures into walls and channels before failure. The predicted results in Fig. 6-3 shows that the developed model introduced in Section 6.2 can describe the cyclic hardening and softening response of 316L SS under LCF at various strain amplitude values.

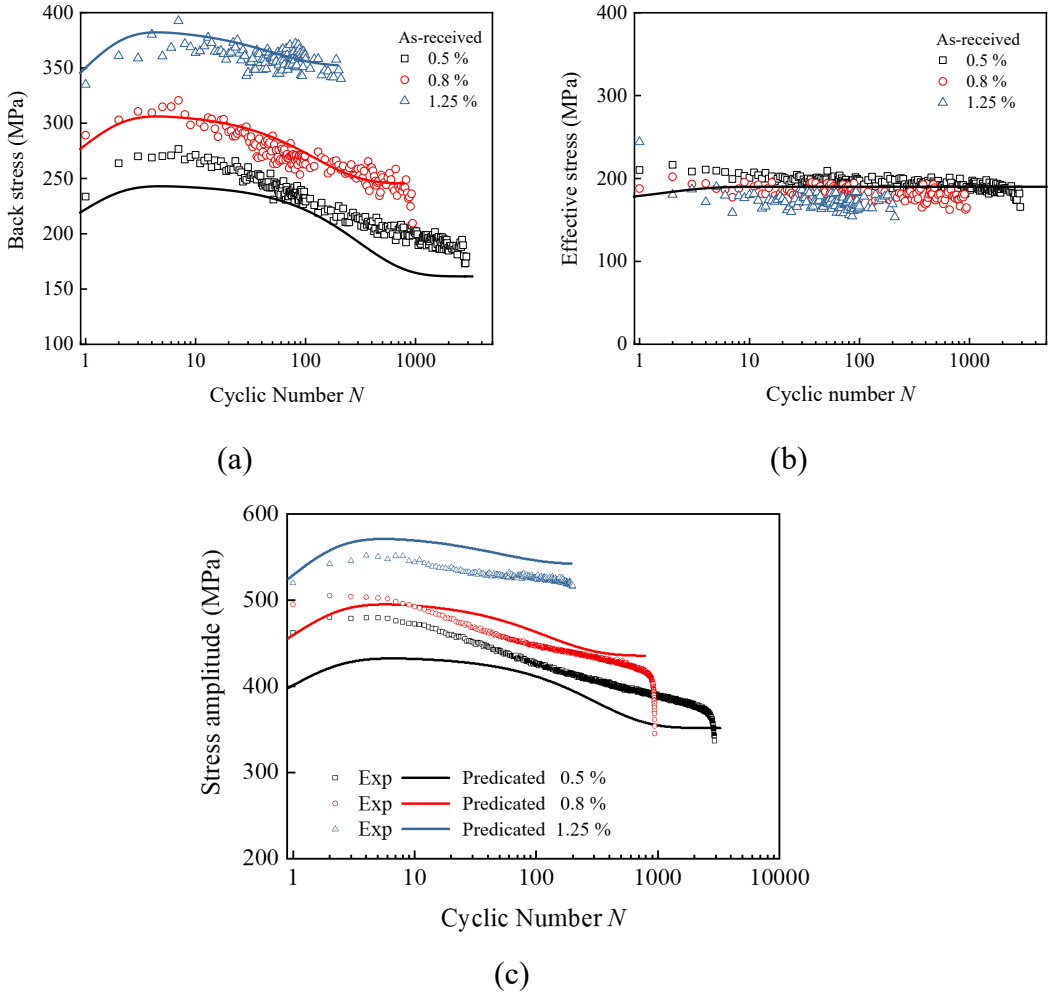

Fig. 6-3. (a) Back stress, (b) effective stress and (c) cyclic stress response versus cyclic number of as-received 316L SS with different strain amplitudes. Data points represent the experimental data obtained from the Chapter 3, while the solid lines indicate predicted curves.

6.3.2 Influence of grain size on cyclic deformation response

Strain-controlled fatigue testing was conducted on 316L SS samples with different grain sizes at room temperature conditions [278]. Due to material preparation constraints, data from the literature [278] with different grain sizes are referenced to verify the effect of grain size on fatigue performance by the model provided in Section 6.2. The varying grain sizes were obtained by heat treatment, resulting in sizes of 78.3 μm, 27.2 μm, 23.5 μm, 19.6 μm and 17 μm, accompanied by corresponding yield stresses (0.2% offset yield strength) of 214 MPa, 230 MPa, 240 MPa, 257 MPa, and 274 MPa, respectively. Fig. 6-4 shows the stress amplitude variation evolving with the

number of cycles at stress amplitude of 0.6%. Similar to other middle to high SFE stainless steels, the stress amplitude exhibits a pattern of initial strengthening, followed by softening, then reaching saturation, and ultimate fracture, as illustrated in Fig. 6-1. In addition, no secondary hardening is observed in the third stage of the cyclic deformation response in Fig. 6-4. Due to higher values of SFE and lower strain amplitudes, it can be inferred that the cyclic deformation behavior of this material is predominantly governed by dislocations, as discussed in Section 6.1. According to Eq. 6-3, the peak value of the inter-granular back stress, the degree of hardening, is determined by the difference between the dislocation densities ρ_b and ρ_i located at the grain boundaries, while the intra-granular back stress is calculated based on the dislocations ρ_w located at the walls/channels with Eq. 6-4. By incorporating grain size factors k_D in dislocation mean free path in Eq. 6-3, the effect of grain size on cyclic deformation response is considered, particularly for the back stress. As shown in Fig 6-5, the intra-granular back stress increases as grain size increases, whereas the inter-granular back stress decreases, as predicted by Eqs. 6-3 and 6-4. Coarse grains provide more space for the formation of heterogeneous dislocation structures. On the one hand, the increased space allows for a higher generation of internal dislocations and decreases the gradient with boundary dislocations, resulting in a decrease in inter-granular back stress as grain size increases. On the other hand, this additional space facilitates the rearrangement to form walls, thereby contributing to an increase in intra-granular back stress.

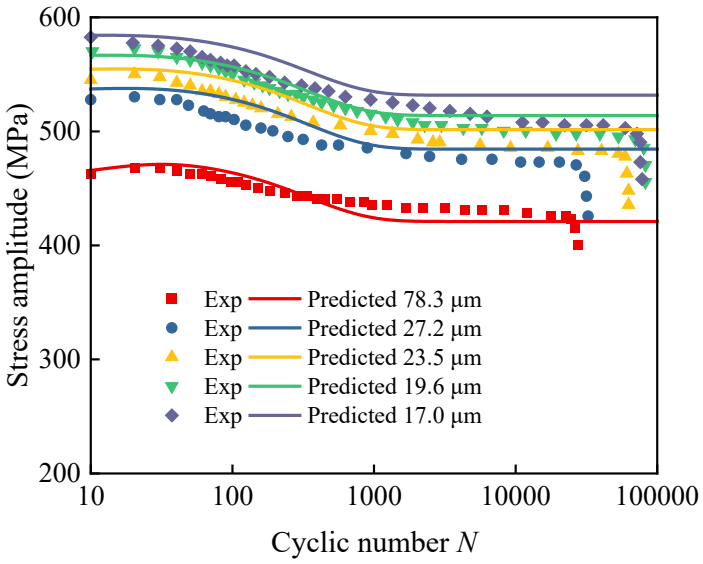

Fig. 6-4. Cyclic stress response with cyclic number of 316L SS with different grain sizes at a strain amplitude 0.6 %. Scattered data points represent experimental data obtained from the literature [278], while the solid lines indicate predicted curves obtained from the model.

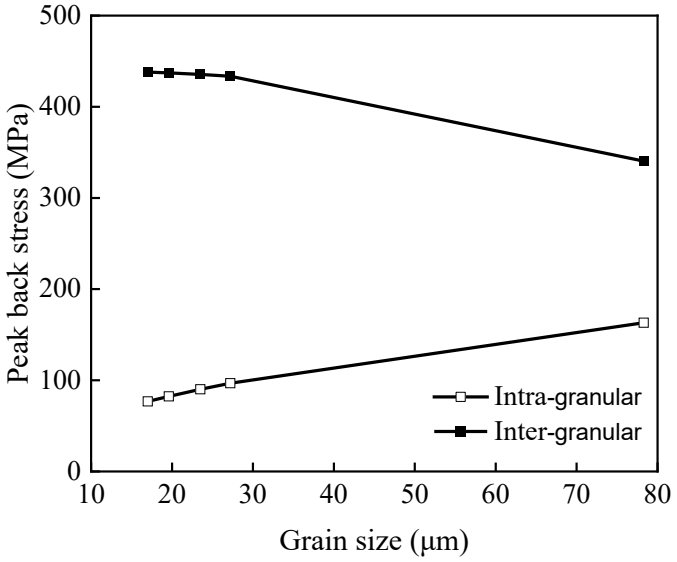

Fig. 6-5. Predicted values of inter-granular and intra-granular back stress at different grain sizes.

6.3.3 Effect of deformation twinning on cyclic deformation response

The experimental results from [265], strain-controlled LCF behavior of commercial pure titanium, is used in this section to investigate the effect of deformation twinning on cyclic deformation response. The low SFE of pure titanium results in the predominance of the twinning deformation mechanism during deformation. Combined with TEM and optical microscopy observations of dislocation patterns and deformation twins, the measured microstructural evolution provides a deeper understanding of the cyclic deformation response, particularly concerning deformation twinning. Fig. 6-6a and 6-6b illustrate the evolution of the twinning volume fraction with the cyclic number under different stress amplitudes. Fig. 6-6a shows that, similar to monotonic loading, there is a significant increase in the mechanical twinning at large strain amplitudes after LCF, with almost no deformation twinning observed at strain amplitudes of 0.5% and 0.75%. Fig. 6-6b clarifies that the twinning volume fraction increases with the cyclic

number, and mechanical twinning forms more rapidly at high strain amplitudes compared to low strain amplitudes.

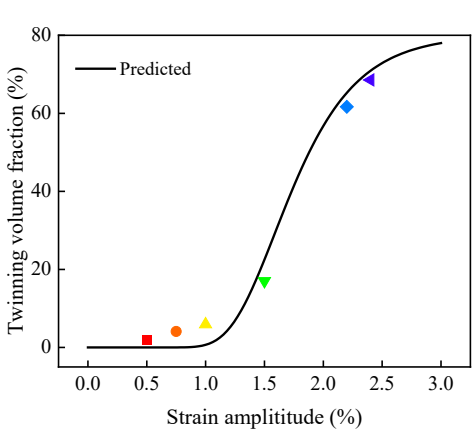

(a)

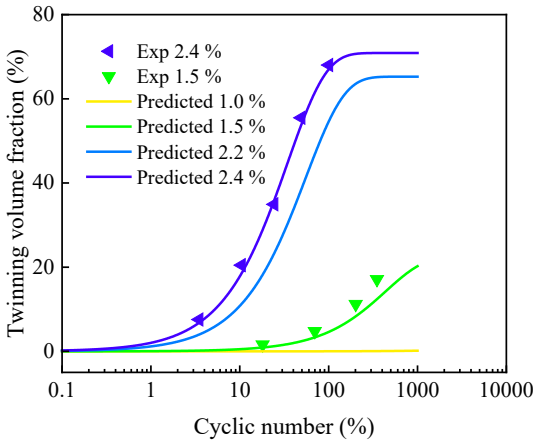

(b)

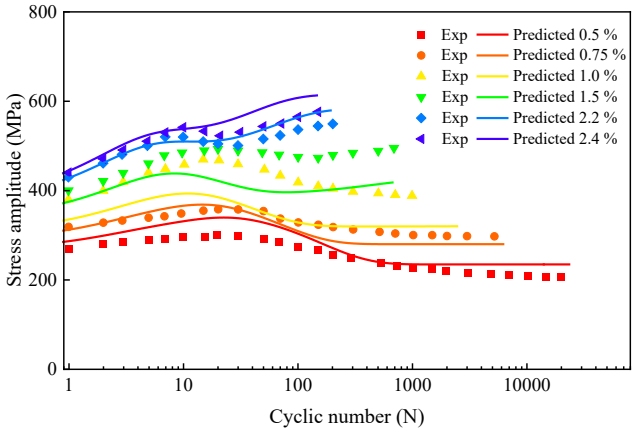

(c)

Fig. 6-6. (a) Twinning volume fraction of samples after fatigue for different strain amplitudes, (b) twinning volume fraction evolutions with cyclic number, (c) cyclic stress response versus cyclic number of commercial-purity titanium under different strain amplitudes. Scattered data points represent experimental data obtained from the literature [265], while the solid lines indicate predicted curves obtained from the model.

At lower strain amplitudes (0.5%, 0.75%, and 1%), the commercial-purity titanium initially exhibits hardening, followed by prolonged softening, saturation, and eventual failure, as plotted in Fig. 6-6c. In contrast, at higher strain amplitudes (1.5%, 2.2%, and 2.4%), significant secondary strengthening was observed during the third stage of the cyclic deformation response, with the TWIP strengthening effect increasing with higher

strain amplitudes. It is found that at low strain amplitudes and a low number of cycles, the material's deformation behavior is dominated by dislocations. Dislocation slip and secondary slip contribute to the initial hardening, while dislocation rearrangement and the formation of a stable dislocations structure contribute to the subsequent softening before saturation. Deformation twins are generated in large volume fraction at high strain amplitudes and at the end of the cycle, thereby dominating the cyclic deformation response.

6.3.4 Effect of gradient microstructure on cyclic deformation response

In Chapter 3, LCF experiments were conducted at room temperature on both the as-received and SMATed 316L SS. Comparison of the cyclic deformation response of the two materials reveals that the SMATed specimen exhibits higher initial hardening, particularly at low strain amplitudes in Fig. 3-3. This phenomenon has also been observed in IN718 [279] and CoCrFeMnNi [280] alloys (Fig. 6-7) with gradient microstructures.

Through SMAT, a gradient microstructure with a characteristic thickness is formed near the surface, characterized by nanograins on the surface. Chapter 2 explores the effect of SMAT on the material's microstructure, and the results show that the treated material inevitably introduces residual fields, including residual dislocation density, deformation twins, and residual stresses. In Chapter 5, the influence of SMAT and the accounting for these different residual fields on monotonic loading is analyzed by FE simulation. The results indicate that the SMATed material exhibits inhomogeneous deformation during tensile loading due to the gradient microstructure and residual fields introduced by SMAT. Due to its low yield strength, the central bulk region begins plastic deformation while the surface nanograins region remains in the elastic phase. It means that the coarse crystalline bulk located in the center of SMATed material experiences higher dislocation and interaction compared to the as-received counterpart. Therefore, it is reasonable to assume that the coarse crystalline bulk in the center contributes to the additional hardening at the initial stage. Notably, at high strain amplitude, the more uniform deformation of the SMATed material weaken the strengthening effect, explaining the cyclic stress response with a reduced strengthening at high strain amplitude.

It is worth noting that SMAT also impacts the softening phase, for example by

influencing residual dislocation density through rearrangement and the formation of dislocation structures. Additionally, nanograins introduce a different mechanism through rotational deformation. Due to this complexity of microstructural changes under fatigue loading in different regions of SMATed materials, further experimental validation would be required.

6.4 Conclusions

This chapter systematically addresses the influence of microstructural evolution of materials on complex cyclic deformation response. Specifically, it analyzes how different deformation mechanisms influenced by SFE, grain size, and strain amplitude, may affect the dislocation structure. Furthermore, a physical-based model is developed to investigate the effects of strain amplitude, grain size, and twinning on the cyclic deformation response. Based on the experimental results and analysis, several conclusions can be drawn as follows:

- The developed model can describe the cyclic hardening and softening response of 316L SS under LCF at various strain amplitude values.
- The effect of grain size on the cyclic deformation response, especially on the back stress, is considered by incorporating the effect of grain size into the intra-grain and inter-grain back stress.
- By studying of the LCF behavior of TWIP materials, it was found that the mechanical twinning increases with both the strain amplitude and the number of cycles. Deformation twins were scarcely observed at the beginning of cycling at low strain amplitudes. Deformation twins dominate the secondary strengthening phase at high strain amplitudes and at the end of cycling, and the strengthening effect increases with increasing strain amplitude. Control of secondary strengthening is achieved by adjusting the twinning volume fraction.
- Comparison of the cyclic deformation response of the as-received and SMATed materials reveals that the SMATed specimen exhibits higher initial hardening, particularly at low strain amplitudes. It is assumed that the inhomogeneous deformation introduced by the gradient structure causes the central bulk region of the SMATed material to experience higher dislocation densities, leading to a higher initial hardening. This point would require additional experiments to confirm.

Chapter 7: Conclusions and prospects

7.1 Conclusion

In this work, the uniaxial tensile and LCF behaviors of SMATed materials were investigated through experimental observation and modeling. The results indicate that the gradient microstructures introduced by SMAT significantly influence the macroscopic mechanical properties of the materials.

In Chapter 2, various characterization techniques, including EBSD, nanoindentation, and XRD, were used to analyze the microstructures, mechanical properties, and residual stresses in the SMATed 316L SS. The results showed that SMAT induces a gradient microstructure near the surface, as evidenced by variations in grain misorientation, microhardness, and residual stress distribution. Although the gradient microstructure was clearly observed, the formation of nanocrystalline grains was not clearly evident.

Subsequently, the LCF behavior of as-received and SMATed 316L SS samples was investigated both macroscopically and microscopically to understand the effect of SMAT on fatigue performance under different loading conditions, as done in Chapter 3. The results indicate that both as-received and SMATed samples undergo significant initial hardening followed by gradual softening during LCF, primarily due to the evolution of back stress. The SMATed samples exhibited higher back stress, suggesting a microstructural heterogeneity. EBSD observations highlighted the uniform distribution of plastic strain and dislocation structures, with no deformation twinning observed, but a notable presence of annealing twins. The evolution of GNDs and GOS during cyclic loading also suggests that GNDs play a crucial role in the internal stress evolution, influencing the back stress and the overall fatigue behavior.

In Chapter 4, a grain size-dependent dislocation density-based constitutive model, incorporating SFE, is developed to explore the influence of deformation mechanisms on the tensile behavior. Lower SFE in 304 SS enable to test our complete model, because it facilitates martensitic transformation and mechanical twinning by reducing the critical shear stress and increasing nucleation rates, particularly in larger grains. These microstructural changes play a significant role in the macroscale response under uniaxial loading. In addition, the interaction between SFE, grain size, and nucleation dynamics is critical in predicting the tensile behavior of 304 SS. Different stages of

deformation are controlled by microstructural evolution, such as dislocation activities, twinning, and martensitic transformation. Initially, dislocation motion governs the deformation behavior. As deformation progresses, the increasing volume fractions of ε-martensite and twin crystals increase strength through the TWIP and TRIP effects, respectively. Further strain leads to additional martensitic transformation, resulting in a further increase in material strength.

The simulations in Chapter 5 show the effect of the GMS on the macroscopic mechanics by analyzing the microstructural changes at different depths during uniaxial strain. The FE model is built by integrating depth-dependent initial residual fields, including grain size, residual stress, dislocation density, and twinning. This point is quite innovative as compared to the existing modeling, and allows to improve the accuracy of the simulations. Compared with experimental observations, the developed FE model accurately predicts the tensile properties of SMATed 316SS. The SMATed sample exhibits inhomogeneous deformation under tensile loading, with coarse bulk grains initiating plastic deformation while the nanocrystallized surface grains remain predominantly elastic. At low strain levels, the bulk coarse grains accommodate most of the external deformation. In addition, dislocation densities and twin volume fractions in layers of different grain sizes increase rapidly during tensile loading and gradually reach saturation. A detailed analysis of the local and global tensile behavior also revealed that the surface compressive residual stress generated by SMAT significantly reduces the yield strength at the initial stage of deformation. However, as the deformation progresses, the influence of residual stresses diminishes due to their internal equilibrium, and their effect further decreases with depth due to the gradient nature of the stress.

In Chapter 6, a dislocation density-based model is established to describe the microstructural evolution of materials under complex cyclic deformation, considering the influence of SFE, grain size, and strain amplitude on the dislocation structures. The proposed model effectively captures the cyclic hardening and softening behavior of 316L SS (SMATed or as-received) under LCF with varying strain amplitudes. The inclusion of grain size in the model, particularly in the intra-grain and inter-grain back stress components, successfully accounts for its impact on cyclic deformation. In TWIP materials, mechanical twinning was found to increase with strain amplitude and cycle number. Deformation twins, which are initially rare at low strain amplitudes, become dominant in the secondary strengthening phase at high strain amplitudes, enhancing the

overall strengthening effect. Comparing the cyclic deformation responses of as-received and SMATed materials, the SMATed specimens exhibited higher initial hardening, particularly at low strain amplitudes. This is attributed to the inhomogeneous deformation in the gradient structure, which leads to increased dislocation densities in the central bulk region, resulting in higher initial hardening.

7.2 Prospects

There are still many interesting points to be carried out by experiments. In this work, an attempt is made to measure the residual stress field in 316L SS after SMAT by using the grazing incidence XRD method. The penetration depth was correlated with the absorption coefficient of the X-ray source, but due to limitations of the material used for the X-ray target, the residual stresses at different locations could not be measured. Further research would be interesting to determine the residual stresses of the SMATed specimen using non-destructive methods, which would reduce the release of residual stresses caused by the destructive experimental preparation process. In addition, macroscopic residual stresses and microstructures, such as dislocations and twins, coexist in SMAT samples. To accurately study these microstructural features, more precise characterization methods, such as TEM, are recommended. This approach allows for a more accurate analysis of the effects of residual stresses in SMAT samples at different scales. In addition, Young's modulus exhibits fluctuation and remains stable with increasing depth. For comparison, conducting the nanoindentation measurement on an as-received sample would have been valuable.

In fatigue testing, measurements at different numbers of cycles are used to approximate the evolution of microscopic features and macroscopic behavior throughout the LCF process. Ideally, in-situ EBSD testing should be performed to document the deformation process (both tensile and compressive) and its evolution with the number of fatigue cycles, providing valuable insights into the deformation mechanisms of LCF. Additionally, TEM should be used to observe potential microstructural changes at various cycle numbers and tensile-compression loading, particularly focusing on grain boundary slip, grain boundary shear, and grain boundary dislocation emission. In tensile experiments on SMATed specimens, it was found that the deformation behavior varied in different regions, especially for nanocrystalline and coarse-crystalline regions. This suggests that the microstructures in these regions must

be different during the tensile-compression fatigue process. This fatigue testing and in-situ observation of different regions can provide a better understanding of the LCF performance of SMATed specimens.

Extensive research has been conducted on SMATed specimens under uniaxial tension and fatigue. Notably, experimental observations indicate that the gradient microstructural field introduced by SMAT is mainly distributed along the radial direction, which is perpendicular to the axial loading direction. This directional inconsistency may lead to an offset or a synergistic enhancement between SMAT-induced strengthening and loading-induced work hardening. Therefore, it would be of great value to investigate the effects of multi-axial loadings on the mechanical properties of SMATed sample.

In addition, several modeling approaches need further improvement. In Chapter 4, a dislocation density-based model is introduced to analyze the mechanical properties and microstructural evolution under uniaxial loading, where the initiation of twinning and phase transformation is calculated using an energy-based method and considering grain size. The dislocation density-based internal stress model developed in Chapter 6 integrates the microstructural evolution over different fatigue cycle numbers and correlates it with strain amplitude, twinning, and grain size. In contrast to crystal plasticity models, these phenomenological models used in this work directly employ physical equations to calculate macroscale mechanical behavior. This saves time but has certain limitations, and corresponds to the mean field approach. For instance, it cannot separately account for information on each slip system or consider misorientation and texture. This should be done by down-scaling to slip systems. A key difference between the models is that uniaxial loading (Chapter 4) calculates mechanical properties and microstructural evolution are calculated based on plastic strain, whereas LCF (Chapter 6) calculates it based on cycle number. Therefore, the development of a numerical framework that combines both uniaxial loading and fatigue models would be beneficial, particularly by linking the cycle number to accumulated plastic strain.

Regarding the multi-scale transition, the core idea of the models in Chapters 4 and 6 are to translate factors (such as twinning and grain size) into changes in dislocation density. However, this approach does not directly address how these changes in grain structure affect macroscopic properties. Additionally, this dislocation density-based model is not compatible with the mechanical properties at the nanoscale, where grain

deformation is governed not by dislocations but by grain rotation. Therefore, it would be valuable to develop an improved multi-scale model that accounts for the scaling effects as the grain size ranges from the nanoscale to the macroscale.

Résumé en français

1 Introduction

Le traitement de grenaillage par ultrason (SMAT), un type de méthode par déformation plastique sévère (SPD), permet de former une couche à gradient de microstructure (GMS) à la surface des matériaux, ce qui améliore significativement les propriétés mécaniques globales telles que la limite d'élasticité et la résistance à la fatigue. Ce traitement provient du procédé conventionnel de grenaillage, mais implique des directions aléatoires et un impact à haute fréquence de billes, généré par un générateur de vibrations à travers une membrane vibrante appelée sonotrode. L'échantillon est placé dans une chambre et est impacté de manière répétée par les billes. La déformation et la vitesse de déformation élevées sont induites par chaque impact dans la couche à la surface de l'échantillon. Par conséquent, les impacts multidirectionnels répétés avec SPD conduisent à la formation d'une nanocristallisation de surface et à une augmentation notable de la limite d'élasticité. En effet, les métaux nanocristallins, caractérisés par une taille de grain moyenne inférieure à 100 nm, présentent généralement des propriétés remarquables en raison d'une proportion accrue de joints de grains, bien que cela s'accompagne souvent d'une ductilité réduite. Comme mentionné ci-dessus, les grains micrométriques des matériaux sont affinés à l'échelle nanométrique sur la couche de surface supérieure sans modifier leur composition chimique grâce au SMAT. Donc la nanocristallisation de surface induite par la déformation plastique est cruciale pour comprendre et développer le SMAT.

Grâce au SMAT, une distribution de la taille des grains allant de l'échelle nanométrique à plusieurs microns est ainsi générée le long de la profondeur, de la surface supérieure vers l'intérieur des échantillons traités. Généralement, les grains affinés et les grandes quantités de dislocations sont deux sources majeures de renforcement dans les matériaux GMS à énergie de défaut d'empilement (SFE) élevée. Pour les matériaux à faible SFE, le maclage de déformation et la transformation de phase ont également été observés dans les échantillons traités par SMAT, car ils peuvent affecter de manière significative le comportement mécanique par les effets de plasticité induite par maclage (TWIP) ou plasticité induite par transformation de phase (TRIP). Il a été découvert que les limites des macles peuvent efficacement entraver le

mouvement des dislocations, ce qui entraîne leur accumulation aux limites des macles dans les matériaux TWIP. Ainsi, les macles de déformation accompagnées de dislocations contribuent à une résistance plus élevé dans les matériaux traités par SMAT.

Parallèlement, des contraintes résiduelles de compression élevées sont inévitablement introduites dans la partie proche de la surface lors du processus SMAT, ce qui peut empêcher l'initiation et la propagation des fissures. La profondeur et les valeurs de la contrainte résiduelle maximale de compression sont sensibles aux paramètres du SMAT.

Des mesures des propriétés mécaniques des matériaux SMAT ont indiqué que la couche de surface nanostructurée et les microstructures à gradient peuvent augmenter significativement la résistance à la traction. Avant la fracture, plusieurs mécanismes de durcissement agissent collectivement pour produire un fort écrouissage en termes de comportement mécanique. Un changement en trois étapes est généralement visible dans les courbes contrainte-déformation. Au cours du premier stade de déformation, une diminution significative du taux d'écrouissage est observée, caractérisée par une faible contrainte d'écoulement, qui est attribuée au glissement des dislocations planes et à la formation de la martensite ε. Le deuxième stade commence par une augmentation rapide du taux d'écrouissage, entraînée par le maclage mécanique induit par la déformation et à la transformation martensitique induite par la déformation. Le dernier stade montre une diminution du taux d'écrouissage qui est attribuée à la saturation des effets TWIP et TRIP avec l'augmentation de la déformation, ainsi qu'à la restauration dynamique des dislocations. Lors du chargement en traction, la déformation se propage vers l'extérieur des gros grains cristallins à cœur (CG) vers les grains nanocristallins en surface. Les incompatibilités mécaniques au sein de la partie affectée par le SMAT près de la surface peuvent générer un gradient de déformation important, ce qui conduit par conséquence à un niveau élevé de dislocations géométriquement nécessaires GND pour s’adapter à la déformation.

Le SMAT fournit également une stratégie de renforcement structurel pour améliorer les propriétés de fatigue des matériaux. Les tests de fatigue ont montré que la durée de vie et la résistance à la fatigue des échantillons SMATés sont considérablement améliorées par rapport aux échantillons bruts de traitement dans les régimes de fatigue à faible nombre de cycles (LCF) et à haut nombre de cycles (HCF).

Les améliorations du comportement en fatigue sont attribuées à l'effet combiné des contraintes résiduelles de compression, de l'écrouissage, de la microstructure à gradient et de la couche de surface nanostructurée. La couche nanostructurée induite par la déformation plastique sévère et se superposant aux contraintes résiduelles de compression élevées renforcent la surface, ce qui peut notamment améliorer efficacement la résistance à la fatigue. De plus, la fraction volumique élevée des joints de grains peut résister au glissement des dislocations et ainsi empêcher la nucléation des fissures. D'autre part, une grande quantité de parois de dislocations, d'enchevêtrements de dislocations, de macles et de sous-grains dans la zone intermédiaire peut également contraindre la croissance des fissures et diminuer la vitesse de propagation des fissures dans une telle zone. Cependant, il est rapporté que les microfissures à la surface et les contraintes résiduelles de traction élevées en sous couche induites par un traitement SMAT de haute intensité peuvent diminuer les performances de fatigue en termes d'initiation des fissures dans le régime de fatigue à très haut nombre de cycles (VHCF).

La réponse à des contraintes cycliques en termes de contrainte interne (c'est-à-dire les contraintes effectives de friction et les contraintes de retour) est utile pour analyser la relation avec la microstructure et pour construire des modèles numériques avec des modèles de durcissement isotrope et cinématique. Pour élucider les différents mécanismes de déformation de l'adoucissement/durcissement cyclique, les évolutions de la contrainte de retour et de la contrainte effective sont séparées et analysées en utilisant les boucles d'hystérésis générées lors de la sollicitation. Au début du chargement cyclique, les dislocations (principalement de type GND) s'accumulent à proximité des joints de grains pour adapter la déformation plastique entre les grains. Pendant le stade de durcissement cyclique, la densité de dislocations à l'intérieur des grains augmente avec la déformation plastique, réduisant ainsi le gradient de densité de dislocations à l'intérieur des grains. De plus, l’activité de glissement secondaire conduit à une augmentation des dislocations et à une distribution plus uniforme des dislocations à l'intérieur des grains. Dans le stade d'adoucissement suivant, lorsque les dislocations deviennent plus denses à l'intérieur des grains, les dislocations commencent à se réorganiser pour former une fragmentation des grains (cellules de dislocations, structure cellulaire, parois de dislocation), ce qui permet de relâcher la contrainte de retour intergranulaire.

La modélisation numérique d'un tel processus est complexe, impliquant une déformation plastique sévère localisée en surface et un raffinement des grains sous des contraintes élevées et des taux de déformation élevés (au moins de l'ordre de 10^4 s^{-1}), en raison des impacts multidirectionnels sur la surface du matériau par les billes. La méthode des éléments finis (FEM) est largement appliquée dans la modélisation numérique du comportement mécanique des matériaux lors du traitement, de la fabrication et de l'exploitation. Des modèles de simulation dépendants de la taille des grains et basés sur les dislocations peuvent être raisonnablement proposés pour tenir compte de l'évolution de la microstructure des matériaux SMATés. À l'échelle mésoscopique, la méthode des éléments finis en plasticité cristalline (CPFEM) est également employée pour étudier les réponses mécaniques des matériaux à gradient de microstructure. D'une part, pour formuler davantage les relations entre la microstructure et la réponse mécanique macroscopique, des modèles multiéchelles combinant CPFEM pour le processus SMAT peuvent être envisagés. Les éléments représentatifs de volume dans le CPFEM permettent de calculer un comportement macroscopique précis et offrir une compréhension fine et détaillée de l'état des microstructures, y compris la taille des grains, les joints de grains et les macles. D'autre part, les modèles de plasticité à gradient de déformation basés sur des mécanismes conventionnels (CMSG) ont la capacité de construire directement une réponse multi-échelle moyennée des matériaux basée sur des équations expérimentales physiques, sans détailler l'ensemble de la géométrie de la microstructure. C'est cette seconde approche que nous avons choisi de mettre en œuvre.

2 Caractérisation des matériaux

2.1 Préparation des matériaux et procédé SMAT

L'acier inoxydable 316L (316L SS), utilisé dans la présente recherche, a la composition chimique suivante (en % en poids) : 0,013 C, 1,70 Mn, 0,26 Si, 0,017 P, 0,003 S, 17,37 Cr, 14,52 Ni, 2,8 Mo, 0,08 Cu, 0,88 N, <0,005 Ti, 0,07 V, et le reste en Fe. Avec une SFE allant de 31,9 à 38,12 mJ/m², ce 316L SS peut être classé comme ayant une SFE moyenne à élevée ou modérée. Des échantillons cylindriques ont été usinés avec un diamètre de jauge de 6 mm et une longueur de jauge de 12 mm. L'échantillon est positionné dans une chambre cylindrique qui peut tourner autour de l'axe central à une vitesse constante, entraînée par un moteur électrique. À l'intérieur de la chambre, des billes d'acier d'un diamètre de 3 mm et d'une masse de 20 g sont

enfermées. L'échantillon est situé à 12 mm de la plate-forme vibrante, appelée sonotrode, qui est amplifiée par un dispositif générateur de vibrations ultrasoniques à une fréquence élevée de 20 kHz. Par conséquent, toute la section utile de l'éprouvette subit de multiples impacts aléatoires à haute déformation et à un taux de déformation élevé, en raison de la rotation de l'échantillon et des impacts des billes d'acier. Dans cette étude, le processus SMAT a été débuté avec une durée de 15 minutes à une faible puissance de générateur (30 % de l'amplitude maximale), suivie d'une période supplémentaire de 5 minutes à une puissance de générateur plus élevée (50 % de l'amplitude maximale).

2.2 Caractérisation de la microstructure par observations EBSD

La Fig. 2-10a illustre la distribution en coupe transverse des dislocations géométriquement nécessaires (GND) pour les échantillons de 316L SS bruts et traités par SMAT, respectivement. Près de la surface traitée, on observe une augmentation correspondante de la densité de GND dans les deux échantillons. Comparé à l'échantillon brut, l'échantillon traité par SMAT présente une région GND plus épaisse, avec une diminution progressive des GND de 9 à environ 126 μm. Les courbes de la Fig. 2-10b représentent la densité moyenne de GND en fonction de la profondeur, calculée à partir de la valeur moyenne de GND à la même profondeur. Notamment, pour l'échantillon traité par SMAT, la densité moyenne de GND connaît initialement une croissance rapide, atteignant une valeur maximale de 250×10^{12} /m² à 35 μm, avant de diminuer progressivement pour revenir au niveau initial de $87{,}5 \times 10^{12}$ /m² à 125 μm.

(a)

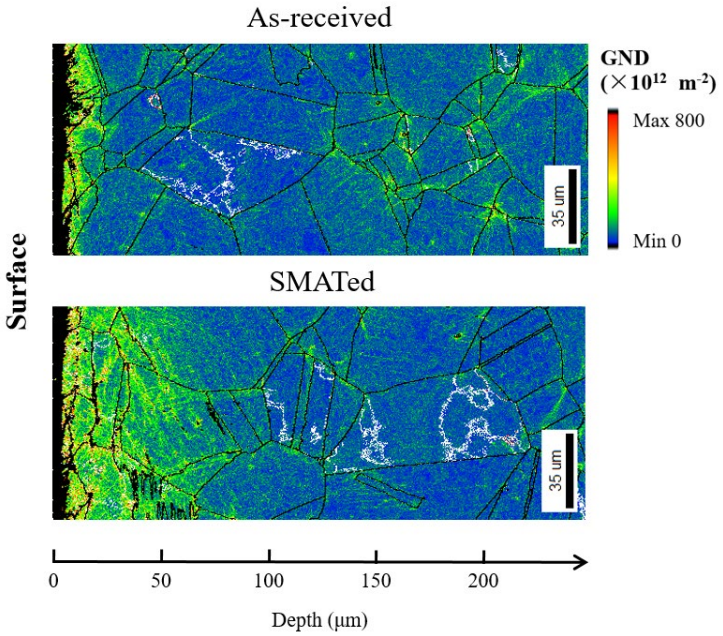

(b)

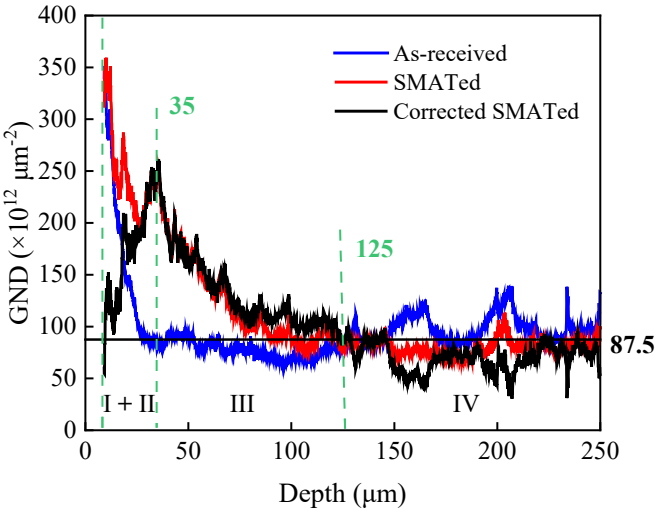

Fig. 2 10. (a) Cartes GND de la section transversale et (b) distribution GND moyenne en fonction de la profondeur des échantillons bruts et traités au SMAT, avec et sans correction de la préparation de l'échantillon.

2.3 Mesure de la dureté et du module d'Young par nanoindentation

Pour déterminer le gradient de microdureté et le module de Young induits par le SMAT, des mesures sont effectuées à différentes profondeurs : 5 µm, 10 µm, 15 µm, 20 µm, 40 µm, 80 µm, 100 µm, 300 µm et 500 µm. Il est à noter que, pour éviter les

effets de bord et la déformation induite par la découpe, la profondeur minimale commence à 5 µm. De plus, cinq indentations sont réalisées pour chaque distance afin de minimiser les erreurs de mesure. Tous les tests d'indentation instrumentée ont été réalisés à l'aide du Nanoindenter®XP équipé d'un pénétrateur Berkovich. La profondeur maximale de pénétration est de 500 nm.

La Fig. 2-14a présente la variation en fonction de la profondeur de la dureté dans la région proche de la surface pour les échantillons traités par SMAT. Elle montre que la dureté près de la surface traitée présente une augmentation notable, avec des valeurs maximales atteignant environ 5,6 GPa, diminuant progressivement pour atteindre environ 3,5 GPa. Il est intéressant de noter qu'il existe un plateau de haute microdureté, s'étendant approximativement jusqu'à une profondeur de 40 µm. La Fig. 2-14b montre la variation en fonction de la profondeur du module de Young pour les échantillons traités par SMAT. On peut voir que le module de Young des échantillons traités par SMAT reste presque constant avec de faibles fluctuations, environ autour de 200 GPa le long de la profondeur, mais qui reste dans le même ordre de grandeur que les incertitudes.

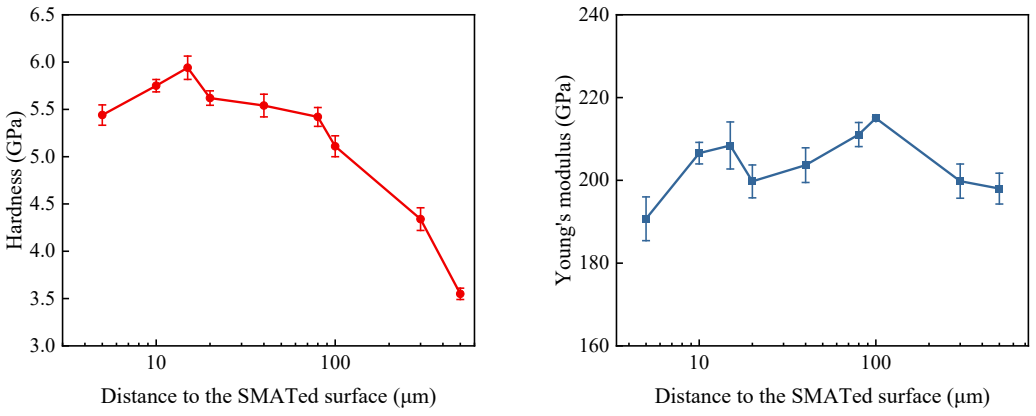

(a) (b)

Fig. 2-14. Variation en fonction de la profondeur à partir de la surface traitée pour les échantillons traités par SMAT : (a) Dureté et (b) Module d'Young.

2.4 Analyse des contraintes résiduelles par diffraction des rayons X à incidence rasante

La méthode $\sin^2\psi$ est un outil intéressant pour l'analyse des contraintes résiduelles. Sur cette base, la méthode d'incidence rasante offre une approche non destructive pour déterminer les contraintes résiduelles à différentes profondeurs de pénétration sous la

surface de l'échantillon en modifiant l'angle d'incidence α. Le faisceau diffracté provient de toute la profondeur de pénétration atteinte par le faisceau incident. Cette profondeur de pénétration moyenne peut être déterminée comme suit [173], [174] :

$$p(\alpha) = \frac{\beta}{\mu\rho}\left(\frac{1}{\sin\alpha} + \frac{1}{\sin(2\theta-\alpha)}\right)^{-1} \quad \text{(Eq. 2-5)}$$

où α est l'angle entre le faisceau et la surface de l'échantillon ; θ est l'angle de Bragg ; μ est le coefficient d'absorption spécifique dépendant du matériau et de la longueur d'onde utilisée pour les photons X ; β est un coefficient sans dimension, qui dépend de la moyenne considérée. Il est important de noter que ψ est défini comme la différence entre l'angle de Bragg et l'angle d'incidence, soit $\psi = \theta - \alpha$. Divers angles d'incidence α (3, 5, 7, 9, 11 ou 15°) ont été choisis pour obtenir différentes profondeurs de pénétration. De plus, pour déterminer les différentes composantes du tenseur des contraintes, chaque mesure de XRD est effectuée pour chaque angle d'incidence (et donc pour chaque profondeur) pour trois orientations φ: 0, 45 et 90°. La position moyenne correspondante représente la valeur moyenne de la profondeur z sur l'épaisseur, pondérée par un facteur d'atténuation [174] :

$$\bar{Z} = \frac{\int_0^L z e^{-z/p} dz}{\int_0^L e^{-z/p} dz} = \begin{cases} p & for\ L\to\infty \\ p - \frac{p e^{-\frac{L}{p}}}{1-e^{-\frac{L}{p}}} = p\left(\frac{1-2e^{-\frac{L}{p}}}{1-e^{-\frac{L}{p}}}\right) & for\ finite\ L \end{cases} \quad \text{(Eq. 2-6)}$$

La déformation moyenne du réseau ε peut être déterminée à partir de la distance interréticulaire d_{hkl} mesurée dans la direction du vecteur de diffusion, reliée à la position du pic de diffraction pour un angle de Bragg θ et à l'angle d'incidence α. Pour un angle d'incidence donné α, correspondant à une position moyenne $\bar{Z}$ de la quantité mesurée, nous pouvons utiliser plusieurs ψ et différentes orientations φ. La déformation moyenne du réseau $\bar{\varepsilon}$ correspond à une moyenne sur la profondeur, pondérée par un facteur d'atténuation, et est reliée à la distance interréticulaire moyenne $\bar{d}_{hkl}$ selon la relation suivante pertinente pour les déformations finies :

$$\bar{\varepsilon}\left(\varphi, \psi = \theta(hkl) - \alpha, \bar{Z}\big(p(\alpha)\big)\right) = \ln\left(\frac{\bar{d}_{hkl}(\varphi,\psi,\bar{Z})}{d^0_{hkl}}\right) \quad \text{(Eq. 2-7)}$$

avec d^0_{hkl} l'espacement des plans réticulaires, libre de contrainte. La contrainte peut alors être évaluée en mesurant les différents angles de Bragg des pics sélectionnés, le long de la direction du vecteur de diffusion pour le ψ correspondant, et pour différentes orientations φ. En effet, selon la loi de Bragg et à partir du modèle de Hooke adapté ici pour les matériaux isotropes [176], [177], nous pouvons écrire :

$$\bar{\varepsilon}(\varphi,\psi,\bar{Z}) = \ln\left(\frac{\sin\theta_0}{\sin\theta}\right) = \ln\left(\frac{1}{\sin\theta}\right) - \ln\left(\frac{1}{\sin\theta_0}\right) = S^1_{\{hkl\}}(\bar{\sigma}_{11} + \bar{\sigma}_{22} + \bar{\sigma}_{33}) + \frac{1}{2}S^2_{\{hkl\}}\bar{\sigma}_{33}\cos^2\psi + \frac{1}{2}S^2_{\{hkl\}}(\bar{\sigma}_{13}\cos\varphi + \bar{\sigma}_{23}\sin\varphi)\sin 2\psi + \frac{1}{2}S^2_{\{hkl\}}(\bar{\sigma}_{11}\cos^2\varphi + \bar{\sigma}_{22}\sin^2\varphi + \bar{\sigma}_{12}\sin 2\varphi)\sin^2\psi \quad \text{(Eq. 2-8)}$$

où $\bar{\sigma}_{ij}$ sont les composantes moyennes de la contrainte macroscopique ; $S^1_{\{hkl\}}$ et $S^2_{\{hkl\}}$ sont les coefficients élastiques radio-cristallographiques calculés pour différentes réflexions ou familles de plans {hkl}.

La Fig. 2-19a présente la distribution des contraintes des échantillons traités par SMAT à des profondeurs allant de 0,5 à 2,3 µm, correspondant aux 6 valeurs choisies des angles d'incidence. On peut observer que les contraintes pour les composantes 11 et 22 présentent une évolution en compression, similaire en fonction de la profondeur. La composante 12 est proche de 0 aux différentes profondeurs. Nous pouvons en conclure qu'il s'agit d'un état de contrainte isotrope dans le plan pour l'échantillon traité par SMAT. Il est également observé que les contraintes maximales (en valeurs absolues) des composantes 11 et 22 sont respectivement de 392,5 ± 119,6 MPa et 421,8 ± 142,9 MPa. Ces contraintes de compression significatives à la surface sont en accord avec la variation observée des contraintes résiduelles en utilisant une méthode de retrait chimique étape par étape. Il est important de noter les grandes valeurs d'erreur des contraintes pour les échantillons traités par SMAT ou pour la poudre de Fe permettant de calibrer l'essai, qui sont associées à l'incertitude sur les positions des pics, comme le montre la Fig. 2-19. Finalement, pour les composantes 11 et 22, l'évolution spatiale de la contrainte est relativement constante dans la plage d'observation. Cette plage de profondeur limitée des mesures est due aux bornes que l'on s'est fixées sur l'angle d'incidence pour avoir une mesure interprétable, ce qui limite l'observation d'un quelconque gradient caractéristique de la présente microstructure dans les résultats de contrainte mécanique.

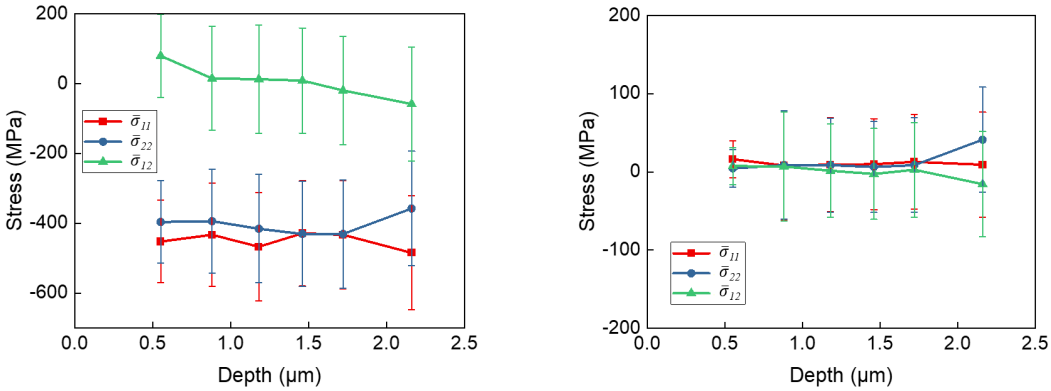

Fig. 2-19. Variations des différentes composantes des contraintes à proximité de la surface de (a) échantillons traités par SMAT et (b) poudre de Fe par définition libre de contrainte.

3 Étude expérimentale du comportement en fatigue à faible nombre de cycles (LCF) de l'acier inoxydable 316L traité par SMAT

3.1 Procédures expérimentales pour les tests de fatigue

Une description détaillée de la préparation des matériaux et des processus SMAT est fournie au chapitre 2. Les tests de fatigue à faible nombre de cycles (LCF) contrôlés par déformation ont été réalisés à l'aide d'un système de test servo-hydraulique à température ambiante. Trois amplitudes de déformation différentes, 0,5 %, 0,8 % et 1,25 %, ont été appliquées à un taux de déformation constant de 4×10^{-3} s^{-1}. Les deux types de chargement, traction/compression uniaxiale (rapport de charge R = -1) et chargement asymétrique (rapport de charge R = -0,5), ont été utilisés pour les échantillons bruts ou traités par SMAT. Après le test LCF, quatre nombres de cycles différents (échantillon brut, 4ème, 20ème et dernier cycle avant rupture) ont été choisis pour l'évaluation des changements microstructuraux par EBSD, en se basant sur les caractéristiques de la variation de l'amplitude de contrainte en fonction du nombre de cycles.

3.2 Comportement en déformation cyclique sous chargement symétrique dans des conditions de LCF

Les courbes d'hystérésis offrent une représentation visuelle des propriétés de déformation cyclique des matériaux. On peut aussi visualiser les amplitudes de contrainte en fonction du nombre de cycles, comme sur la Fig. 3-3, pour les échantillons bruts et traités par SMAT, sur une échelle semi-logarithmique. D'une part, les résultats révèlent globalement que l'amplitude de contrainte augmente avec les amplitudes de déformation dans les différents échantillons. Comparativement aux échantillons bruts, les résistances à la fatigue des échantillons traités par SMAT sont significativement améliorées pour chaque amplitude de déformation pendant le processus LCF. De plus, les durées de vie en fatigue des échantillons traités par SMAT sont nettement supérieures à celles des échantillons bruts. D'autre part, un durcissement significatif est observé lors des cycles initiaux, tant pour les échantillons bruts (jusqu'au quatrième cycle) que pour les échantillons traités par SMAT (jusqu'au troisième cycle). Un adoucissement progressif se produit ensuite à mesure que le chargement cyclique se poursuit, sans qu'aucun stade de saturation ne soit atteint avant la rupture finale, comme le montre la Fig. 3-3. Il est à noter que l'évolution de l'amplitude de contrainte présente un adoucissement marqué à la fin pour les échantillons traités par SMAT et bruts, à l'exception de l'échantillon brut à l'amplitude de déformation spécifique de 1,25 % (courbes en triangle bleu dans la Fig. 3-3a), qui semble rester quasiment constante jusqu'à la rupture.

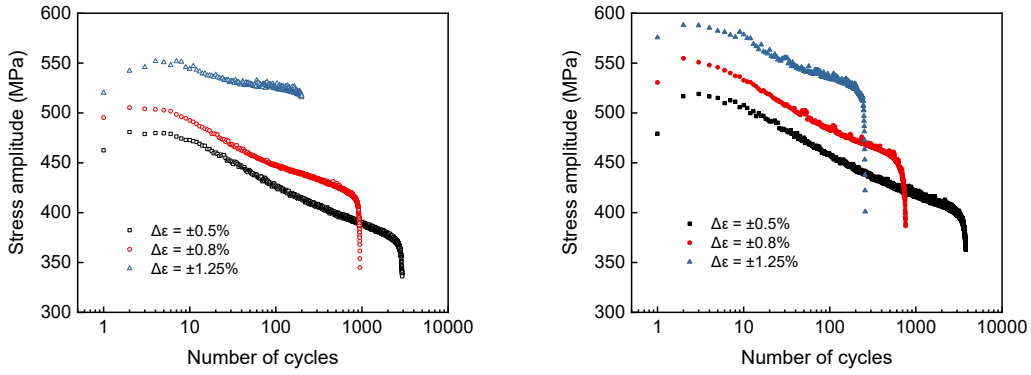

Fig. 3-3. Amplitude de contrainte en fonction du nombre de cycles pour (a) les échantillons 316L SS bruts et (b) les échantillons traités par SMAT, aux amplitudes de déformation de 0,5 %, 0,8 % et 1,25 % sous chargement symétrique (rapport de charge R = -1). Notez que le nombre de cycles est représenté sur une échelle logarithmique.

Pour caractériser davantage le comportement cyclique en LCF, la méthode de Cottrell est utilisée pour extraire l'évolution de la contrainte effective de friction et de la contrainte de retour à partir des boucles d'hystérésis. La Fig. 3-5 présente les évolutions de la contrainte effective et de la contrainte de retour avec la déformation plastique cumulée pour les échantillons 316L bruts et traités par SMAT. On peut voir dans la Fig. 3-5b que la contrainte effective présente une tendance à la diminution avec l'augmentation de la déformation plastique cumulative, tant pour les échantillons bruts que pour les échantillons traités par SMAT. De plus, la réduction de la contrainte effective s'amplifie avec des niveaux de déformation plus élevées. Les échantillons traités par SMAT montrent un adoucissement plus faible par rapport aux échantillons bruts. Une légère augmentation de l'intensité de la contrainte de retour est observée à faible déformation plastique cumulée pendant la phase initiale de fatigue, puis diminue progressivement jusqu'à la fin du chargement en fatigue, comme le montre la Fig. 3-5b. Comparés aux échantillons bruts, les échantillons traités par SMAT présentent systématiquement une contrainte de retour plus élevée pour toutes les amplitudes de déformation en LCF. Les résultats indiquent que le SMAT favorise la contrainte de retour, augmentant systématiquement au cours de la déformation cyclique.

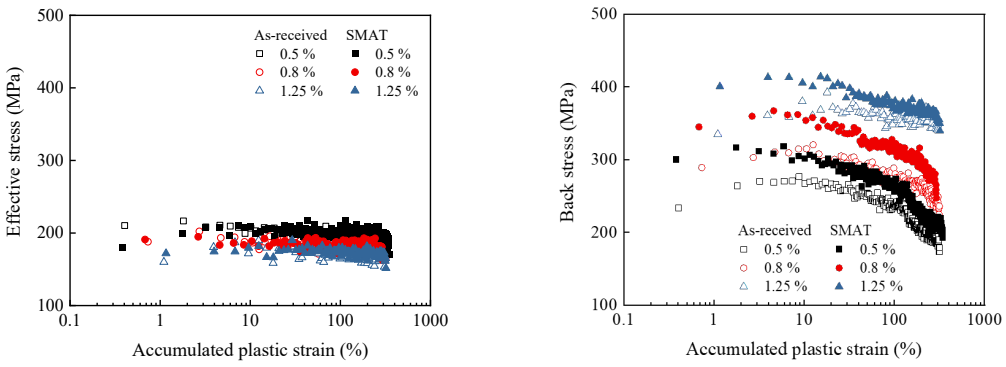

(a) (b)

Fig. 3-5. Comparaison des évolutions de (a) la contrainte effective et (b) la contrainte de retour en fonction de la déformation plastique cumulée, entre les échantillons 316L bruts et les échantillons traités par SMAT.

3.3 Effet du chargement asymétrique sur le comportement en LCF

De manière similaire, un durcissement significatif se produit au stade initial et s'adoucit progressivement jusqu'à la rupture sous chargement asymétrique. De la même

manière, le SMAT améliore la résistance cyclique et la durée de vie en fatigue. Les résultats montrent qu'il y a une petite déviation de l'amplitude de contrainte (avec un maximum d'environ 20 MPa) entre les chargements symétriques et asymétriques pour toutes les amplitudes de déformation. Cela indique que le chargement asymétrique a une influence moindre sur l'amplitude de contrainte pour les échantillons bruts ou traités par SMAT, pour un rapport de charge de -0,5 dans les régimes de LCF. De plus, cette influence du chargement asymétrique est légèrement plus élevée pour les matériaux bruts que pour les matériaux traités par SMAT, du moins pour les amplitudes de déformation de 0,5 % et 0,8 %.

3.4 Investigation de la microstructure de l'acier inoxydable 316Lreçu

La déformation plastique homogène entraîne une distribution globale uniforme des angles de désorientation et des dislocations géométriquement nécessaires (GND) entre les grains, comme le montre les Fig. 3-11(a) et (b). À l'intérieur du grain, la désorientation et les GND s'accumulent aux joints de grains (GBs), ainsi qu'aux frontières des macles pour accommoder la déformation. La densité moyenne de GND, calculée à partir des valeurs locales de GND aux mêmes profondeurs, est présentée dans la Fig. 3-11c, permettant de révéler son évolution en fonction de la profondeur de l'échantillon issu des essais de fatigue.

(a)

(b)

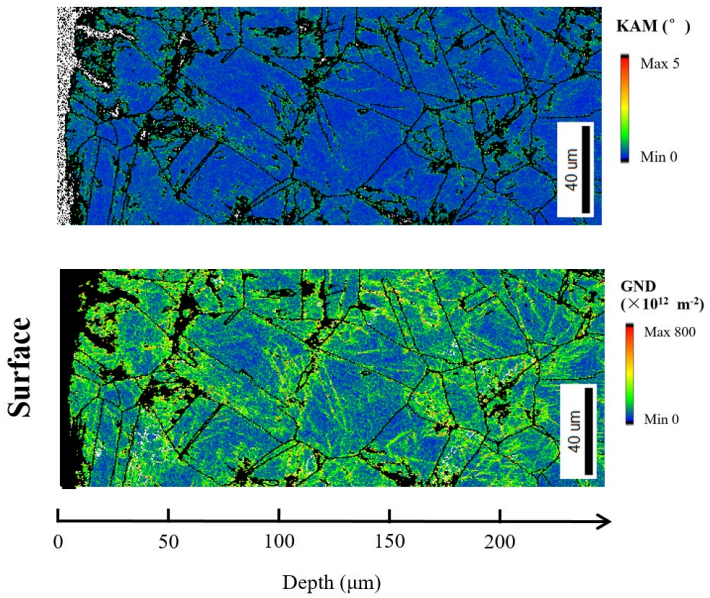

(c)

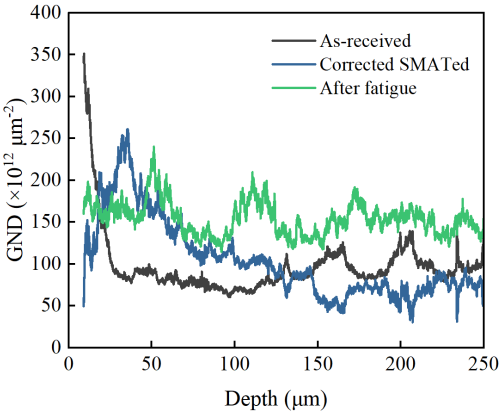

Fig. 3-11. (a) Cartes EBSD de l'angle de désorientation de la microstructure locale (KAM) et (b) cartes des dislocations géométriquement nécessaires (GND) sur la section transversale (c) GND moyen en fonction de la profondeur, basé sur les cartes GND ; de l'échantillon issu des essais de fatigue à une amplitude de déformation de 1,25 % sous chargement symétrique.

Avec l'augmentation des amplitudes de déformation, les GND montrent une augmentation progressive pour un même nombre de cycles. De même, avec l'augmentation du nombre de cycles, il y a une augmentation graduelle des GND pour une amplitude de déformation donnée. Une augmentation de l'amplitude de déformation ou du nombre de cycles entraîne une augmentation de la déformation plastique, ce qui conduit à une augmentation des GND. Il est intéressant de noter que les GND ont tendance à se concentrer dans les régions des joints de grains (GB) à de faibles nombres de cycles et à faible amplitude de déformation, ce qui indique un faible niveau de déformation. Cependant, à mesure que le nombre de cycles et l'amplitude de déformation augmentent, suggérant un niveau de déformation plus élevé, les GND à l'intérieur des grains augmentent alors également progressivement.

4. Influence des effets TRIP et TWIP sur le comportement en déformation, basé sur un modèle de densité de dislocations

4.1 Description du modèle de maclage et de la transformation martensitique

Le SFE influence directement la génération de défauts d'empilement et détermine les mécanismes de déformation des matériaux. Pour déterminer les contraintes critiques pour la nucléation des macles ou de la martensite ε, la considération de l'énergie totale

associée à la configuration des dislocations s'est avérée être une méthode efficace, basée sur un modèle à l'échelle mésoscopique. L'énergie totale E_i, telle qu'exprimée dans l'équation 5-1, est composée de l'énergie nécessaire pour le chevauchement des défauts d'empilement E_{dis} de l'énergie pour former un embryon E_{emb} et de l'énergie associée à la formation des défauts d'empilement E_τ.

$$E_i = E_{dis} + E_{emb} - E_\tau,\ i = \varepsilon, t \quad \text{(Eq. 4-1)}$$

$$E_{dis} = \frac{n_i^2 \mu b^2 r}{8\pi(1-\nu)_i} \ln\left(\frac{r_i}{2n_i l_i}\right) \quad \text{(Eq.4-1a)}$$

$$E_{emb} = (\gamma_{SFE} - 2\sigma_{HCP}) r_i t_i n_i \quad \text{(Eq. 4-1b)}$$

$$E_\tau = \frac{\tau b r_i^2 n_i}{m_{SF}} \quad \text{(Eq. 4-1c)}$$

où ε et t représentent respectivement la martensite ε et le maclage. n_i est le nombre de couches de défauts d'empilement dans un embryon, r_i est la largeur d'un défaut d'empilement, t_i est l'épaisseur d'un défaut d'empilement, l_i est la longueur d'un défaut d'empilement, γ_{SFE} est l'énergie de défaut d'empilement, b est la magnitude du vecteur de Burgers, m_{SF} est le facteur de Schmid, μ est le module de cisaillement, ν est le coefficient de Poisson, σ_{HCP} est l'énergie interfaciale entre la structure CFC et HC, τ est la contrainte de cisaillement appliquée aidant à former les défauts d'empilement. Nous pouvons minimiser l'énergie totale par rapport à la largeur pour déterminer la largeur critique r_i^* et la contrainte de cisaillement critique τ_i^* pour la nucléation du maclage ou de la martensite ε en utilisant :

$$\frac{\partial E_i}{\partial r_i} = 0 \quad \text{(Eq. 4-2)}$$

Pour la martensite α', la nucléation se produit aux intersections des bandes de cisaillement de la martensite ε. Par conséquent, la largeur critique $r_{\alpha'}^*$ et la contrainte de cisaillement $\tau_{\alpha'}^*$ d'un embryon α' sont supposées être égales à celles de la martensite ε. La fraction volumique de chaque microstructure f_i ($i=\alpha', \varepsilon, t$) est calculée en multipliant le nombre de densité N_i par le volume $V_i = r_i^* t_i l_i$ ($i=\alpha', \varepsilon, t$) dans les équations 4-3a à 4-3c.

$$f_\varepsilon = N_\varepsilon V_\varepsilon (1 - f_{\alpha'}) \quad \text{(Eq. 4-3a)}$$

$$f_{\alpha'} = N_{\alpha'} V_{\alpha'} \quad \text{(Eq. 4-3b)}$$

$$f_t = N_t V_t (1 - f_{\alpha'}) \quad \text{(Eq. 4-3c)}$$

Lorsque la contrainte appliquée est égale ou supérieure au seuil, la nucléation devient active. Le taux de nucléation pour chaque densité est décrit par:

$$\frac{dN_\varepsilon}{d\varepsilon} = \frac{\tau_{nuc}}{\tau_{CRSS}} \frac{r_\varepsilon^*}{bm_{SF}} N_\varepsilon (1 - f_\varepsilon) \quad \text{(Eq. 4-4a)}$$

$$\frac{dN_{\alpha'}}{d\varepsilon} = \frac{1}{2} \frac{dN_\varepsilon}{dt} \quad \text{(Eq. 4-4b)}$$

$$\frac{dN_t}{d\varepsilon} = \frac{\tau_{nuc}}{3\tau_{CRSS}} \frac{r_t^*}{bm_{SF}} N_t \left(1 - f_t\right) \quad \text{(Eq. 4-4c)}$$

où τ_{nuc} est la contrainte de cisaillement nécessaire pour nucléer une dislocation, et τ_{crss} est la contrainte de cisaillement résolue critique. La longueur moyenne de la microstructure est limitée par la taille des grains D. De plus, cette longueur moyenne l_i en fonction de la déformation peut être exprimée comme :

$$\frac{dl_i}{d\varepsilon} = \frac{1}{N_i} \frac{dN_i}{d\varepsilon} (D - l_i) \quad \text{(Eq. 4-5)}$$

Pour prendre en compte la contribution de la martensite ε et α', l'incrément total de la déformation plastique $d\varepsilon$ peut être exprimé par une loi de mélange de déformation, associée à la déformation de la martensite α' notée $\varepsilon_{\alpha'}$ et à la déformation austénitique ε_γ comme suit :

$$d\varepsilon = \left(1 - f_{\alpha'}\right) d\varepsilon_\gamma + \varepsilon_{\alpha'} df_{\alpha'} \quad \text{(Eq. 4-6)}$$

La déformation de la martensite α' est finalement négligée dans ce modèle ($\varepsilon_{\alpha'}$ = 0). En tenant compte de cette hypothèse, l'équation 4-6 devient $d\varepsilon_\gamma/d\varepsilon = 1/(1-f_{\alpha'})$. De plus, il est supposé que la martensite ε et le maclage affectent le comportement des dislocations dans les structures austénitiques. En conséquence, la déformation dans l'austénite ε_γ a une relation avec la martensite ε et le maclage comme suit :

$$d\varepsilon_\gamma = \left(1 - f_t - f_\varepsilon\right) d\varepsilon_{dis} + \frac{1}{\sqrt{2}M} df_t + \frac{2}{3} f_\varepsilon d\varepsilon_{dis} \quad \text{(Eq. 4-7)}$$

où M est le facteur de Taylor, et ε_{dis} est la déformation plastique due au glissement des dislocations. En réarrangeant les expressions décrites par l'équation 4-7, on obtient :

$$\frac{d\varepsilon_{dis}}{d\varepsilon_\gamma} = \frac{1 - \frac{1}{\sqrt{2}M} \frac{df_t}{d\varepsilon_\gamma}}{1 - f_t - \frac{1}{3} f_\varepsilon} \quad \text{(Eq. 4-8)}$$

En combinant les équations 4-6, 4-7 et 4-8, l'évolution de la densité de dislocations peut être exprimée en fonction de la déformation totale ε comme :

$$\frac{d\rho}{d\varepsilon}=\frac{d\rho}{d\varepsilon_{dis}}\frac{d\varepsilon_{dis}}{d\varepsilon_{\gamma}}\frac{d\varepsilon_{\gamma}}{d\varepsilon}=\frac{d\rho}{d\varepsilon_{dis}}\frac{1-\frac{1}{\sqrt{2}M}\frac{df_t}{d\varepsilon_{\gamma}}}{1-f_t-\frac{1}{3}f_{\varepsilon}}\frac{1}{(1-f_{\alpha'})} \qquad \text{(Eq. 4-9)}$$

où ε_{dis} est la déformation causée par le glissement des dislocations. L'accumulation dynamique et l'annihilation des dislocations ont été prises en compte, en suivant le modèle classique de Kocks–Mecking–Estrin (KME) comme suit :

$$\frac{d\rho}{d\varepsilon_{dis}}=\frac{d\rho^{+}}{d\varepsilon_{dis}}+\frac{d\rho^{-}}{d\varepsilon_{dis}} \qquad \text{(Eq. 4-10)}$$

L'équation généralisée pour le taux d'évolution des forêts de dislocations en fonction de la déformation peut être exprimée comme :

$$\frac{d\rho^{+}}{d\varepsilon_s}=\frac{M}{b}(k_1\sqrt{\rho}+\frac{1}{D}+\sum_i\frac{1}{\Lambda_i}),\ i=\varepsilon,\ t \qquad \text{(Eq. 4-11)}$$

où k_1 est un facteur géométrique lié aux joints de grains et aux forêts de dislocations. L'espacement moyen est relié à la largeur w_i et à la fraction volumique f_i de la martensite ε et du maclage, donné par :

$$\frac{1}{\Lambda_i}=\frac{1}{2w_i}\cdot\frac{f_i}{1-f_i} \qquad \text{(Eq. 4-12)}$$

Un terme supplémentaire de restauration dynamique lié à la taille des grains doit être ajouté pour décrire la diminution de l'écrouissage due à l'affinement des grains.

$$\frac{d\rho^{-}}{d\varepsilon_s}=-M\rho\left[k_{20}\left(\frac{\dot{\varepsilon}^p}{\dot{\varepsilon}_0}\right)^{-\frac{1}{n_0}}-\left(\frac{D_e}{D}\right)^2\right] \qquad \text{(Eq. 4-13)}$$

où k_{20} est la constante de restauration dynamique, n_0 est un exposant inversement proportionnel à la température, $\dot{\varepsilon}_0$ est le taux de déformation de référence, et D_e est la taille de grain de référence. La contrainte totale du matériau peut être calculée par une loi de mélange basée sur les fractions volumiques de la martensite α' et de l'austénite γ :

$$\sigma_{total}=(1-f_{\alpha'})\sigma_{\gamma}+f_{\alpha'}\sigma_{\alpha'} \qquad \text{(Eq. 4-14)}$$

où σ_{γ} et $\sigma_{\alpha'}$ représentent respectivement la contrainte dans l'austénite et la martensite.

4.2 Application à l'évolution des microstructures de l'acier inoxydable 304 avec les

effets TWIP/TRIP

Pour tester nos modèles, il est intéressant d'étudier le comportement de matériaux avec différents SFE, permettant de mieux comprendre l'influence des différents ingrédients du modèle développé. Avec un acier à faible SFE (SFE = 17,8 mJ/m² à température ambiante), il a été observé expérimentalement que l'acier inoxydable 304 subit une transformation martensitique et un maclage de déformation. La Fig. 4-4a montre l'évolution de la longueur caractéristique de la microstructure en fonction de la déformation, calculée à partir de l'équation 4-5. On peut observer qu'au début de la déformation, lorsque la déformation est inférieure à 0,2, la longueur caractéristique de la microstructure augmente rapidement de 0 à environ 10 microns. À mesure que la déformation continue d'augmenter, cette longueur caractéristique de la microstructure croît plus lentement jusqu'à atteindre une saturation correspondant à la taille des grains.

La Fig. 4-4b présente les courbes d'évolution de la fraction volumique mesurée [227] et prédite, calculées à partir des équations 4-3a à 4-3c. Au cours de la phase initiale de déformation, les fractions volumiques de la martensite ε et du maclage augmentent avec la déformation, atteignant des maxima de 57 % et 44 % pour des déformations de 0,45 et 0,52, respectivement. À mesure que la déformation continue d'augmenter, les fractions volumiques de la martensite ε et du maclage diminuent progressivement à 37 % et 32 %, respectivement. À l'inverse, la fraction volumique de la martensite α' augmente progressivement pour atteindre 62 %, indiquant une transformation des macles et de la martensite ε en martensite α' à des déformations plus élevées.

La Fig. 4-4c présente la courbe contrainte-déformation macroscopique prédite, calculée à partir de l'équation 4-14, ainsi que les courbes expérimentales issues de la référence [227]. À mesure que la déformation augmente, la contrainte augmente progressivement de 268,6 MPa jusqu'à 1033,6 MPa. Les courbes expérimentales indiquent notamment que lorsque la déformation atteint 0,58, la contrainte chute brusquement et l'échantillon se rompt. Cette chute signifie que le matériau s'est fracturé et ne peut plus supporter de charge. Il est important de noter que l'effet de l'endommagement du matériau sur les propriétés est négligé dans cette simulation, expliquant qu'il n'est possible de reproduire l'effet.

Sur la base de la contribution des microstructures individuelles pour la relation contrainte-déformation, montrée dans la Fig. 4-4d, il est possible d'analyser l'effet des

différents mécanismes de déformation sur les contraintes macroscopiques. Au début de la phase de déformation (déformation inférieure à 0,3), la fraction volumique des microstructures individuelles est faible, et la densité de dislocations détermine principalement le comportement de déformation du matériau. À mesure que les fractions volumiques de la martensite ε et des macles augmentent avec la déformation de 0,3 à 0,58, elles contribuent davantage à l'augmentation de la contrainte par le biais des effets TWIP et TRIP, respectivement. Les bandes de cisaillement produites par la martensite ε et les macles entravent le mouvement des dislocations, permettant à celles-ci de s'accumuler aux limites des bandes.

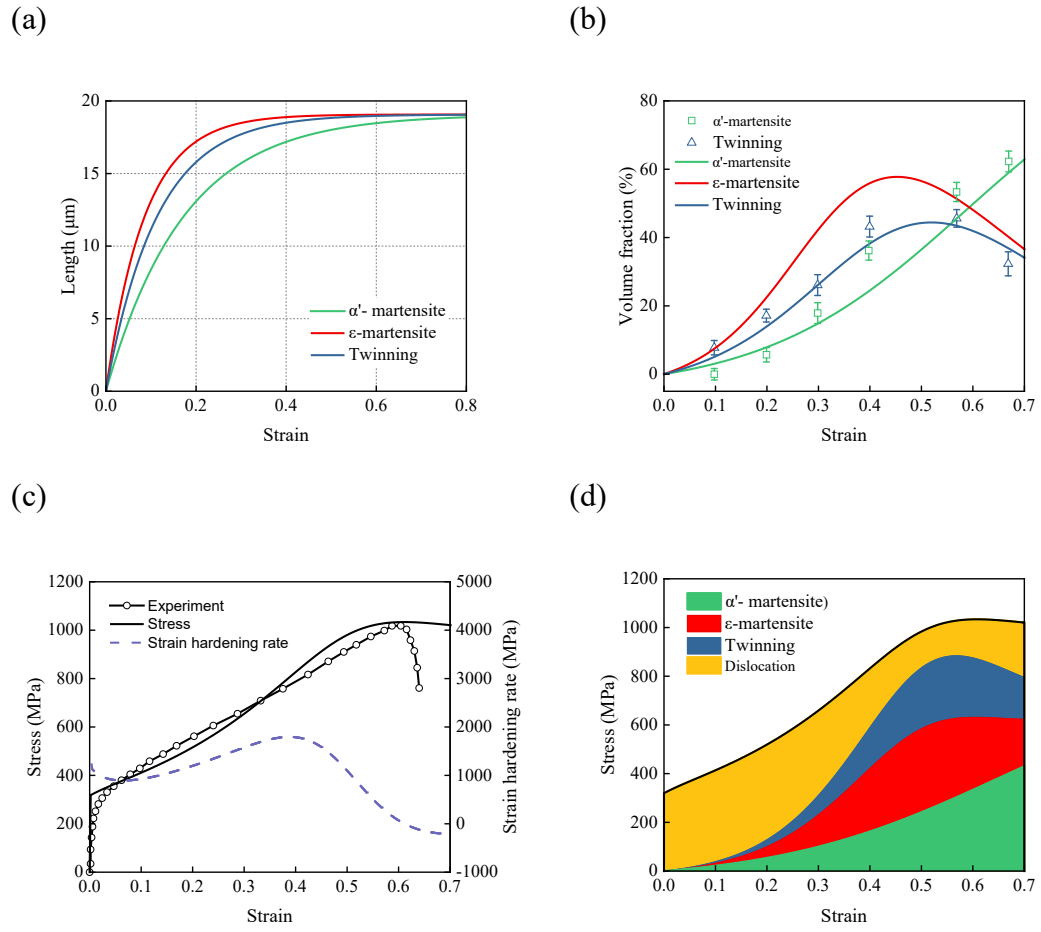

Fig. 4-4. (a) Longueurs et (b) fractions volumiques en fonction de la déformation axiale de la martensite ε, du maclage et de la martensite α'. (c) Courbe contrainte-déformation macroscopique et taux d'écrouissage en fonction de la déformation axiale. Les données expérimentales correspondantes de l'acier inoxydable 304 sont affichées par des points dans (b) et (c) lors du chargement en traction. (d) Contributions de la martensite, du maclage et des dislocations pour la relation contrainte-déformation.

5 Comportement en traction de l'acier inoxydable 316L SMATé avec TWIP en tenant compte des champs résiduels

5.1 Champs résiduels dépendant de la profondeur

Pour décrire avec précision le comportement mécanique du matériau traité par SMAT, les champs résiduels, comprenant la taille des grains, l'épaisseur des macles et la fraction volumique des macles, sont pris en compte sur la base de mesures expérimentales. Une relation exponentielle est largement utilisée pour décrire la variation de la taille des grains :

$$D = D_c\left(1-\left\{1+\exp\left[\left(z-h_g\right)/c_1\right]\right\}^{-1}\right) \qquad \text{(Eq. 5-1)}$$

où D_c est la taille des gros grains dans la région non affectée à cœur, h_g et c_1 sont des constantes d'ajustement, et z est la distance par rapport à la surface traitée. Pour décrire la distribution des macles, la fraction volumique initiale des macles dans toute la région à gradient peut être exprimée comme :

$$f_{t0} = f_{t1} - f_{t2}\exp\left(-z/c_2\right) \qquad \text{(Eq. 5-2)}$$

où f_{t1}, f_{t2}, et c_2 sont des constantes. En l'absence de résultats expérimentaux actuels, la distribution de l'épaisseur initiale des macles est établie selon les travaux réalisés par [230] :

$$D_t = D_{t1} - D_{t2}\exp\left(z/c_3\right) \qquad \text{(Eq. 5-3)}$$

où D_{t1}, D_{t2}, et c_3 sont des constantes. Des fonctions exponentielles basées sur les conditions d'équilibre global des contraintes sont utilisées pour décrire la distribution en fonction de la profondeur des contraintes résiduelles :

$$\begin{cases} \sigma_{zz}^{rs} = \sum_{i=1}^{2} L_i\left(\mathrm{e}^{-l_i\left(r_{\max}-r\right)}\right) + L_0 \\ \sigma_{\theta\theta}^{rs} = \sum_{i=1}^{2} T_i\left(\mathrm{e}^{-t_i\left(r_{\max}-r\right)}\right) + T_0 \\ \sigma_{rr}^{rs} = \dfrac{1}{r}\left[\sum_{i=1}^{2}\dfrac{T_i}{t_i}\left(\mathrm{e}^{-t_i\left(r_{\max}-r\right)}-1\right) - T_0\left(r_{\max}-r\right)\right] \end{cases} \qquad \text{(Eq. 5-4)}$$

où L_0, L_i, l_i, T_0, T_i et t_i sont des constantes ajustées à partir des profils de contraintes résiduelles obtenus expérimentalement. Il est bien documenté qu'il existe un lien entre la déformation plastique cumulée et la densité de dislocations initiale ρ_0. Ce lien peut être établi par la relation exprimée dans :

$$\rho_0 = 2\sqrt{3}\frac{\varepsilon_{rs}^p}{bD} \quad \text{(Eq. 5-5)}$$

où b est la magnitude du vecteur de Burgers, ε_{rs}^p est la déformation plastique cumulée résiduelle, et D est la taille des grains donnée par l'équation 5-1.

5.2 Modèle constitutif pour le matériau à gradient de microstructure

Généralement, des grains affinés et de grandes quantités de dislocations sont deux sources majeures de renforcement dans les matériaux à gradient de microstructure. Ainsi, l'évolution de la contrainte d'écoulement peut être déterminée en tenant compte des contributions des dislocations stockées et de la taille des grains comme :

$$\sigma_y = \sigma_0 + \frac{k_{HP}}{\sqrt{D}} + M\alpha\mu b\sqrt{\rho} \quad \text{(Eq. 5-6)}$$

où σ_0 est la contrainte de frottement du réseau ; k_{HP} est la pente de Hall-Petch ; D est la taille des grains ; M est le facteur de Taylor ; α est une constante du matériau ; b est la norme du vecteur de Burgers ; μ est le module de cisaillement ; et ρ est la densité de dislocations. Avant le chargement, la contrainte d'écoulement initiale pour chaque profondeur peut être calculée par l'équation 5-6, en prenant la densité de dislocations égale à la densité de dislocations initiale ρ_0 donnée par l'équation 5-5.

La déformation macroscopique ε et la déformation de cisaillement γ sont liées au facteur de Taylor par la relation suivante : $\varepsilon=\gamma/M$. Par ailleurs, pour prendre en compte la contribution du maclage, l'incrément total de déformation $d\varepsilon$ peut être exprimé par une loi de mélange incorporant les contributions du glissement des dislocations et du maclage :

$$d\varepsilon = (1-f_t)\,d\varepsilon_s + \varepsilon_t df_t \quad \text{(Eq. 5-7)}$$

où ε_s est la déformation causée par le glissement des dislocations, et ε_t est la déformation associée au maclage. La déformation de cisaillement du maclage γ_t est $1/\sqrt{2}$. En réarrangeant les expressions décrites par les équations 5-6 et 5-7, on obtient :

$$\frac{d\varepsilon_s}{d\varepsilon} = \frac{1}{1-f_t}\left(1-\frac{\gamma_t}{M}\frac{df_t}{d\varepsilon}\right) \quad \text{(Eq. 5-8)}$$

où M est le facteur de Taylor, f_t est la fraction volumique des macles, exprimée comme suit :

$$f_t = F_{\max}\left(1-e^{-\beta_t(\varepsilon-\varepsilon_{t0})}\right)^m \quad , \quad \varepsilon > \varepsilon_{t0} \quad \text{(Eq. 5-9)}$$

où F_{max} est la fraction maximale des macles, β_t est un paramètre de la cinétique du

maclage, *m* est le paramètre d'intensité de l'effet TWIP, et ε_{t0} est la déformation critique pour l'initiation du maclage. En différenciant l'équation 5-9, le taux de fraction volumique des macles peut être obtenu comme :

$$\frac{df_t}{d\varepsilon} = F_{max}\beta m \exp\left[-\beta\left(\varepsilon-\varepsilon_{t0}\right)\right]\left\{1-\exp\left[-\beta\left(\varepsilon-\varepsilon_{t0}\right)\right]\right\}^{m-1} \qquad \text{(Eq. 5-10)}$$

Les processus d'accumulation et d'annihilation dynamiques des dislocations sont pris en compte via le modèle classique de Kocks–Mecking–Estrin (KME). Ainsi, l'équation généralisée pour le taux d'évolution des forêts de dislocations en fonction de la déformation peut être exprimée comme :

$$\frac{d\rho^{+}}{d\varepsilon_s} = \frac{M}{\Lambda b} = \frac{M}{b}\left(\frac{1}{D}+\frac{1}{t}+k_1\sqrt{\rho}\right) \qquad \text{(Eq. 5-11)}$$

où k_1 est un facteur géométrique lié aux joints de grains et aux forêts de dislocations. L'espacement moyen des macles *t* est lié à l'épaisseur des macles D_t et à la fraction volumique des macles f_t , et est donné par:

$$\frac{1}{t} = \frac{1}{2D_t}\cdot\frac{f_t}{1-f_t} \qquad \text{(Eq. 5-12)}$$

Un terme supplémentaire de restauration dynamique relié à la taille des grains est ajouté pour décrire la diminution de l'écrouissage due à l'affinement des grains:

$$\frac{d\rho^{-}}{d\varepsilon_s} = -M\rho\left[k_{20}\left(\frac{\dot{\varepsilon}^p}{\dot{\varepsilon}_0}\right)^{-\frac{1}{n_0}}-\left(\frac{D_e}{D}\right)^2\right] \qquad \text{(Eq. 5-13)}$$

où k_{20} est la constante de restauration dynamique, n_0 est un exposant inversement proportionnel à la température, $\dot{\varepsilon}_0$ est le taux de déformation de référence, et D_e est la taille de grain de référence. Il convient de noter que le paramètre n_0 est relié au SFE, ce qui peut affecter la génération des GNDs et l'affinement des grains pendant le SMAT. En combinant les équations 5-8, 5-11 et 5-13, l'évolution de la densité de dislocations peut finalement être exprimée en fonction de la déformation totale ε :

$$\begin{aligned}&\frac{d\rho}{d\varepsilon} = \frac{d\rho}{d\varepsilon_s}\frac{d\varepsilon_s}{d\varepsilon} = \left(\frac{d\rho^{+}}{d\varepsilon_s}+\frac{d\rho^{-}}{d\varepsilon_s}\right)\frac{d\varepsilon_s}{d\varepsilon} = \\ &\frac{1}{1-f_t}\left(M-\frac{1}{\sqrt{2}}\frac{df_t}{d\varepsilon}\right)\left[\frac{1}{b}\left(\frac{1}{D}+\frac{1}{t}+k\sqrt{\rho}\right)-k_{20}\left(\frac{\dot{\varepsilon}^p}{\dot{\varepsilon}_0}\right)^{-\frac{1}{n_0}}\rho-\left(\frac{d_e}{d}\right)^2\rho\right]\end{aligned} \qquad \text{(Eq. 5-14)}$$

5.3 Modélisation par éléments finis

Comme illustré sur la Fig. 5-4a, la section centrale de l'échantillon cylindrique après SMAT est prise comme la zone d'intérêt. Afin de réduire le temps de résolution, un modèle représentatif 2D axisymétrique est construit pour analyser les propriétés en traction du matériau à GMS. Une condition aux limites de symétrie est appliquée à la section transversale. Pour simuler l'essai de traction uniaxiale, un déplacement est appliqué à la bordure supérieure du GMS via une contrainte de couplage. Le modèle est maillé en utilisant des éléments axisymétriques à quatre nœuds (CAX4). Une taille de maille hétérogène allant de 5 μm (à la surface traitée) à 100 μm (dans la masse à cœur) a été adoptée pour le modèle aux éléments finis, comme illustré à la Fig. 5b.

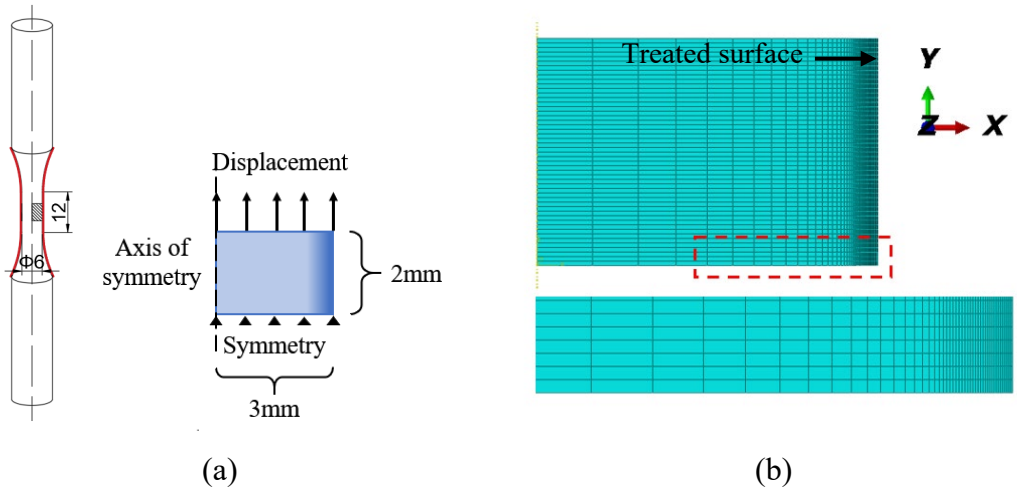

Fig. 5-4. Section d'un échantillon traité par SMAT : (a) modèle géométrique et conditions aux limites, (b) modèle par éléments finis montrant le maillage.

5.4 Résultats de la simulation pour les quantités microstructurales et discussion

La Fig. 5-7a illustre la distribution de la contrainte de von Mises obtenue par simulation éléments finis pour le matériau à GMS. Le GMS, qui entoure la région non affectée à cœur, limite la déformation dans la direction de traction. Cela entraîne un niveau de contrainte élevé (1592 MPa) à la surface. En comparaison, on peut observer que la contrainte résiduelle influence principalement le comportement mécanique au stade initial de la déformation. À mesure que la déformation augmente, il y a moins d'influence sur des contraintes résiduelles du comportement mécanique en traction pour différentes tailles de grains. Cela s'explique par le fait que la contrainte résiduelle est équilibrée à l'intérieur de l'ensemble de la structure pendant la déformation plastique, comme le montre la Fig. 5-7b.

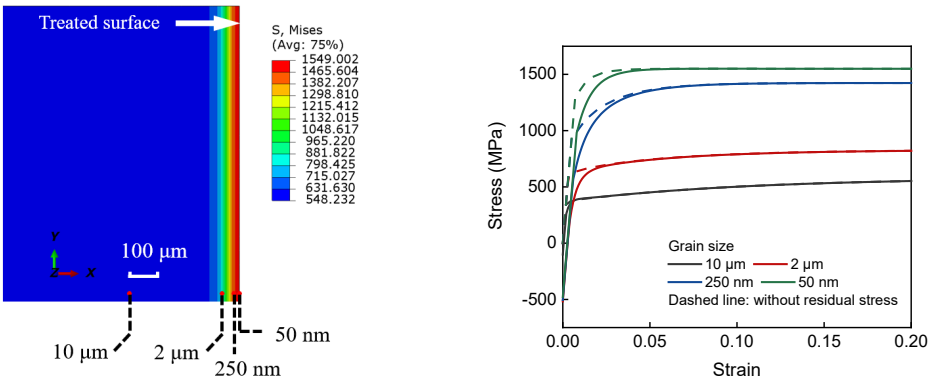

(a) (b)

Fig. 5-7. (a) Distribution de la contrainte de von Mises après le chargement en traction, et (b) courbe contrainte-déformation pour différentes tailles de grains avec contrainte résiduelle (ligne pleine) et sans contrainte résiduelle (ligne pointillée).

À partir de la distribution de la fraction volumique initiale des macles, montrée dans la Fig. 5-9a, on peut voir que les points de taille de grain de 50 nm et 250 nm sont situés du côté droit de la valeur de pic, tandis que les points de taille de grain de 2 µm et 10 µm sont situés du côté opposé. Le processus SMAT affine les grains jusqu'à l'échelle nanométrique (allant de 50 nm à 250 nm) dans la région proche de la surface, et, en même temps, la structure des macles existante est détruite par cet effet d'affinement des grains. En plus de la nucléation des macles, la fraction volumique des macles dépend fortement de la taille des grains dans les matériaux dominés par le glissement [231]. Par conséquent, l'effet de la taille des grains est pris en compte dans le calcul de la fraction volumique des macles dans l'équation 5-9 en remplaçant le β_t supposé calculable par l'équation 5-15 :

$$\beta_t = \beta_0 \times coefficient(D)$$
$$coefficient(D) = \left(D / D_{e2}\right)^2 \qquad \text{(Eq.5-15)}$$

où β_0 est le paramètre de la cinétique du maclage et D_{e2} est la taille de grain de référence pour le maclage. La Fig. 5-9b montre l'évolution des fractions volumiques des macles à différentes profondeurs (c'est-à-dire avec des tailles de grains variées) en fonction de l'augmentation de la déformation plastique pendant le chargement en traction. On peut voir que pendant le chargement en traction, la fraction volumique des macles augmente avec la déformation essentiellement dans les gros grains.

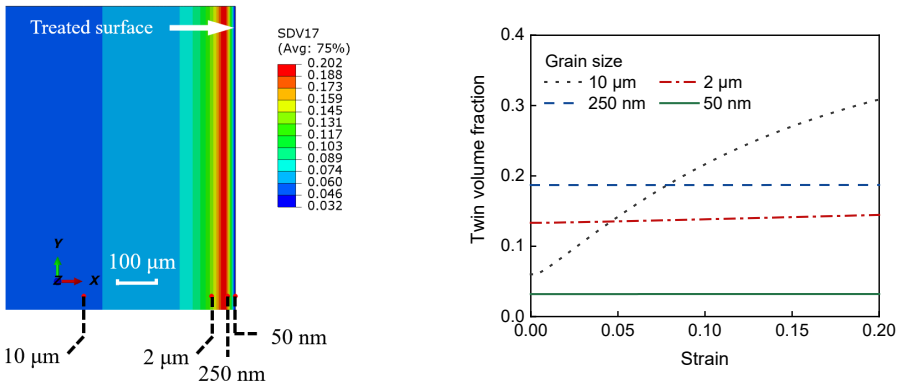

(a) (b)

Fig. 5-9. (a) Distribution de la fraction volumique initiale des macles (b) Évolution prédite de la fraction volumique des macles avec différentes tailles de grains (correspondant à différentes profondeurs sous la surface traitée par SMAT).

6 Réponse en déformation cyclique avec prise en compte de la microstructure

6.1 Modèle des contraintes internes basé sur les dislocations

Dans la présente section, nous ne rapportons que les équations supplémentaires nécessaires pour modéliser le LCF. L'évolution de la densité de dislocations pendant la déformation plastique peut être réécrite comme suit :

$$\frac{d\rho}{d\varepsilon_p}=\frac{d\rho^{+}}{d\varepsilon_p}-\frac{d\rho^{-}}{d\varepsilon_p}=k_1\frac{1}{\Lambda}-k_2\rho=k_1k_\Lambda\sqrt{\rho}-k_2\rho$$
$$\sqrt{\rho}=\frac{k_1k_\Lambda}{k_2}(1-e^{-k_2\varepsilon_p/2}) \qquad \text{(Eq.6-1)}$$

où k_1 et k_2 sont les coefficients du taux de génération et du taux d'annihilation de la densité de dislocations, respectivement. k_Λ est le taux de génération du libre parcours moyen des dislocations. $k_\Lambda=k_Dk_t$, où k_D et k_t sont les coefficients de l'effet de la taille des grains et de l'effet des macles de déformation sur le libre parcours moyen des dislocations, respectivement. Combiné avec la relation de Taylor permettant de calculer la contrainte induite par la densité de dislocations, cela conduit à :

$$\sigma=M\alpha Gb\sqrt{\rho}=M\alpha Gb\frac{k_1k_\Lambda}{k_2}(1-e^{-k_2\varepsilon_p/2}) \qquad \text{(Eq.6-2)}$$

La contrainte de retour intergranulaire dépend de la différence entre les

dislocations aux joints de grains et les dislocations internes. L'évolution de cette contrainte de retour intergranulaire pendant le chargement cyclique peut alors être décrite par :

$$X_{inter} = M\alpha Gb\left\{f_b\left[\sqrt{\rho_b}\cdot(1-e^{-k_{2b}N_f/2})-\sqrt{\rho_i}\cdot(1-e^{-k_{2I}N_f/2})\right]+\sqrt{\rho_{GNDs}^{sat}}\right\} \quad \text{(Eq.6-3)}$$

où f_b est la fraction de surface occupée par les dislocations aux joints de grains, qui est généralement inférieure à 20 % de celle de l'ensemble des grains. $\frac{k_{1b}k_{\Lambda b}}{k_{2b}}(1-e^{-k_{2b}\varepsilon_p/2})$ et $\frac{k_{1I}k_{\Lambda I}}{k_{2I}}(1-e^{-k_{2I}\varepsilon_p/2})$ représentent respectivement l'évolution de ρ_b et ρ_i avec le nombre de cycles, développée par l'équation 6-1. ρ_{GNDs}^{sat} est la densité minimale de GNDs requise pour accommoder l'incompatibilité de la déformation plastique de grain à grain dans des conditions stabilisées. En suivant la même approche utilisée pour la formulation de la contrainte de retour intergranulaire, la contrainte de retour intragranulaire est exprimée par :

$$X_{intra} = M\alpha Gb\cdot f_w\left\{\left[\Delta\sqrt{\rho_w}(1-e^{-k_{2w}N_f/2})\right]+\sqrt{\rho_{GNDs}^{0}}\right\} \quad \text{(Eq.6-4)}$$

où f_w est la fraction de parois. ρ_{GNDs}^{0} est la GND initiale, qui est proportionnelle à la différence entre la densité à la racine carrée des dislocations dans les murs et les canaux. Le taux de réarrangement des dislocations pour former des structures de dislocations, k_{2w} est généralement inférieur au taux d'annihilation des dislocations internes k_{2i}, avec $k_{2w} \approx k_{2i}$. L'évolution de la contrainte effective pendant le chargement cyclique peut être écrite comme :

$$\sigma_r = M\alpha Gb\cdot\sqrt{f_j\rho_I} \quad \text{(Eq.6-5)}$$

où f_j est la fraction des jonctions de dislocations fixes.

6.2 Résultats sur l'évolution des contraintes et discussion

Comme discuté dans la section 6.1, la réponse en déformation cyclique dominée par les dislocations indique que la résistance au durcissement initial augmente avec l'amplitude de déformation, probablement en raison de l'activation du glissement planaire et du glissement secondaire à des amplitudes de déformation élevées. Le léger adoucissement cyclique observé à une amplitude de déformation plus élevée de 1,25 % peut être attribué à la promotion du glissement croisé et à la réorganisation des

structures de dislocations en murs et canaux avant la rupture. Les résultats prédits dans la Fig. 6-3 montrent que le modèle développé présenté à la section 6.2 peut décrire la réponse de durcissement et d'adoucissement cyclique de l'acier inoxydable 316L sous LCF à différentes valeurs d'amplitude de déformation.

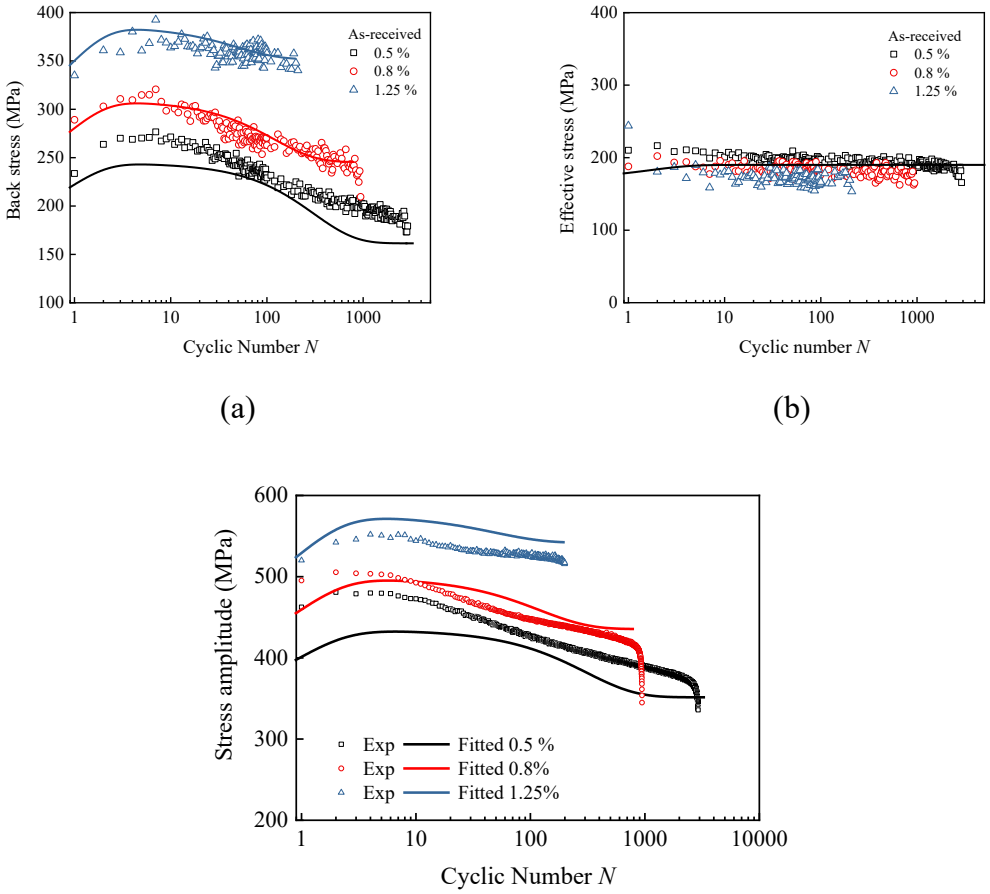

Fig. 6-3. (a) Contrainte de retour, (b) contrainte effective et (c) réponse en contrainte cyclique en fonction du nombre de cycles pour l'acier inoxydable 316L brut, pour différentes amplitudes de déformation. Les points de données représentent les données expérimentales obtenues au chapitre 3, tandis que les lignes pleines indiquent les courbes prédites.

7. Conclusions et perspectives

7.1 Conclusion

Dans ce travail, les comportements en traction uniaxiale pour des sollicitations de type LCF de matériaux traités par SMAT ont été étudiés à travers des observations

expérimentales et une modélisation. Les résultats indiquent que les microstructures en gradient introduites par le SMAT influencent de manière significative les propriétés mécaniques macroscopiques des matériaux.

Le chapitre 2 a employé diverses techniques de caractérisation, notamment EBSD, nanoindentation et XRD, pour analyser les microstructures, les propriétés mécaniques et les contraintes résiduelles dans l'acier inoxydable 316L traité par SMAT. Ces résultats ont démontré que le SMAT induit une microstructure à gradient près de la surface, mise en évidence notamment par des variations dans la désorientation des grains, la microdureté et la distribution des contraintes. Bien que la microstructure en gradient ait été clairement observée, la formation de grains nanocristallins n'a pas été directement mise en évidence.

Ensuite, le comportement en LCF des échantillons de 316L traités par SMAT et bruts a été étudié à la fois macroscopiquement et microscopiquement pour comprendre l'impact du SMAT sur les performances en fatigue sous différentes conditions de chargement, comme abordé au chapitre 3. Les résultats indiquent que les échantillons bruts ou traités par SMAT subissent un durcissement initial significatif, suivi d'un adoucissement progressif pendant le LCF, principalement dû à l'évolution de la contrainte de retour. Les échantillons traités par SMAT ont montré une contrainte de retour plus élevée, suggérant une hétérogénéité microstructurale. Les observations EBSD ont mis en évidence la distribution uniforme de la déformation plastique et des structures de dislocations, sans maclage de déformation observé, mais une présence notable de macles de recuit. L'évolution des GNDs (dislocations géométriquement nécessaires) et de l'orientation des grains pendant le chargement cyclique suggère également que les GNDs jouent un rôle crucial dans l'évolution des contraintes internes, influençant la contrainte de retour et le comportement global en fatigue.

Au chapitre 4, un modèle constitutif basé sur la densité de dislocations et dépendant de la taille des grains, intégrant l'énergie de faute d'empilement (SFE), a été développé pour explorer l'influence des mécanismes de déformation sur le comportement en traction. Une SFE plus faible dans l'acier inoxydable 304 permet de tester notre modèle complet, car elle facilite la transformation martensitique et le maclage mécanique en réduisant la contrainte de cisaillement critique et en augmentant les taux de nucléation, en particulier dans les grains plus grands. Ces changements microstructuraux jouent un rôle significatif dans la réponse macroscopique sous

chargement uniaxial. De plus, l'interaction entre la SFE, la taille des grains et la dynamique de nucléation est cruciale pour prédire le comportement en traction de l'acier inoxydable 304. Les différentes étapes de la déformation sont contrôlées par l'évolution microstructurale, telles que les activités de dislocation, le maclage et la transformation martensitique. Initialement, le mouvement des dislocations gouverne le comportement de déformation. À mesure que la déformation progresse, l'augmentation des fractions volumiques de la martensite ε et des cristaux maclage renforce la résistance par les effets TWIP et TRIP, respectivement. Une déformation supplémentaire entraîne une transformation martensitique supplémentaire, entraînant une augmentation continue de la résistance du matériau.

Les simulations du chapitre 5 révèlent l'effet des microstructures à gradient (GMS) sur la réponse mécanique macroscopique en analysant les changements microstructuraux à différentes profondeurs lors d'une traction uniaxiale. Un modèle éléments finis (FEM) a été établi en intégrant des champs résiduels initiaux dépendant de la profondeur, y compris la taille des grains, les contraintes résiduelles, la densité de dislocations et le maclage. Ce point est assez innovant par rapport à la modélisation existante et permet d'améliorer la précision des simulations. Comparé aux observations expérimentales, le modèle éléments finis développé prédit avec précision les propriétés en traction de l'acier inoxydable 316L traité par SMAT. L'échantillon traité par SMAT présente notamment une déformation inhomogène pendant le chargement en traction, où les gros grains à cœur amorcent la déformation plastique tandis que les grains nanocristallisés en surface restent principalement élastiques. À de faibles niveaux de déformation, les gros grains à cœur accommodent la plupart de la déformation externe. De plus, les densités de dislocations et les fractions volumiques des macles dans les couches avec des tailles de grains variables augmentent rapidement pendant le chargement en traction, et atteignent progressivement la saturation. Une analyse détaillée du comportement en traction local et global a également révélé que la contrainte résiduelle de compression superficielle générée par le SMAT réduit significativement la limite d'élasticité au stade initial de la déformation. Cependant, à mesure que la déformation progresse, l'influence des contraintes résiduelles diminue en raison de leur équilibre global interne, leur effet diminuant davantage avec la profondeur en raison de la nature en gradient de la contrainte.

Au chapitre 6, un modèle de contraintes internes basé sur la densité de dislocations

est établi pour décrire l'évolution microstructurale des matériaux sous déformation cyclique complexe, en tenant compte de l'influence de la SFE, de la taille des grains et de l'amplitude de déformation sur les structures de dislocations. Le modèle proposé capture efficacement le comportement de durcissement et d'adoucissement cyclique de l'acier inoxydable 316L (brut ou traité par SMAT) sous LCF avec différentes amplitudes de déformation. L'intégration de la taille des grains dans le modèle, en particulier dans les composantes de contrainte de retour intra-grain et inter-grain, permet de rendre compte de son impact sur la déformation cyclique. Dans les matériaux TWIP, le maclage mécanique a été identifié comme augmentant avec l'amplitude de déformation et le nombre de cycles. Les macles de déformation, initialement rares à de faibles amplitudes de déformation, deviennent ensuite dominantes dans la phase de renforcement secondaire à des amplitudes de déformation élevées, renforçant l'effet global de renforcement. En comparant les réponses en déformation cyclique des matériaux bruts et traité par SMAT, les échantillons traités par SMAT ont montré un durcissement initial plus élevé, en particulier à de faibles amplitudes de déformation. Cela est attribué à une déformation non homogène dans la microstructure à gradient, ce qui conduit à des densités de dislocations élevées dans la région centrale à cœur, entraînant un durcissement initial plus élevé.

7.2 Perspectives

Il reste de nombreux points intéressants à explorer notamment expérimentalement. Dans ce travail, une tentative a été faite pour mesurer le champ de contraintes résiduelles dans l'acier inoxydable 316L après SMAT en utilisant la méthode XRD à incidence rasante. La profondeur de pénétration a été corrélée au coefficient d'absorption de la source de rayons X, mais en raison des limitations du matériau utilisé pour la cible à rayon X, les contraintes résiduelles à différents emplacements n’ont pas pu être mesurées. Des recherches supplémentaires seraient intéressantes pour déterminer les contraintes résiduelles de l’échantillon traité par SMAT en utilisant des méthodes non destructives, ce qui permettrait de réduire la libération des contraintes résiduelles causée par le processus de préparation expérimentale destructif. De plus, des contraintes résiduelles macroscopiques et des microstructures, telles que des dislocations et des macles, coexistant dans les échantillons SMAT. Pour étudier avec précision ces caractéristiques microsctructurelles, des méthodes de caractérisation plus

précises, telle que la microscopie électronique en transmission (MET), sont recommandées. Cette approche permet une analyse plus précise des effets des contraintes résiduelles dans les échantillons SMAT à différentes échelles.

Dans les tests de fatigue, des mesures à différents nombres de cycles sont utilisées pour approximer l'évolution des caractéristiques microscopiques et du comportement macroscopique tout au long du processus LCF. Idéalement, des tests in situ devraient être effectués pour documenter le processus de déformation (à la fois en traction et en compression) et son évolution avec le nombre de cycles de fatigue, fournissant des informations précieuses sur les mécanismes de déformation en LCF. De plus, la microscopie électronique à transmission (TEM) devrait être plus systématiquement utilisée pour observer les changements microstructuraux potentiels pour chaque cycle à différents niveaux de chargement en traction-compression, en se concentrant particulièrement sur le glissement des joints de grains, le cisaillement des joints de grains et l'émission de dislocations aux joints de grains. Dans les expériences de traction sur les échantillons traités par SMAT, il a été constaté que le comportement de déformation variait dans différentes régions, en particulier pour les régions nanocristallines et celles à plus gros grains. Cela suggère que les microstructures dans ces régions doivent différer pendant le processus de fatigue en traction-compression. Ce test de fatigue et l'observation in situ des différentes régions pourraient alors fournir une meilleure compréhension des performances en LCF des échantillons traités par SMAT.

Des recherches approfondies ont été menées sur les échantillons traités par SMAT sous traction uniaxiale en fatigue. Notamment, les observations expérimentales indiquent que la microstructure à gradient introduit par le SMAT est principalement distribuée le long de la direction radiale, qui est perpendiculaire à la direction de chargement axial. Cette incohérence directionnelle peut conduire à un une amélioratuib compensée ou synergique entre le renforcement induit par le SMAT et l'écrouissage induit par la charge. Par conséquent, il serait très intéressant d'explorer les effets des chargements multiaxiaux sur les propriétés mécaniques des échantillons traités par SMAT.

De plus, les différentes approches de modélisation peuvent nécessiter des améliorations supplémentaires. Au chapitre 4, un modèle basé sur la densité de dislocations est introduit pour analyser les propriétés mécaniques et l'évolution

microstructurale sous chargement uniaxial, avec l'initiation du maclage et de la transformation de phase calculée en utilisant une méthode basée sur l'énergie et en tenant compte de la taille des grains. Le modèle de contrainte interne basé sur la densité de dislocations développé au chapitre 6 intègre l'évolution microstructurale pour différents nombres de cycles de fatigue et les corrèle avec l'amplitude de déformation, en tenant compte du maclage et de la taille des grains. Contrairement aux modèles de plasticité cristalline, ces modèles phénoménologiques utilisés dans ce travail emploient directement des équations physiques pour calculer le comportement mécanique macroscopique. Cela permet de gagner du temps, mais présente certaines limitations et correspond à une approche de champ moyen. Par exemple, il ne peut pas traiter séparément les informations sur chaque système de glissement ou prendre en compte la désorientation et la texture. Cela pourrait être fait en réduisant l'échelle de description en tenant compte des différents systèmes de glissement. Une différence clé entre les modèles est que, lors du chargement uniaxial (chapitre 4), les propriétés mécaniques et l'évolution microstructurale sont calculées en fonction de la déformation plastique, tandis que dans le LCF (chapitre 6), elles sont calculées en fonction du nombre de cycles. Par conséquent, développer un cadre numérique qui combine à la fois les modèles de chargement uniaxial et de fatigue serait bénéfique, en particulier en liant le nombre de cycles à la déformation plastique cumulée.

Concernant la transition multiéchelles, l'idée centrale des modèles des chapitres 4 et 6 est de traduire les facteurs (tels que le maclage et la taille des grains) en changement dans la densité de dislocations. Cependant, cette approche ne traite pas directement comment ces changements dans la structure des grains impactent les propriétés macroscopiques. De plus, ce modèle basé sur la densité de dislocations n'est pas compatible avec les propriétés mécaniques à l'échelle nanométrique, où la déformation des grains est gouvernée non pas par les dislocations, mais plus raisonnablement par la rotation des grains. Par conséquent, il serait précieux de développer un modèle multiéchelles amélioré qui prenne en compte de façon plus systématique des effets d'échelle lorsque la taille des grains varie de l'échelle nanométrique à l'échelle macroscopique.

Appendix

The consideration of the effect of the microstructure on the macroscopic behavior is implemented iteratively in finite elements by the subroutine UMAT. The UMAT subroutine is implemented in finite elements as shown in Fig. A.1. In addition, the radial regression algorithm is used in the solution method, which is shown schematically in Fig. A.2.

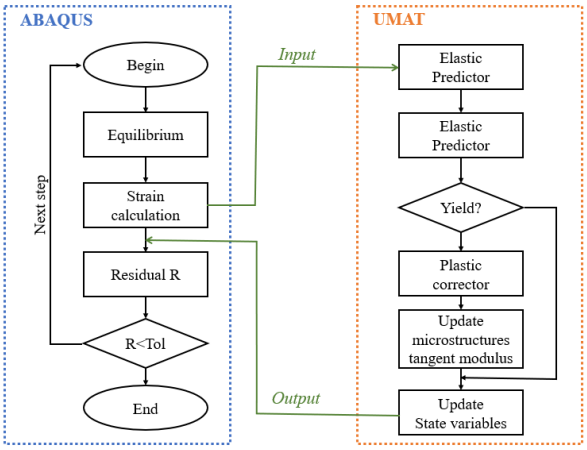

Fig. A-1. Flowchart for the computational integration of ABAQUS and subroutine UMAT.

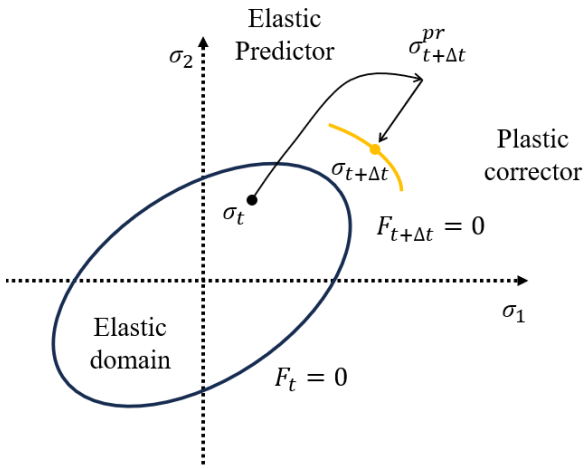

Fig. A-2. Radial return algorithm.

Appendix A: Numerical integration

The deviatoric stress for the step n+1 is expressed as follows:

$$s_{n+1} = s_n + 2G\Delta\varepsilon^e \tag{A1}$$

Taking $\Delta e^e = \Delta e \ - \Delta e^p$ in Eq. A1 to get:

$$s_{n+1} = s_{n+1}^{pr} - 2G\Delta e^p,\ s_{n+1}^{pr} = s_n + 2G\Delta e \tag{A2}$$

The back stress can be expressed by:

$$X_{n+1}^{(i)} = w_i\left(X_n^{(i)} + \frac{2}{3}C_i\Delta e^p\right),\ X_{n+1} = \sum_{i=1}^{N} X_{n+1}^{(i)}$$

$$\Delta X^{(i)} = X_{n+1}^{(i)} - X_n^{(i)} = \frac{2}{3}C_i\Delta e^p - \gamma_i\varphi_i X_{n+1}^{(i)}\Delta\overline{e}^p, \tag{A3}$$

$$w_i = \frac{1}{1+\gamma_i\varphi_i(\overline{e}_n^p + \Delta\overline{e}^p)\Delta\overline{e}^p}$$

$$\varphi_i(\overline{e}^p) = \varphi_{\infty i} + (1-\varphi_{\infty i})e^{-\overline{w}_i\overline{e}^p}$$

Substitute Eq. A3 into $\Delta e^p = \frac{3}{2}\Delta\overline{e}^p\overline{n}_{n+1}$:

$$\begin{aligned} s_{n+1} - X_{n+1} &= s_{n+1}^{pr} - 2\mu\Delta e^p - \sum_{i=1}^{N} X_{n+1}^{(i)} \\ &= s_{n+1}^{pr} - 3\mu\Delta\overline{e}^p\overline{n}_{n+1} - \sum_{i=1}^{M} w_i\,(X_n^{(i)} + C_i\Delta\overline{e}^p\overline{n}_{n+1}) \end{aligned} \tag{A4}$$

By organizing, we get:

$$s_{n+1} - X_{n+1} = s_{n+1}^{pr} - \left(3\mu + \sum_{i=1}^{N} w_i C_i\right)\Delta\overline{e}^p\overline{n}_{n+1} - \sum_{i=1}^{M} w_i X_n^{(i)} \tag{A5}$$

Substitute into $\overline{n}_{n+1} = \frac{s_{n+1} - X_{n+1}}{J_2(s_{n+1} - X_{n+1})}$, we get:

$$\left(s_{n+1} - X_{n+1}\right)\cdot Z(\Delta\overline{e}^p) = H,$$

$$\alpha(\Delta\overline{e}^p) = 1 + \left(3\mu + \sum_{i=1}^{N} w_i C_i\right)\left(\frac{\Delta\overline{e}^p}{J_2\left(s_{n+1} - X_{n+1}\right)}\right), \tag{A6}$$

$$Z = s_{n+1}^{pr} - \sum_{i=1}^{N} w_i X_n^{(i)}$$

The equivalent efficiency strain can be expressed as:

$$\Delta\overline{e}_{n+1}^p = \dot{\varepsilon}\left(\frac{J_2\left(s_{n+1} - X_{n+1}\right)}{\sigma_{yield}}\right)^m \tag{A7}$$

Eq. A-7 can be rewritten as:

$$J_2\left(s_{n+1}-X_{n+1}\right)=\sigma_{yield}\cdot\left(\frac{\Delta\overline{e}^{p}_{n+1}}{\dot{\varepsilon}}\right)^{\frac{1}{m}}=H(\Delta\overline{e}^{p}_{n})$$
$$J_2\left(s_{n+1}-X_{n+1}\right)\cdot\alpha(\Delta\overline{e}^{p})=J_2\left(Z\right) \tag{A8}$$

Employ the Newton-Raphson method to solve the equivalent plastic strain increment

$$R(\Delta\overline{e}^{p})=H(\Delta\overline{e}^{p}_{n})\cdot\alpha(\Delta\overline{e}^{p})-J_2\left(Z\right)$$
$$correction=-\frac{R(\Delta\overline{e}^{p})}{\left.\frac{\partial R(\Delta\overline{e}^{p})}{\partial\Delta\overline{e}^{p}}\right|_{\Delta\overline{e}^{p}=\Delta\overline{e}^{p}_{i}}} \tag{A9}$$

The derivative of Eq. A9 can be obtained:

$$\frac{\partial R(\Delta\overline{e}^{p})}{\partial\Delta\overline{e}^{p}}=\frac{\partial H(\Delta\overline{e}^{p})}{\partial\Delta\overline{e}^{p}}\cdot\alpha(\Delta\overline{e}^{p})+H(\Delta\overline{e}^{p})\cdot\frac{\partial\alpha(\Delta\overline{e}^{p})}{\partial\Delta\overline{e}^{p}}-\frac{\partial J_2\left(Z\right)}{\partial\Delta\overline{e}^{p}}$$
$$\frac{\partial H(\Delta\overline{e}^{p})}{\partial\Delta\overline{e}^{p}}=\frac{dR(\overline{e}^{p}_{n+1})}{d\Delta\overline{e}^{p}}\left(\frac{\Delta\overline{e}^{p}_{n+1}}{\dot{\varepsilon}}\right)^{\frac{1}{m}}+\sigma_{yield}\frac{1}{m}\frac{1}{\dot{\varepsilon}}\left(\frac{\Delta\overline{e}^{p}_{n+1}}{\dot{\varepsilon}}\right)^{\frac{1}{m}-1} \tag{A10}$$
$$\frac{\partial J_2\left(Z\right)}{\partial\Delta\overline{e}^{p}}=\frac{3}{2}\sum_{i=1}^{N}\gamma_i\varphi_i\chi_i w_i^{2}(\overline{\mathrm{n}}_{n+1}X_{n}^{(i)})$$
$$\frac{\partial\alpha(\Delta\overline{e}^{p})}{\partial\Delta\overline{e}^{p}}=\frac{1}{H(\Delta\overline{e}^{p})}\left[3\mu+\sum_{i=1}^{N}w_i C_i(1-\gamma_i w_i\chi_i\Delta\overline{e}^{p})+(1-\alpha(\Delta\overline{e}^{p}))k\right]$$

After the calculation of $\Delta\overline{e}^{p}$, the back stress can be updated according to Eq. A3 and the deviatoric stress can be calculated:

$$s_{n+1}=X_{n+1}+\frac{Z}{\alpha\left(\Delta\overline{e}^{p}\right)} \tag{A11}$$

Appendix B: Consistent tangent modulus

Variation of the deviatoric stress with respect to all quantities

$$\delta s_{n+1}=\delta s^{pr}_{n+1}-3\mu\Delta\overline{e}^{p}\overline{n}_{n+1}-3\mu\Delta\overline{e}^{p}\overline{n}_{n+1} \tag{B1}$$

In order to determine the formula for the consistent tangent operator, the $\delta\Delta\overline{e}^{p}$ and $\delta\overline{n}_{n+1}$ are found by taking the variation on Eq. A9:

$$\delta h(\Delta\overline{e}^{p})\alpha(\Delta\overline{e}^{p})+h(\Delta\overline{e}^{p})\delta\alpha(\Delta\overline{e}^{p})-\delta J_2(\Delta\overline{e}^{p})=0 \tag{B2}$$

The variation $\delta h(\Delta\overline{e}^{p})$ can be found by taking the variation on Eq. A8:

$$\delta h(\Delta\bar{e}^p) = k(\Delta\bar{e}^p)\delta\bar{e}^p \quad k(\Delta\bar{e}^p) = \frac{K}{m\Delta t}\left(\frac{\Delta\bar{e}^p}{\Delta t}\right)^{\frac{1-m}{m}} + \frac{dR(\bar{e}^p)}{d\bar{e}^p} \tag{B3}$$

The variation $\delta J_2(\Delta\bar{e}^p)$ is determined by Eq. A6:

$$\begin{aligned} \delta Z &= \delta s_{n+1}^{pr} - \sum_{i=1}^{M} \delta w_i X_n^{(i)} \\ \delta w_i &= \gamma_i w_i^2 \left(\frac{d\varphi_i}{d\bar{e}^p}\Delta\bar{e}^p + \varphi_i\right)\delta\bar{e}^p \end{aligned} \tag{B4}$$

Then,

$$\begin{aligned} \delta J_2(\Delta\bar{e}^p) &= \frac{3}{2}\bar{n}_{n+1}\bullet\delta s_{n+1}^{pr} + \frac{3}{2}\sum_{i=1}^{M}\gamma_i w_i^2(\bar{n}_{n+1}\bullet X_n^{(i)})x_i\delta\Delta\bar{e}^p \\ x_i &= \frac{d\varphi_i(\Delta\bar{e}_{n+1}^{p})}{d\bar{e}^p}\Delta\bar{e}^p + \varphi_i(\Delta\bar{e}_{n+1}^{p}) \end{aligned} \tag{B5}$$

And,

$$\delta\alpha(\Delta\bar{e}^p) = \frac{\delta\Delta\bar{e}^p}{h(\Delta\bar{e}^p)}\left[3\mu + \sum_{i=1}^{M} C_i w_i\,(1-\gamma_i w_i\,x_i) + (1-\alpha(\Delta\bar{e}^p))k\right] \tag{B6}$$

Taking Eqs. B3-6 into Eq. B2, $\delta\Delta\bar{e}^p$ can be solved as:

$$\delta\Delta\bar{e}^p = \frac{\frac{3}{2}\bar{n}_{n+1}\bullet\delta s_{n+1}^{pr}}{3\mu + h^*} \tag{B7}$$

The effective hardening modulus has been introduced:

$$h^* = \sum_{i=1}^{M} C_i w_i\,(1-\gamma_i w_i\,x_i\Delta\bar{e}^p) + k - \frac{3}{2}\sum_{i=1}^{M}\gamma_i w_i^2(\bar{n}_{n+1}\bullet X_n^{(i)})x_i \tag{B8}$$

Taking a variation to get:

$$\delta\bar{n}_{n+1} = \frac{1}{J_2(Z)}\left(\mathrm{I} - \frac{3}{2}\bar{n}_{n+1}\otimes\bar{n}_{n+1}\right)\bullet\left(\delta s_{n+1}^{pr} + \frac{3}{2}\sum_{i=1}^{M}\gamma_i w_i^2 X_n^{(i)} x_i\delta\bar{e}^p\right) \tag{B9}$$

A linear relation between the variations of stress and strain:

$$\delta\sigma_{n+1} = C_{n+1}^{vp}\bullet\delta\varepsilon_{n+1} \tag{B10}$$

With the consistent tangent operator:

$$C_{n+1}^{vp} = \lambda^* 1 \otimes 1 + 2\mu^* \mathrm{I} + \left(\frac{h^*}{1 + \frac{h^*}{3\mu^*}} - 3\mu^* \right) \overline{n}_{n+1} \otimes \overline{n}_{n+1}$$

$$- \frac{1 - \frac{\mu^*}{\mu}}{1 + \frac{h^*}{3\mu^*}} \sum_{i=1}^{M} \gamma_i w_i^2 x_i \left[X_n^{(i)} \otimes \overline{n}_{n+1} - \frac{3}{2} (\overline{n}_{n+1} \bullet X_n^{(i)}) \overline{n}_{n+1} \otimes \overline{n}_{n+1} \right] \tag{B11}$$

with

$$\mu^* = \mu \left(1 - \frac{3\mu \Delta \overline{e}^p}{J_2(Z)} \right)$$

$$\lambda^* = B - \frac{2}{3} \mu^*$$

$$C^e = \left(B - \frac{2}{3} \mu \right) 1 \otimes 1 + 2\mu \mathrm{I}$$

References

[1] H. W. Huang, Z. B. Wang, J. Lu, and K. Lu, 'Fatigue behaviors of AISI 316L stainless steel with a gradient nanostructured surface layer', *Acta Mater.*, vol. 87, pp. 150–160, Apr. 2015, doi: 10.1016/j.actamat.2014.12.057.

[2] Q. Li *et al.*, 'Mechanical properties and corrosion behaviors of AZ31 alloy with dual-phase glass-crystal coating', *Mater. Charact.*, vol. 154, pp. 200–211, Aug. 2019, doi: 10.1016/j.matchar.2019.05.035.

[3] Y. Sun, 'Sliding wear behaviour of surface mechanical attrition treated AISI 304 stainless steel', *Tribol. Int.*, vol. 57, pp. 67–75, Jan. 2013, doi: 10.1016/j.triboint.2012.07.015.

[4] T. Gao, Z. Sun, H. Xue, and D. Retraint, 'Effect of surface mechanical attrition treatment on high cycle and very high cycle fatigue of a 7075-T6 aluminium alloy', *Int. J. Fatigue*, vol. 139, p. 105798, Oct. 2020, doi: 10.1016/j.ijfatigue.2020.105798.

[5] T. Roland, D. Retraint, K. Lu, and J. Lu, 'Enhanced mechanical behavior of a nanocrystallised stainless steel and its thermal stability', *Mater. Sci. Eng. A*, vol. 445–446, pp. 281–288, Feb. 2007, doi: 10.1016/j.msea.2006.09.041.

[6] N. Ao *et al.*, 'The effect of residual stress and gradient nanostructure on the fretting fatigue behavior of plasma electrolytic oxidation coated Ti–6Al–4V alloy', *J. Alloys Compd.*, vol. 811, p. 152017, Nov. 2019, doi: 10.1016/j.jallcom.2019.152017.

[7] Y. Yan, W. Song, and S. Ma, 'Enhanced mechanical properties of a large-size metallic alloy through a gradient microstructure', *Mater. Sci. Eng. A*, vol. 764, p. 138193, Sep. 2019, doi: 10.1016/j.msea.2019.138193.

[8] X. H. Chen, J. Lu, L. Lu, and K. Lu, 'Tensile properties of a nanocrystalline 316L austenitic stainless steel', *Scr. Mater.*, vol. 52, no. 10, pp. 1039–1044, May 2005, doi: 10.1016/j.scriptamat.2005.01.023.

[9] X. Wu, P. Jiang, L. Chen, F. Yuan, and Y. T. Zhu, 'Extraordinary strain hardening by gradient structure', *Proc. Natl. Acad. Sci.*, vol. 111, no. 20, pp. 7197–7201, May 2014, doi: 10.1073/pnas.1324069111.

[10] K. Skowron *et al.*, 'Gradient Microstructure Induced by Surface Mechanical Attrition Treatment (SMAT) in Magnesium Studied Using Positron Annihilation Spectroscopy and Complementary Methods', *Materials*, vol. 13, no. 18, p. 4002, Sep. 2020, doi: 10.3390/ma13184002.

[11] N. R. Tao, Z. B. Wang, W. P. Tong, M. L. Sui, J. Lu, and K. Lu, 'An investigation of surface nanocrystallization mechanism in Fe induced by surface mechanical attrition treatment', *Acta Mater.*, vol. 50, no. 18, pp. 4603–4616, Oct. 2002, doi: 10.1016/S1359-6454(02)00310-5.

[12] X. Lu *et al.*, 'Crystal plasticity finite element analysis of gradient nanostructured TWIP steel', *Int. J. Plast.*, vol. 130, p. 102703, Jul. 2020, doi: 10.1016/j.ijplas.2020.102703.

[13] S. Bahl, S. Suwas, T. Ungàr, and K. Chatterjee, 'Elucidating microstructural evolution and strengthening mechanisms in nanocrystalline surface induced by surface mechanical attrition treatment of stainless steel', *Acta Mater.*, vol. 122, pp. 138–151, Jan. 2017, doi: 10.1016/j.actamat.2016.09.041.

[14] L. Bathini, M. J. N. V. Prasad, and N. P. Wasekar, 'Development of continuous compositional gradient Ni-W coatings utilizing electrodeposition for superior wear resistance under sliding contact', *Surf. Coat. Technol.*, vol. 445, p. 128728, Sep. 2022, doi: 10.1016/j.surfcoat.2022.128728.

[15] Y. Lin, Q. Yu, J. Pan, F. Duan, R. O. Ritchie, and Y. Li, 'On the impact toughness of gradient-structured metals', *Acta Mater.*, vol. 193, pp. 125–137, Jul. 2020, doi: 10.1016/j.actamat.2020.04.027.

[16] H. Ding and Y. C. Shin, 'Dislocation density-based modeling of subsurface grain refinement with laser-induced shock compression', *Comput. Mater. Sci.*, vol. 53, no. 1, Art. no. 1, Feb. 2012, doi: 10.1016/j.commatsci.2011.08.038.

[17] J. Zhao *et al.*, 'Laser shock peened Ti-6Al-4 V alloy: Experiments and modeling', *Int. J.*

Mech. Sci., vol. 213, p. 106874, Jan. 2022, doi: 10.1016/j.ijmecsci.2021.106874.
[18] A. K. Rai *et al.*, 'Study on the effect of multiple laser shock peening on residual stress and microstructural changes in modified 9Cr-1Mo (P91) steel', *Surf. Coat. Technol.*, vol. 358, pp. 125–135, Jan. 2019, doi: 10.1016/j.surfcoat.2018.11.027.
[19] J. Park *et al.*, 'Compositional gradient induced enhancement of Dzyaloshinskii–Moriya interaction in Pt/Co/Ta heterostructures modulated by Pt–Co alloy intralayers', *Acta Mater.*, vol. 241, p. 118383, Dec. 2022, doi: 10.1016/j.actamat.2022.118383.
[20] H. Wang and W. Yang, 'Nitriding simulation for polycrystals of grain size gradient', *Scr. Mater.*, vol. 50, no. 4, Art. no. 4, Feb. 2004, doi: 10.1016/j.scriptamat.2003.10.023.
[21] Q. Y. Long, J. X. Lu, and T. H. Fang, 'Microstructure and mechanical properties of AISI 316L steel with an inverse gradient nanostructure fabricated by electro-magnetic induction heating', *Mater. Sci. Eng. A*, vol. 751, pp. 42–50, Mar. 2019, doi: 10.1016/j.msea.2019.02.061.
[22] P. Dong, Z. Liu, X. Zhai, Z. Yan, W. Wang, and P. K. Liaw, 'Incredible improvement in fatigue resistance of friction stir welded 7075-T651 aluminum alloy via surface mechanical rolling treatment', *Int. J. Fatigue*, vol. 124, pp. 15–25, Jul. 2019, doi: 10.1016/j.ijfatigue.2019.02.023.
[23] Y. Lin, J. Pan, H. F. Zhou, H. J. Gao, and Y. Li, 'Mechanical properties and optimal grain size distribution profile of gradient grained nickel', *Acta Mater.*, vol. 153, pp. 279–289, Jul. 2018, doi: 10.1016/j.actamat.2018.04.065.
[24] N. Ao, D. Liu, X. Xu, X. Zhang, and D. Liu, 'Gradient nanostructure evolution and phase transformation of α phase in Ti-6Al-4V alloy induced by ultrasonic surface rolling process', *Mater. Sci. Eng. A*, vol. 742, pp. 820–834, Jan. 2019, doi: 10.1016/j.msea.2018.10.098.
[25] Z. Xiong, Y. Jiang, M. Yang, Y. Zhang, and L. Lei, 'Achieving superior strength and ductility in 7075 aluminum alloy through the design of multi-gradient nanostructure by ultrasonic surface rolling and aging', *J. Alloys Compd.*, vol. 918, p. 165669, Oct. 2022, doi: 10.1016/j.jallcom.2022.165669.
[26] K. Y. Zhu, A. Vassel, F. Brisset, K. Lu, and J. Lu, 'Nanostructure formation mechanism of α-titanium using SMAT', *Acta Mater.*, vol. 52, no. 14, pp. 4101–4110, Aug. 2004, doi: 10.1016/j.actamat.2004.05.023.
[27] H. Wei, Y. Cui, H. Cui, C. Zhou, L. Hou, and Y. H. Wei, 'Evolution of grain refinement mechanism in Cu-4wt.%Ti alloy during surface mechanical attrition treatment', *J. Alloys Compd.*, vol. 763, pp. 835–843, Sep. 2018, doi: 10.1016/j.jallcom.2018.06.043.
[28] D. Kumar Pandey, P. Kumar Verma, A. Bhattacharyya, and A. Sarkar, 'A Back-stress deconvolution method towards modelling of low cycle fatigue behavior of type 316L(N) stainless steel at room temperature', *Int. J. Fatigue*, vol. 166, p. 107297, Jan. 2023, doi: 10.1016/j.ijfatigue.2022.107297.
[29] Y. Wu, B. Guelorget, Z. Sun, R. Déturche, and D. Retraint, 'Characterization of gradient properties generated by SMAT for a biomedical grade 316L stainless steel', *Mater. Charact.*, vol. 155, p. 109788, Sep. 2019, doi: 10.1016/j.matchar.2019.109788.
[30] T. Roland, D. Retraint, K. Lu, and J. Lu, 'Fatigue life improvement through surface nanostructuring of stainless steel by means of surface mechanical attrition treatment', *Scr. Mater.*, vol. 54, no. 11, pp. 1949–1954, Jun. 2006, doi: 10.1016/j.scriptamat.2006.01.049.
[31] X. Yang, X. Wang, X. Ling, and D. Wang, 'Enhanced mechanical behaviors of gradient nano-grained austenite stainless steel by means of ultrasonic impact treatment', *Results Phys.*, vol. 7, pp. 1412–1421, 2017, doi: 10.1016/j.rinp.2017.04.002.
[32] Y. Zhang, G. Proust, D. Retraint, H. Wang, and Y. Gan, 'Predicting mechanical properties of 316L stainless steel subjected to SMAT: A sequential DEM-FEM investigation', *Int. J. Mech. Sci.*, vol. 193, p. 106173, Mar. 2021, doi: 10.1016/j.ijmecsci.2020.106173.
[33] X. Liu *et al.*, 'Effect of stacking fault energy on deformation mechanisms in Cu and Cu-30% Zn alloy with gradient structure obtained by SMAT', *J. Alloys Compd.*, vol. 865, p. 158863, Jun. 2021, doi: 10.1016/j.jallcom.2021.158863.
[34] Y. Zhang *et al.*, 'Effect of stacking fault energy on microstructural feature and back stress hardening in Cu-Al alloys subjected to surface mechanical attrition treatment', *Mater. Sci. Eng. A*, vol. 740–741, pp. 235–242, Jan. 2019, doi: 10.1016/j.msea.2018.10.106.

[35] Y. Samih, B. Beausir, B. Bolle, and T. Grosdidier, 'In-depth quantitative analysis of the microstructures produced by Surface Mechanical Attrition Treatment (SMAT)', *Mater. Charact.*, vol. 83, pp. 129–138, Sep. 2013, doi: 10.1016/j.matchar.2013.06.006.

[36] S. M. Hassani-Gangaraj, K. S. Cho, H.-J. L. Voigt, M. Guagliano, and C. A. Schuh, 'Experimental assessment and simulation of surface nanocrystallization by severe shot peening', *Acta Mater.*, vol. 97, pp. 105–115, Sep. 2015, doi: 10.1016/j.actamat.2015.06.054.

[37] K. Dai, J. Villegas, Z. Stone, and L. Shaw, 'Finite element modeling of the surface roughness of 5052 Al alloy subjected to a surface severe plastic deformation process', *Acta Mater.*, vol. 52, no. 20, pp. 5771–5782, Dec. 2004, doi: 10.1016/j.actamat.2004.08.031.

[38] C. Ye *et al.*, 'Gradient nanostructure and residual stresses induced by Ultrasonic Nano-crystal Surface Modification in 304 austenitic stainless steel for high strength and high ductility', *Mater. Sci. Eng. A*, vol. 613, pp. 274–288, Sep. 2014, doi: 10.1016/j.msea.2014.06.114.

[39] S. Ghosh, N. Bibhanshu, S. Suwas, and K. Chatterjee, 'Surface mechanical attrition treatment of additively manufactured 316L stainless steel yields gradient nanostructure with superior strength and ductility', *Mater. Sci. Eng. A*, vol. 820, p. 141540, Jul. 2021, doi: 10.1016/j.msea.2021.141540.

[40] N. R. Tao, J. Lu, and K. Lu, 'Surface Nanocrystallization by Surface Mechanical Attrition Treatment', *Mater. Sci. Forum*, vol. 579, pp. 91–108, Apr. 2008, doi: 10.4028/www.scientific.net/MSF.579.91.

[41] A. Dumay, J.-P. Chateau, S. Allain, S. Migot, and O. Bouaziz, 'Influence of addition elements on the stacking-fault energy and mechanical properties of an austenitic Fe–Mn–C steel', *Mater. Sci. Eng. A*, vol. 483–484, pp. 184–187, Jun. 2008, doi: 10.1016/j.msea.2006.12.170.

[42] J. Petit, L. Waltz, G. Montay, D. Retraint, A. Roos, and M. François, 'Multilayer modelling of stainless steel with a nanocrystallised superficial layer', *Mater. Sci. Eng. A*, vol. 536, pp. 124–128, Feb. 2012, doi: 10.1016/j.msea.2011.12.085.

[43] C. Yuan, R. Fu, D. Sang, Y. Yao, and X. Zhang, 'The tensile properties and fracture behavior of gradient nano-grained/coarse-grained zirconium', *Mater. Lett.*, vol. 107, pp. 134–137, Sep. 2013, doi: 10.1016/j.matlet.2013.05.142.

[44] M. Wen, G. Liu, J. Gu, W. Guan, and J. Lu, 'The tensile properties of titanium processed by surface mechanical attrition treatment', *Surf. Coat. Technol.*, vol. 202, no. 19, pp. 4728–4733, Jun. 2008, doi: 10.1016/j.surfcoat.2008.04.054.

[45] J. Zhou, D. Retraint, Z. Sun, and P. Kanouté, 'Comparative study of the effects of surface mechanical attrition treatment and conventional shot peening on low cycle fatigue of a 316L stainless steel', *Surf. Coat. Technol.*, vol. 349, pp. 556–566, Sep. 2018, doi: 10.1016/j.surfcoat.2018.06.041.

[46] D. Li, H. N. Chen, and H. Xu, 'The effect of nanostructured surface layer on the fatigue behaviors of a carbon steel', *Appl. Surf. Sci.*, vol. 255, no. 6, pp. 3811–3816, Jan. 2009, doi: 10.1016/j.apsusc.2008.10.037.

[47] P. Maurel, L. Weiss, P. Bocher, and T. Grosdidier, 'Effects of SMAT at cryogenic and room temperatures on the kink band and martensite formations with associated fatigue resistance in a β-metastable titanium alloy', *Mater. Sci. Eng. A*, vol. 803, p. 140618, Jan. 2021, doi: 10.1016/j.msea.2020.140618.

[48] Z. Sun *et al.*, 'Experimental study of microstructure changes due to low cycle fatigue of a steel nanocrystallised by Surface Mechanical Attrition Treatment (SMAT)', *Mater. Charact.*, vol. 124, pp. 117–121, Feb. 2017, doi: 10.1016/j.matchar.2016.12.017.

[49] C. Wang, C. Wang, L. Wang, Y. Lai, K. Li, and Y. Zhou, 'A dislocation density–based comparative study of grain refinement, residual stresses, and surface roughness induced by shot peening and surface mechanical attrition treatment', *Int. J. Adv. Manuf. Technol.*, vol. 108, no. 1–2, pp. 505–525, May 2020, doi: 10.1007/s00170-020-05413-8.

[50] Z. Chen, Z. Sun, and B. Panicaud, 'Constitutive modeling of TWIP/TRIP steels and numerical simulation of single impact during Surface Mechanical Attrition Treatment', *Mech. Mater.*, vol. 122, pp. 69–75, Jul. 2018, doi: 10.1016/j.mechmat.2018.04.005.

[51] A. Heydari Astaraee, R. Miresmaeili, S. Bagherifard, M. Guagliano, and M. Aliofkhazraei, 'Incorporating the principles of shot peening for a better understanding of surface mechanical attrition treatment (SMAT) by simulations and experiments', *Mater. Des.*, vol. 116, pp. 365–373, Feb. 2017, doi: 10.1016/j.matdes.2016.12.045.
[52] J. Zhao *et al.*, 'The tension-compression behavior of gradient structured materials: A deformation-mechanism-based strain gradient plasticity model', *Mech. Mater.*, vol. 159, p. 103912, Aug. 2021, doi: 10.1016/j.mechmat.2021.103912.
[53] J. Li and A. K. Soh, 'Modeling of the plastic deformation of nanostructured materials with grain size gradient', *Int. J. Plast.*, vol. 39, pp. 88–102, Dec. 2012, doi: 10.1016/j.ijplas.2012.06.004.
[54] W.-S. Lee, T.-H. Chen, C.-F. Lin, and W.-Z. Luo, 'Dynamic Mechanical Response of Biomedical 316L Stainless Steel as Function of Strain Rate and Temperature', *Bioinorg. Chem. Appl.*, vol. 2011, pp. 1–13, 2011, doi: 10.1155/2011/173782.
[55] J. Long, Q. Pan, N. Tao, M. Dao, S. Suresh, and L. Lu, 'Improved fatigue resistance of gradient nanograined Cu', *Acta Mater.*, vol. 166, pp. 56–66, Mar. 2019, doi: 10.1016/j.actamat.2018.12.018.
[56] H. Xu, D. Ye, and L. Mei, 'A study of the back stress and the friction stress behaviors of Ti-6Al-4V alloy during low cycle fatigue at room temperature', *Mater. Sci. Eng. A*, vol. 700, pp. 530–539, Jul. 2017, doi: 10.1016/j.msea.2017.06.051.
[57] F. K. Yan, G. Z. Liu, N. R. Tao, and K. Lu, 'Strength and ductility of 316L austenitic stainless steel strengthened by nano-scale twin bundles', *Acta Mater.*, vol. 60, no. 3, pp. 1059–1071, Feb. 2012, doi: 10.1016/j.actamat.2011.11.009.
[58] J. Lu, '8.14 Surface Nanocrystallization (SNC) of Materials and its E¡ect on Mechanical Behavior'.
[59] A. L. Ortiz, J.-W. Tian, L. L. Shaw, and P. K. Liaw, 'Experimental study of the microstructure and stress state of shot peened and surface mechanical attrition treated nickel alloys', *Scr. Mater.*, vol. 62, no. 3, pp. 129–132, Feb. 2010, doi: 10.1016/j.scriptamat.2009.10.015.
[60] R. Ji *et al.*, 'Efficient fabrication of gradient nanostructure layer on surface of commercial pure copper by coupling electric pulse and ultrasonics treatment', *J. Alloys Compd.*, vol. 764, pp. 51–61, Oct. 2018, doi: 10.1016/j.jallcom.2018.06.042.
[61] B. Cai, X. Ma, J. Moering, H. Zhou, X. Yang, and X. Zhu, 'Enhanced mechanical properties in Cu–Zn alloys with a gradient structure by surface mechanical attrition treatment at cryogenic temperature', *Mater. Sci. Eng. A*, vol. 626, pp. 144–149, Feb. 2015, doi: 10.1016/j.msea.2014.12.070.
[62] C. W. Shao, P. Zhang, Y. K. Zhu, Z. J. Zhang, Y. Z. Tian, and Z. F. Zhang, 'Simultaneous improvement of strength and plasticity: Additional work-hardening from gradient microstructure', *Acta Mater.*, vol. 145, pp. 413–428, Feb. 2018, doi: 10.1016/j.actamat.2017.12.028.
[63] A. Molotnikov, R. Lapovok, C. H. J. Davies, W. Cao, and Y. Estrin, 'Size effect on the tensile strength of fine-grained copper', *Scr. Mater.*, vol. 59, no. 11, pp. 1182–1185, Dec. 2008, doi: 10.1016/j.scriptamat.2008.08.004.
[64] X. Yang *et al.*, 'Influence of gradient structure volume fraction on the mechanical properties of pure copper', *Mater. Sci. Eng. A*, vol. 645, pp. 280–285, Oct. 2015, doi: 10.1016/j.msea.2015.08.037.
[65] Z. Y. Liang, Y. Z. Li, and M. X. Huang, 'The respective hardening contributions of dislocations and twins to the flow stress of a twinning-induced plasticity steel', *Scr. Mater.*, vol. 112, pp. 28–31, Feb. 2016, doi: 10.1016/j.scriptamat.2015.09.003.
[66] K. Lu and J. Lu, 'Nanostructured surface layer on metallic materials induced by surface mechanical attrition treatment', *Mater. Sci. Eng. A*, vol. 375–377, pp. 38–45, Jul. 2004, doi: 10.1016/j.msea.2003.10.261.
[67] H.-Y. Guo *et al.*, 'Nanocrystalline-grained tungsten prepared by surface mechanical attrition treatment: Microstructure and mechanical properties', *J. Nucl. Mater.*, vol. 480, pp. 281–288, Nov. 2016, doi: 10.1016/j.jnucmat.2016.08.032.
[68] M. Wen, G. Liu, J. Gu, W. Guan, and J. Lu, 'Dislocation evolution in titanium during

surface severe plastic deformation', *Appl. Surf. Sci.*, vol. 255, no. 12, pp. 6097–6102, Apr. 2009, doi: 10.1016/j.apsusc.2009.01.048.

[69] N. Tao, H. Zhang, J. Lu, and K. Lu, 'Development of Nanostructures in Metallic Materials with Low Stacking Fault Energies During Surface Mechanical Attrition Treatment (SMAT)', *Mater. Trans.*, vol. 44, no. 10, pp. 1919–1925, 2003, doi: 10.2320/matertrans.44.1919.

[70] Y. Wang *et al.*, 'Shear band stability and uniform elongation of gradient structured material: Role of lateral constraint', *Extreme Mech. Lett.*, vol. 37, p. 100686, May 2020, doi: 10.1016/j.eml.2020.100686.

[71] Z. Yin *et al.*, 'Strength and ductility of gradient structured copper obtained by surface mechanical attrition treatment', *Mater. Des.*, vol. 105, pp. 89–95, Sep. 2016, doi: 10.1016/j.matdes.2016.05.015.

[72] Z. Cheng, T. Wan, L. Bu, and L. Lu, 'Effect of volume fractions of gradient transition layer on mechanical behaviors of nanotwinned Cu', *Acta Mater.*, vol. 242, p. 118456, Jan. 2023, doi: 10.1016/j.actamat.2022.118456.

[73] L. Meng *et al.*, 'The influence of stacking fault energy on mechanical properties of Cu-Al-Zn alloys processed by surface mechanical attrition treatment', *Mater. Sci. Eng. A*, vol. 744, pp. 235–240, Jan. 2019, doi: 10.1016/j.msea.2018.12.021.

[74] V. Shterner, A. Molotnikov, I. Timokhina, Y. Estrin, and H. Beladi, 'A constitutive model of the deformation behaviour of twinning induced plasticity (TWIP) steel at different temperatures', *Mater. Sci. Eng. A*, vol. 613, pp. 224–231, Sep. 2014, doi: 10.1016/j.msea.2014.06.073.

[75] H. W. Zhang, Z. K. Hei, G. Liu, J. Lu, and K. Lu, 'Formation of nanostructured surface layer on AISI 304 stainless steel by means of surface mechanical attrition treatment', *Acta Mater.*, vol. 51, no. 7, pp. 1871–1881, Apr. 2003, doi: 10.1016/S1359-6454(02)00594-3.

[76] Y. Jia, Y. Liang, A. Chen, and D. Pan, 'Strain Hardening of a Layered and Nanostructured AISI 304 Stainless Steel', *J. Iron Steel Res. Int.*, vol. 21, no. 4, pp. 439–443, Apr. 2014, doi: 10.1016/S1006-706X(14)60068-6.

[77] X. Wu, N. Tao, Y. Hong, J. Lu, and K. Lu, 'γ→ε martensite transformation and twinning deformation in fcc cobalt during surface mechanical attrition treatment', *Scr. Mater.*, vol. 52, no. 7, pp. 547–551, Apr. 2005, doi: 10.1016/j.scriptamat.2004.12.004.

[78] A. Q. Lii' and Y. Li, 'EFFECT OF NANOCRYSTAUJIW AND TWIN BOUNDARIES ON CORROSION BEHAVIOR OF 316L STAINLESS STEEL USING SMAT'.

[79] G. Proust, D. Retraint, M. Chemkhi, A. Roos, and C. Demangel, 'Electron Backscatter Diffraction and Transmission Kikuchi Diffraction Analysis of an Austenitic Stainless Steel Subjected to Surface Mechanical Attrition Treatment and Plasma Nitriding', *Microsc. Microanal.*, vol. 21, no. 4, pp. 919–926, Aug. 2015, doi: 10.1017/S1431927615000793.

[80] R. Kalsar and S. Suwas, 'A novel way to enhance the strength of twinning induced plasticity (TWIP) steels', *Scr. Mater.*, vol. 154, pp. 207–211, Sep. 2018, doi: 10.1016/j.scriptamat.2018.05.045.

[81] E. O. Hall, 'The Deformation and Ageing of Mild Steel: III Discussion of Results', *Proc. Phys. Soc. Sect. B*, vol. 64, no. 9, pp. 747–753, Sep. 1951, doi: 10.1088/0370-1301/64/9/303.

[82] B. P. Kashyap and K. Tangri, 'On the Hall-Petch relationship and substructural evolution in type 316L stainless steel', *Acta Metall. Mater.*, vol. 43, no. 11, pp. 3971–3981, Nov. 1995, doi: 10.1016/0956-7151(95)00110-H.

[83] O. Muránsky, L. Balogh, M. Tran, C. J. Hamelin, J.-S. Park, and M. R. Daymond, 'On the measurement of dislocations and dislocation substructures using EBSD and HRSD techniques', *Acta Mater.*, vol. 175, pp. 297–313, Aug. 2019, doi: 10.1016/j.actamat.2019.05.036.

[84] M. F. Ashby, 'The deformation of plastically non-homogeneous materials', *Philos. Mag. J. Theor. Exp. Appl. Phys.*, vol. 21, no. 170, pp. 399–424, Feb. 1970, doi: 10.1080/14786437008238426.

[85] X. Lu, X. Zhang, M. Shi, F. Roters, G. Kang, and D. Raabe, 'Dislocation mechanism based size-dependent crystal plasticity modeling and simulation of gradient nano-grained copper',

Int. J. Plast., vol. 113, pp. 52–73, Feb. 2019, doi: 10.1016/j.ijplas.2018.09.007.
[86] M. S. Pham, S. R. Holdsworth, K. G. F. Janssens, and E. Mazza, 'Cyclic deformation response of AISI 316L at room temperature: Mechanical behaviour, microstructural evolution, physically-based evolutionary constitutive modelling', *Int. J. Plast.*, vol. 47, pp. 143–164, Aug. 2013, doi: 10.1016/j.ijplas.2013.01.017.
[87] G. Sparks, P. A. Shade, M. D. Uchic, S. R. Niezgoda, M. J. Mills, and M. Obstalecki, 'High-precision orientation mapping from spherical harmonic transform indexing of electron backscatter diffraction patterns', *Ultramicroscopy*, vol. 222, p. 113187, Mar. 2021, doi: 10.1016/j.ultramic.2020.113187.
[88] F. Ram, S. Zaefferer, T. Jäpel, and D. Raabe, 'Error analysis of the crystal orientations and disorientations obtained by the classical electron backscatter diffraction technique', *J. Appl. Crystallogr.*, vol. 48, no. 3, pp. 797–813, Jun. 2015, doi: 10.1107/S1600576715005762.
[89] G. K. Williamson and R. E. Smallman, 'III. Dislocation densities in some annealed and cold-worked metals from measurements on the X-ray debye-scherrer spectrum', *Philos. Mag.*, vol. 1, no. 1, pp. 34–46, Jan. 1956, doi: 10.1080/14786435608238074.
[90] L. Balogh, G. Ribárik, and T. Ungár, 'Stacking faults and twin boundaries in fcc crystals determined by x-ray diffraction profile analysis', *J. Appl. Phys.*, vol. 100, no. 2, p. 023512, Jul. 2006, doi: 10.1063/1.2216195.
[91] R. J. Asaro and S. Suresh, 'Mechanistic models for the activation volume and rate sensitivity in metals with nanocrystalline grains and nano-scale twins', *Acta Mater.*, vol. 53, no. 12, pp. 3369–3382, Jul. 2005, doi: 10.1016/j.actamat.2005.03.047.
[92] S. S. Hecker, M. G. Stout, K. P. Staudhammer, and J. L. Smith, 'Effects of Strain State and Strain Rate on Deformation-Induced Transformation in 304 Stainless Steel: Part I. Magnetic Measurements and Mechanical Behavior', *Metall. Trans. A*, vol. 13, no. 4, pp. 619–626, Apr. 1982, doi: 10.1007/BF02644427.
[93] M. Novelli, J.-J. Fundenberger, P. Bocher, and T. Grosdidier, 'On the effectiveness of surface severe plastic deformation by shot peening at cryogenic temperature', *Appl. Surf. Sci.*, vol. 389, pp. 1169–1174, Dec. 2016, doi: 10.1016/j.apsusc.2016.08.009.
[94] D. Molnár, X. Sun, S. Lu, W. Li, G. Engberg, and L. Vitos, 'Effect of temperature on the stacking fault energy and deformation behaviour in 316L austenitic stainless steel', *Mater. Sci. Eng. A*, vol. 759, pp. 490–497, Jun. 2019, doi: 10.1016/j.msea.2019.05.079.
[95] Y. F. Shen, X. X. Li, X. Sun, Y. D. Wang, and L. Zuo, 'Twinning and martensite in a 304 austenitic stainless steel', *Mater. Sci. Eng. A*, vol. 552, pp. 514–522, Aug. 2012, doi: 10.1016/j.msea.2012.05.080.
[96] A. Ghaderi and M. R. Barnett, 'Sensitivity of deformation twinning to grain size in titanium and magnesium', *Acta Mater.*, vol. 59, no. 20, pp. 7824–7839, Dec. 2011, doi: 10.1016/j.actamat.2011.09.018.
[97] Y. B. Lei, Z. B. Wang, B. Zhang, Z. P. Luo, J. Lu, and K. Lu, 'Enhanced mechanical properties and corrosion resistance of 316L stainless steel by pre-forming a gradient nanostructured surface layer and annealing', *Acta Mater.*, vol. 208, p. 116773, Apr. 2021, doi: 10.1016/j.actamat.2021.116773.
[98] A. Y. Chen *et al.*, 'The influence of strain rate on the microstructure transition of 304 stainless steel', *Acta Mater.*, vol. 59, no. 9, pp. 3697–3709, May 2011, doi: 10.1016/j.actamat.2011.03.005.
[99] J.-B. Seol, J. E. Jung, Y. W. Jang, and C. G. Park, 'Influence of carbon content on the microstructure, martensitic transformation and mechanical properties in austenite/ε-martensite dual-phase Fe–Mn–C steels', *Acta Mater.*, vol. 61, no. 2, pp. 558–578, Jan. 2013, doi: 10.1016/j.actamat.2012.09.078.
[100] J. Zhou, Z. Sun, P. Kanouté, and D. Retraint, 'Reconstruction of residual stress and work hardening and their effects on the mechanical behaviour of a shot peened structure', *Mech. Mater.*, vol. 127, pp. 100–111, Dec. 2018, doi: 10.1016/j.mechmat.2018.09.005.
[101] V. Pandey, K. Chattopadhyay, N. C. Santhi Srinivas, and V. Singh, 'Role of ultrasonic shot peening on low cycle fatigue behavior of 7075 aluminium alloy', *Int. J. Fatigue*, vol. 103, pp. 426–435, Oct. 2017, doi: 10.1016/j.ijfatigue.2017.06.033.
[102] Q. He, Y. F. Wang, M. S. Wang, F. J. Guo, Y. Wen, and C. X. Huang, 'Improving

strength-ductility synergy in 301 stainless steel by combining gradient structure and TRIP effect', *Mater. Sci. Eng. A*, vol. 780, p. 139146, Apr. 2020, doi: 10.1016/j.msea.2020.139146.

[103]Z. Cheng, H. Zhou, Q. Lu, H. Gao, and L. Lu, 'Extra strengthening and work hardening in gradient nanotwinned metals', *Science*, vol. 362, no. 6414, p. eaau1925, Nov. 2018, doi: 10.1126/science.aau1925.

[104]S. Kanou, M. Nishikawa, and H. Soyama, 'Analysis of the formation of plastic deformation layer on the surface of polycrystalline metals subjected to a micro-size high-rate shot impact', *Int. J. Mech. Sci.*, vol. 75, pp. 316–323, Oct. 2013, doi: 10.1016/j.ijmecsci.2013.07.014.

[105]X. L. Wu, M. X. Yang, F. P. Yuan, L. Chen, and Y. T. Zhu, 'Combining gradient structure and TRIP effect to produce austenite stainless steel with high strength and ductility', *Acta Mater.*, vol. 112, pp. 337–346, Jun. 2016, doi: 10.1016/j.actamat.2016.04.045.

[106]Z. Yin, L. Sun, J. Yang, Y. Gong, and X. Zhu, 'Mechanical behavior and deformation kinetics of gradient structured Cu-Al alloys with varying stacking fault energy', *J. Alloys Compd.*, vol. 687, pp. 152–160, Dec. 2016, doi: 10.1016/j.jallcom.2016.06.155.

[107]G. L. Huang, Dk. Matlock, and G. Krauss, 'Martensite formation, strain rate sensitivity, and deformation behavior of type 304 stainless steel sheet', *Metall. Trans. A*, vol. 20, no. 7, pp. 1239–1246, Jul. 1989, doi: 10.1007/BF02647406.

[108]J. Talonen, H. Hänninen, P. Nenonen, and G. Pape, 'Effect of strain rate on the strain-induced $\gamma \rightarrow \alpha'$-martensite transformation and mechanical properties of austenitic stainless steels', *Metall. Mater. Trans. A*, vol. 36, no. 2, pp. 421–432, Feb. 2005, doi: 10.1007/s11661-005-0313-y.

[109]K. O. Findley, J. Hidalgo, R. M. Huizenga, and M. J. Santofimia, 'Controlling the work hardening of martensite to increase the strength/ductility balance in quenched and partitioned steels', *Mater. Des.*, vol. 117, pp. 248–256, Mar. 2017, doi: 10.1016/j.matdes.2016.12.065.

[110]J. Li, S. Chen, X. Wu, and A. K. Soh, 'A physical model revealing strong strain hardening in nano-grained metals induced by grain size gradient structure', *Mater. Sci. Eng. A*, vol. 620, pp. 16–21, Jan. 2015, doi: 10.1016/j.msea.2014.09.117.

[111]X. L. Wu, P. Jiang, L. Chen, J. F. Zhang, F. P. Yuan, and Y. T. Zhu, 'Synergetic Strengthening by Gradient Structure', *Mater. Res. Lett.*, vol. 2, no. 4, pp. 185–191, Oct. 2014, doi: 10.1080/21663831.2014.935821.

[112]X. Meng *et al.*, 'The deformation behavior of AZ31 Mg alloy with surface mechanical attrition treatment', *Mater. Sci. Eng. A*, vol. 707, pp. 636–646, Nov. 2017, doi: 10.1016/j.msea.2017.09.094.

[113]C. X. Ren, Q. Wang, J. P. Hou, Z. J. Zhang, H. J. Yang, and Z. F. Zhang, 'Revealing the maximum microhardness and thickness of hardened layers for copper with various grain sizes', *Mater. Sci. Eng. A*, vol. 778, p. 139113, Mar. 2020, doi: 10.1016/j.msea.2020.139113.

[114]S. Kumar, K. Chattopadhyay, V. Singh, D. V. V. Satyanarayana, and V. Kumar, 'Low cycle fatigue life of the alloy IN718 enhanced through surface nanostructuring', *Mater. Charact.*, vol. 159, p. 110066, Jan. 2020, doi: 10.1016/j.matchar.2019.110066.

[115]C. Dureau, M. Arzaghi, R. Massion, Y. Nadot, and T. Grosdidier, 'On the high cycle fatigue resistance of austenitic stainless steels with surface gradient microstructures: Effect of load ratio and associated residual stress modification', *Mater. Sci. Eng. A*, vol. 840, p. 142916, Apr. 2022, doi: 10.1016/j.msea.2022.142916.

[116]C. W. Shao *et al.*, 'Improving the high-cycle fatigue properties of twinning-induced plasticity steel by a novel surface treatment process', *Mater. Sci. Eng. A*, vol. 740–741, pp. 28–33, Jan. 2019, doi: 10.1016/j.msea.2018.10.046.

[117]M. Ardeljan and M. Knezevic, 'Explicit modeling of double twinning in AZ31 using crystal plasticity finite elements for predicting the mechanical fields for twin variant selection and fracture analyses', *Acta Mater.*, vol. 157, pp. 339–354, Sep. 2018, doi: 10.1016/j.actamat.2018.07.045.

[118]H. Xue, Z. Sun, X. Zhang, T. Gao, and Z. Li, 'Very High Cycle Fatigue of a Cast

Aluminum Alloy: Size Effect and Crack Initiation', *J. Mater. Eng. Perform.*, vol. 27, no. 10, pp. 5406–5416, Oct. 2018, doi: 10.1007/s11665-018-3617-y.
[119]C. Wang, J. Petit, Z. Huang, and D. Wagner, 'Investigation of crack initiation mechanisms responsible for the fish eye formation in the Very High Cycle Fatigue regime', *Int. J. Fatigue*, vol. 119, pp. 320–329, Feb. 2019, doi: 10.1016/j.ijfatigue.2018.06.016.
[120]D. Kuhlmann-Wilsdorf and C. Laird, 'Dislocation behavior in fatigue II. Friction stress and back stress as inferred from an analysis of hysteresis loops', *Mater. Sci. Eng.*, vol. 37, no. 2, pp. 111–120, Feb. 1979, doi: 10.1016/0025-5416(79)90074-0.
[121]X. Feaugas, 'On the origin of the tensile flow stress in the stainless steel AISI 316L at 300 K: back stress and effective stress', *Acta Mater.*, vol. 47, no. 13, pp. 3617–3632, Oct. 1999, doi: 10.1016/S1359-6454(99)00222-0.
[122]R. J. Amodeo and N. M. Ghoniem, 'Dislocation dynamics. II. Applications to the formation of persistent slip bands, planar arrays, and dislocation cells', *Phys. Rev. B*, vol. 41, no. 10, pp. 6968–6976, Apr. 1990, doi: 10.1103/PhysRevB.41.6968.
[123]A. H. Cottrell, 'LX. The formation of immobile dislocations during slip', *Lond. Edinb. Dublin Philos. Mag. J. Sci.*, vol. 43, no. 341, pp. 645–647, Jun. 1952, doi: 10.1080/14786440608520220.
[124]X. Liu, F. Yuan, Y. Zhu, and X. Wu, 'Extraordinary Bauschinger effect in gradient structured copper', *Scr. Mater.*, vol. 150, pp. 57–60, Jun. 2018, doi: 10.1016/j.scriptamat.2018.03.007.
[125]T. Hama, T. Suzuki, S. Hatakeyama, H. Fujimoto, and H. Takuda, 'Role of twinning on the stress and strain behaviors during reverse loading in rolled magnesium alloy sheets', *Mater. Sci. Eng. A*, vol. 725, pp. 8–18, May 2018, doi: 10.1016/j.msea.2018.03.124.
[126]L. Sun, X.-G. Bao, S.-J. Guo, R.-Z. Wang, X.-C. Zhang, and S.-T. Tu, 'The creep-fatigue behavior of a nickel-based superalloy: Experiments study and cyclic plastic analysis', *Int. J. Fatigue*, vol. 147, p. 106187, Jun. 2021, doi: 10.1016/j.ijfatigue.2021.106187.
[127]C. Gaudin and X. Feaugas, 'Cyclic creep process in AISI 316L stainless steel in terms of dislocation patterns and internal stresses', *Acta Mater.*, vol. 52, no. 10, pp. 3097–3110, Jun. 2004, doi: 10.1016/j.actamat.2004.03.011.
[128]S. C. Cao *et al.*, 'A constitutive model incorporating grain refinement strengthening on metallic alloys', *J. Mater. Sci. Technol.*, vol. 88, pp. 233–239, Oct. 2021, doi: 10.1016/j.jmst.2021.02.004.
[129]H. L. Chan, H. H. Ruan, A. Y. Chen, and J. Lu, 'Optimization of the strain rate to achieve exceptional mechanical properties of 304 stainless steel using high speed ultrasonic surface mechanical attrition treatment', *Acta Mater.*, vol. 58, no. 15, pp. 5086–5096, Sep. 2010, doi: 10.1016/j.actamat.2010.05.044.
[130]Z. Chen, Z. Sun, and B. Panicaud, 'Investigation of ductile damage during surface mechanical attrition treatment for TWIP steels using a dislocation density based viscoplasticity and damage models', *Mech. Mater.*, vol. 129, pp. 279–289, Jan. 2019, doi: 10.1016/j.mechmat.2018.12.009.
[131]Y. Zhang, G. Proust, D. Retraint, H. Wang, and Y. Gan, 'Discrete element simulation of surface mechanical attrition treatment with rough-surface sonotrode', *Int. J. Mech. Sci.*, vol. 161–162, p. 105060, Oct. 2019, doi: 10.1016/j.ijmecsci.2019.105060.
[132]Z. Zeng, X. Li, D. Xu, L. Lu, H. Gao, and T. Zhu, 'Gradient plasticity in gradient nano-grained metals', *Extreme Mech. Lett.*, vol. 8, pp. 213–219, Sep. 2016, doi: 10.1016/j.eml.2015.12.005.
[133]F. Aurenhammer, 'Voronoi diagrams—a survey of a fundamental geometric data structure', *ACM Comput. Surv.*, vol. 23, no. 3, pp. 345–405, Sep. 1991, doi: 10.1145/116873.116880.
[134]Y. Huang, S. Qu, K. C. Hwang, M. Li, and H. Gao, 'A conventional theory of mechanism-based strain gradient plasticity', *Int. J. Plast.*, vol. 20, no. 4–5, pp. 753–782, Apr. 2004, doi: 10.1016/j.ijplas.2003.08.002.
[135]R. K. Abu Al-Rub and G. Z. Voyiadjis, 'A physically based gradient plasticity theory', *Int. J. Plast.*, vol. 22, no. 4, pp. 654–684, Apr. 2006, doi: 10.1016/j.ijplas.2005.04.010.
[136]Y. Estrin, 'Dislocation theory based constitutive modelling: foundations and applications',

J. Mater. Process. Technol., vol. 80–81, pp. 33–39, Aug. 1998, doi: 10.1016/S0924-0136(98)00208-8.

[137]U. F. Kocks and H. Mecking, 'Physics and phenomenology of strain hardening: the FCC case', *Prog. Mater. Sci.*, vol. 48, no. 3, pp. 171–273, Jan. 2003, doi: 10.1016/S0079-6425(02)00003-8.

[138]C. O. Frederick and P. J. Armstrong, 'A mathematical representation of the multiaxial Bauschinger effect', *Mater. High Temp.*, vol. 24, no. 1, pp. 1–26, Apr. 2007, doi: 10.3184/096034007X207589.

[139]J. L. Chaboche, 'Time-independent constitutive theories for cyclic plasticity', *Int. J. Plast.*, vol. 2, no. 2, pp. 149–188, Jan. 1986, doi: 10.1016/0749-6419(86)90010-0.

[140]W. Prager, 'A New Method of Analyzing Stresses and Strains in Work-Hardening Plastic Solids', *J. Appl. Mech.*, vol. 23, no. 4, pp. 493–496, Dec. 1956, doi: 10.1115/1.4011389.

[141]Ojima, M., 'Weak Beam TEM Study on Stacking Fault Energy of High Nitrogen Steels', *Steel Res. Int.*, no. 80 (2009) No. 7 477-481, Jul. 2009, doi: 10.2374/SRI09SP038.

[142]P. J. Brofman and G. S. Ansell, 'On the Effect of Carbon on the Stacking Fault Energy of Austenitic Stainless Steels', *Metall. Trans. A*, vol. 9, no. 6, pp. 879–880, Jun. 1978, doi: 10.1007/BF02649799.

[143]G. Meric De Bellefon, J. C. Van Duysen, and K. Sridharan, 'Composition-dependence of stacking fault energy in austenitic stainless steels through linear regression with random intercepts', *J. Nucl. Mater.*, vol. 492, pp. 227–230, Aug. 2017, doi: 10.1016/j.jnucmat.2017.05.037.

[144]A. Khorsand Zak, W. H. Abd. Majid, M. E. Abrishami, and R. Yousefi, 'X-ray analysis of ZnO nanoparticles by Williamson–Hall and size–strain plot methods', *Solid State Sci.*, vol. 13, no. 1, pp. 251–256, Jan. 2011, doi: 10.1016/j.solidstatesciences.2010.11.024.

[145]K. Venkateswarlu, A. Chandra Bose, and N. Rameshbabu, 'X-ray peak broadening studies of nanocrystalline hydroxyapatite by Williamson–Hall analysis', *Phys. B Condens. Matter*, vol. 405, no. 20, pp. 4256–4261, Oct. 2010, doi: 10.1016/j.physb.2010.07.020.

[146]S. Sinha, J. A. Szpunar, N. A. P. Kiran Kumar, and N. P. Gurao, 'Tensile deformation of 316L austenitic stainless steel using in-situ electron backscatter diffraction and crystal plasticity simulations', *Mater. Sci. Eng. A*, vol. 637, pp. 48–55, Jun. 2015, doi: 10.1016/j.msea.2015.04.005.

[147]M. Calcagnotto, D. Ponge, E. Demir, and D. Raabe, 'Orientation gradients and geometrically necessary dislocations in ultrafine grained dual-phase steels studied by 2D and 3D EBSD', *Mater. Sci. Eng. A*, vol. 527, no. 10–11, pp. 2738–2746, Apr. 2010, doi: 10.1016/j.msea.2010.01.004.

[148]S. Qin *et al.*, 'Designing structures with combined gradients of grain size and precipitation in high entropy alloys for simultaneous improvement of strength and ductility', *Acta Mater.*, vol. 230, p. 117847, May 2022, doi: 10.1016/j.actamat.2022.117847.

[149]Z. Sun *et al.*, 'Experimental study of microstructure changes due to low cycle fatigue of a steel nanocrystallised by Surface Mechanical Attrition Treatment (SMAT)', *Mater. Charact.*, vol. 124, pp. 117–121, Feb. 2017, doi: 10.1016/j.matchar.2016.12.017.

[150]S. Bahl, S. Suwas, T. Ungàr, and K. Chatterjee, 'Elucidating microstructural evolution and strengthening mechanisms in nanocrystalline surface induced by surface mechanical attrition treatment of stainless steel', *Acta Mater.*, vol. 122, pp. 138–151, Jan. 2017, doi: 10.1016/j.actamat.2016.09.041.

[151]S. R. Kalidindi, 'Modeling anisotropic strain hardening and deformation textures in low stacking fault energy fcc metals', *Int. J. Plast.*, vol. 17, no. 6, Art. no. 6, Jul. 2001, doi: 10.1016/S0749-6419(00)00071-1.

[152]Z. Yin, L. Sun, J. Yang, Y. Gong, and X. Zhu, 'Mechanical behavior and deformation kinetics of gradient structured Cu-Al alloys with varying stacking fault energy', *J. Alloys Compd.*, vol. 687, pp. 152–160, Dec. 2016, doi: 10.1016/j.jallcom.2016.06.155.

[153]K. Y. Zhu, A. Vassel, F. Brisset, K. Lu, and J. Lu, 'Nanostructure formation mechanism of α-titanium using SMAT', *Acta Mater.*, vol. 52, no. 14, Art. no. 14, Aug. 2004, doi: 10.1016/j.actamat.2004.05.023.

[154]E. Vasilev and M. Knezevic, 'Role of microstructural heterogeneities in damage

formation and fracture of oligocrystalline Mg under tensile loading', *Mater. Sci. Eng. A*, vol. 827, p. 142096, Oct. 2021, doi: 10.1016/j.msea.2021.142096.
[155]R. K. Abu Al-Rub and G. Z. Voyiadjis, 'A physically based gradient plasticity theory', *Int. J. Plast.*, vol. 22, no. 4, Art. no. 4, Apr. 2006, doi: 10.1016/j.ijplas.2005.04.010.
[156]J. Zhao *et al.*, 'The tension-compression behavior of gradient structured materials: A deformation-mechanism-based strain gradient plasticity model', *Mech. Mater.*, vol. 159, p. 103912, Aug. 2021, doi: 10.1016/j.mechmat.2021.103912.
[157]P. Chakravarty, G. Pál, and J. J. Sidor, 'The dependency of work hardening on dislocation statistics in cold rolled 1050 aluminum alloy', *Mater. Charact.*, vol. 191, p. 112166, Sep. 2022, doi: 10.1016/j.matchar.2022.112166.
[158]Y. T. Sun, X. Kong, and Z. B. Wang, 'Superior mechanical properties and deformation mechanisms of a 304 stainless steel plate with gradient nanostructure', *Int. J. Plast.*, vol. 155, p. 103336, Aug. 2022, doi: 10.1016/j.ijplas.2022.103336.
[159]Y. He, J. Gao, Y. He, and K. Shin, 'The mechanisms of γ (fcc) → ε (hcp) → α′ (bcc) and direct γ (fcc) → α′ (bcc) martensitic transformation in a gradient austenitic stainless steel', *J. Mater. Sci.*, vol. 57, no. 8, pp. 5230–5240, Feb. 2022, doi: 10.1007/s10853-022-06936-z.
[160]Y. Samih, B. Beausir, B. Bolle, and T. Grosdidier, 'In-depth quantitative analysis of the microstructures produced by Surface Mechanical Attrition Treatment (SMAT)', *Mater. Charact.*, vol. 83, pp. 129–138, Sep. 2013, doi: 10.1016/j.matchar.2013.06.006.
[161]L. Kang, X. Mi, X. Zhang, L. Xin, Y. Lu, and T. Shoji, 'Detail characterization on the microstructure evolution of nickel-base alloy 600MA via surface mechanical attrition treatment', *Mater. Charact.*, vol. 195, p. 112498, Jan. 2023, doi: 10.1016/j.matchar.2022.112498.
[162]N. Allain-Bonasso, F. Wagner, S. Berbenni, and D. P. Field, 'A study of the heterogeneity of plastic deformation in IF steel by EBSD', *Mater. Sci. Eng. A*, vol. 548, pp. 56–63, Jun. 2012, doi: 10.1016/j.msea.2012.03.068.
[163]Y. Shu, Z. Wang, H. Yang, X. Chen, J. Bai, and F. Pan, 'Optimized method for the identification of slip directions in Mg alloy based on intragranular misorientation axes analysis', *J. Mater. Res. Technol.*, vol. 23, pp. 6140–6149, Mar. 2023, doi: 10.1016/j.jmrt.2023.02.204.
[164]M. Duan, L. Luo, and Y. Liu, 'Microstructural evolution of AZ31 Mg alloy with surface mechanical attrition treatment: Grain and texture gradient', *J. Alloys Compd.*, vol. 823, p. 153691, May 2020, doi: 10.1016/j.jallcom.2020.153691.
[165]Y. Wu, B. Guelorget, Z. Sun, R. Déturche, and D. Retraint, 'Characterization of gradient properties generated by SMAT for a biomedical grade 316L stainless steel', *Mater. Charact.*, vol. 155, p. 109788, Sep. 2019, doi: 10.1016/j.matchar.2019.109788.
[166]S. Lu *et al.*, 'Grain boundary effect on nanoindentation: A multiscale discrete dislocation dynamics model', *J. Mech. Phys. Solids*, vol. 126, pp. 117–135, May 2019, doi: 10.1016/j.jmps.2019.02.003.
[167]C. Ye, J. Chen, M. Xu, X. Wei, and H. Lu, 'Multi-scale simulation of nanoindentation on cast Inconel 718 and NbC precipitate for mechanical properties prediction', *Mater. Sci. Eng. A*, vol. 662, pp. 385–394, Apr. 2016, doi: 10.1016/j.msea.2016.03.081.
[168]K. O. Kese, Z. C. Li, and B. Bergman, 'Method to account for true contact area in soda-lime glass during nanoindentation with the Berkovich tip', *Mater. Sci. Eng. A*, vol. 404, no. 1–2, pp. 1–8, Sep. 2005, doi: 10.1016/j.msea.2005.06.006.
[169]J. Gong, H. Miao, and Z. Peng, 'Analysis of the nanoindentation data measured with a Berkovich indenter for brittle materials: effect of the residual contact stress', *Acta Mater.*, vol. 52, no. 3, pp. 785–793, Feb. 2004, doi: 10.1016/j.actamat.2003.10.013.
[170]A. Heydari Astaraee, R. Miresmaeili, S. Bagherifard, M. Guagliano, and M. Aliofkhazraei, 'Incorporating the principles of shot peening for a better understanding of surface mechanical attrition treatment (SMAT) by simulations and experiments', *Mater. Des.*, vol. 116, pp. 365–373, Feb. 2017, doi: 10.1016/j.matdes.2016.12.045.
[171]J. Zhou, Z. Sun, and D. Retraint, 'Elastic and elastic-plastic stress release due to material removal in measurement of in-depth residual stresses', *Int. J. Press. Vessels Pip.*, vol. 191,

p. 104380, Jun. 2021, doi: 10.1016/j.ijpvp.2021.104380.
[172]T. Gao, Z. Sun, H. Xue, and D. Retraint, 'Effect of surface mechanical attrition treatment on high cycle and very high cycle fatigue of a 7075-T6 aluminium alloy', *Int. J. Fatigue*, vol. 139, p. 105798, Oct. 2020, doi: 10.1016/j.ijfatigue.2020.105798.
[173]Noyan. I. C., 'Residual Stress and Stress Relaxation', *Sagamore Army Mater. Res. Conf. Proc.*, 1982.
[174]M. Marciszko, A. Baczmański, C. Braham, M. Wróbel, S. Wroński, and G. Cios, 'Stress measurements by multi-reflection grazing-incidence X-ray diffraction method (MGIXD) using different radiation wavelengths and different incident angles', *Acta Mater.*, vol. 123, pp. 157–166, Jan. 2017, doi: 10.1016/j.actamat.2016.10.029.
[175]S. Wroński, K. Wierzbanowski, A. Baczmański, A. Lodini, Ch. Braham, and W. Seiler, 'X-ray grazing incidence technique—corrections in residual stress measurement—a review', *Powder Diffr.*, vol. 24, no. S1, pp. S11–S15, Jun. 2009, doi: 10.1154/1.3139054.
[176]C. Genzel, 'X-ray residual stress analysis in thin films under grazing incidence – basic aspects and applications', *Mater. Sci. Technol.*, vol. 21, no. 1, pp. 10–18, 2005, doi: 10.1179/174328405X14100.
[177]V. Hauk and H. Behnken, *Structural and residual stress analysis by nondestructive methods : evaluation, application, assessment*. Amsterdam : Elsevier, 1997. [Online]. Available: http://lib.ugent.be/catalog/rug01:000819033
[178]I. C. Noyan and J. B. Cohen, *Residual Stress*. New York, NY: Springer New York, 1987. doi: 10.1007/978-1-4613-9570-6.
[179]*Essais non-destructifs - Méthode d'essai pour l'analyse des contraintes résiduelles par diffraction des rayons X*, EN 15305:2008, avril 2009.
[180]J. Zhou, D. Retraint, Z. Sun, and P. Kanouté, 'Comparative study of the effects of surface mechanical attrition treatment and conventional shot peening on low cycle fatigue of a 316L stainless steel', *Surf. Coat. Technol.*, vol. 349, pp. 556–566, Sep. 2018, doi: 10.1016/j.surfcoat.2018.06.041.
[181]B. Fournier, M. Sauzay, C. Caës, M. Noblecourt, and M. Mottot, 'Analysis of the hysteresis loops of a martensitic steel', *Mater. Sci. Eng. A*, vol. 437, no. 2, Art. no. 2, Nov. 2006, doi: 10.1016/j.msea.2006.08.086.
[182]A. H. Cottrell, 'LX. The formation of immobile dislocations during slip', *Lond. Edinb. Dublin Philos. Mag. J. Sci.*, vol. 43, no. 341, pp. 645–647, Jun. 1952, doi: 10.1080/14786440608520220.
[183]H. Xu, D. Ye, and L. Mei, 'A study of the back stress and the friction stress behaviors of Ti-6Al-4V alloy during low cycle fatigue at room temperature', *Mater. Sci. Eng. A*, vol. 700, pp. 530–539, Jul. 2017, doi: 10.1016/j.msea.2017.06.051.
[184]J. Zhou, Z. Sun, P. Kanouté, and D. Retraint, 'Experimental analysis and constitutive modelling of cyclic behaviour of 316L steels including hardening/softening and strain range memory effect in LCF regime', *Int. J. Plast.*, vol. 107, pp. 54–78, Aug. 2018, doi: 10.1016/j.ijplas.2018.03.013.
[185]B. Fournier, M. Sauzay, C. Caës, M. Noblecourt, and M. Mottot, 'Analysis of the hysteresis loops of a martensitic steel', *Mater. Sci. Eng. A*, vol. 437, no. 2, pp. 183–196, Nov. 2006, doi: 10.1016/j.msea.2006.08.086.
[186]S. C. Roy, S. Goyal, R. Sandhya, and S. K. Ray, 'Low cycle fatigue life prediction of 316 L(N) stainless steel based on cyclic elasto-plastic response', *Nucl. Eng. Des.*, vol. 253, pp. 219–225, Dec. 2012, doi: 10.1016/j.nucengdes.2012.08.024.
[187]O. S. Hopperstad and S. Remseth, 'A return mapping algorithm for a class of cyclic plasticity models', *Int. J. Numer. Methods Eng.*, vol. 38, no. 4, pp. 549–564, Feb. 1995, doi: 10.1002/nme.1620380404.
[188]A. F. Armas, S. Hereñú, R. Bolmaro, and I. Alvarez-Armas, 'Cyclic softening mechanisms of Zircaloy-4', *J. Nucl. Mater.*, vol. 326, no. 2–3, pp. 195–200, Mar. 2004, doi: 10.1016/j.jnucmat.2004.01.004.
[189]N. Wang *et al.*, 'Influence of microstructural heterogeneity on strain partitioning behavior of metals containing columnar grains', *Mater. Sci. Eng. A*, vol. 814, p. 141247, May 2021, doi: 10.1016/j.msea.2021.141247.

[190]E. Vasilev and M. Knezevic, ‘Role of microstructural heterogeneities in damage formation and fracture of oligocrystalline Mg under tensile loading’, *Mater. Sci. Eng. A*, vol. 827, p. 142096, Oct. 2021, doi: 10.1016/j.msea.2021.142096.

[191]J. A. Muñoz and A. Komissarov, ‘Back stress and strength contributions evolution of a heterogeneous austenitic stainless steel obtained after one pass by equal channel angular sheet extrusion (ECASE)’, *Int. J. Adv. Manuf. Technol.*, vol. 109, no. 3–4, pp. 607–617, Jul. 2020, doi: 10.1007/s00170-020-05630-1.

[192]M. F. Ashby, ‘The deformation of plastically non-homogeneous materials’, *Philos. Mag. J. Theor. Exp. Appl. Phys.*, vol. 21, no. 170, pp. 399–424, Feb. 1970, doi: 10.1080/14786437008238426.

[193]B. Klusemann and D. M. Kochmann, ‘Microstructural pattern formation in finite-deformation single-slip crystal plasticity under cyclic loading: Relaxation vs. gradient plasticity’, *Comput. Methods Appl. Mech. Eng.*, vol. 278, pp. 765–793, Aug. 2014, doi: 10.1016/j.cma.2014.05.015.

[194]C. O. Frederick and P. J. Armstrong, ‘A mathematical representation of the multiaxial Bauschinger effect’, *Mater. High Temp.*, vol. 24, no. 1, pp. 1–26, Jan. 2007, doi: 10.1179/096034007X207589.

[195]A. Sarkar, M. Okazaki, A. Nagesha, P. Parameswaran, R. Sandhya, and K. Laha, ‘Mechanisms of failure under low cycle fatigue, high cycle fatigue and creep interactions in combined cycling in a type 316LN stainless steel’, *Mater. Sci. Eng. A*, vol. 683, pp. 24–36, Jan. 2017, doi: 10.1016/j.msea.2016.11.062.

[196]J. Jiang, T. B. Britton, and A. J. Wilkinson, ‘Measurement of geometrically necessary dislocation density with high resolution electron backscatter diffraction: Effects of detector binning and step size’, *Ultramicroscopy*, vol. 125, pp. 1–9, Feb. 2013, doi: 10.1016/j.ultramic.2012.11.003.

[197]S. I. Wright, D. P. Field, and M. M. Nowell, ‘Post processing effects on GND calculations from EBSD-based orientation measurements’, *IOP Conf. Ser. Mater. Sci. Eng.*, vol. 89, p. 012049, Aug. 2015, doi: 10.1088/1757-899X/89/1/012049.

[198]A. Weiß, H. Gutte, and J. Mola, ‘Contributions of ε and α′ TRIP Effects to the Strength and Ductility of AISI 304 (X5CrNi18-10) Austenitic Stainless Steel’, *Metall. Mater. Trans. A*, vol. 47, no. 1, pp. 112–122, Jan. 2016, doi: 10.1007/s11661-014-2726-y.

[199]E. Polatidis *et al.*, ‘The interplay between deformation mechanisms in austenitic 304 steel during uniaxial and equibiaxial loading’, *Mater. Sci. Eng. A*, vol. 764, p. 138222, Sep. 2019, doi: 10.1016/j.msea.2019.138222.

[200]T. T. Huang, W. J. Dan, and W. G. Zhang, ‘Study on the Strain Hardening Behaviors of TWIP/TRIP Steels’, *Metall. Mater. Trans. A*, vol. 48, no. 10, pp. 4553–4564, Oct. 2017, doi: 10.1007/s11661-017-4245-0.

[201]X. Zhang and T. Sawaguchi, ‘Twinning of deformation-induced ε-martensite in Fe-30Mn-6Si shape memory alloy’, *Acta Mater.*, vol. 143, pp. 237–247, Jan. 2018, doi: 10.1016/j.actamat.2017.10.009.

[202]E. I. Galindo-Nava and P. E. J. Rivera-Díaz-del-Castillo, ‘Understanding martensite and twin formation in austenitic steels: A model describing TRIP and TWIP effects’, *Acta Mater.*, vol. 128, pp. 120–134, Apr. 2017, doi: 10.1016/j.actamat.2017.02.004.

[203]G. B. Olson and M. Cohen, ‘Kinetics of strain-induced martensitic nucleation’, *Metall. Trans. A*, vol. 6, no. 4, pp. 791–795, Apr. 1975, doi: 10.1007/BF02672301.

[204]C. Cayron, ‘Continuous atomic displacements and lattice distortion during fcc–bcc martensitic transformation’, *Acta Mater.*, vol. 96, pp. 189–202, Sep. 2015, doi: 10.1016/j.actamat.2015.06.010.

[205]C. Cayron, F. Barcelo, and Y. D. Carlan, ‘The mechanisms of the fcc–bcc martensitic transformation revealed by pole figures’, *Acta Mater.*, vol. 58, no. 4, pp. 1395–1402, Feb. 2010, doi: 10.1016/j.actamat.2009.10.046.

[206]S. Kibey, J. B. Liu, D. D. Johnson, and H. Sehitoglu, ‘Predicting twinning stress in fcc metals: Linking twin-energy pathways to twin nucleation’, *Acta Mater.*, vol. 55, no. 20, pp. 6843–6851, Dec. 2007, doi: 10.1016/j.actamat.2007.08.042.

[207]S. Pramanik, A. A. Gazder, A. A. Saleh, and E. V. Pereloma, ‘Nucleation, coarsening and

deformation accommodation mechanisms of ε-martensite in a high manganese steel', *Mater. Sci. Eng. A*, vol. 731, pp. 506–519, Jul. 2018, doi: 10.1016/j.msea.2018.06.024.
[208]B. CINAt, 'IN CERTAIN Fe-BASE ALLOYS', *ACTA Metall.*, vol. 6, 1958.
[209]J.-K. Kim and B. C. De Cooman, 'Stacking fault energy and deformation mechanisms in Fe-xMn-0.6C-yAl TWIP steel', *Mater. Sci. Eng. A*, vol. 676, pp. 216–231, Oct. 2016, doi: 10.1016/j.msea.2016.08.106.
[210]Y. Koizumi *et al.*, 'Strain-induced martensitic transformation near twin boundaries in a biomedical Co–Cr–Mo alloy with negative stacking fault energy', *Acta Mater.*, vol. 61, no. 5, pp. 1648–1661, Mar. 2013, doi: 10.1016/j.actamat.2012.11.041.
[211]D. T. Pierce, J. A. Jiménez, J. Bentley, D. Raabe, and J. E. Wittig, 'The influence of stacking fault energy on the microstructural and strain-hardening evolution of Fe–Mn–Al–Si steels during tensile deformation', *Acta Mater.*, vol. 100, pp. 178–190, Nov. 2015, doi: 10.1016/j.actamat.2015.08.030.
[212]J. S. Aristeidakis and G. N. Haidemenopoulos, 'Constitutive and transformation kinetics modeling of ε -, α ′ -Martensite and mechanical twinning in steels containing austenite', *Acta Mater.*, vol. 228, p. 117757, Apr. 2022, doi: 10.1016/j.actamat.2022.117757.
[213]A. Dutta, D. Ponge, S. Sandlöbes, and D. Raabe, 'Strain partitioning and strain localization in medium manganese steels measured by in situ microscopic digital image correlation', *Materialia*, vol. 5, p. 100252, Mar. 2019, doi: 10.1016/j.mtla.2019.100252.
[214]N. Nakada *et al.*, 'Quantification of Large Deformation with Punching in Dual Phase Steel and Change of its Microstructure –Part II: Local Strain Mapping of Dual Phase Steel by a Combination Technique of Electron Backscatter Diffraction and Digital Image Correlation Methods', *ISIJ Int.*, vol. 56, no. 11, pp. 2077–2083, 2016, doi: 10.2355/isijinternational.ISIJINT-2016-310.
[215]K. Lu and J. Lu, 'Nanostructured surface layer on metallic materials induced by surface mechanical attrition treatment', *Mater. Sci. Eng. A*, vol. 375–377, pp. 38–45, Jul. 2004, doi: 10.1016/j.msea.2003.10.261.
[216]J. Li and A. K. Soh, 'Modeling of the plastic deformation of nanostructured materials with grain size gradient', *Int. J. Plast.*, vol. 39, pp. 88–102, Dec. 2012, doi: 10.1016/j.ijplas.2012.06.004.
[217]G.-H. Zhao, X. Xu, D. Dye, and P. E. J. Rivera-Díaz-del-Castillo, 'Microstructural evolution and strain-hardening in TWIP Ti alloys', *Acta Mater.*, vol. 183, pp. 155–164, Jan. 2020, doi: 10.1016/j.actamat.2019.11.009.
[218]G. B. Olson and M. Cohen, 'A General Mechanism of Martensitic Nucleation= Part I. General Concepts and the FCC HCP Transformation', *Metall. Trans. A*.
[219]J. W. Brooks, M. H. Loretto, and R. E. Smallman, 'Direct observations of martensite nuclei in stainless steel', *Acta Metall.*, vol. 27, no. 12, pp. 1839–1847, Dec. 1979, doi: 10.1016/0001-6160(79)90074-9.
[220]K. M. Rahman, V. A. Vorontsov, and D. Dye, 'The effect of grain size on the twin initiation stress in a TWIP steel', *Acta Mater.*, vol. 89, pp. 247–257, May 2015, doi: 10.1016/j.actamat.2015.02.008.
[221]Y. T. Zhu, X. Z. Liao, X. L. Wu, and J. Narayan, 'Grain size effect on deformation twinning and detwinning', *J. Mater. Sci.*, vol. 48, no. 13, pp. 4467–4475, Jul. 2013, doi: 10.1007/s10853-013-7140-0.
[222]T. Gorkaya, K. D. Molodov, D. A. Molodov, and G. Gottstein, 'Concurrent grain boundary motion and grain rotation under an applied stress', *Acta Mater.*, vol. 59, no. 14, pp. 5674–5680, Aug. 2011, doi: 10.1016/j.actamat.2011.05.042.
[223]J. W. Cahn and J. E. Taylor, 'A unified approach to motion of grain boundaries, relative tangential translation along grain boundaries, and grain rotation', *Acta Mater.*, vol. 52, no. 16, pp. 4887–4898, Sep. 2004, doi: 10.1016/j.actamat.2004.02.048.
[224]J. Zhao *et al.*, 'The tension-compression behavior of gradient structured materials: A deformation-mechanism-based strain gradient plasticity model', *Mech. Mater.*, vol. 159, p. 103912, Aug. 2021, doi: 10.1016/j.mechmat.2021.103912.
[225]S. Allain, J.-P. Chateau, and O. Bouaziz, 'A physical model of the twinning-induced plasticity effect in a high manganese austenitic steel', *Mater. Sci. Eng. A*, vol. 387–389, pp.

143–147, Dec. 2004, doi: 10.1016/j.msea.2004.01.060.
[226]I. Karaman, H. Sehitoglu, H. J. Maier, and Y. I. Chumlyakov, 'Competing mechanisms and modeling of deformation in austenitic stainless steel single crystals with and without nitrogen', *Acta Mater.*, vol. 49, no. 19, pp. 3919–3933, Nov. 2001, doi: 10.1016/S1359-6454(01)00296-8.
[227]Y. F. Shen, X. X. Li, X. Sun, Y. D. Wang, and L. Zuo, 'Twinning and martensite in a 304 austenitic stainless steel', *Mater. Sci. Eng. A*, vol. 552, pp. 514–522, Aug. 2012, doi: 10.1016/j.msea.2012.05.080.
[228]J. Li and A. K. Soh, 'Modeling of the plastic deformation of nanostructured materials with grain size gradient', *Int. J. Plast.*, vol. 39, pp. 88–102, Dec. 2012, doi: 10.1016/j.ijplas.2012.06.004.
[229]Z. Guo, J. Zhou, Z. Sun, D. Retraint, and B. Panicaud, 'Modelling mechanical behaviour of a gradient-microstructured material obtained by surface mechanical attrition treatment accounting for residual stresses', *Mech. Mater.*, vol. 184, p. 104713, Sep. 2023, doi: 10.1016/j.mechmat.2023.104713.
[230]L. Zhu, H. Ruan, A. Chen, X. Guo, and J. Lu, 'Microstructures-based constitutive analysis for mechanical properties of gradient-nanostructured 304 stainless steels', *Acta Mater.*, vol. 128, pp. 375–390, Apr. 2017, doi: 10.1016/j.actamat.2017.02.035.
[231]A. Ghaderi and M. R. Barnett, 'Sensitivity of deformation twinning to grain size in titanium and magnesium', *Acta Mater.*, vol. 59, no. 20, pp. 7824–7839, Dec. 2011, doi: 10.1016/j.actamat.2011.09.018.
[232]A. Chen, C. Wang, J. Jiang, H. Ruan, and J. Lu, 'Microstructure Evolution and Mechanical Properties of Austenite Stainless Steel with Gradient Twinned Structure by Surface Mechanical Attrition Treatment', *Nanomaterials*, vol. 11, no. 6, p. 1624, Jun. 2021, doi: 10.3390/nano11061624.
[233]K. M. Rahman, V. A. Vorontsov, and D. Dye, 'The effect of grain size on the twin initiation stress in a TWIP steel', *Acta Mater.*, vol. 89, pp. 247–257, May 2015, doi: 10.1016/j.actamat.2015.02.008.
[234]A. Heydari Astaraee, R. Miresmaeili, S. Bagherifard, M. Guagliano, and M. Aliofkhazraei, 'Incorporating the principles of shot peening for a better understanding of surface mechanical attrition treatment (SMAT) by simulations and experiments', *Mater. Des.*, vol. 116, pp. 365–373, Feb. 2017, doi: 10.1016/j.matdes.2016.12.045.
[235]J. Zhou, Z. Sun, P. Kanouté, and D. Retraint, 'Reconstruction of residual stress and work hardening and their effects on the mechanical behaviour of a shot peened structure', *Mech. Mater.*, vol. 127, pp. 100–111, Dec. 2018, doi: 10.1016/j.mechmat.2018.09.005.
[236]A. K. Rai *et al.*, 'Study on the effect of multiple laser shock peening on residual stress and microstructural changes in modified 9Cr-1Mo (P91) steel', *Surf. Coat. Technol.*, vol. 358, pp. 125–135, Jan. 2019, doi: 10.1016/j.surfcoat.2018.11.027.
[237]J. Zhou, Z. Sun, and D. Retraint, 'Elastic and elastic-plastic stress release due to material removal in measurement of in-depth residual stresses', *Int. J. Press. Vessels Pip.*, vol. 191, p. 104380, Jun. 2021, doi: 10.1016/j.ijpvp.2021.104380.
[238]J. Zhou, 'Experimental Study and Multi-scale Modelling of LCF Behaviour of Austenitic Steels Treated by SMAT', UNIVERSITE DE TECHNOLOGIE DE TROYES, 2018.
[239]X. C. Liu, H. W. Zhang, and K. Lu, 'Formation of nano-laminated structure in nickel by means of surface mechanical grinding treatment', *Acta Mater.*, vol. 96, pp. 24–36, Sep. 2015, doi: 10.1016/j.actamat.2015.06.014.
[240]K. Y. Zhu, A. Vassel, F. Brisset, K. Lu, and J. Lu, 'Nanostructure formation mechanism of α-titanium using SMAT', *Acta Mater.*, vol. 52, no. 14, pp. 4101–4110, Aug. 2004, doi: 10.1016/j.actamat.2004.05.023.
[241]O. Bouaziz, S. Allain, C. P. Scott, P. Cugy, and D. Barbier, 'High manganese austenitic twinning induced plasticity steels: A review of the microstructure properties relationships', *Curr. Opin. Solid State Mater. Sci.*, vol. 15, no. 4, pp. 141–168, Aug. 2011, doi: 10.1016/j.cossms.2011.04.002.
[242]S. Allain, J.-P. Chateau, and O. Bouaziz, 'A physical model of the twinning-induced plasticity effect in a high manganese austenitic steel', *Mater. Sci. Eng. A*, vol. 387–389, pp.

143–147, Dec. 2004, doi: 10.1016/j.msea.2004.01.060.
[243]O. Bouaziz and N. Guelton, 'Modelling of TWIP effect on work-hardening', *Mater. Sci. Eng. A*, vol. 319–321, pp. 246–249, Dec. 2001, doi: 10.1016/S0921-5093(00)02019-0.
[244]J. Li and A. K. Soh, 'Modeling of the plastic deformation of nanostructured materials with grain size gradient', *Int. J. Plast.*, vol. 39, pp. 88–102, Dec. 2012, doi: 10.1016/j.ijplas.2012.06.004.
[245]G.-H. Zhao, X. Xu, D. Dye, and P. E. J. Rivera-Díaz-del-Castillo, 'Microstructural evolution and strain-hardening in TWIP Ti alloys', *Acta Mater.*, vol. 183, pp. 155–164, Jan. 2020, doi: 10.1016/j.actamat.2019.11.009.
[246]E. I. Galindo-Nava and P. E. J. Rivera-Díaz-del-Castillo, 'Understanding martensite and twin formation in austenitic steels: A model describing TRIP and TWIP effects', *Acta Mater.*, vol. 128, pp. 120–134, Apr. 2017, doi: 10.1016/j.actamat.2017.02.004.
[247]S. Sinha, J. A. Szpunar, N. A. P. Kiran Kumar, and N. P. Gurao, 'Tensile deformation of 316L austenitic stainless steel using in-situ electron backscatter diffraction and crystal plasticity simulations', *Mater. Sci. Eng. A*, vol. 637, pp. 48–55, Jun. 2015, doi: 10.1016/j.msea.2015.04.005.
[248]Y. Zhang *et al.*, 'Effect of stacking fault energy on microstructural feature and back stress hardening in Cu-Al alloys subjected to surface mechanical attrition treatment', *Mater. Sci. Eng. A*, vol. 740–741, pp. 235–242, Jan. 2019, doi: 10.1016/j.msea.2018.10.106.
[249]G. Z. Liu, N. R. Tao, and K. Lu, '316L Austenite Stainless Steels Strengthened by Means of Nano-scale Twins', *J. Mater. Sci. Technol.*, vol. 26, no. 4, pp. 289–292, Apr. 2010, doi: 10.1016/S1005-0302(10)60048-5.
[250]S. Sinha, J. A. Szpunar, N. A. P. Kiran Kumar, and N. P. Gurao, 'Tensile deformation of 316L austenitic stainless steel using in-situ electron backscatter diffraction and crystal plasticity simulations', *Mater. Sci. Eng. A*, vol. 637, pp. 48–55, Jun. 2015, doi: 10.1016/j.msea.2015.04.005.
[251]X. H. Chen, J. Lu, L. Lu, and K. Lu, 'Tensile properties of a nanocrystalline 316L austenitic stainless steel', *Scr. Mater.*, vol. 52, no. 10, pp. 1039–1044, May 2005, doi: 10.1016/j.scriptamat.2005.01.023.
[252]S. Ghosh, N. Bibhanshu, S. Suwas, and K. Chatterjee, 'Surface mechanical attrition treatment of additively manufactured 316L stainless steel yields gradient nanostructure with superior strength and ductility', *Mater. Sci. Eng. A*, vol. 820, p. 141540, Jul. 2021, doi: 10.1016/j.msea.2021.141540.
[253]B. Kashyap, 'Hall-Petch relationship and substructural evolution in boron containing type 316L stainless steel', *Acta Mater.*, vol. 45, no. 6, pp. 2383–2395, Jun. 1997, doi: 10.1016/S1359-6454(96)00341-2.
[254]İ. Üçok, T. Ando, and N. J. Grant, 'Property enhancement in Type 316L stainless steel by spray forming', *Mater. Sci. Eng. A*, vol. 133, pp. 284–287, 1991, doi: https://doi.org/10.1016/0921-5093(91)90070-4.
[255]Y. Samih, B. Beausir, B. Bolle, and T. Grosdidier, 'In-depth quantitative analysis of the microstructures produced by Surface Mechanical Attrition Treatment (SMAT)', *Mater. Charact.*, vol. 83, pp. 129–138, Sep. 2013, doi: 10.1016/j.matchar.2013.06.006.
[256]C. W. Shao, P. Zhang, Y. K. Zhu, Z. J. Zhang, Y. Z. Tian, and Z. F. Zhang, 'Simultaneous improvement of strength and plasticity: Additional work-hardening from gradient microstructure', *Acta Mater.*, vol. 145, pp. 413–428, Feb. 2018, doi: 10.1016/j.actamat.2017.12.028.
[257]M. S. Pham, S. R. Holdsworth, K. G. F. Janssens, and E. Mazza, 'Cyclic deformation response of AISI 316L at room temperature: Mechanical behaviour, microstructural evolution, physically-based evolutionary constitutive modelling', *Int. J. Plast.*, vol. 47, pp. 143–164, Aug. 2013, doi: 10.1016/j.ijplas.2013.01.017.
[258]A. H. Cottrell, 'LX. The formation of immobile dislocations during slip', *Lond. Edinb. Dublin Philos. Mag. J. Sci.*, vol. 43, no. 341, pp. 645–647, 1952, doi: 10.1080/14786440608520220.
[259]W. M. Lomer, 'A dislocation reaction in the face-centred cubic lattice', *Lond. Edinb. Dublin Philos. Mag. J. Sci.*, vol. 42, no. 334, pp. 1327–1331, 1951, doi:

10.1080/14786444108561389.
[260]S. A. A. Shams *et al.*, 'Low-cycle fatigue properties of CoCrFeMnNi high-entropy alloy compared with its conventional counterparts', *Mater. Sci. Eng. A*, vol. 792, p. 139661, Aug. 2020, doi: 10.1016/j.msea.2020.139661.
[261]C. W. Shao, P. Zhang, R. Liu, Z. J. Zhang, J. C. Pang, and Z. F. Zhang, 'Low-cycle and extremely-low-cycle fatigue behaviors of high-Mn austenitic TRIP/TWIP alloys: Property evaluation, damage mechanisms and life prediction', *Acta Mater.*, vol. 103, pp. 781–795, Jan. 2016, doi: 10.1016/j.actamat.2015.11.015.
[262]I. Nikulin, T. Sawaguchi, and K. Tsuzaki, 'Effect of alloying composition on low-cycle fatigue properties and microstructure of Fe–30Mn–(6−x)Si–xAl TRIP/TWIP alloys', *Mater. Sci. Eng. A*, vol. 587, pp. 192–200, Dec. 2013, doi: 10.1016/j.msea.2013.08.061.
[263]L. Kubin and M. Sauzay, 'Persistent slip bands: The bowing and passing model revisited', *Acta Mater.*, vol. 132, pp. 517–524, Jun. 2017, doi: 10.1016/j.actamat.2017.04.064.
[264]A. D. Murphy-Leonard, D. C. Pagan, A. Beaudoin, M. P. Miller, and J. E. Allison, 'Quantification of cyclic twinning-detwinning behavior during low-cycle fatigue of pure magnesium using high energy X-ray diffraction', *Int. J. Fatigue*, vol. 125, pp. 314–323, Aug. 2019, doi: 10.1016/j.ijfatigue.2019.04.011.
[265]Z. F. Zhang, H. C. Gu, and X. L. Tan, 'Low-cycle fatigue behaviors of commercial-purity titanium', *Mater. Sci. Eng. A*, vol. 252, no. 1, pp. 85–92, Aug. 1998, doi: 10.1016/S0921-5093(98)00650-9.
[266]H. K. Yang, Y. Z. Tian, and Z. F. Zhang, 'Revealing the mechanical properties and microstructure evolutions of Fe–22Mn–0.6C–(x)Al TWIP steels via Al alloying control', *Mater. Sci. Eng. A*, vol. 731, pp. 61–70, Jul. 2018, doi: 10.1016/j.msea.2018.06.037.
[267]A. Pambudi, M. Badaruddin, and S. Sugiyanto, 'LOW-CYCLE FATIGUE OF COLD-DRAWN TYPE 304 AUSTENITIC STAINLESS STEEL IN ANNEALING CONDITIONS', *Indones. J. Eng. Sci.*, vol. 3, no. 2, pp. 039–046, Feb. 2022, doi: 10.51630/ijes.v3i2.39.
[268]Q. Yang, Q. Sun, W. Yang, Q. Hao, X. Wang, and B. Zhang, 'Correlation between microstructure evolution and mechanical response in a moderately low stacking-fault-energy austenitic Fe–Mn–Si–Al alloy during low-cycle fatigue deformation', *Mater. Sci. Eng. A*, vol. 824, p. 141766, Sep. 2021, doi: 10.1016/j.msea.2021.141766.
[269]H. Mughrabi, 'Cyclic slip irreversibility and fatigue life: A microstructure-based analysis', *Acta Mater.*, vol. 61, no. 4, pp. 1197–1203, Feb. 2013, doi: 10.1016/j.actamat.2012.10.029.
[270]K.-T. Park, K. G. Jin, S. H. Han, S. W. Hwang, K. Choi, and C. S. Lee, 'Stacking fault energy and plastic deformation of fully austenitic high manganese steels: Effect of Al addition', *Mater. Sci. Eng. A*, vol. 527, no. 16–17, pp. 3651–3661, Jun. 2010, doi: 10.1016/j.msea.2010.02.058.
[271]C. W. Shao *et al.*, 'A remarkable improvement of low-cycle fatigue resistance of high-Mn austenitic TWIP alloys with similar tensile properties: Importance of slip mode', *Acta Mater.*, vol. 118, pp. 196–212, Oct. 2016, doi: 10.1016/j.actamat.2016.07.034.
[272]K. Lu *et al.*, 'Deformation mechanisms of CoCrFeMnNi high-entropy alloy under low-cycle-fatigue loading', *Acta Mater.*, vol. 215, p. 117089, Aug. 2021, doi: 10.1016/j.actamat.2021.117089.
[273]K. Lu, A. Chauhan, D. Litvinov, M. Schneider, G. Laplanche, and J. Aktaa, 'Cooperative deformation mechanisms in a fatigued CoCrNi multi-principal element alloy: A case of low stacking fault energy', *J. Mech. Phys. Solids*, vol. 180, p. 105419, Nov. 2023, doi: 10.1016/j.jmps.2023.105419.
[274]P. Guo, L. Qian, J. Meng, S. Liu, and F. Zhang, 'Effect of Al on the low cycle fatigue deformation behavior and microstructure evolution of Fe–22Mn-0.6C TWIP steel', *J. Mater. Res. Technol.*, vol. 30, pp. 2086–2098, May 2024, doi: 10.1016/j.jmrt.2024.03.221.
[275]X. Hao *et al.*, 'Adding N to enhance low-cycle fatigue properties of high-Mn austenitic steel', *Mater. Sci. Eng. A*, vol. 897, p. 146357, Apr. 2024, doi: 10.1016/j.msea.2024.146357.
[276]S. A. A. Shams, G. Kim, J. W. Won, J. N. Kim, H. S. Kim, and C. S. Lee, 'Effect of grain size on the low-cycle fatigue behavior of carbon-containing high-entropy alloys', *Mater.*

Sci. Eng. A, vol. 810, p. 140985, Apr. 2021, doi: 10.1016/j.msea.2021.140985.
[277]A. Acharya and A. J. Beaudoin, 'Grain-size effect in viscoplastic polycrystals at moderate strains', *J. Mech. Phys. Solids*, vol. 48, no. 10, pp. 2213–2230, Oct. 2000, doi: 10.1016/S0022-5096(00)00013-2.
[278]M. Kamaya, 'Influence of grain size on fatigue strength of austenitic stainless steel (Investigation of ultimate strength dependency of fatigue strength)', *Int. J. Fatigue*, vol. 177, p. 107947, Dec. 2023, doi: 10.1016/j.ijfatigue.2023.107947.
[279]S. Kumar, K. Chattopadhyay, V. Singh, D. V. V. Satyanarayana, and V. Kumar, 'Low cycle fatigue life of the alloy IN718 enhanced through surface nanostructuring', *Mater. Charact.*, vol. 159, p. 110066, Jan. 2020, doi: 10.1016/j.matchar.2019.110066.
[280]S. A. A. Shams *et al.*, 'Low-cycle fatigue behavior and surface treatment of a twinning-induced plasticity high-entropy alloy', *Mater. Sci. Eng. A*, vol. 853, p. 143724, Sep. 2022, doi: 10.1016/j.msea.2022.143724.

Zihao GUO

Doctorat : Matériaux, Mécanique, Optique et Nanotechnologie

Année 2024

Étude expérimentale et modélisation multi-échelles des évolutions d'un acier inoxydable induites par SMAT

Ce travail explore la réponse mécanique et l'évolution microstructurale associée de matériaux traités par SMAT. Des analyses expérimentales complètes sont menées pour étudier en profondeur la microdureté, les contraintes résiduelles et les microstructures dans un acier inoxydable 316L traité par SMAT. La réponse à la déformation cyclique de l'acier traité par SMAT est également analysée à différentes amplitudes de déformation, afin d'examiner le comportement macroscopique en fatigue oligocyclique. De plus, des analyses comparatives des microstructures entre des échantillons à l'état initial et des échantillons traités par SMAT fournissent des informations sur le comportement macroscopique et microscopique pendant la fatigue oligocyclique. Un modèle basé sur la densité de dislocations, incorporant la plasticité induite par transformation, la plasticité induite par maclage et les effets de la taille des grains, est introduit pour décrire les réponses en traction, en tenant particulièrement compte des différentes énergies de défaut d'empilement associées aux mécanismes de déformation. L'influence du maclage dynamique et des contraintes résiduelles sur la réponse en traction est étudiée à l'aide d'un modèle par éléments finis en 2D. De plus, un modèle basé sur des principes physiques est développé pour relier la réponse à la déformation cyclique à l'évolution microstructurale correspondante. Les effets de la taille des grains et du maclage mécanique sur les comportements de déformation cyclique sont pris en compte.

Mots clés : traitements de surface – modélisation multi-échelle – acier inoxydable – microstructure (physique) – écrouissage – fatigue oligocyclique.

Experimental Study and Multi-scale Modeling of Stainless Steel Evolutions Induced by SMAT

This work explores the mechanical response and associated microstructural evolution of SMATed materials. Comprehensive experimental analyses are conducted to investigate the in-depth microhardness, residual stress and microstructures in SMATed 316L stainless steel. The cyclic deformation response of SMATed 316L stainless steel is also analyzed at different strain amplitudes to examine the macroscopic low cycle fatigue behavior. In addition, comparative analyses of microstructures between as-received and SMATed samples provide insights into both macroscopic and microscopic behavior during low cycle fatigue. A dislocation density-based model, incorporating transformation-induced plasticity, twinning-induced plasticity and grain size effects, is introduced to describe the tensile responses, particularly considering the different stacking fault energy associated with the deformation mechanisms. The influence of dynamic twinning and residual stress on tensile response is studied using a 2D finite element model. Moreover, a physically-based model is developed to link the cyclic deformation response with the corresponding microstructural evolution. The effects of grain size and mechanical twining on cyclic deformation behavior are considered. The effect of SMAT on cyclic deformation response is ultimately discussed based on the microstructural features.

Keywords: surface treatment – multiscale modeling – stainless steel – microstructure – strain hardening – low cycle fatigue.

Thèse réalisée en partenariat entre :

Ecole Doctorale "Sciences pour l'Ingénieur"